Sede Amministrativa: *Università degli Studi di Padova*

CISAS - Centro d'Ateneo di studi ed Attività Spaziali "G. Colombo"

SCUOLA DI DOTTORATO DI RICERCA IN: Scienze Tecnologie e Misure Spaziali (STMS)

INDIRIZZO: Misure Meccaniche per l'Ingegneria e lo Spazio (MMIS)

CICLO XXX

Design and testing of a vision based navigation system for a spacecraft formation flying simulator

Direttore della Scuola: *Ch.mo Prof. Giampiero Naletto*

Coordinatore d'indirizzo: *Ch.mo Prof. Stefano Debei*

Supervisore: *Ch.mo Prof. Enrico Lorenzini*

Co-supervisori: *Dott. Andrea Valmorbida, Dott. Ing. Marco Pertile*

Dottorando: *Mattia Mazzucato*

Alla mia famiglia

Abstract

In the last decades, Spacecraft Formation Flight (SFF) and proximity operations have aroused a great deal of interest within the international space community for the wide range of advantages generated with respect to traditional mission architectures. The idea of distributing the capabilities of space systems over multiple satellites, in general, results in lower development costs, redundancy to failure, flexibility and improved measurement performances of the payloads. Moreover, in sight of the extension of the operational lifetimes of orbiting spacecraft, performing on orbit inspections, maintenance and repair provides significant advantages from an economical point of view. Nonetheless, all these advantages comes at a cost as the execution of coordinated maneuvers between two or more spacecraft impose requirements not only on the absolute state, but also on the relative dynamic state. This reason pushes researchers and institutions to advance, from a technical and technological point of view, the development of accurate and robust Guidance, Navigation and Control (GN&C) strategies to enable the autonomous execution of relative navigation tasks on orbit. Prior to be accepted for the flight, each strategy has to be validated in a relevant and representative environment: one popular and effective way to reach this objective is means of ground-based testbeds.

The current work focuses on the development of vision based estimation strategies for relative navigation tasks in the context of Spacecraft Formation Flight and proximity operations. In order to validate the developed GN&C strategies in a relevant environment, part of my activities are focused on the development and realization of the cooperating spacecraft testbed for autonomous proximity operations experiments, called SPARTANS, whose design and realization started in 2010 at the Center of Studies and Activities for Space (CISAS) "G. Colombo" of the University of Padova. SPARTANS is a ground-based hardware simulator that features robotic units that allow to reproduce the relative motion of two ore more spacecraft flying in formation or in close

proximity, allowing therefore to validate advanced relative GN&C strategies developed within this context.

The first activity of my Ph.D. regards the characterization of a monocular vision system for relative pose estimation in the context of cooperative spacecraft. An original custom-made set of fiducial markers is proposed along with the required image analysis procedure to extract relevant points from the acquired images. The estimation of the relative pose is obtained by solving the perspective-from-three points problem followed by a subsequent pose refinement procedure. The metrological performances of the proposed approach are assessed following an experimental approach: known displacements are imposed to a satellite mock-up and, by comparing the estimated poses with the imposed ones, the measurement error is characterized. Finally an uncertainty analysis, validated by a series of tests, was performed yielding an average accuracy of about 1 cm and 1 deg on the relative position and attitude, respectively.

This activity is followed by the implementation of new features for the SPARTANS testbed. At the beginning of my Ph.D., the testbed featured only one spacecraft module capable of performing 3 degrees of freedom attitude maneuvers exploiting the measurements coming from incremental quadrature encoders and actuating control actions thanks to a cold gas thrusters system. A small contribution is initially given in the development of the Translational Module (TM), that enables low friction planar displacements to the robotic platforms, and in the design and development of the laboratory test table that provides the testbed with a planar surface on top of which the spacecraft simulators can translate. Subsequently, I was involved in the realization, from a practical point of view, of the laboratory setup: in particular, the second main activity I have been working on regards the development, the implementation and the characterization of a global navigation system that allows to estimate the position and the orientation of each spacecraft module within the laboratory operative volume. The first step of this activity consists in the development of a cost-effective prototype based on a monocular system and a set of three Optical Flow Sensors to obtain planar pose estimations of the TM. The estimation scheme relies on two sets of measurements that are conveniently merged by means of an Extended Kalman Filter. The second development phase consists in the extension of the proposed estimation approach by adapting it to the laboratory characteristics: a Motion Capture system consisting of six infrared cameras is employed to this purpose. A pose estimation strategy is proposed

in this context and a proper calibration procedure is developed. The results of the characterization of the Motion Capture system shows sub-degree and sub-millimeter accuracy respectively on the estimated orientations and positions, allowing to obtain reference measurements to assess the performances of the GN&C algorithms tested with the spacecraft simulator.

The last part of my activity is focused on the development of a relative navigation strategy based on an Extended Kalman Filter that exploits only visual data provided by a stereoscopic vision system. The proposed estimation scheme relies on the a priori knowledge of the geometry of the observed object (target) and it is implemented in C++ in sight of a foreseen implementation on embedded systems. The filter capabilities are assessed by means of numerical simulations in two different scenarios. In the first scenario, the relative dynamic state of two spacecraft orbiting in a leader-follower formation at short range is simulated numerically by means of a software orbital propagator. In the second scenario, the operative conditions of the laboratory setup are reproduced by means of a 3D simulated environment. Finally, the proposed navigation strategy is validated by means of laboratory testing exploiting the robotic spacecraft units. The proposed navigation algorithm proves to be capable of estimating the relative dynamic state of an observed target with centimeter-level and degree-level accuracy.

In its current configuration, the SPARTANS testbed features a first complete spacecraft unit, a 3 x 2 m flat test table, a global navigation system consisting of 6 infrared cameras and an external control station. Once the construction of the second spacecraft unit will be completed, the testbed will allow to perform coordinated maneuvers between two (or more) spacecraft units for the study and validation of strategies related to SFF, automated rendez-vous and docking and, in general, proximity maneuvers.

Sommario

Negli ultimi decenni, il volo in formazione e le manovre di prossimità sono applicazioni che hanno suscitato un crescente interesse in ambito spaziale per i vantaggi ad ampio spettro forniti rispetto alle tradizionali architetture di missione. L'idea di sostituire un singolo satellite con sistemi satellitari formati da più unità, in generale, ha il risultato di ridurre i costi di sviluppo, di garantire maggiore robustezza alle avarie, un maggiore livello di flessibilità e migliori prestazioni di misura. In aggiunta, la prospettiva di estendere il periodo operativo di sistemi satellitari attualmente in orbita attraverso operazioni di ispezione, manutenzione e riparazione, apre la possibilità di ottenere grandi vantaggi da un punto di vista economico. Tuttavia, i citati vantaggi si scontrano con la necessità di sviluppare adeguate strategie di Guida, Navigazione e Controllo (GN&C) con requisiti non solo sulla dinamica assoluta di ogni satellite, ma anche sul loro stato relativo. Questo aspetto spinge ricercatori e istituzioni allo sviluppo di adeguate tecniche di GN&C che permettano l'esecuzione autonoma e affidabile di manovre coordinate tra più satelliti in orbita. Perché una nuova proposta o strategia sia considerata matura per essere impiegata in uno scenario spaziale, è necessario dimostrarne l'affidabilità e l'efficacia in un ambiente rappresentativo di quello spaziale. Una delle più interessanti metodologie per raggiungere questo obiettivo prevede l'utilizzo di simulatori satellitari di terra.

Il presente lavoro si focalizza sullo sviluppo di strategie di stima basate su sistemi di visione per la gestione delle fasi di navigazione relativa tra satelliti nell'ambito del volo in formazione e, più generale, delle operazioni di prossimità che coinvolgano due o più satelliti. Con il fine di validare le strategie di GN&C sviluppate, parte delle mie attività ha riguardato lo sviluppo e la realizzazione del simulatore satellitare di terra, chiamato SPARTANS, in sviluppo dal 2010 presso il Centro di Ateneo di Studi e Attività Spaziali (CISAS) "G. Colombo" dell'Università di Padova. Questo simulatore satellitare presenta unità robotiche che permettono di simulare a terra moti relativi, sia

rotazionali che traslazionali, tra unità satellitari operanti in formazione o in prossimità. Questa caratteristica fondamentale permette la validazione, da un punto di vista sperimentale, delle strategie di GN&C sviluppate.

La prima attività svolta durante il mio dottorato riguarda la caratterizzazione, da un punto di vista metrologico, di un sistema di visione monoculare utilizzato per stime di posa relative nel contesto di satelliti cooperanti. Un contributo originale consiste nella proposta di un set di 'fiducial markers' per i quali è stata sviluppata un apposita procedura di analisi d'immagine con lo scopo di estrarre punti salienti dalle immagini acquisite. La procedura di stima della posa si basa sulla soluzione del problema noto come 'Perspective-from-Three Points' (P3P), soluzione che successivamente viene raffinata per via di una procedura iterativa, seguita a sua volta da un'ottimizzazione non lineare. La caratterizzazione dell'algoritmo di misura proposto segue un approccio sperimentale: un modello semplificato, rappresentativo della geometria di un satellite è impiegato come satellite target la cui posa, in relazione al sistema di visione, rappresenta l'incognita da stimare. Al satellite target, in questo contesto, sono imposti spostamenti noti sia in termini traslazionali che rotazionali e, attraverso il confronto tra gli stati imposti e quelli misurati, viene determinato l'errore di stima. Infine un'analisi di incertezza è stata effettuata fornendo indicazioni, supportate dai risultati della campagna di test sperimentali, sull'accuratezza media di stima che risulta essere dell'ordine di 1 cm e di 1^o sulla posizione e sull'orientazione relativa rispettivamente.

La seconda attività del mio dottorato riguarda lo sviluppo e l'implementazione di nuove funzionalità per il simulatore SPARTANS. All'inizio del mio dottorato, il setup sperimentale consisteva di una sola unità satellitare capace di effettuare manovre d'assetto a tre assi utilizzando come dati di navigazione le misure fornite da un sistema di encoder ottici in quadratura, e eseguendo azioni di controllo grazie a un sistema di thrusters a gas freddo. In una prima fase, ho fornito un piccolo contributo allo sviluppo del Modulo di Traslazione (TM), che abilita spostamenti planari a basso attrito per le unità satellitari, e alla progettazione e sviluppo di una tavolo piano per il laboratorio che fornisce di fatto la base su cui le unità satellitari possono traslare. Successivamente, il mio apporto si è focalizzato sull'implementazione delle componenti hardware per di laboratorio. In particolare l'attività principale in questo contesto riguarda la progettazione, l'implementazione e la caratterizzazione di un sistema di navigazione globale con lo scopo di stimare la posizione e l'orientazione delle unità

satellitari all'interno del volume operativo del laboratorio. Quest'attività consiste di due fasi principali. Dapprima un prototipo a basso costo è stato realizzato utilizzando come sensori un sistema di visione monoculare accoppiato a un set di tre sensori ottici di tipo mouse (Optical Flow Sensors - OFS) per stimare la posa planare del TM. La strategia di stima si basa su due set di misure, fornite con diverse frequenze di acquisizione, le quali sono fuse opportunamente per mezzo di un filtro di Kalman esteso (Extended Kalman Filter - EKF). La seconda fase di sviluppo estende lo schema di stima sviluppato adattandolo al setup complessivo del laboratorio. Nel fare questo, il sistema monoculare è sostituito da un sistema di Motion Capture composto da sei camere operanti nell'infrarosso e da una Control Station. In questo contesto, una strategia per la stima della posa delle unità satellitari è proposta assieme alla definizione di una procedura di calibrazione per il sistema di Motion Capture. I risultati ottenuti attestano la capacità dell'approccio di misura di fornire stime di posa con incertezze inferiori al millimetro sulla posizione e al grado sull'orientazione.

Nella parte finale del mio dottorato, le mie attività si sono incentrate sullo sviluppo di una strategia di stima per la navigazione relativa tra due spacecraft basata su un filtro di Kalman esteso (EKF), il quale incorpora solamente le misure fornite da un sistema di visione stereo montato a bordo del satellite chaser. L'approccio alla stima presuppone che la geometria del target sia nota nel momento in cui le manovre di prossimità hanno inizio. Nell'ottica di una futura implementazione dello schema di filtraggio a bordo delle unità satellitari del simulatore di terra, il filtro è stato scritto in linguaggio C/C++. Le prestazioni del filtro di navigazione sviluppato sono quindi valutate in due differenti scenari. Nel primo scenario, il filtro è applicato ad un contesto spaziale nel quale il moto orbitale di due satelliti è riprodotto per via numerica. Nel secondo caso invece, le condizioni operative del setup di laboratorio sono modellate in un ambiente di simulazione 3D. La strategia di navigazione è in ultima istanza testata per via sperimentale grazie all'utilizzo del simulatore satellitare. L'algoritmo di navigazione proposto dimostra di essere capace di stimare lo stato relativo tra i due satelliti con accuratezze dell'ordine del centimetro sulla posizione e del grado sull'orientazione.

Nello stato attuale, il simulatore satellitare di terra SPARTANS si compone di un'unità satellitare completa, di un tavolo di test con una superficie di $3 \text{x} 2$ m^2, di un sistema di navigazione globale basato sul sistema di Motion Capture e di una Control Station esterna. Nel momento in cui la costruzione della seconda unità satel-

litare sarà ultimata, il simulatore permetterà l'esecuzione di manovre coordinate per l'investigazione e lo studio di problematiche relative a volo in formazione, rendez-vous and docking e, in generale, manovre di prossimità.

Aknowledgments

I would like to express my deepest gratitude to my supervisor Prof. Enrico Lorenzini for his continuous guidance and invaluable support, both from a professional and a personal point of view, throughout my Ph.D. I would like to thank Prof. Marco Pertile for the fruitful discussions and for providing me with new ideas and challenges. My sincere and deep gratitude goes to Dott. Andrea Valmorbida for his invaluable suggestions and encouragement, and for sharing the with me his expretise and passion in facing, day by day, new challenges.

Contents

List of Figures

List of Tables

Chapter 1

Introduction

The idea of Spacecraft Formation Flight (SFF) and proximity operations has its origin in the work of Clohessy and Wiltshire that, in the 1960's, presented a closed form solution to the rendez-vous problem providing a guidance strategy to enable the rendez-vous of satellites in circular orbit [1].

Starting from the 1990's, the idea of distributing the capabilities of a space system over multiple spacecraft flying in formation started gaining popularity in the international space community. This is due to the fact that, since the beginning of the space exploration era, the requirements for spacecraft has increased constantly over the years, leading to the necessity of designing and manufacturing satellites with increasing dimensions, level of complexity and cost. This fact represents a critical aspect in terms of reliability of monolithic large spacecraft as the possibility of occurrence of minor unpredicted events may lead to catastrophic events with a consequent failure of the whole mission.

SFF allows to overcome many limitations and downsides of the traditional monolithic mission architectures. In particular it provides: (1) better performances as the distribution of instruments and tasks allows to overcome the mass and volume limitations imposed by the available launchers; (2) new capabilities (i.e. performing simultaneous measurements at different locations); (3) robustness to failure, provided by an inherent redundancy of the system which lowers the probability that the failure of a single component of the formation leads to the failure of the whole formation; and (4) cost reduction due to lower costs for the launches and to the possibility of employing, at some extent, series production. The aforementioned advantages make this mission architecture very appealing for applications like interferometry, imaging, data relay

and Earth gravitational field mapping.

Nonetheless, distributed payloads impose stringent requirements on the relative position and orientation of the members of the formation. This aspect has important aftermaths as: (1) it requires the definition, the development and the implementation of accurate and reliable Guidance, Navigation and Control (GN&C) strategies; (2) often, the development of new kind of sensors and actuators is required to fulfill the relative navigation requirements; (3) inter-satellite communications are required to continuously assess the relative dynamic state between the members of the formation.

The executions of autonomous proximity operations is of great interest for applications like on-orbit servicing (OOS), active debris removal (ADR), comet and asteroid exploration and in-space modular assembly. The need of autonomy in this field is dictated by the fact that, in many practical scenarios, the idea of controlling the spacecraft operations from the ground is not feasible due to possible lacks of coverage or delays in the communications. One of the key components that enable the execution of these operations is the capability of an active spacecraft of determining its dynamic state with respect to a target object, that may be either artificial or natural, cooperative or not cooperative. The complexity of this task is strictly related to the nature of the observed object (target) and to the information available on the target characteristics. The choice of the navigation sensors and techniques therefore has to be performed according to the specific scenario under investigation.

As regards the execution of proximity operations with respect to a cooperative space objects, the chaser spacecraft is provided with all the information necessary to estimate its pose with respect to the target. Actively cooperating targets exploits dedicated communication links with the chaser as in the case of SFF or OOS operations. In the case of uncooperative targets, two different scenarios can be identified, depending on whether the geometrical information of the target are available or they are completely unknown: the first case can occur for OOS or ADR missions whenever the target, which may be an orbiting spacecraft or a debris, is already on orbit when the inspection/servicing mission is conceived and at least a simplified model of the object is provided; the second case is instead relevant whenever a chaser satellite has to deal with completely unknown targets as in the case of some active debris removal scenarios as well as comets and asteroid exploration.

Without regard of the specific considered mission profile, all the aforementioned

scenarios require the development of robust and accurate relative GN&C algorithms along with sensors and actuators architectures that have to be validated in relevant environments prior to be employed on orbit. Ground-based testbeds are employed from the beginning of the space exploration era to this purpose as a valuable mean for the validation on the ground of space systems since they allow to reproduce, at some extent, the actual orbital operative environment. Even though on-orbit testing provides the ideal environmental conditions to validate space systems, the possibility of performing extensive test campaign for technological validation purposes is a matter of concern due to the limited possibility of interacting with the payload and changing its configuration. With respect to this aspect, ground-based facilities respond to the need of interacting in a reliable and fault-tolerant way with the spacecraft modules during the design and validation phases, allowing to reproduce the behavior of spacecraft flying in close proximity. Moreover they represent a cost-effective, controllable, easy accessible and flexible way to interact with the space systems during the development and validation phases.

Several testbeds for formation flight are present on the ground in form of robotic systems. To name a few, JPL-Caltech developed the Formation Control Testbed (FCT), DLR is active in this research field with the Test Environment for Applications of Multiple Spacecraft (TEAMS) and Georgia Tech realized the Autonomous Spacecraft Testing of Robotic Operations in Space (ASTROS). These systems allow combined rotational and translational motions up to five degrees of freedom. The MIT Synchronized Position Hold Engage and Reorient Experimental Satellite (SPHERES) project is peculiar as it can be used into two different configurations: on the ground it provides the capability of performing planar motions while, on-board the International Space Station, it operates in a fully representative microgravity environment with six degrees of freedom motions allowed.

1.1 Spacecraft Formation Flight missions

Spacecraft Formation Flight involves the employment of two or more satellites operating in a cooperative scenario and, in general, with the same instrumentation on board. The idea of distributing a payload over several spacecraft units allow to obtain improvements in the measurement performances due to the fact that the resulting

payload can be compared to a single measurement instrument with increased capabilities. This improvement on the measurement performances therefore can be ascribed to the possibility of obtaining larger measurement areas and/or increased measurement resolutions.

Currently, numerous spacecraft formations are operative and more are planned to be launched in the future. Some of them are described in the following part of this section.

The TanDEM-X mission, developed by the German Space Agency (DLR), is conceived with the aim of acquiring Digital Elevation Models of the Earth with a horizontal and vertical resolutions of respectively 12 m and 2 m, as a new reference for commercial and scientific applications. The formation consists of two satellites flying in close formation, each provided with radar remote sensing instrumentation to form a radar interferometer with a baseline of 1 km. The mission started in 2010 and successfully performed the acquisition tasks for the subsequent years.

The GRACE (Gravity Recovery and Climate Experiment) mission is another successful formation flight mission involving two spacecraft orbiting in a Low Earth orbit. The mission, resulting from a partnership between DLR and NASA, is aimed at measuring the Earth's gravity field anomalies to gather important informations in the fields of geology, oceanography and climate evolution. The mission, launched in 2002, consists of two twin spacecraft flying in a leader-follower configuration in a polar orbit and equipped with laser range systems, GPS receivers and accelerometers. The achievement of the mission goals relies on the accurate measurement of the relative position of the two satellites (10 μm) allowing to extract information on the differential accelerations acting on the two spacecraft due to the gravity field anomalies.

The Evolved Laser Interferometer Space Antenna (eLISA) is a ESA mission designed to detect and accurately measure gravitational waves. Three spacecraft arranged in an equilateral triangle with 1 million-kilometers arms are planned to be inserted in a Earth-like heliocentric orbit. eLISA will observe gravitational waves by measuring differential changes in the length of its arms, as sensed by laser interferometry. The mission is planned to be launched in 2034.

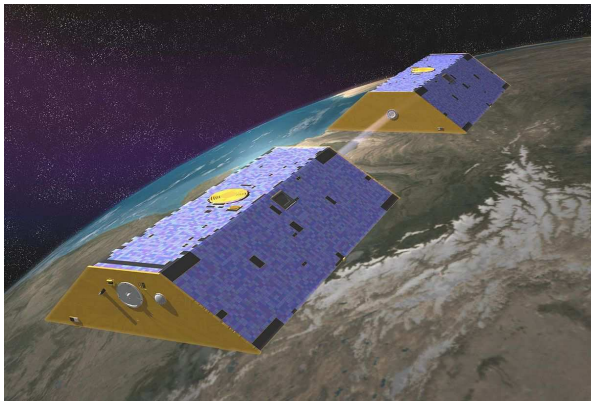
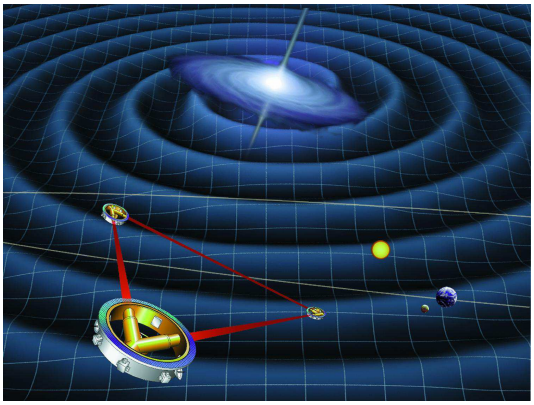

Figure 1.1: Artist's conception of GRACE (left) and LISA (right).

1.2 Spacecraft proximity operations

Over the years a great variety of sensors have been employed for proximity navigation. One of the first examples of autonomous relative navigation systems is the Russian Kurs system, employed for the rendez-vous of the Soyuz and Progress vehicles with the Russian space station first, and then with the International Space Station. This system relies on Radio-Frequency antennas that allow to measure relative range, range-rate, and attitude [2]. However this technology is not suitable for space applications based on small spacecraft, for which power and mass budgets are limited.

Another solution in which the target is considered actively cooperative consists in the use of satellite navigation technology. In particular, it requires the employment of Global Navigation Satellite System (GNSS) receivers and antennas on board the chaser and the target, as well as the presence of a communication link between the spacecraft units to the purpose of exchanging measurements. Even if this technology can lead to good accuracies in range estimations [3], it does not provide any information about the attitude and, furthermore, accurate positioning in close proximity is not guaranteed due to possible multi-path phenomena and partial occlusions of the GNSS signals.

Given the limitations of the RF-based and GNSS-based technologies, Opto-Electronic (OE) devices represent the best available option to enable pose estimation capabilities in close proximity. These sensors can be active, as in the case of Light Detection and Ranging (LIDAR) system, or passive, as in the case of monocular or stereo cameras. One of the advantageous aspects related to the employment of these systems is that they does not require any data to be exchanged with the target spacecraft in order pro-

vide pose estimations. Moreover, they represent the only available solution for relative navigation in close proximity to completely uncooperative targets.

In the last two decades, vision-based systems able to estimate the complete pose of a cooperative targets are developed and tested in space as technological demonstrators aimed at enabling OOS and SFF capabilities.

In the context of the 7th mission of the Engineering Test Satellite Program (ETS-VII), launched in 1997, the Proximity Operation Sensor (PXS) designed by the National Space Development Agency of Japan was used for relative navigation during the docking phase with the target. In particular, PXS allowed to obtain estimations of the relative position and orientation of the target and chaser docking frames. ETS-VII was the first unmanned spacecraft to conduct autonomous rendezvous docking operations successfully.

The US-sponsored DARPA's Orbital Express mission, launched in 2007, was conceived as a technological demonstrator aimed at validating several satellite servicing operations and technologies including rendez-vous, proximity operations, capture, docking, fluid transfer and orbital replacement units (ORU) transfer. The mission consisted of two spacecraft: the Boeing's ASTRO spacecraft, equipped with a robotic arm and with an embedded monocular system, and the NEXTsat satellite conceived as a serviceable unit and equipped with corner cube reflectors. The principal docking sensor employed during this mission was the Advanced Video Guidance Sensor (AVGS), employed also on the partially successful DART mission. Orbital express proved to be successful in achieving all the mission objectives, including the replacement of a functional computer ORU.

The PRISMA program is a cooperative effort between Swedish National Space Board (SNSB), Centre National d'Etudes Spatiales (CNES), German aerospace research center (DLR) and the Danish Technical University (DTU) aimed at performing on orbit GN&C demonstrations and sensor technology experiments for a family of future missions for which formation flight and proximity operations are fundamental prerequisites. The PRISMA mission was launched in 2010 and consists of two spacecraft namely Mango, the chaser, and Tango, the target. In this context the Vision Based Sensor was one of the primary navigation sensors being tested during the mission. The visual navigation system consisted in two cameras mounted aboard Mango, and a set of active markers (LEDs) on the target. In particular, a far range camera

is employed to provide line-of-sight only navigation capabilities up to 500 km, while a short range camera allows to carry out pose determination, by imaging target's LEDs, in the interval of distances that goes from a few tens of meters to few centimeters.

1.3 Thesis outline

In the last seven years, a team of Ph.D. students, Master Degree students and some CISAS researchers leaded by prof. Enrico Lorenzini of the Department of Industrial Engineering (DII) at the University of Padova has been, and some of them are, currently involved in research activities concerning SFF and OOS.

In this context, the cooperating SPAcecRaft Testbed for Autonomous proximity operatioNs experimentS (SPARTANS) project is being developed and tested with the aim of providing a testing facility, as representative as possible of the orbital environment, to allow the execution on the ground of coordinated maneuvers involving two or more spacecraft units operating in close proximity. As discussed in the previous sections, the experimental validation of GN&C strategies along with new sensors and actuators architectures is of utmost importance to enable new capabilities for future missions.

During my Ph.D. I gave my contribution mainly in the following activities:

- development, integration and characterization of new features for the SPARTANS testbed, in particular as regards the development of the vision-based global navigation system;
- development of software modules, written in C/C++, to enable the capability of simulating the spacecraft dynamics on orbit and to handle the operational phases of the SPARTANS modules during the execution of experimental tests on the ground;
- investigation of monocular approaches for relative pose estimations in the context of cooperative spacecraft;
- development of a stereoscopic vision-based navigation strategy for the relative navigation of a spacecraft with respect to a known target.

Figure 1.2 summarizes the main activities conducted during my doctoral activities.

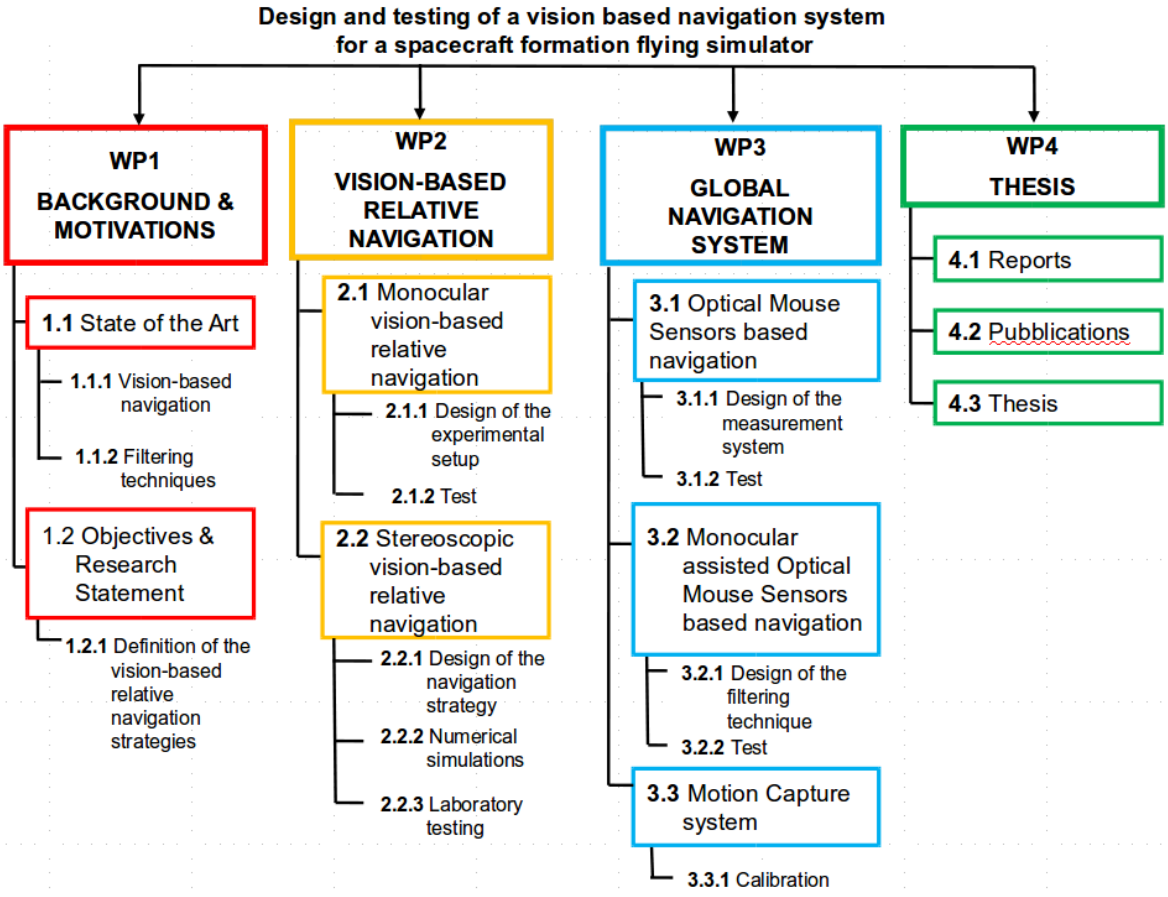

Figure 1.2: Work breakdown structure.

Chapter 2 provides a detailed description of the SPARTANS testbed. The first sections of the chapter illustrate the characteristics of the main subsystems of the spacecraft units. Subsequently the main features of the testbed are presented to complete the overview on the facility. Finally, a series of preliminary experimental activities devoted to the characterization of the spacecraft units is presented.

Chapter 3 focuses on the metrological characterization of a monocular system for relative pose estimation in the context of cooperative spacecraft. After discussing the preliminary mathematical aspects underlying the estimation problem, a custom-made set of fiducial markers is described along with the employed image processing procedure. Thereafter, the pose estimation approach is presented in its three main parts involving, in this order, the solution of the perspective-from-three points problem, the employment of an iterative procedure to exclude outliers from the datasets and refinement of the estimated pose by means of a non-linear optimization procedure.

The experimental setup used to assess the estimation performances of the proposed algorithm is then presented and, finally, the results of an extensive test campaign are shown and discussed.

Chapter 4 is aimed at presenting the activities performed to develop the global navigation system for the SPARTANS testbed. This system is exploited to provide a shared, common reference frame for all the spacecraft units operating within the laboratory and to track their positions and orientations during the execution of maneuvers. The first part of the chapter presents the development of a first prototype of the global measurement system: in particular, it describes the sensors used in the estimation procedure and discusses the filtering strategy which is employed to merge measurements coming at different rates and with different accuracies. The second part of the chapter illustrates the development and the implementation of the global navigation system in its final configuration: first, a pose estimation procedure along with a calibration procedure is presented and, subsequently, the performances of the estimation scheme are assessed by means of experimental tests.

Chapter 5 presents the development of a stereoscopic vision-based relative navigation strategy based on an Extended Kalman Filter. After an initial discussion about the adopted methodological approach, the filter is presented and its performances are assessed by means of numerical simulations in two different scenarios. In the first scenario, the relative dynamic state of two spacecraft orbiting in a leader-follower formation at short range is simulated numerically by means of a software orbital propagator. In the second scenario, the operative conditions of the SPARTANS laboratory setup are reproduced by means of a 3D simulated environment. Finally, the proposed navigation strategy is validated by means of laboratory testing exploiting the robotic spacecraft units.

Chapter 2

Formation flight hardware simulator

2.1 Introduction

The current chapter presents the cooperating spacecraft testbed for proximity operations experiments called SPARTANS being developed at the Center of Studies and Activities for Space (CISAS) "G. Colombo" at University of Padova. The final aim of the project is to design and validate a representative facility to carry out research in the field of spacecraft formation flight (SFF), rendez-vous and docking (RVD) and, in a broader sense, on-orbit proximity operations.

The SPARTANS ground-based testbed is thought to be a micro-satellite simulator able to mimic, as close as reasonably possible in a ground-based laboratory, the behavior of two or more satellites flying in close proximity on-orbit. This separated vehicles testbed allows the development and verification on the ground of coupled relative attitude and position Guidance, Navigation and Control (GN&C) algorithms.

The main requirements that led the design and realization of the SPARTANS testbed are:

- faithful representation of the dynamics of satellites flying in close proximity;
- easy interaction of the experimenter with the setup;
- cost-effectiveness;
- easily reconfigurable system;
- reliability and safety.

The SPARTANS facility consists of two or more spacecraft simulators, representing the units of an on-orbit formation. Each mini satellite consists of an upper part, called Attitude Module (AM), characterized by three rotational degrees of freedom, and a lower part, the Translational Module (TM), enabling planar low friction displacements. The testbed is completed by a Control Station (computer), a glass-covered flat table that supports the mini satellites and allows for displacements, and an infrared (IR) cameras based external global measurement system to track the motion of each micro-satellite. Figure 2.1 shows the conceptual layout of the SPARTANS testbed, while Figure 2.2 show the laboratory setup, where only one spacecraft simulator is visible.

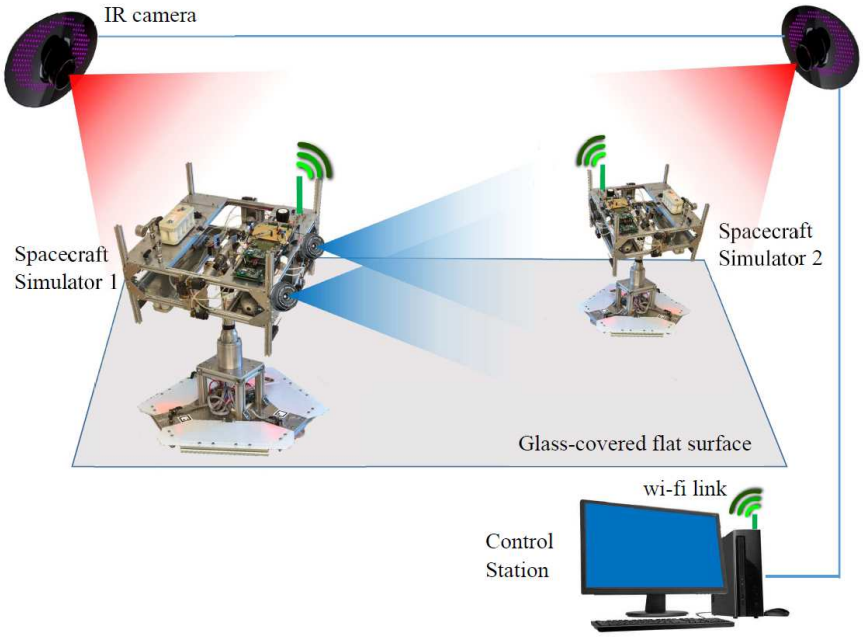

Figure 2.1: SPARTANS facility schematic overview.

At the moment of the writing of this thesis, one complete spacecraft simulator is fully developed and tested, while a second module is under development. The flat table that support the motion of the mini satellites is fully operational as well as the IR cameras measurement system.

The chapter is structured as follows: after a brief overview of spacecraft simulators, the main components of the SPARTANS facility are described in detail. To conclude, some experimental activities related to the development of the ground-based testbed are presented.

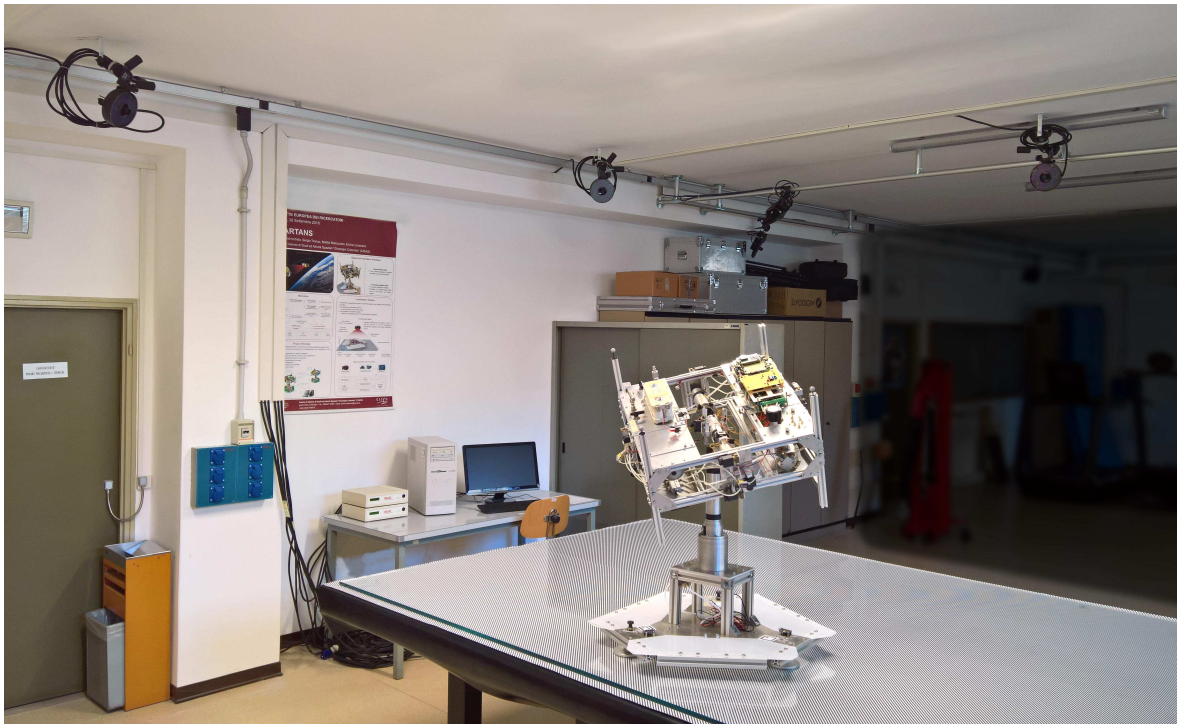

Figure 2.2: The SPARTANS laboratory.

2.2 Review of Spacecraft Simulators

Spacecraft simulators have been widely used since the beginning of the space exploration era for software development and hardware verification. The problem of reproducing the space dynamics for testing purposes have been tackled in different ways and, depending on the specific objective of the investigation scenario, some techniques proved to be more effective than others. Table 2.1 shows a commonly used classification for spacecraft testbeds, whose main advantages and disadvantages are summarized in Table 2.2.

Schwartz et al. [4] provide a broad overview over the last decades until the beginning if the 21th century of air-bearings spacecraft simulators, dividing them into three main categories: planar, rotational and combination systems. All these kind of test facilities share a common feature: a thin air layer is exploited to minimize the interactions between coupled surfaces, allowing to obtain an almost torque-free rotational and force-free translational displacements.

Planar systems provide a payload with the capability of spinning and translating over a planar surface. In the field of formation flight, rendez-vous and docking and flexible structures investigation, planar testbeds revealed to be a commonly used so-

Table 2.1: Classification of spacecraft testbeds.

<table>
<tr><td rowspan="8">Ground-based testbeds</td><td rowspan="5">Spacecraft simulators</td><td rowspan="4">Rotational systems</td><td rowspan="3">Air-bearing</td><td>Tabletop</td></tr>
<tr><td>Umbrella</td></tr>
<tr><td>Dumbbell</td></tr>
<tr><td>Ball-and-socketed joints</td></tr>
<tr><td>Multiple gimbals</td></tr>
<tr><td colspan="2">Planar systems</td></tr>
<tr><td colspan="2">Combination systems</td></tr>
<tr><td rowspan="2">Water tanks</td></tr>
<tr><td>Drop towers</td></tr>
<tr><td>Parabolic flights</td></tr>
<tr><td>On-orbit testbeds</td></tr>
</table>

lution. University of Stanford developed several air-bearing test facilities to perform investigations related to the use of robotic arms for on-orbit servicing, assembly and construction. Also University of Victoria takes advantage of a planar testbed to test robotic arms joint trajectory optimization strategies during maneuvers in space. More recently, University of Rome La Sapienza developed the PINOCCHIO (Platform Integrating Navigation and Orbital Control Capabilities Hosting Intelligence On-board) testbed to develop and test vision based navigation and control strategies during space rendez-vous operations [5].

Rotational air-bearing systems ideally allow unconstrained attitude maneuvers in the three dimensional space. However, achieving this level of rotational freedom is difficult from a technical point of view. Rotational systems are typically employed for the development and experimental validation of attitude determination and control strategies.

Unconstrained motions about the yaw axis can be obtained by means of tabletop and umbrella configurations (see respectively Figure 2.3(a) and 2.3(b)), but roll and pitch angles are typically limited in a range lower than ± 90 deg. U.S. Army Ballistic Missile Agency, NASA Ames Research Center and NASA Goddard Space Flight Center

Table 2.2: Comparison between advantages and disadvantages of spacecraft testbeds.

TESTBED	PROS	CONS
On-orbit testbeds	Fully representative	Very expensive
Parabolic flights	Good microgravity Easy interaction with the experiment	Expensive Microgravity time-window lasts less than 20s
Drop towers	Excellent microgravity	Expensive Only few seconds of microgravity
Water tanks	Long-lasting microgravity Good microgravity	Viscous forces/torques Water resistant payload required
Spacecraft simulators	Long-lasting microgravity Good microgravity Easy interaction with the payload	Disturbances to be compensated for Partial reduction of degrees-of-freedom

were at the forefront in the development of tabletop and umbrella style air-bearings starting from the beginning of the 1960s. With the development of dumbbell-style air-bearings (see Figure 2.3(c)), structural interference is reduced allowing unconstrained rotations about both roll and yaw axes: this result can be achieved thanks to two opposing arms that increase the distance between the mounting area and the center of rotation. University of Michigan's Triaxial Air Bearing Testbed and Virginia Tech's WHORL-II represent two examples of dumbbell-style-based testbeds.

Combination system represent the most elaborate and interesting facilities: they combine both rotational and planar air-bearings to obtain up to six completely unconstrained degrees of freedom. These facilities allow the design and verification of precision autonomous maneuvers, including coupled position and attitude maneuvers, rendez-vous and docking, on-orbit servicing, inspection and assembly.

A large number of institutions have been developing combination systems in the last decades. To name a few, JPL-Caltech developed the Formation Control Testbed (FCT) [6], DLR is active in this research field with the Test Environment for Applications of Multiple Spacecraft (TEAMS) [7] (see Figure 2.4a) and Georgia Tech realized the Autonomous Spacecraft Testing of Robotic Operations in Space (ASTROS) [8] (see Figure 2.4b). These systems allow combined translations and rotations up to five

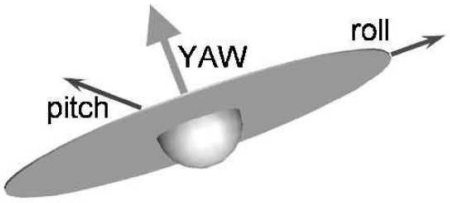

(a) Tabletop configuration.

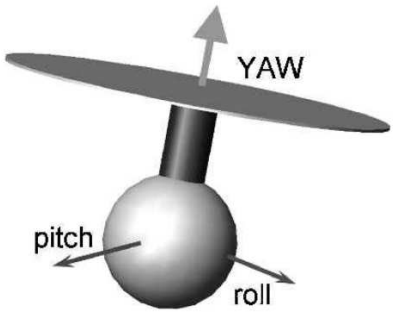

(b) Umbrella configuration.

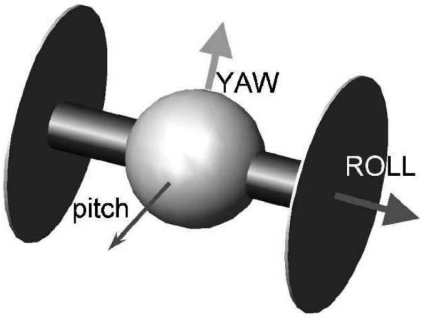

(c) Dumbbell configuration.

Figure 2.3: Rotational air-bearings configuration. Tabletop and umbrella provides unconstrained rotation about the yaw axis, while dumbbell is free to rotate about roll and yaw axes.

degrees of freedom. The MIT Synchronized Position Hold Engage and Reorient Experimental Satellite (SPHERES) project represents a peculiar example of spacecraft testbed since it can be used into two different configurations: the Flat Floor and Glass Table test facility at SSL allow to employ the testbed in a planar configuration while, on-board the International Space Station, the SPHERES micro-satellites operate in a fully representative microgravity environment [9].

(a) Experimental platform and test area of the TEAMS testbed [7].

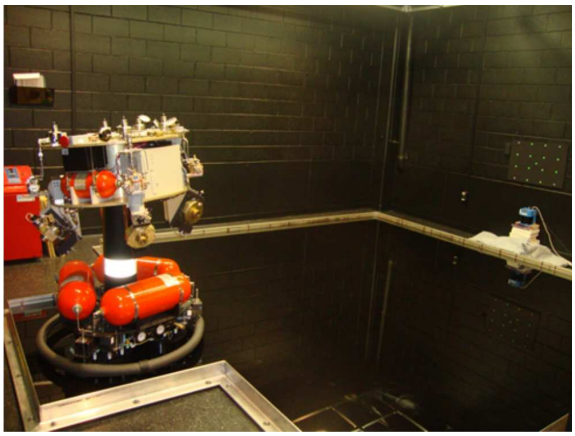

(b) Experimental platform and test area of the ASTROS testbed [8].

Figure 2.4: Examples of ground-based spacecraft testbeds.

2.3 Attitude Module

The Attitude Module (AM) represents the core part of the SPARTANS testbed as it mimics the on-orbit behavior of a real micro-satellite. It consists of five main subsystems that are sufficient to allow autonomous attitude maneuvers:

- Structural subsystem;
- Attitude Determination and Control Subsystem (ADCS);
- Propulsion subsystem;
- Electric and Power subsystem;
- On-board Data Handling and Communications subsystem.

The following subsections are devoted to provide a detailed insight on the on-board AM subsystems.

2.3.1 Structural subsystem

The AM is characterized by a squared-base parallelepiped-shaped structure, whose dimensions are of 54 cm x 54 cm x 40 cm. It consists of the following main components:

- an aluminum framework made of a 20 mm x 20 mm profile beams with T-grooves, joined together by means of quick connectors;

- four main rectangular plates, necessary to house the on-board equipment;
- reinforcing lateral corner plates;
- reinforcing lateral rectangular plates;
- right angle brackets supporting the cold gas thrusters system;
- five removable 3 mm thick black plastic sheets;
- a three-joint system that enable low-friction rotations about three independent directions in space.

Connections between the structural components are realized by means of either T-nuts or sliding nuts. The black plastic sheets are connected to the AM framework in order to form an outer shell that shields the on-board equipment and constitutes a support for visual patterns. The shape of the plastic sheets is thought to avoid interference with the on-board propulsion system. Figure 2.5 shows the model of the AM structure, highlighting its main components.

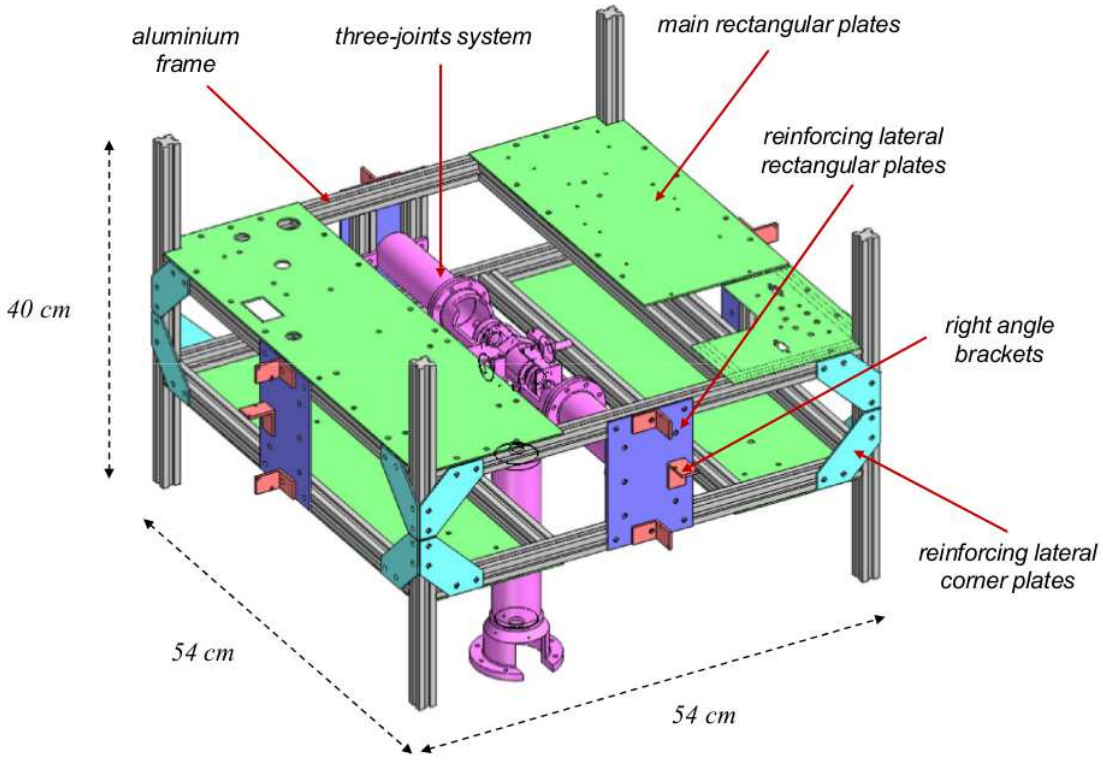

Figure 2.5: Main components of the Attitude Module structure.

The three-joint system (see Figure 2.6) is thought to enable triaxial low-friction rotational displacements to the AM. The joint system consists of three cylindrical joints, whose axes meets at the center of rotation. A vertical rod is responsible for supporting the whole structure and for housing the first cylindrical joint, whose axis is coincident to the vertical direction (yaw axis). The second and third axes allow rotations about the pitch and roll axes respectively. This mechanical configuration allows the AM to freely rotate about the yaw axis, while both roll and pitch angles are constrained within a range of ± 40 deg.

In nominal conditions, the following conditions hold: (a) the AM center of mass is perfectly coincident to the AM center of rotation, (b) the rotational motion is not affected by friction. Thus, the AM attitude dynamics depends only on the initial conditions and the control torques.

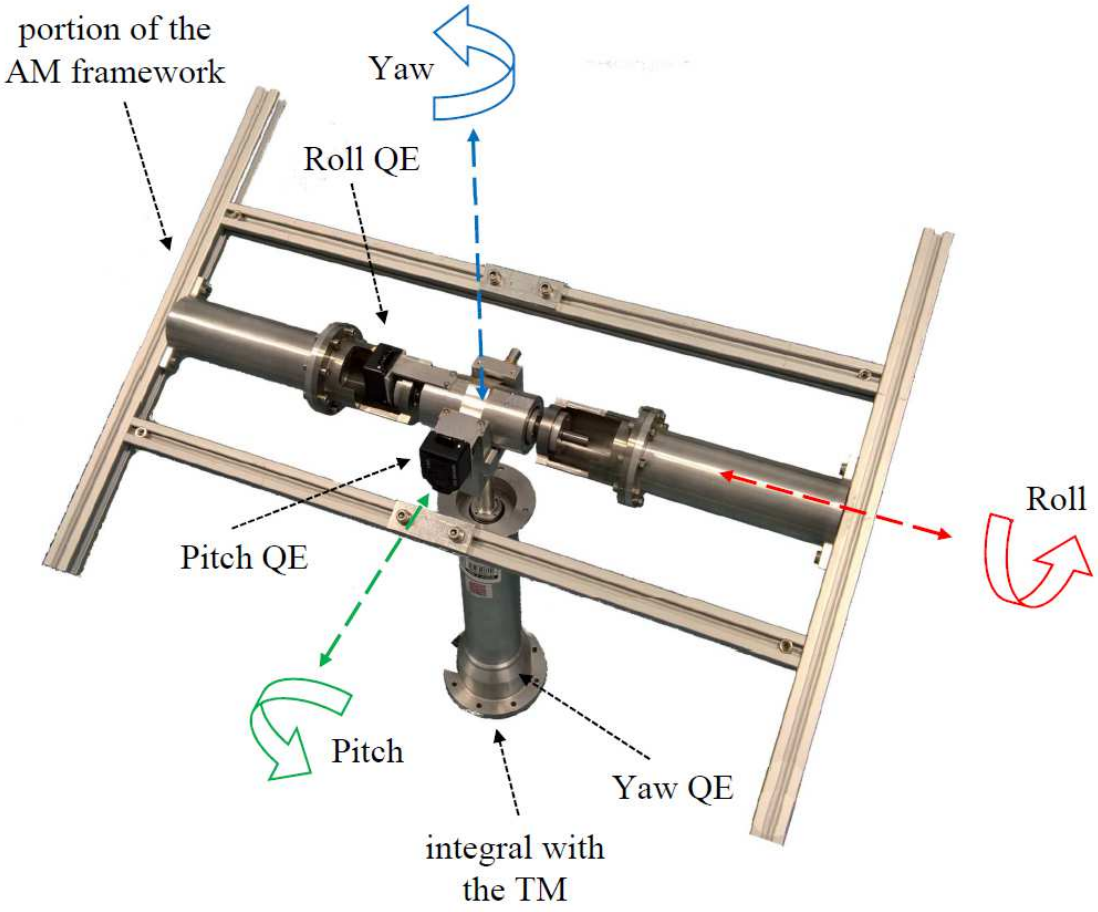

Figure 2.6: Three-joint system: roll, pitch and yaw axes are shown in red, green and blue respectively.

2.3.2 Attitude Determination and Control Subsystem

The ADCS consists of two main components: the on-board sensors and the electronic boards subsystem.

Each simulator is equipped with two kind of attitude sensors, used to provide an attitude estimation of the AM with respect to the Local Vertical-Local Horizontal (LVLH) reference frame:

- three Avago Technologies HEDM 5500-B13 incremental quadrature encoders (QE), providing measurements of the joints angular displacement, thus providing a direct measurement of the roll, pitch and yaw angles, with a resolution of 0.09 deg. The QE mounting configuration is shown in Figure 2.6.

- a Microstrain 3DM-GX1 Inertial Measurement Unit (IMU), that provides an estimation of both attitude and attitude rate of the AM with respect to an external reference frame.

Since the measurements provided by the QE system are much more accurate than the ones provided by the IMU, the QE measurements are used as a reference to estimate drift and bias affecting the IMU.

A DUO-M stereo camera will be placed on-board the AM with the aim of handling relative vision-based navigation tasks between two micro-satellites of the SPARTANS constellation, or between a chaser and a generic target. The stereo camera is a lightweight and compact system (mass: 6.5 g, baseline: 3 cm) with global shutter, wide field of view (170 deg) and frame-rates up to 320 fps at 320 x120 pxl.

An Odroid XU3 single board computer collects data coming from the on-board sensors and is responsible for the execution of the Guidance, Navigation and Control (GN&C) tasks. Custom electronics was developed to interface the avionics with the propulsion subsystem (Thrusters Command Board).

2.3.3 Propulsion subsystem

The propulsion subsystem is responsible for the actuation of control actions for both attitude and position control. It consists of two main sections: the high pressure and the low pressure section as shown in Figure 2.7.

The high pressure section allow to store air up to 200 bar. It consist of:

- four tanks in composite materials containing a total volume of dry air equal to 4 Lt up to a pressure of 200 bar;
- a fill and vent system, consisting in a quick connector and two ball valves, to load the pneumatic system;
- a pressure regulator that regulates the air pressure from a maximum of 200 bar to the operative pressure of the thrust actuator's nozzle, i.e. 10 bar;
- steel pipes fittings to connect the high pressure components.

The low pressure section is required to feed the actuators with an operative pressure of 10 bar. It features:

- four six-ways and two two-ways manifolds that divide the air flow coming from the pressure regulator outlet supplying the on-board thrusters;
- on-board thrusters:

  12 thrusters, responsible for the actuation of control torques;

  8 thrusters, responsible for the actuation of position control forces;
- plastic pipes fittings to connect the low pressure components.

Each thruster consists of an electro-valve and a converging nozzle. The electro-valve is a solenoid valve that opens when supplied with an input voltage ($12 - 24$ VDC), letting the air through the nozzle. Each nozzle is a M5 screw with an axial 0.75 mm diameter hole.

The mounting of the thrusters on-board the AM is realized in a way that, by properly setting the firing direction of the actuators, both translational and rotational control actions can be actuated either along or about each direction in space. To overcome the limitations of the ON/OFF functioning mode of the electro-valves while executing control actions, a pulse-width-modulation (PWM) scheme is employed.

2.3.4 Electric and Power subsystem

The electric and power subsystem is responsible for providing all the on-board components with the required operational voltage and current. Two 12 VDC Li-Po batteries connected in series allow the storage of electrical power on-board the attitude

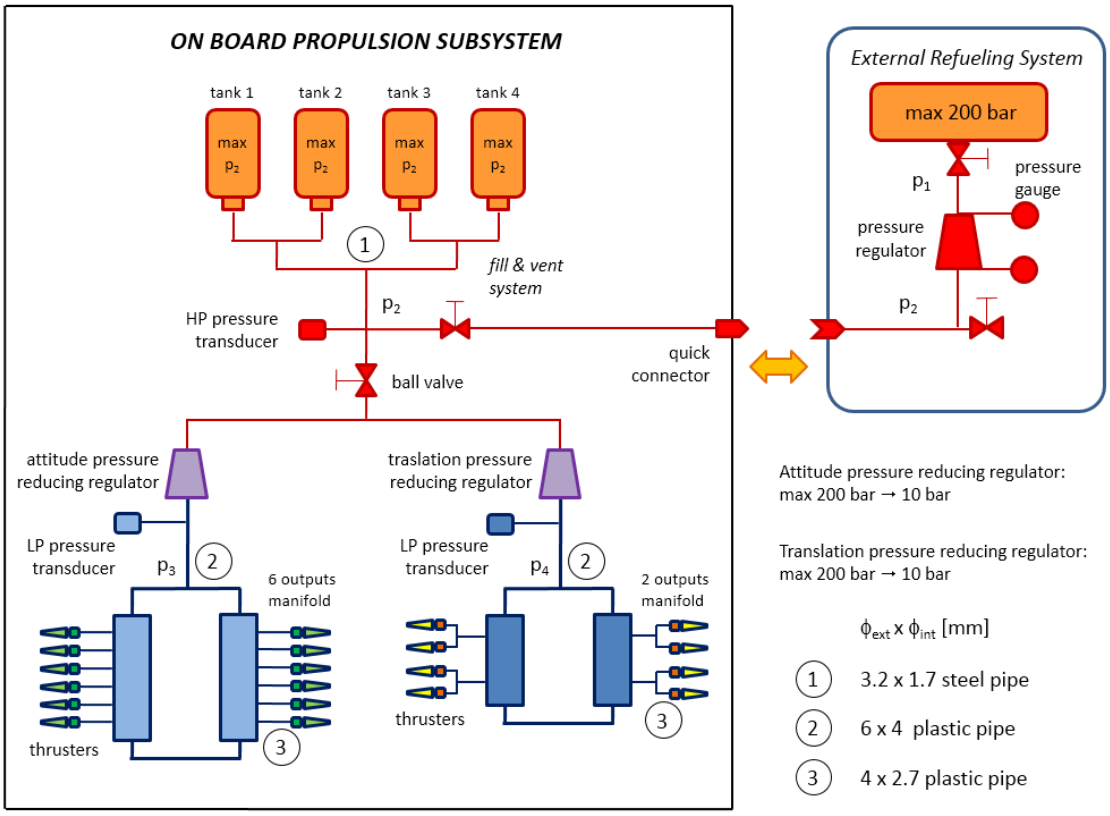

Figure 2.7: Schematic drawing of the Attitude Module pneumatic system.

module. By means of a custom board with DC/DC converters, sensors, electronic boards and actuators are fed with the required power. The architecture of the electric and power subsystem is shown in Figure 2.8.

2.3.5 On-board data handling and communication

In its final configuration, the SPARTANS micro-satellites and the control station are provided with the capability of communicating to each other in a peer-to-peer network by means of a dedicated communication module (Zig-Bee). Two separate channel are planned to be used: (1) a Simulator-to-Simulator channel allow two units flying in formation to share information and navigation data, allowing to reproduce different formation flight scenarios, and (2) a Simulator-to-Laptop channel that allow the transmission of commands and the receiving of telemetry data. This architecture enables the user/experimenter to setup and start a specific test and, once the test is initialized, the spacecraft modules are autonomous in performing maneuvers.

The communication protocol consists of five types of messages:

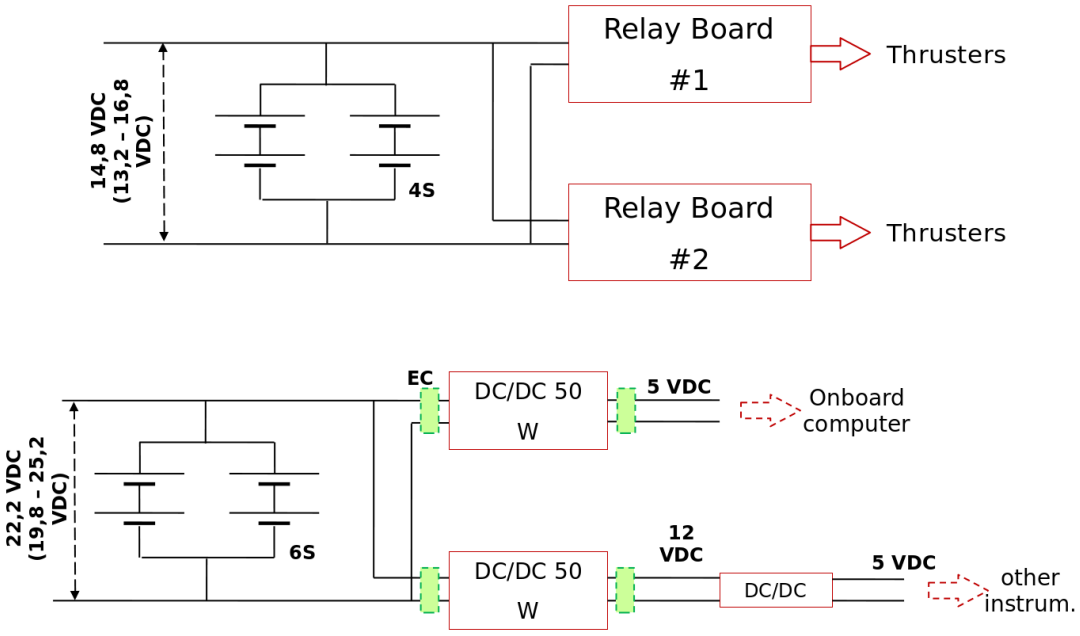

Figure 2.8: Schematic drawing of the Attitude Module electric and power subsystem.

(1) Initiate Link messages are used to initialize the communication link between units;

(2) Acknowledge messages assure that commands sent from the laptop or from a micro-satellite are received and parsed synchronously between different units;

(3) Data Request messages are used to request the transmission of specific packets;

(4) Data messages serve as a vehicle to share telemetry, housekeeping and GN&C data;

(5) Command messages are used to command the execution of specific tasks.

At the current development stage of the project, only Simulator-to-Laptop communication was tested while the Simulator-to-Simulator link will be enabled as soon as the second AM will be fully operational.

2.4 Translational Module

The Translational Module (TM) is the lower part of each micro-satellite of the SPARTANS testbed. The TM has two main functions: (1) it supports the AM and (2) it enables low-friction planar motions by means of the air-cushion system. It is developed

following a modular design approach: this feature provides the possibility of easily change its configuration if malfunctioning or damaged components must be replaced; moreover, it allows to easily add new features in terms of on-board instrumentation.

The TM consists of five main subsystems:

- Structural subsystem;
- Pneumatic subsystem;
- Position and Attitude determination subsystem (PADS);
- Electric and power subsystem;
- Data Handling and Communication subsystem.

At the current status of the project, both the TM design and assembly are complete, and preliminary tests in performing combined rotational and translational maneuvers assessed the effectiveness of the module design. In the following sections, the main characteristics of the main TM subsystems are presented.

2.4.1 Structural subsystem

The structure of the TM consists of the following components:

- two aluminum hexagonal plates connected to three aluminum profile beams, with the function of supporting the AM interface structure and the pneumatic system circuitry components;
- three square-shaped aluminum plates, placed at the outer part of the TM, with the function of housing the navigation sensors and the air skids;
- three Plexiglas plates, supporting the on-board air tanks;
- lateral aluminum profile beams with the function of reinforcing and stiffening the structure;
- a central structure, obtained by joining aluminum profile beams, is placed on the central hexagonal plate. On this structure an aluminum cylinder is housed with the aim of providing an interface to directly connect the AM with the TM structure.

Figure 2.9 shows the 3D model of the TM with its main components labeled.

The height of the TM structure (i.e. the distance between the air outlet section of the skids and the top section of the interface cylinder) is roughly of 330 mm while, if seen from above, it is characterized by a triangular shape that can be inscribed inside a circumference of radius approximatively equal to 330 mm. The triangular shape allows to distribute uniformly masses on top of the structure, thus providing the air skids with the same load in terms of mass to be sustained.

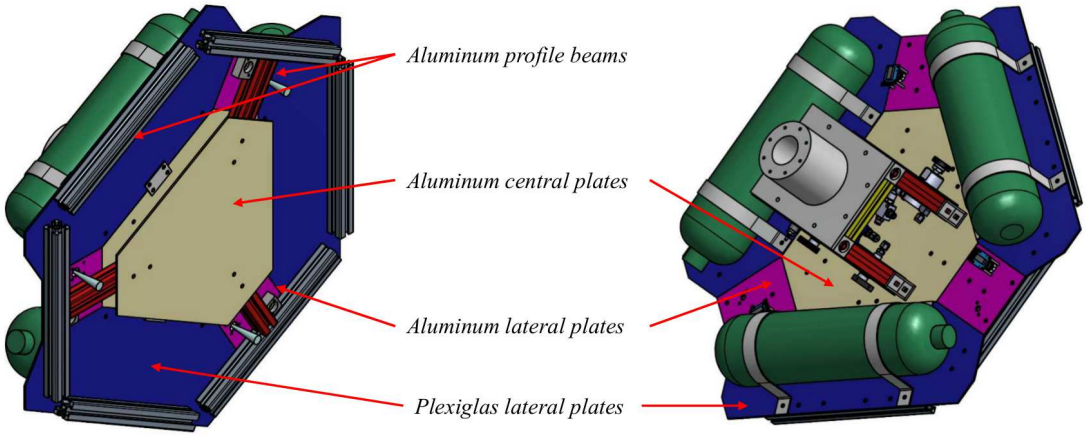

Figure 2.9: 3D model of the Translational Module. In figure, the main structural components are labeled.

The central part of the structure and the interface cylinder are responsible for providing the AM with sufficient clearance in order to avoid possible mechanical interference between the AM and the TM structures.

Different configurations can be enabled in terms of activated degrees of freedom (DOF). By means of an additional aluminum plate, the interface cylinder can be rigidly joined to the the AM frame, avoiding de facto relative displacements between the TM and the AM. In this configuration, the SPARTANS micro-satellite is provided with 3 DOF (i.e. planar displacements and rigid rotations about the local vertical), thus it behaves as a rigid body. In its nominal conditions, i.e. when the additional plate is removed and the yaw supporting axis is connected to the support cylinder, the micro-satellite can operate with the 5 DOF enabled.

To validate the structural design of the TM, a series of Finite Element Analyses (FEA) were performed in order to assess the behavior of the structure in presence of static and dynamic loads. The main contributions to the static loads are (1) the

AM, with a mass of about 23 kg, and (2) the on-board tanks, with a total mass of about 8 kg in full air charge. Considering a safety factor of $K_1 = 2.17$ and of $K_2 = 1.5$ respectively on the AM and the tanks mass, the FEA shows that the maximum foreseen displacement for the TM structure is equal to $s_{max} = 0.15\,\text{mm}$. The result is 15 times smaller than the maximum allowable displacement defined during the requirements definition phase. Further details on the numerical analysis performed can be found in [10].

2.4.2 Pneumatic subsystem

The pneumatic subsystem is responsible for the storage of pressurized air on-board the TM and the generation of a thin air layer that is needed to enable low-friction planar motions. It consists of two main parts: (1) the pneumatic circuit and (2) the air skids.

The pneumatic circuit, is divided into two main sections: the high pressure and the low pressure section. It includes the following components:

- three air tanks, each with a capacity of 1 Lt and a maximum operative pressure of 200 bar;
- steel pipes fittings to connect the high pressure components;
- a fill and vent system to load the air tanks;
- a three-ways manifold;
- plastic pipes fittings to connect the low pressure components;
- a pressure regulator, needed to supply the low pressure section with the nominal operative pressure.

Figure 2.10 shows the schematic drawing of the pneumatic subsystem.

Through the pressure regulator, the air pressure is reduced to reach the operative level. The low pressure section of the circuitry drives the airflow to the air skids, allowing the generation of the thin air layer between the skids outlet and the planar surface on which they are placed.

The weight of the SPARTANS micro-satellite drives the selection of the correct operative pressure in order to generate an air layer that is able to bare the overall weight

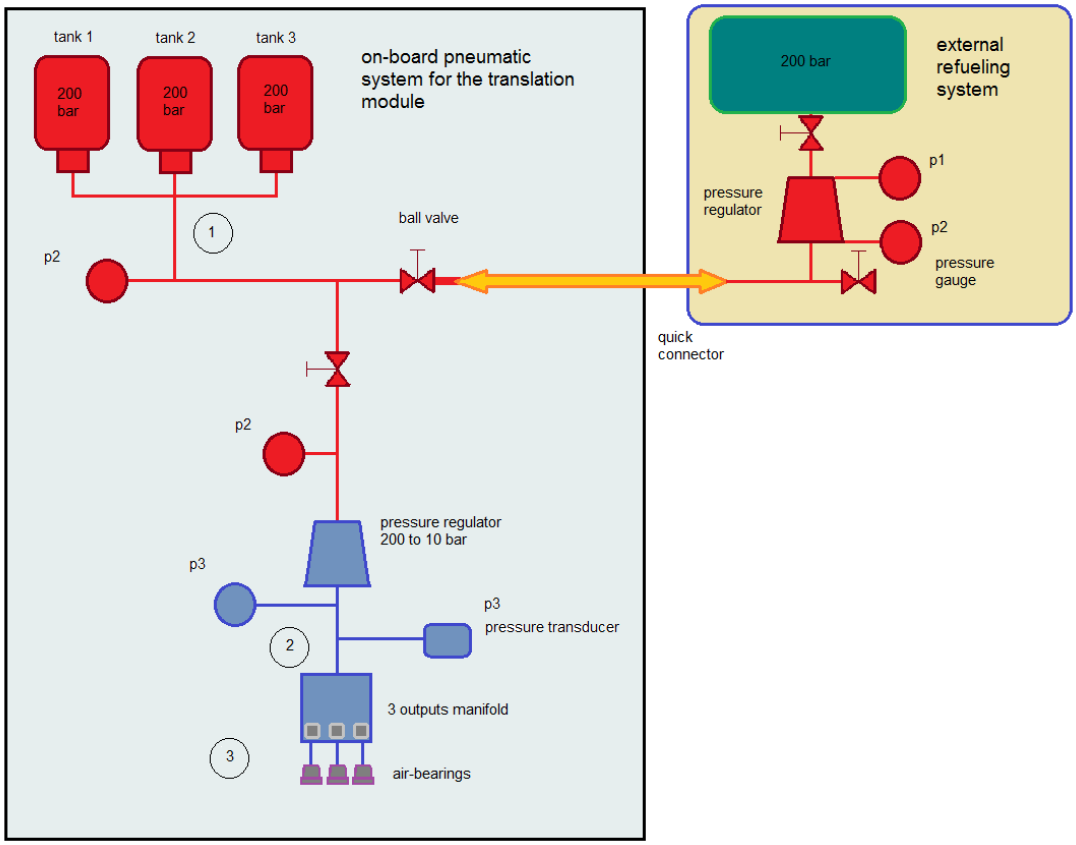

Figure 2.10: Schematic drawing of the pneumatic subsystem on-board the Translational Module.

of the simulator. Experimental tests were performed with the aim of determining the optimal operative pressure that (1) ensure to avoid interference between the skids and the underlying surface (i.e. friction), and (2) that maximize the time window in which smooth planar displacements can be obtained by means of the air stored on-board the TM. Further details about the experimental characterization will be provided in Section 2.8.4.

2.4.3 Position and Attitude Determination Subsystem

The position and attitude determination subsystem (PADS) is responsible for providing an estimation of the pose (position and attitude) of the TM with respect to a given reference frame. Since the TM has only three DOF enabled, the PADS is required to estimate the planar position of the TM and its orientation about the local vertical.

The PADS consists of two main components:

- three Optical Flow Sensors (OFS) units, each with an Avago Technology ADNS3080 optical mouse chip, a PCB and a lens;
- a low-cost micro-controller (Arduino UNO).

The main PADS components are shown in Figure 2.11.

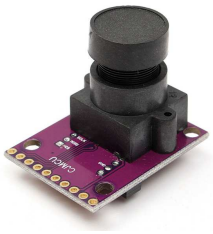

(a) Optical Flow Sensor.

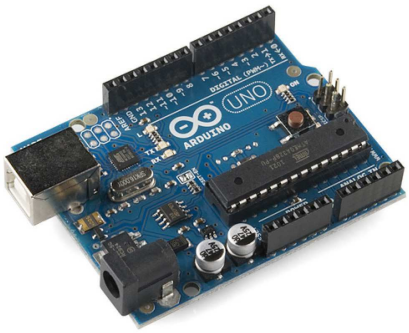

(b) Arduino UNO micro-controller.

Figure 2.11: Main components of the Position and Attitude Determination Subsystem of the Translational Module.

The Optical Flow Sensors are low-cost mouse-like sensors that provide incremental measurements in terms of planar translations with respect to a sensor-fixed reference frame. They provide high-rate measurements, with a programmable frame rate up to more than 6400 fps. By combining at least two OFS, and after a proper calibration procedure, also rotational displacements can be measured. Details on the development of the measurement system will be provided in Section 4.2.

The on-board micro-controller is responsible for triggering the acquisition of the OFS, for collecting data and finally for parsing them in order to provide an estimation of the incremental displacement that the TM undergoes in the considered sampling interval.

2.4.4 Electric and Power subsystem

The electric power on-board the TM is provided by rechargeable batteries. The electric architecture of the TM is thought to be as simple as possible and the only components that require to be fed with electrical power are the Arduino UNO board,

the three Optical Flow Sensors and the pressure transducers that are used to monitor the pressure of the airflow to the skids.

2.4.5 Communication and Data Handling Subsystem

The communication and data handling subsystem of the TM is thought to make navigation data and housekeeping data available to the AM electronics. A single channel communication link is exploited to exchange data between the modules. The types of messages that can be sent follows exactly the architecture of the communication module of the AM, as presented in Section 2.3.5. From a practical point of view, the physical connection between the electronics is provided by a slip ring connection contained inside the yaw axis support.

The Arduino UNO board is equipped with the software required to implement the communication, to save data coming from the PADS and to store housekeeping data.

2.5 The Simulator Test Table

The execution of coordinated maneuvers between the spacecraft units of the SPARTANS testbed is made possible by the development of the simulator test table. The test table has the function of providing a flat surface that supports the micro-satellites and enables low-friction planar displacements.

Two main requirements were considered in the design phase of the facility: (1) the table must provide an operative area of at least 2 x3 m and (2) the maximum allowable disturbance force due to surface deformations must be lower than 10^{-3} N. The first requirement comes from the need of having the widest possible operative surface taking into account the spatial constraints imposed by the available laboratories, while the latter states the need of keeping disturbance forces acting on the spacecraft units under a predefined threshold. In addition the test table should provide the possibility of adjusting its inclination and it should be as lightweight as possible in order to avoid possible deformations of the floor. Another important parameter to be considered in the design is the cost of the overall system.

Several conceptual design were proposed and analyzed. A first solution foresees the development of a modular structure composed of aluminum profile beams connected to each other to build the structure framework, which is in turn responsible for supporting

the upper part of aluminum, rubber and glass sheets. Even if this design represented a cost-effective solution, this concept was discarded due to the fact that the structural stiffness and the table planarity were highly dependent on the joining accuracy of the profile beams. A second solution consisted in the employment of granite tables, available on the market with an embedded leveling system. The main drawback of this configuration include the limited size of the available tables, resulting in the need of joining at least three tables to satisfy the requirements on the test surface and thus in a high probability of having discontinuities in terms of inclination and height of the tables themselves. Moreover, difficulties in manipulating and setting up the table in the laboratory would have arisen because of the massive weight of the system. Also this second solution was discarded.

The solution that is adopted consists of the following components:

- two sets of levelable steel legs;
- two aluminum honeycomb panels, each with a total area of $2\,\mathrm{x}1.5\ \mathrm{m}^2$ and a thickness of 10 cm;
- a layer of rubber;
- a non tempered glass sheet, with a thickness of 15 mm.

The two sets of legs are responsible for the support of the flat portion of the table: in particular each set of legs is provided with four supports on top of which the honeycomb panels are placed. Each support is connected to the legs by means of a threaded connection: this feature allow to adjust the inclination of the panels in order to ensure their horizontal configuration. The selection of the honeycomb panels is the results of FEM simulations which showed that, under the static gravitational load of the micro-satellites, the induced deformations were compatible with the requirement on the maximum allowable disturbance forces. The rubber layer is placed between the honeycomb panels and the glass sheet: its main function is to compensate for local irregularities in the substrate and to distribute stresses. Finally, the glass sheet provides a planar seamless surface in high polish quality, on top of which the spacecraft simulators can float. Figure 2.12 shows all the main components of the test table except for the glass sheet.

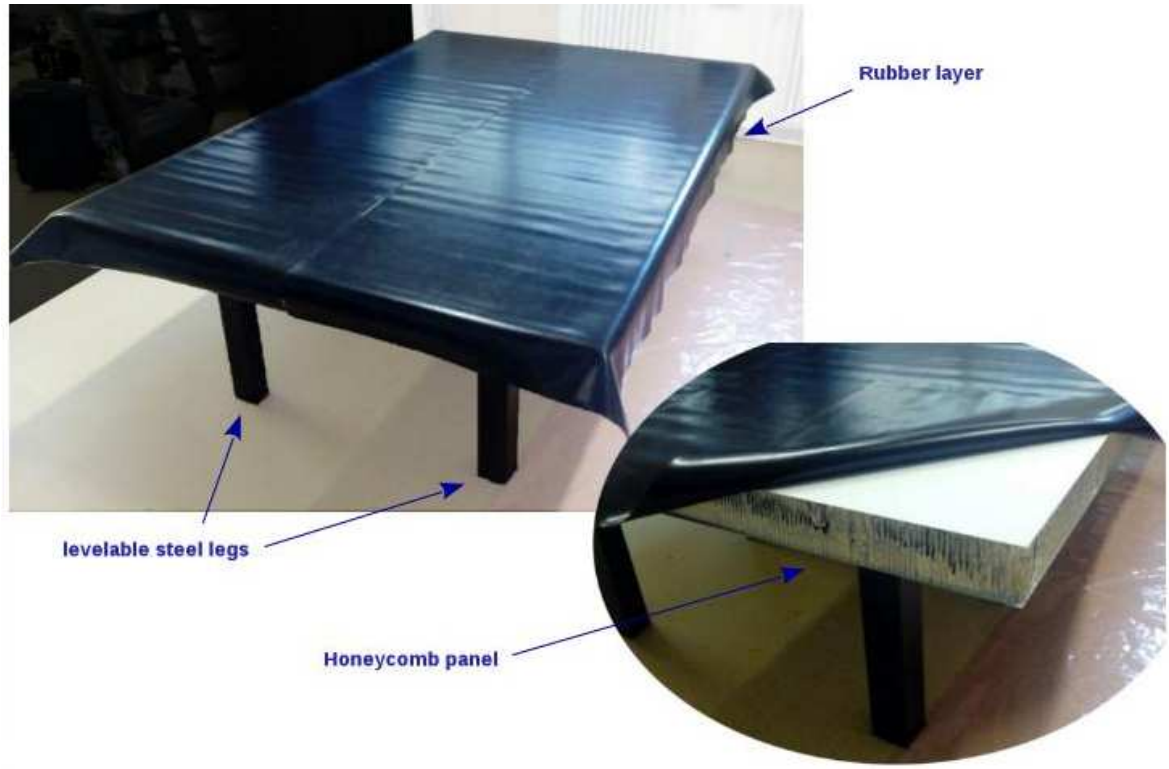

Figure 2.12: Test table with levelable steel legs, rubber layer and honeycomb panel. The glass sheet is not shown in the picture

2.6 The global navigation system

The global navigation system consists in a measurement system that provides the capability of estimating both the position and the attitude of each AM with respect to a common external Global reference frame. The global navigation system is needed for two main reasons: (1) it overcomes the limitations of the incremental measurement systems (i.e. quadrature encoders, optical flow sensors) and (2) the measurements provided can be used to assess the metrological performances of the sensors on-board the SPARTANS micro-satellites.

The global navigation system consists of:

- a set of 6 inrared digital cameras, placed around the low-friction table so that their fields of view cover the operative volume uniformly and from the top;
- some passive and retro-reflecting markers placed on board each AM;
- an external computer that combines the images coming from the IR cameras and provides an estimation of each AM motion.

The procedure that lead to the definition, design and realization of the global navigation system is the object of Section 4.4.

2.7 The SPARTANS software

All the GN&C procedures defined within the SPARTANS context require the development of dedicated software tools. The software is required (1) to handle all the operational phases of the spacecraft simulators, (2) to develop a simulation environment for validating GN&C strategies, extending the validity of the results in a range which is wider that the one reproduced inside the SPARTANS laboratory (i.e. orbital dynamic simulations), and (3) to post-process the results obtained after the simulations and the test campaigns.

A first version of the SPARTANS software was based on two separate development environments: all the dynamic simulations were performed in MATLAB, while the operations on-board the micro-satellites were handled by means of code written in C[1]. This approach, even if effective, required to implement, debug and test the GN&C algorithms twice.

Currently, in order to unify the software development environment and to boost the computational performances of the algorithms, a new software architecture is adopted. The new version of the SPARTANS software is written in C/C++ following a modular, object-oriented paradigm. The software consists of two main simulation frameworks:

(1) **Laboratory framework**, which is used for implementing and testing GN&C maneuvers taking advantage of the micro-satellite hardware simulators;

(2) **Simulation framework**, which reproduces dynamics conditions typical of satellites in orbit. Experimenters and guest scientists can use this framework to validate their own GN&C algorithms in a representative orbit environment adopting the same software routines exploited within the laboratory framework.

One of the main advantages of this new architecture is that it allows to develop software modules that can be validated within the simulation framework and then to be directly used within the laboratory framework.

[1]The actual language used was the Dynamic C, a proprietary version of C needed to program the micro-controller on-board the first version of the AM. Further details can be found in [11].

Projects are built by means of CMake. The Robot Operating System (ROS)[2] tools are employed to facilitate the implementation of communication paradigms between different software modules. Contributions to the software are handled by means of the *git* version control system ensuring data integrity, speed and flexibility for non-linear workflows.

The SPARTANS software is built on top of two distinct layers, that can be defined as Classes and ROS nodes. Classes implement variables and procedures in a pure C/C++ fashion, while ROS nodes are thought to wrap Classes and to provide a flexible and easy way to share information between different software modules. Classes are thought to be completely independent from the structures of the ROS tools: to a certain extent, this design provides flexibility in changing the software architecture as it allows to modify the inter-modular communication without altering the core of the Classes.

External libraries are exploited to build the software up: in particular, the main external contributions regard the OpenCV libraries, used to tackle vision-based navigation problems, the GNU scientific library and the TooN library which are used mostly for linear algebra, numerical integration and differentiation.

Following an approach similar to the one described in [12], SPARTANS onboard operations are divided into three hierarchical levels: programs, tests, and maneuvers. Each program is associated with a particular executable file developed by either the SPARTANS team or a guest scientist. Each program consists of one or more tests that are standalone experiments starting when explicitly commanded by the operator through the external control station. Each test may in turn consist of a linear or non-linear sequence of maneuvers. Maneuvers are a convenient convention intended to assist guest scientists in implementing complex sequencing within a single test.

Maneuvers can be used to separate a complex motion into a series of simpler movements. For example, a test may begin with each simulator translating from its deployment location to a specified initial position suitable for the test. In this maneuver, the desired positions could simply be fixed, and a simple PID control law on each simulator could be used to perform the translation. When all the simulators reach the desired locations, a new maneuver begins wherein the simulators perform a coordinated formation rotation using a more complex decentralized control law and a distributed estimation scheme. Maneuvers may be defined by a specific trajectory, control law,

[2] http://www.ros.org/

estimation algorithm, pulse modulation scheme, or any other parameter.

Figure 2.13 shows the diagram of the main processes handled by the SPARTANS software.

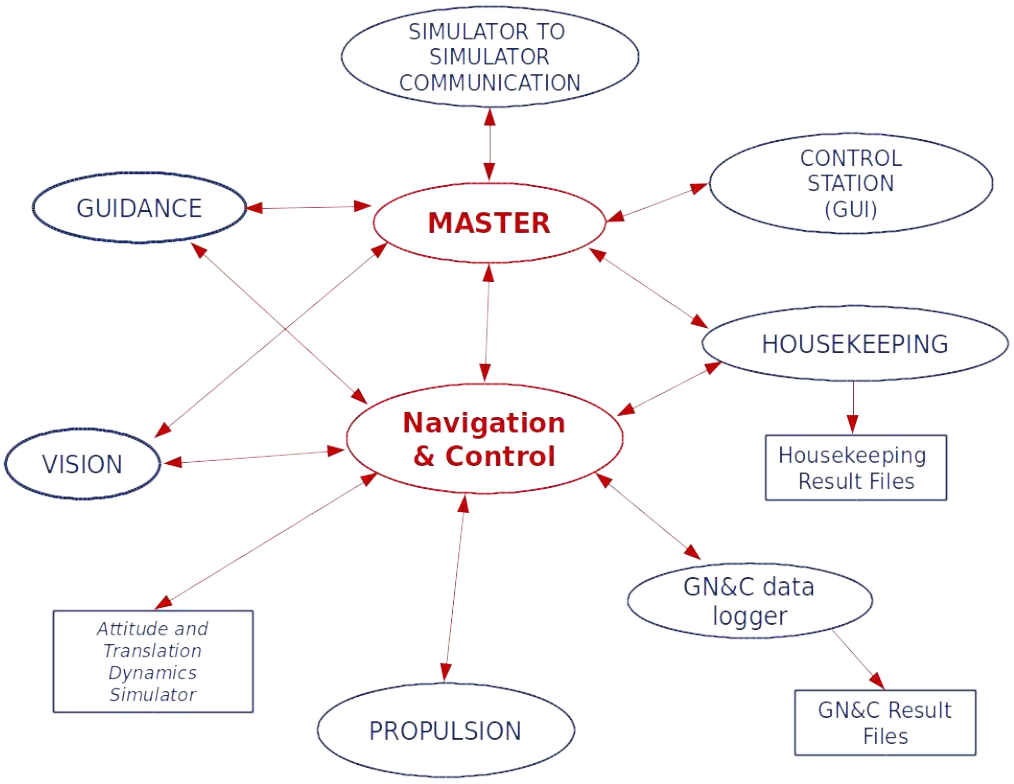

Figure 2.13: Block diagram showing the main processes handled by the SPARTANS software.

2.8 Experimental activities related to the development of the SPARTANS testbed

The current section presents a series of experimental activities performed during the development phase of the SPARTANS testbed, mostly aimed at the characterization of the spacecraft simulators. In particular the following tests will be presented:

1. Estimation of the torsional stiffness of a steel wire by means of the measurements of the free oscillation period of a torque pendulum;

2. Estimation of the thrust force provided by the thrusters on-board the micro-satellites by means of a torque balance;

3. Estimation of the inertial properties of the AM by means of the measurements of the free oscillation period of a torque pendulum;

4. Estimation of the operative pressure and the autonomy of the air suspension system responsible for allowing the TM to float on the test table.

2.8.1 Torque wire characterization

The current section describes the procedure that was followed to characterize the steel wire that is used as sensitive element for the tests described in the two following paragraphs: in particular, the test aims at estimating the wire torsional stiffness. To achieve this objective a torsional pendulum is realized by means of the following main components: (1) a steel wire, (2) an aluminum profile beam, (3) two aluminum cylinders whose mass and geometry are known with high accuracy. The steel wire extremities are clamped to a fixed support and to the profile beam respectively; the two masses are connected to the profile beam at its extremities, as shown in Figure 2.14, taking care that the center of mass of the mechanical assembly lies on the direction of the wire axis. The inertial moment I of the assembly is determined analytically thanks to the prior knowledge on masses and geometries.

The stiffness is estimated by measuring the pendulum free oscillation period T. Thus, by making the system oscillating around its equilibrium position about the wire axis direction, the wire stiffness k is determined by means of the following:

$$k = 4\pi^2 \frac{I}{T^2} \tag{2.1}$$

A simple acquisition system is used to measure the free oscillation period: a laser is mounted on the torsional pendulum and a photo-resistance is placed along the trajectory that the laser beam tracks during the pendulum oscillations. An Arduino UNO board is then responsible for the acquisition of the signal provided by the photo-resistance (the simple scheme of the acquisition system is shown in Figure 2.14): the basic idea is that the light beam, when passing over the photo-resistance, causes a variation in the sensor resistance thus inducing a sudden variation of the measured voltage. The voltage time profile is then parsed to measure the period T of the pendulum oscillations.

The uncertainty on the estimated torsional stiffness i_k is then retrieved by means

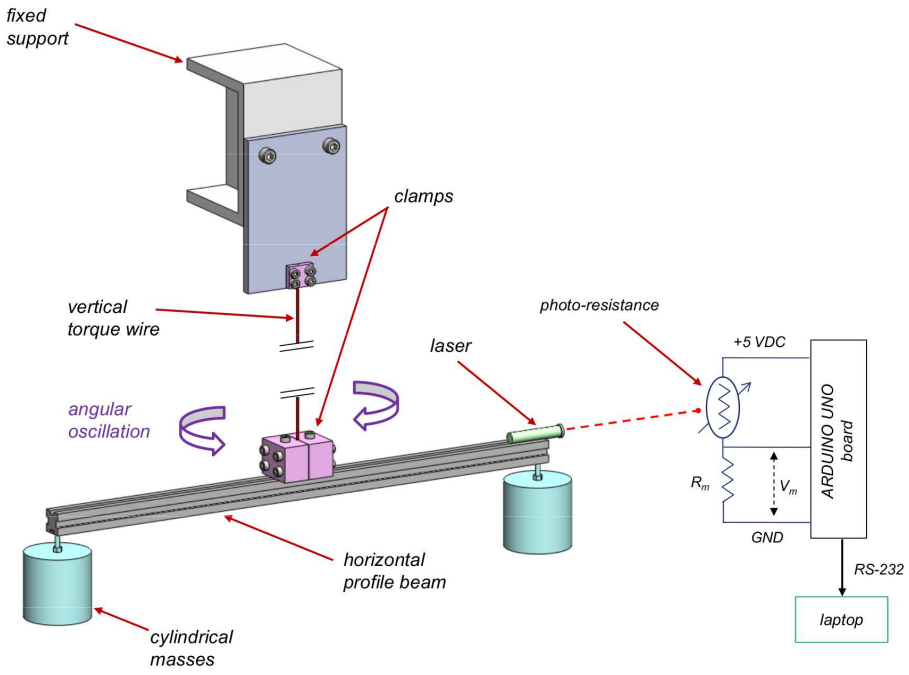

Figure 2.14: Model of the experimental setup used for the torque wire stiffness estimation.

of the Kline-McClintock propagation formula as:

$$\begin{aligned} i_k &= \sqrt{\left(\frac{\partial k}{\partial I}\right)^2 {i_I}^2 + \left(\frac{\partial k}{\partial T}\right)^2 {i_T}^2} \\ &= \frac{4\pi^2 I}{T^2}\sqrt{\frac{{i_I}^2}{I} + \frac{{i_T}^2}{T}}\,. \end{aligned} \tag{2.2}$$

Using equation 2.1 and 2.2, the rotational elastic wire stiffness is

$$k = 0.109\,\frac{\text{Nm}}{\text{rad}} \pm 0.003\,\frac{\text{Nm}}{\text{rad}}(3\sigma) \tag{2.3}$$

The expected value k_{th} for a wire with radius $r = 1 \pm 0.02\,\text{mm}$, length $l = 965 \pm 1\,\text{mm}$ and modulus $G = 75 \pm 6\,\text{GPa}$ is retrieved by means of:

$$k_{th} = \frac{\pi r^4 G}{2l} \pm i_{k_{th}} = 0.123 \pm 0.014\,\text{GPa} \tag{2.4}$$

The obtained results show that the expected measurement is compatible with the one obtained by means of the experimental procedure. Thus, the value of k can be used as a given quantity in the two following tests.

2.8.2 Thrust force estimation

The objective of the current section is to present the experimental methodology used to characterize the thrust provided by the electro-valves on-board the spacecraft simulators. The tests performed take advantage of a torque balance system, whose schematic layout can be seen in Figure 2.15. The experimental setup consists of a vertical torque wire (whose characterization is discussed in Section 2.8.1), two thrusters placed on an horizontal profile beam at a distance equal to $b/2$ from the wire, a pneumatic system similar to the one mounted on-board the AM and, at the extremities of the profile beam, two lasers pointing downward toward a goniometer with an angular resolution of 0.5 deg. The assembly is balanced in order to align its center of mass with the wire axis.

The actuation of the couple of thrusters generates a torque that lead the torque balance, after a temporary transient, to a new equilibrium configuration. In this condition, the torque τ generated by the thrusters is balanced by the elastic torque due to the wire:

$$\tau = Sb = k\theta_{eq} \tag{2.5}$$

where S is the thrust force and θ_{eq} is the equilibrium angle.

Thus, given k and b and by measuring θ_{eq}, the thrust provided by the electro-valves can be easily determined as:

$$S = \frac{k\theta_{eq}}{b}. \tag{2.6}$$

The experimental investigation allowed to identify a linear relationship between the thrust and the upstream pressure p_0 in the range 1.5 bar $\leq p_0 \leq$ 10 bar, resulting in:

$$S(p_0) = 0.0435p_0 - 0.0457 \text{ N} \tag{2.7}$$

with a linear correlation coefficient $r \geq 99\%$.

2.8.3 Inertial properties determination

As described in [13] different methods for the inertia tensor identification are available. Torsional or torque pendulum methods can be used to estimate the moment of inertia about a specified rotation axis passing through the system center of mass. This methodology is adopted to estimate the AM inertial properties, following an approach similar to the one described in Section 2.8.1. Also in this case, the vertical wire is

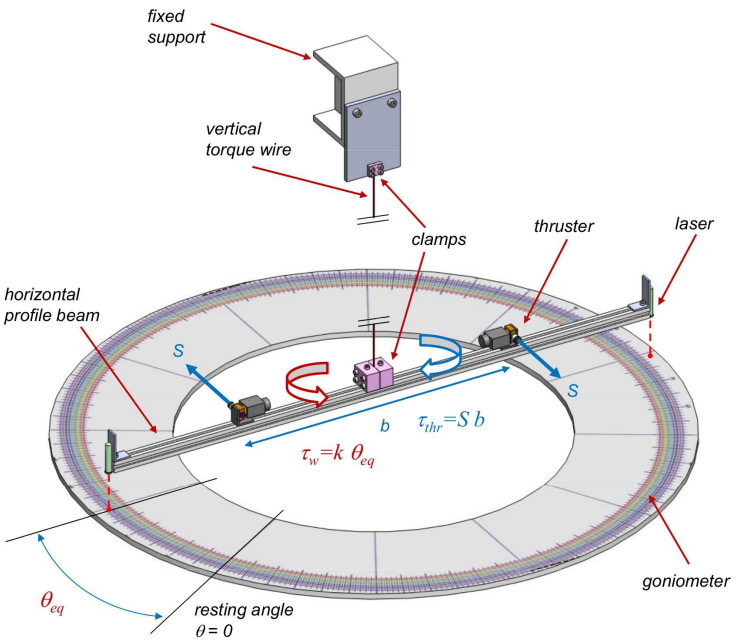

Figure 2.15: Layout of the torque balance system used for the thrust force estimation.

the sensitive element. A support structure allows the connection of the AM to the horizontal profile beam, which in turn supports at its extremities two lasers pointing downwards. Given the requirement of keeping the AM center of mass aligned with the wire axis, the support structure is thought to allow the AM to be oriented in different configurations so that it can be put to rotate about different directions with respect to the body frame. The free oscillation period of the pendulum is measured by means of a photo-resistance and an acquisition system equivalent to the one used for the torque wire characterization. Figure 2.15 shows the layout of the experimental setup used for the characterization.

Measuring the free oscillation period T of the torque pendulum, the total moment of inertia I_{tot} (i.e. the AM's moment of inertia I_{AM} plus the moment of inertia of the support system I_{supp}) can be estimated:

$$I_{tot} = I_{AM} + I_{supp} = \frac{kT_i^2}{4\pi^2}. \tag{2.8}$$

I_{supp} can then be estimated following the same methodology when the AM is removed from the assembly.

Since the inertia tensor has six independent components in a non-principal reference frame, at least six independent measurements are required.

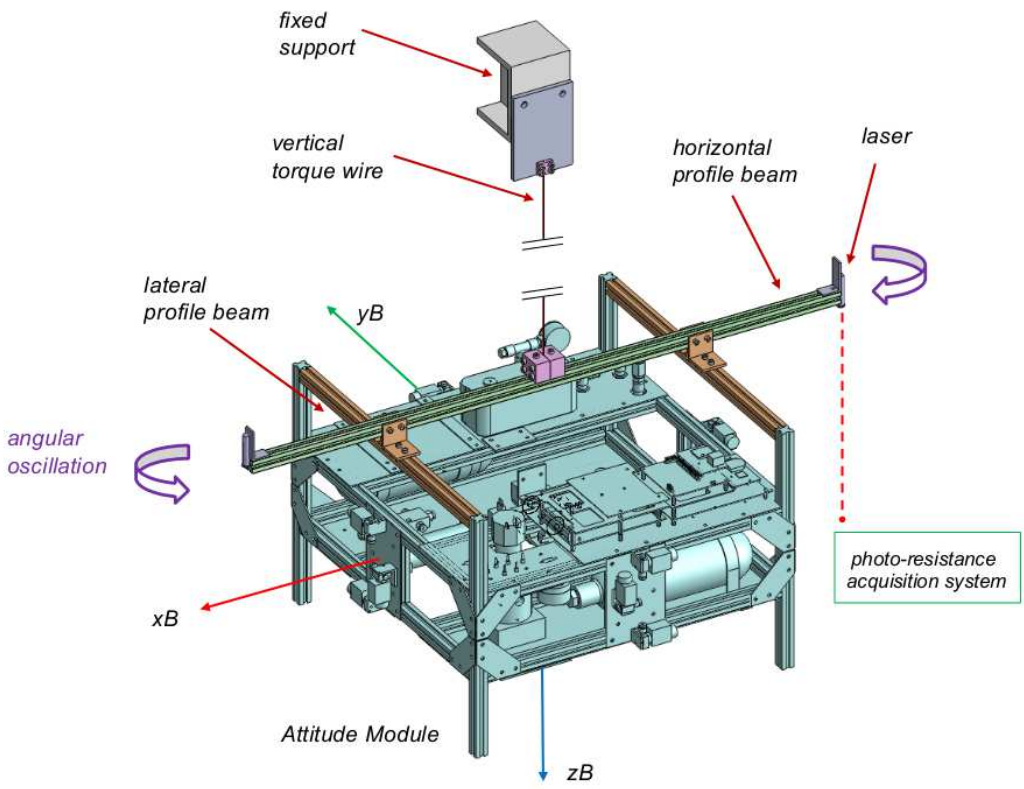

Figure 2.16: 3D model of the experimental setup used for inertial properties estimation. In this particular configuration, the moment I_{zz} is measured.

Let $I = [I_{xx},\ I_{yy},\ I_{zz},\ I_{xy},\ I_{xz},\ I_{yz}]$ be the vector of the unknowns, and $\mathbf{N}$ the coefficient matrix containing the components of the unit vectors $\hat{n}_i$ (expressed in the AM body reference frame) about which the AM oscillates. The vector of the measurements I_m can be related to the vector I through the following:

$$\mathbf{N}I = I_m \qquad\qquad I_m \in \mathbb{R}^n, n \geq 6. \tag{2.9}$$

The number of measurements and the choice of the measurement directions is a critical factor in terms of estimation accuracy. Therefore, taking into account the geometric constraints in connecting the AM to the support structure, a preliminary numerical analysis is performed in order to identify the number of measurements and measurement directions that lead to a better estimation of the AM inertia tensor. Based on data obtained by previous tests and considering the AM geometry, a guess value for the three principal moment of inertia of the AM are set up: this assumption allows to obtain the value of $I_{m,i}$ with respect to the measurement direction $\hat{n}_i$ by

means of

$$I_{m.i} = \hat{n}_i^T \mathbf{J} \hat{n}_i + r_i \tag{2.10}$$

where $\mathbf{J} \in \mathbb{R}^{3x3}$ is the unknown inertia tensor and r_i is a zero mean random noise used to generate more representative measurements.

Two main parameters are used as indicators to understand the quality of different sets of measurement directions: (1) the conditioning number of the coefficient matrix $\kappa(\mathbf{N})$ and (2) the eigenvalues of the covariance matrix of the error affecting $\mathbf{J}$. In addition, the simplicity of the hardware system required to support the AM is considered. This preliminary procedure results in the definition of 9 different measurement directions: the corresponding measurements obtained by means of the torque pendulum are summarized in Table 2.3[3].

Table 2.3: Moments of inertia values obtained through the experimental tests. The measurement directions are determined by means of the preliminary numerical analysis.

Estimated quantity	**Azimuth** [deg]	**Elevation** [deg]	**Estimate** kg m^2	**Uncertainty** [%](1σ)
I_{xx}	0	0	0.8851	3.05
I_{yy}	90	0	0.7760	2.82
I_{zz}	0	90	1.4213	1.66
I_{xy}	45	0	0.7210	2.11
I_{yx}	-45	0	0.9329	2.10
I_{xz}	0	45	1.1520	2.50
I_{zx}	0	-45	1.1454	2.57
I_{yz}	90	45	1.0943	2.63
I_{zy}	90	-45	1.0961	2.68

Solving equation 2.9, the AM inertia tensor is obtained with a maximum uncertainty of 4%(2σ):

$$\mathbf{J} = \begin{bmatrix} 0.8823 & -0.1060 & 0.0033 \\ -0.1060 & 0.7739 & -0.0009 \\ 0.0033 & -0.0009 & 1.4186 \end{bmatrix} \text{ kg m}^2. \tag{2.11}$$

[3]Azimuth and elevation refer to the spherical coordinates that define the direction of measurement with respect to the AM body reference frame

The described experimental method, even if time consuming, reveals to be safe, simple as regards both the required hardware and software and with basic skill requirements of the testing personnel.

2.8.4 Characterization of the Air Suspension System

The current section aims at presenting the preliminary experimental activities performed to characterize the air suspension system, which provides the TM with low-friction planar motions. In particular, the tests have the objective of (1) estimating the operative pressure that ensure a smooth motion of the TM and (2) of determining the autonomy time-window that is granted if the air skids are fed with a certain operative pressure under a given load. The investigation is performed by following an experimental practical approach.

The experimental setup used for the characterization consists of three air skids (the same mounted on the TM) supporting a test platform on top of which additional loads can be placed. A minimal pneumatic circuit is employed to feed the skids with a pressurized airflow which is in turn provided by a compressor with a capacity of 50 Lt and a maximum operative pressure of 8 bar.

Several tests are performed to determine the most convenient pressure that ensure smooth motions at different load conditions: in practice, the pressurized airflow must be sufficient to support the platform load by generating a thin air cushion that avoid contacts between the skids lower surface and the test table. Each test is performed by varying the additional mass placed on top of the platform, ranging from a minimum of 20 kg to a maximum of 50 kg approximatively. Once the most suitable pressure is determined for a given load, the time of discharge of the compressor from 8 to 6 bar is recorded with a chronometer. Tab 2.4 summarizes the obtained results: it can be seen that, given a certain load, the time of discharge in some cases remains constant at the level of second, while in others it varies in the order of few seconds. It is reasonable to assume that the higher variability is due to non-optimal pressure levels that may induce instabilities in the airflow. Only stable configurations are therefore considered for the analyses.

The data obtained are used to determine parametric curves to be employed in the design phase of the TM's pneumatic system. Assuming that the air tanks on-board the TM can store air with a pressure ranging from 100 to 200 bar approximatively, the

Table 2.4: Results of the experimental characterization of the air skids.

TEST 1. Load: 20.4 kg	
Pressure [**bar**]	**Autonomy** [**s**]
3.5	66 ± 1
3.5	65 ± 1
3.5	64 ± 1

TEST 2. Load: 31.4 kg	
Pressure [**bar**]	**Autonomy** [**s**]
4	58 ± 1
5	48 ± 1
5	48 ± 1

TEST 3. Load: 37.4 kg	
Pressure [**bar**]	**Autonomy** [**s**]
4	55 ± 1
4	57 ± 1
5	46 ± 1
5	48 ± 1

TEST 4. Load: 43.4 kg	
Pressure [**bar**]	**Autonomy** [**s**]
4.5	54 ± 1
4.5	44 ± 1
6	42 ± 1
6	44 ± 1

TEST 5. Load: 49.4 kg	
Pressure [**bar**]	**Autonomy** [**s**]
4.5	52 ± 1
4.5	42 ± 1
5	50 ± 1
5	50 ± 1
6	44 ± 1
6	45 ± 1

curves of autonomy and mass of air in the tanks are determined for each pair of load and air skid pressure level (as reported in Table2.4). In performing this parametric study the air is considered as an ideal gas.

Figure 2.17 show the expected autonomy level with tanks loaded at a pressure of and 200 bar. The analysis led to the design of the air support system as presented in Section 2.4.2. It can be noticed that, depending on the overall mass to be supported by the air skids, the autonomy for 3
unitLt of air is comprised between 4 and 7 minutes. The total mass of air contained inside the tanks result to be approximatively of 0.8 kg.

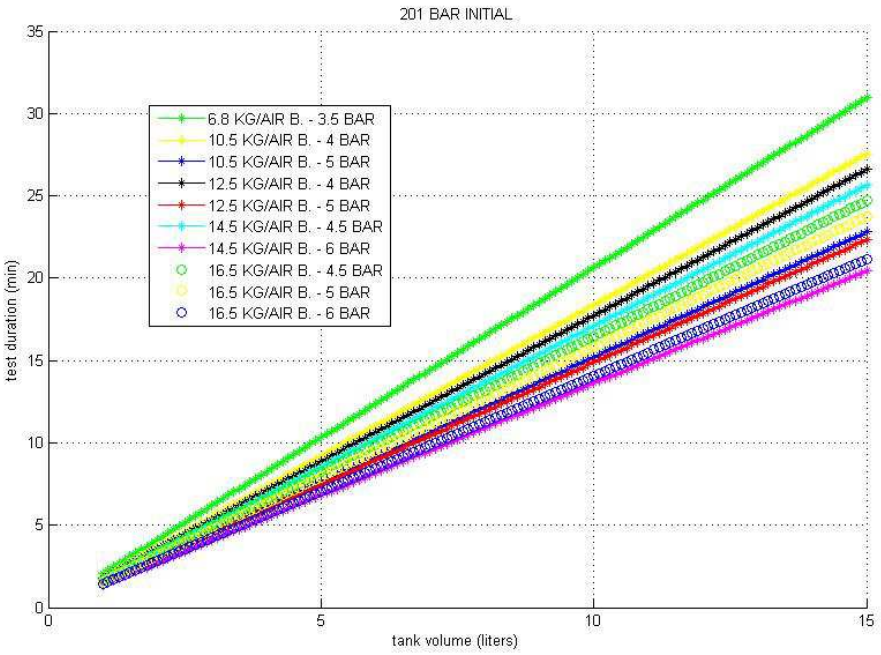

Figure 2.17: Autonomy level curves for the air skids given an initial pressure of 200 bar in the tanks.

Chapter 3

Metrological characterization of a monocular system for relative pose estimation

3.1 Introduction

The current chapter focuses on the characterization of a monocular vision system used for relative pose estimation. The investigation considers a scenario in which a target spacecraft, provided with fiducial markers on top of its surface, is observed by a chaser satellite by means of a monocular system employed as primary sensor.

Automated rendez-vous and docking is an open and active topic in space research. Several missions in the past were conceived with the aim of demonstrating, from a technological point of view, the capability of performing autonomous rendez-vous and docking maneuvers. The US-sponsored DARPA's Orbital Express mission, in 2007, was able to accomplish this objective: the Boeing ASTRO and the Ball Aerospace NEXTSat spacecraft performed multiple rendez-vous and docking, demonstrating indeed some of the technology required for on-orbit servicing [14]. Orbital Express exploited the Advanced Video Guidance Sensor (AVGS), which is a laser-based system that provides bearing at midrange distances and a complete pose estimation at near ranges. This kind of sensor consists of two main parts: at least one laser light source and a receiving detector. The emitter generates a flash or pulse and part of the radiation reflected by a target object is collected by the detector, which is sensitive only to the laser wavelength. Following a similar approach, many researchers took advantage of a flash light detection and ranging (LIDAR) sensor as a primary sensor [15] (a broad overview

on the topic is presented in [16]).

The main advantage of LIDAR systems is that they provide a direct measurement of an observed object by measuring the time of flight of an emitted laser impulse. However, given their complexity, costs and power requirements, they revealed to be unsuitable for low budget missions (i.e. CubeSat).

One of the most widely adopted solutions that allow to overcome the limitations of LIDAR systems consists in the employment of cameras, either in monocular or stereoscopic configuration, as a primary navigation sensors: they are cost-effective, with low power requirements and capable of encoding huge amount of information (e.g. shape, color, brightness). However simplicity has a downside: (1) image quality is highly dependent on the lighting conditions and (2) 3D scenes are mapped into a 2D space through the prospective projection (see Section 3.2.2). As regards the first aspect, illuminators can be used to ensure better lighting conditions (leading to an higher power consumption), while the latter requires the employment of proper algorithms and procedures to interpret three-dimensional scenes starting from the information encapsulated in a planar array.

The chapter is structured as follows: after introducing the mathematical concepts laying under the adopted formulation, the image analysis procedure and the measurement approach are presented. Details on the laboratory setup are provided and the schedule of the performed tests is presented. Results of the relative pose estimation are shown and the uncertainty sources affecting the measurement are discussed.

3.1.1 Overview of the investigation approach

The proposed measurement approach relies entirely on visual navigation data exploiting fiducial markers. The algorithm is thought to provides pose estimations without embedding any prior knowledge of both forces and torques applied to the target spacecraft.

The general estimation approach consists of five sequential steps:

- image acquisition;
- removal of image distortions;
- image processing;

- feature detection;
- solution of the exterior orientation problem.

The image processing step is crucial to ensure that the features of interest are correctly identified and recognized. Once that this objective is achieved, the exterior orientation problem is solved by means of the perspective-from-three-point (P3P) solver. Redundancy is considered in the design of the fiducial markers to ensure the robustness of the measurement algorithm. Two subsequent steps to improve the accuracy are considered: (1) the first one relies only on a RANdom Sample and Consensus (RANSAC) approach [17], while (2) the second combines the RANSAC scheme with a non-linear optimization to refine the estimated pose. These two approaches are discussed considering also the computational aspects.

From a practical point of view, the performances of the algorithms are assessed by means of experimental tests: a simple but representative laboratory setup comprising a simple satellite mock-up is employed and several acquisitions are performed to investigate how the measurement algorithm behaves in different operative conditions.

3.2 Mathematical preliminaries

The notation used to represent coordinate transformations is presented prior to be employed throughout the current chapter: the three-by-one vector of real numbers ${}^{A}t_{P}$ represents the position of the point P with respect to the reference frame A, while the three-by-three matrix ${}^{B}_{A}R$ is the rotation matrix used to transform coordinates from reference frame A to reference frame B. The employed attitude parametrization is discussed in the next section.

3.2.1 Attitude parametrization

The attitude parametrization employed throughout the chapter is the simplest to understand from a physical point of view and it exploits the Euler angles.

Euler angles consist of three angles (ϕ, θ, ψ) that describe right-handed rotations about the x-axis, y-axis and z-axis respectively.

Even if the Euler angle representation is minimal as it describe three degrees of freedom by means of three parameters, it can lead to singular configurations, namely the

gimbal lock, that lead to the loss of a degree of freedom. Therefore it is often convenient employing a representation with more than three parameters, such as quaternions, to avoid singularities. As it will be seen later, the methodology under investigation in the current chapter does not require such a precaution as the conditions in which gimbal lock occurs are avoided.

In general any set of rotations does not commute and therefore it is necessary to define and adhere to a convention for the order of the applied rotations. The parametrization adopted makes use of rotation matrices, or direction cosine matrices, that allow to represent the attitude by means of 9 parameters.

A general rotation matrix is the result of the multiplication of rotation matrices expressing rotations about the x, y and z axes which are in turn respectively defined as:

$$R(\phi) = \begin{bmatrix} 1 & 0 & 0 \\ 0 & c(\phi) & s(\phi) \\ 0 & -s(\phi) & c(\phi) \end{bmatrix}$$

$$R(\theta) = \begin{bmatrix} c(\theta) & 0 & -s(\theta) \\ 0 & 1 & 0 \\ s(\theta) & 0 & c(\theta) \end{bmatrix}$$

$$R(\psi) = \begin{bmatrix} c(\psi) & s(\psi) & 0 \\ -s(\psi) & c(\psi) & 0 \\ 0 & 0 & 1 \end{bmatrix}.$$

A three-dimensional rotation R_{321} can be expressed as $R_{321} = R_1(\phi)R_2(\theta)R_3(\psi)$. The notation employed in this chapter relies on a sequence of rotations 321 which assumes that the first rotation is performed about the z direction, followed by one about y and finally about x, thus leading to the following parametrization of the rotation matrix:

$$R_{321} = \begin{bmatrix} c(\psi)c(\theta) & c(\theta)s(\psi) & -s(\theta) \\ c(\psi)s(\phi)s(\theta) - c(\phi)s(\psi) & c(\phi)c(\psi) + s(\phi)s(\psi)s(\theta) & c(\theta)s(\phi) \\ s(\phi)s(\psi) + c(\phi)c(\psi)s(\theta) & c(\phi)s(\psi)s(\theta) - c(\psi)s(\phi) & c(\phi)c(\theta) \end{bmatrix} \tag{3.1}$$

where c and s stand respectively for cos and sin.

The rotation matrix is constrained by the following condition:

$$R_{123}^{-1} = R_{123}^{T} \tag{3.2}$$

which implies the orthonormallity of the matrix R_{123}.

3.2.2 Camera model

To perform measurements by means of a vision system, a mathematical model of the camera is required: this section is aimed at introducing the model employed in the measurement algorithm.

The starting point to interpret how images are formed is the pinhole perspective projection model, that is the simplest and most basic model used in photogrammetry. The model is based on two main assumptions: (1) the aperture of the camera is infinitesimally small and (2) the light falls onto the image plane by following a straight path passing through the aperture. This model is widely employed in literature since it is simple and flexible in embedding lens distortion models.

Figure 3.1 shows a three-dimensional view of the pinhole projection model: in this schematic the image plane (or focal plane, shown as a gray rectangle) is located at a distance f, the focal length, from the focal point (or center of projection) O. Let P be an object whose position with respect to the $Oxyz$ reference frame is $P = [x_P, y_P, z_P]$, while the point $P' = [x'_P, y'_P, z'_P]$ is the projection of P onto the image plane. By exploiting similarity relationships between triangles, the coordinates of P' can be determined as:

$$x'_P = f\frac{x_P}{z_P} \tag{3.3}$$

$$y'_P = f\frac{y_P}{z_P} \tag{3.4}$$

$$z'_P = f \tag{3.5}$$

where all the quantities are expressed in meters.

The line-of-sight angle from the focal point to the object P can be expressed as a function of the a priori knowledge of the focal length and the coordinates of the projection P':

$$\theta_x = 2tan^{-1}\left(\frac{x_P}{z_P}\right) = 2tan^{-1}\left(\frac{x'_P}{f}\right) \tag{3.6}$$

$$\theta_y = 2tan^{-1}\left(\frac{y_P}{z_P}\right) = 2tan^{-1}\left(\frac{y'_P}{f}\right). \tag{3.7}$$

The angles θ_x and θ_y can be seen as the azimuth and elevation that univocally identify the unit vector joining the focal point to the feature P. The dimensions of the

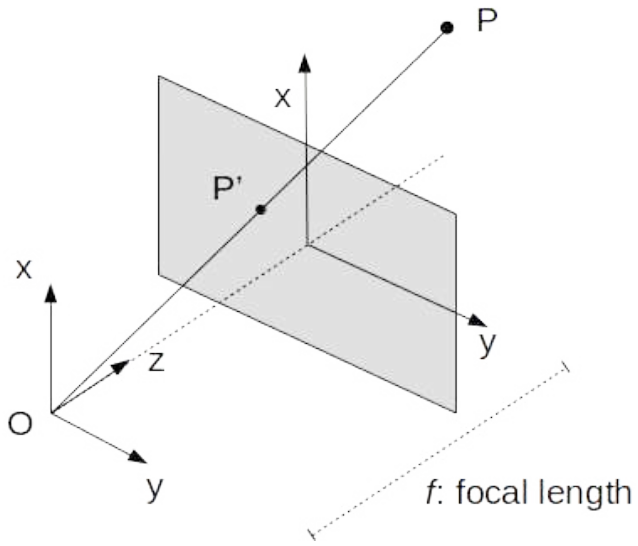

Figure 3.1: Three-dimensional view of the pinhole projection model.

focal plane and the focal length determine the maximum value for θ_x and θ_y: these values are coincident with the actual field of view (FOV) of the camera.

The focal planes are usually built by means of either the Charge-Coupled Device (CCD) or the Complementary Metal–Oxide–Semiconductor (CMOS) technology. These sensors allow to determine the position of a feature on the image plane at discrete locations which are physically coincident with the pixels. Therefore the mathematical model must be extended to transform the coordinates of projected points from meters to pixels.

Let s be the scale factor that represent the number of pixel per unit length, the skew factor s_θ the parameter that accounts for the shape of pixels and $(c_x,\ c_y)$ the coordinates in pixel of the principal point (intersection between the focal plane and the optical axis). If the coordinates of P are known with respect to a global reference frame G, completely independent from the camera, a transformation matrix ${}^C_G T$ is required to express the coordinates of P in the camera frame C. This matrix is defined as:

$$ {}^C_G T = \begin{bmatrix} {}^C_G R & {}^C t_G \\ 0_{1\,\mathrm{x}3} & 1 \end{bmatrix} = \begin{bmatrix} r_{11} & r_{12} & r_{13} & t_x \\ r_{21} & r_{22} & r_{23} & t_y \\ r_{31} & r_{32} & r_{33} & t_z \\ 0 & 0 & 0 & 1 \end{bmatrix} \tag{3.8} $$

and describe the position and orientation of C in G.

Therefore, the projection P'' of P on the focal plane in pixels can be written, by means of homogeneous coordinates through the following equation:

$$P'' = \frac{1}{\lambda} K \Pi_0 {}^C_G T P \tag{3.9}$$

that can be written also in extended form as

$$\begin{bmatrix} x_{P''} \\ y_{P''} \\ & 1 \end{bmatrix} = \frac{1}{\lambda} \begin{bmatrix} f_x & s_\theta & c_x \\ 0 & f_y & c_y \\ 0 & 0 & 1 \end{bmatrix} \begin{bmatrix} 1 & 0 & 0 & 0 \\ 0 & 1 & 0 & 0 \\ 0 & 0 & 1 & 0 \end{bmatrix} \begin{bmatrix} {}^C_G R & {}^C t_G \\ 0_{1\,\mathrm{x}3} & 1 \end{bmatrix} \begin{bmatrix} {}^G x_P \\ {}^G y_P \\ {}^G z_P \\ 1 \end{bmatrix} \tag{3.10}$$

where λ is a scale factor, whose value is equal to z_P. K, the camera matrix or matrix of the intrinsic parameters, is dependent on the specific characteristics of the camera and it is obtained through the process of calibration. Usually the parameter s_θ is assumed to be zero, while the diagonal elements are defined as $f_x = f s_x$ and $f_y = f s_y$. Π_0 is the standard projection matrix. The matrix ${}^C_G T$ is also referred to as exterior orientation.

The only restrictive assumption in the model is that the camera aperture is infinitely small, resulting in a non-realistic model of the camera. In fact, the amount of light falling onto the image sensor is dependent on the size of the aperture and, by using a infinitely small aperture the exposure time should be increased significantly to collect enough radiation, resulting in an increased noise level. Thus, in real applications, the aperture of lenses is increased to avoid this downside, leading to a finite depth of field. As a result, lenses introduce distortion in the image.

The introduced distortion must be considered and removed at software level. This task requires the distortion model to be embedded into the perspective projection equations. Two main distortion mechanism can be identified: (1) radial distortions, which are also known as barrel or pincushion distortions, are due to defects in the lens design, and (2) tangential distortions, which are due to the fact that the image sensor is not orthogonal to the optical axis.

For radial distortions, the distortion at the principal point (optical center of the image) is 0, while it grows as we move toward the outer part of the image. A simple quartic model of distortion can produce good results for most lenses. The radial position of a point on the focal plane is rescaled according to the following equations:

$$\begin{aligned} x_{corrected} &= x \left(1 + k_1 r^2 + k_2 r^4 + k_3 r^6\right) \\ y_{corrected} &= y \left(1 + k_1 r^2 + k_2 r^4 + k_3 r^6\right) \end{aligned} \tag{3.11}$$

where $k_1,\ k_2,\ k_3$ are the first terms of the Taylor series expansion around the principal point, $(x,\ y)$ is the original location of the distorted point, $(x_{corrected},\ y_{corrected})$ the new location resulting from the undistort operation and r is defined as $r = \sqrt{(x-c_x)^2 + (y-c_y)^2}$.

Tangential distortions are characterized by means of two additional parameters $p_1,\ p_2$. Corrections can be applied according to the following equations:

$$\begin{aligned} x_{corrected} &= x\left[2p_1 y + p_2(r^2 + 2x^2)\right] \\ y_{corrected} &= y\left[p_1(r^2 + 2y^2) + 2p_2 x\right]. \end{aligned} \tag{3.12}$$

Eq. 3.11 and 3.12 provide a simplified model to remove distortions that exploits only five parameters. However this model is not able to accurately account for distortions produced by complex lenses (e.g. wide angle lenses, fisheye): these distortion models are not covered in this work as they go beyond the scope of the thesis. Further details on the topic can be found in [18], [19] and [20].

To summarize, the presented camera model represents a non-linear model that incorporates radial and tangential distortion. The projection of a point ${}^{G}P$ onto the image plane and the correction of distortions can be described by means of the non-linear function $\mathscr{P}$:

$${}^{C}P_{corrected} = \mathscr{P}({}^{G}P, \mathscr{I}, \mathscr{E}) \tag{3.13}$$

where $\mathscr{I}$ and $\mathscr{E}$ are the vector of the intrinsic and the extrinsic parameters respectively

$$\begin{aligned} \mathscr{I} &= (\ f_x, f_y, c_x, c_y, k_1, k_2, k_3, p_1, p_2\ ) \\ \mathscr{E} &= (\ {}^{C}_{G}R, {}^{C}t_G\ ). \end{aligned}$$

3.2.3 Camera calibration

The camera calibration procedure is aimed at estimating the camera intrinsic parameters vector $\mathscr{I}$ as it is defined in the previous section, leading to the solution of the so called interior orientation problem. Except for cases in which zoom lenses are used, $\mathscr{I}$ is a vector containing constant quantities that are dependent only on the specific camera. Thus $\mathscr{I}$ are usually estimated by means of a dedicated procedure whose outcomes are then employed as an a priori knowledge in the solution of photogrammetric problems.

Several methods have been proposed for estimating these parameters (see [21], [22], [23], [24]) and a wide range overview on the topic can be found in [25].

The employment of a calibration pattern to solve the interior orientation problem is now considered. The main idea is to collect a number of points, whose coordinates are known with respect to an arbitrary global frame, from different positions and orientations. Relevant points are usually provided by means of either chessboards or circular patterns. Once n points are identified from m different views, both the intrinsic and the extrinsic parameters can be estimated at the same time through the solution of a nonlinear problem with the objective of minimizing the reprojection error as follows:

$$[\mathscr{I}, \mathscr{E}_k] = \underset{\mathscr{I},\mathscr{E}_j}{\arg\min} \sum_{i=1}^{n} \sum_{j=1}^{m} \left\| {}^{C}P_i - \mathscr{P}({}^{G}P_i, \mathscr{I}, \mathscr{E}_j) \right\|^2 \qquad \forall k \in \mathbb{N},\ k \leq m \tag{3.14}$$

where ${}^{C}P_i$ contains the coordinates of the i-th point in camera frame and $\mathscr{P}({}^{G}P_i, \mathscr{I}, \mathscr{E}_j)$ is the reprojection of ${}^{G}P_i$ onto the image plane through the camera model. The minimization problem is usually solved by means of nonlinear least square methods (i.e. Levenberg-Marquardt algorithm).

Throughout this thesis, the algorithm proposed by Zhang [22] is employed for camera calibration.

3.3 Target design

The relative pose estimation algorithm relies on an optical pattern of known geometry. The design of the pattern drives some important aspects such as the accuracy of the estimation procedure and the complexity of both the image processing and pattern recognition algorithms.

Fiducial markers systems consist of two main parts: (1) a set of either active or passive markers and (2) the software routines aimed at pattern detection and recognition. Several options were considered during the design phase.

The simplest option exploits points as fiducial markers (i.e. retro-reflective spheres, adhesive dots): even if the detection of these features is possible through simple segmentation techniques in controlled conditions, the pattern recognition step requires the evaluation of the mutual position of points, leading to complex processes. Another possibility in designing the pattern involves the employment of active markers, such as LEDs or IR emitters: the functioning of these systems determines a power drain

that make their use either unfavorable or impossible in all those cases in which the target spacecraft is decommissioned or out of service. The option of exploiting optical reflectors (i.e. Corner-cubes) is also discarded since they introduce additional mass that may be unacceptable for small satellites (i.e. CubeSat).

Among the the category of passive fiducial markers several alternatives have been proposed in the field of virtual reality (see [26], [27], [28]): in general the employment of these markers is particularly suitable in the case when there are several markers available in the same observed scene. However in spacecraft rendez-vous and docking applications, the surface available for housing fiducial markers may be tight [29], allowing indeed the employment of a low number of markers.

Given all the considerations above, it was taken the decision of developing a custom made set of markers considering four main functional requirements:

1. the markers must be visible also for non-operating target spacecraft;

2. the markers must be as simple as possible while encoding enough information to be recognized;

3. the markers dimensions must be sufficient to be detected from mid range to short range distance;

4. the markers must have small dimensions in order to be suitable for being attached on the surface of a spacecraft.

From the functional requirements it stems the design of the fiducial markers. Each marker consists of a squared black frame on a white background, with dimensions of 8 x8 cm. Each marker can be univocally identified by means of a predetermined number of black squared features, called holes, which are contained within the external frame. So, if a marker contains three holes, it will be univocally identified as *Marker n.3*. Both the position and the dimension of the holes are chosen in order to avoid that the effects of the spatial resolution make two neighboring holes indistinguishable, avoiding thus conditions that may lead to false detections. Preliminary analysis confirmed that, in the range of interest for laboratory testings (discussed in Section 3.6), this last condition is satisfied. The final layout of the markers with identifier ranging from 1 to 4 are shown in Figure 3.2.

Figure 3.2: Overview of the fiducial markers: markers with identifier ranging from 1 to 4 are shown.

3.4 Image analysis and pattern recognition

Once the vision system has acquired a frame, radial and tangential distortions are corrected by means of eq. 3.11 and 3.12. Therefore the pinhole camera model can be exploited to associate the 3D point coordinates with their 2D projections as discussed in Section 3.2.2.

Each image, acquired in the RGB colorspace, is converted to grayscale and it is subsequently segmented by means of a binary thresholding operation such that

$$dst(x,y) = \begin{cases} maxVal & \text{if } src(x,y) \geq \text{threshold} \\ 0 & \text{if } src(x,y) \leq \text{threshold} \end{cases} \tag{3.15}$$

where $src(x,y)$ and $dst(x,y)$ refer to the intensity of the pixel of coordinates (x,y) of the source and destination images respectively. In order to adjust the threshold level according to the light conditions of the overall scene, the threshold is determined adaptively following the approach of [30]. It should be observed that, even if a grayscale camera would be the optimal sensor to perform the acquisitions, a RGB sensor is employed as it was, at the moment of conducting the experimental activity, the only sensor available within the laboratory facilities.

In order to limit the effects of noise in the thresholded image, residual speckles are filtered out by means of morphologic operations, in particular by means of a proper combination of erosion and dilation. The size of the regions modified by these operations (i.e. size and shape of the structuring element) is tuned such that the holes contained within the markers are not affected or altered.

Once these operations are performed, the processed image is made available to the pattern recognition algorithm. The first step to identify the markers consists in the

identification of the boundaries of object and holes in the binary image, taking into account the relationship parent-child existing between the detected regions.

Considering the estimated pose of the target with respect to the camera frame it is possible to estimate the upper and lower perimetral length, in terms of pixels and with an adequate safety factor, of connected regions that can be considered as valid candidates to be labeled as markers. As a remark, even if this operation reduces the computational burden of the pattern recognition step, when the image acquisition begins, the lack of an a priori knowledge of the relative pose dictate the analysis of the overall regions.

The selected regions are then processed by means of the Douglas-Peucker algorithm [31] with the aim of reducing the number of points defining the boundaries. In fact, if a boundary is considered as the union of line segments, the algorithm allows to determine a similar curve, with fewer points, which ensure that the maximum distance between the original curve and the simplified curve remains under a user-defined threshold. Therefore the simplified curve results to be composed of a subset of points that defined the original curve.

Given the squared shape of the fiducial markers, all the regions whose boundaries have a number of vertex not equal to 4 are neglected. The selection of the threshold to be employed in the Douglas-Peucker algorithm is crucial to maximize the probability of identifying correctly the markers. In fact, if the threshold is too small, the simplified curve surrounding the connected region would be characterized by an high number of points while, on the other hand, a too large threshold would lead to underestimate the number of vertex with the consequent possibility of having false positives.

The selected regions are then parsed to identify the number of holes contained within the squared black frame, leading to the correct identification of the markers.

Finally, once a marker is recognized, it is possible to extract relevant points to be employed in the pose estimation procedure. The corners of the squared frame and the center of the markers are employed to this purpose.

The main steps of the procedure are summarized in Algorithm 1.

Algorithm 1 Image analysis and pattern recognition

```
1: procedure IMAGE ANALYSIS AND PATTERN RECOGNITION
2: loop:
3:     boundaries[ ], markers[ ];
4:     j ← 0;
5:     src ← captureImage();
6:     dst ← undistort(src);
7:     boundaries ← segmentation(dst);
8:     for i = 0 to boundaries.length do
           %comment: perimeter evaluation to search for valid candidates%
9:         flag ← checkPerimeter(boundaries[i],relativePose);
10:        if ( flag = Success ) then
               %comment: apply the Douglas-Peucker algorithm%
11:            boundaries[i] ← DouglasPeucker();
12:            if ( boundaries.numberOfVertices = 4 ) then
13:                marker[j] ← getMarkerID();
14:                return feature coordinates;
15:            end if
16:        end if
17:    end for
18:    goto loop .
19: end procedure
```

3.5 Pose estimation approach

The fundamental step in the measurement procedure consists in the solution of the exterior orientation problem. According to [17] the problem is also named Location Determination Problem (LDP) and it is defined as follows: *Given a set of m control points, whose 3-dimensional coordinates are known in some coordinate frame, and given an image in which some subset of the m control points is visible, determine the location (relative to the coordinate system of the control points) from which the image was obtained.* In literature the problem is also referred to as Perspective from n Points (PnP) or resection problem and numerous solutions have been proposed (e.g. [32–36]).

The minimum number of points that can be used to find a solution for the PnP problem is three, yielding to the so called P3P problem. In this scenario it was proved that the problem admits four possible solutions. A fourth point is therefore required to remove the ambiguity.

Even if in usual scenarios the number of features available is greater than three, there are two main reasons that make the P3P problem appealing to researchers: (1) direct solutions of the P3P problem are available in literature and (2) the algorithm can be conveniently embedded into a RANSAC scheme to reduce the presence of outliers (i.e. points in the image plane that are erroneously associated to 3D points). As regards direct methods, [37] describes and compares the main direct solutions of the P3P problem up to 1993. More recent solutions to the same problem are presented in [38] and [39].

Commonly P3P algorithms first estimate the distance between the center of projection of the camera and the feature points and, once the distances are known, the feature coordinates can be expressed in the camera frame. Thus two cloud of points are identified, one in the camera frame and the other in the object/global frame. The relative pose of the object is then retrieved as the transformation that align the two point clouds: this problem can be solved in closed-form by means of Singular Value Decomposition [40], eigenvalues/eigenvectors [41] or quaternions [42].

Of particular interest is the work presented in 2011 by Kneip et al. [43] which provides a direct and efficient solution to the P3P problem. In contrast with the previous approaches the algorithm computes in one single stage the position and orientation of the camera in the object/global frame by exploiting image coordinates and their corresponding 3D points in the object frame.

In the following sections the solution proposed by Kneip is employed for relative pose estimation. After a brief overview of the Kneip algorithm, the measurement approach is described in detail.

3.5.1 Solution of the Perspective from 3 Points problem: the Kneip algorithm

The P3P problem, as already pointed out, is solved adopting the Kneip algorithm. This section is devoted to provide an overview of the employed mathematical model.

Let $P_1,\ P_2,\ P_3$ be three control points whose coordinates are known with respect to an arbitrary global reference frame G, that can be conveniently chosen to be the target/object fixed reference frame.

Assuming the camera to be optically calibrated, it is possible to define three unit vectors $f_1,\ f_2,\ f_3$ defining the spatial directions that join the camera optical center to

the three control points (see Fig 3.3).

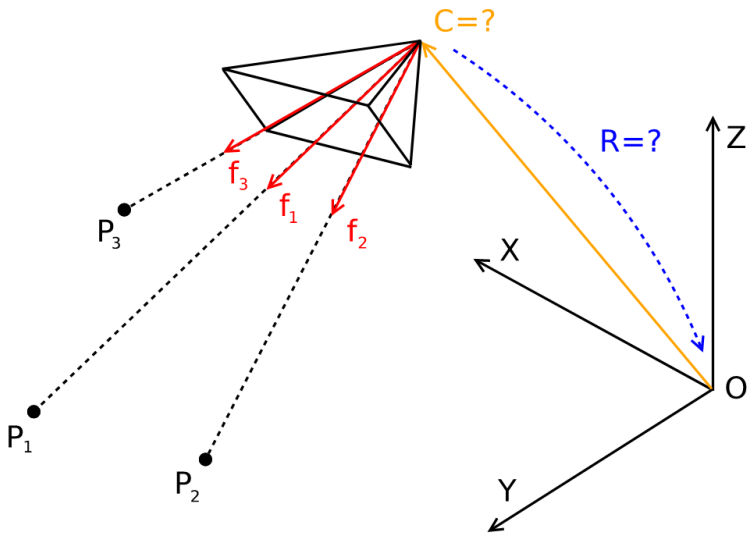

Figure 3.3: Survey of the problem.

The first step of the solution consists in the definition of two intermediate frames: (1) the intermediate camera frame $\tau = (C, t_x, t_y, t_z)$ and (2) the intermediate world frame $\eta = (P_1,\ n_1,\ n_2,\ n_3)$, where $t_i,\ n_i \in \mathbb{R}^3\ \forall i \in [1, 3]$. The unit vectors defining the intermediate reference frames are defined by means of the following:

$$\begin{aligned} t_x &= f_1 \\ t_z &= \frac{f_1 \times f_2}{||f_1 \times f_2||} \\ t_y &= t_z \times t_x \end{aligned} \tag{3.16}$$

$$\begin{aligned} n_x &= \frac{\overrightarrow{P_1P_2}}{||\overrightarrow{P_1P_2}||} \\ n_z &= \frac{n_x \times \overrightarrow{P_1P_3}}{||f_1 \times \overrightarrow{P_1P_3}||} \\ n_y &= n_z \times n_x \end{aligned} \tag{3.17}$$

To ensure the existence of η it is required that $P_1,\ P_2,\ P_3$ are not aligned, i.e. $\overrightarrow{P_1P_2} \times \overrightarrow{P_1P_3} \neq \vec{0}$.

Let T and N be two rotation matrices: via $T = [t_x\ t_y\ t_z]^T$ feature vectors can be

transformed into τ, while $N = [n_x\ n_y\ n_z]^T$ transforms world points into η:

$$^{\tau}f_i = T\ f_i \tag{3.18}$$

$$^{\eta}P_i = N\ (P_i - P_1) \tag{3.19}$$

The problem of estimating the relative pose requires now the estimation of the mutual position and orientation of the two intermediate reference frames. Let π be the plane containing the points P_1, P_2 and C. Considering the triangle defined by these three points (see Figure 3.4), the distance $d_{12} = ||\overrightarrow{P_1P_2}||$ is known and the angle β in C can be computed through a simple dot product as:

$$cos\beta = f_1 \cdot f_2. \tag{3.20}$$

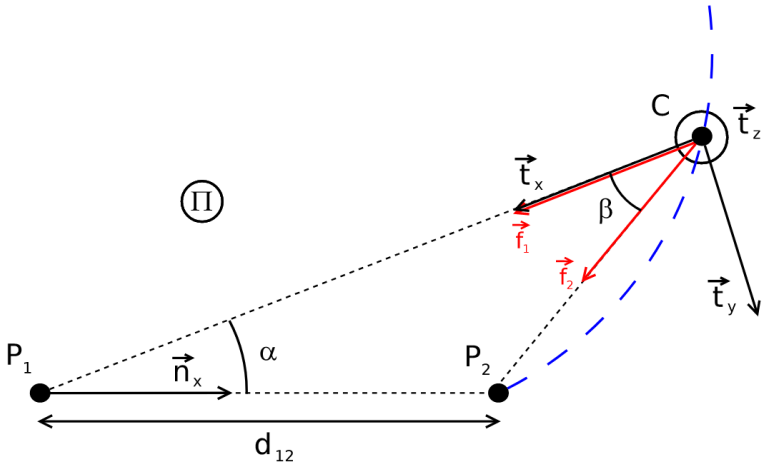

Figure 3.4: Semi-plane π containing the triangle (P_1, P_2, C).

By exploiting trigonometric relations, the above equation in β can be conveniently written in terms of $cot\beta$ as follows:

$$b = cot\beta = \pm\sqrt{\frac{1}{1 - (\cos^2\beta)} - 1}. \tag{3.21}$$

The vectors $\overrightarrow{P_1P_2}$ and $\overrightarrow{P_1C}$ define the angle α which is the only free parameter that univocally identifies the position of C onto the plane π. By exploiting the law of sines, the following equation holds:

$$\frac{||\overrightarrow{P_1C}||}{d_12} = \frac{\sin(\pi - \alpha - \beta)}{\sin\beta}. \tag{3.22}$$

The location of C onto the plane π can therefore be find as a function of α, β and d_{12}:

$$C^{\pi}(\alpha) = ||\overrightarrow{P_1C}|| \begin{bmatrix} \cos\alpha \\ \sin\alpha \\ 0 \end{bmatrix} = d_{12} \begin{bmatrix} cos\alpha(bsin\alpha + \cos\alpha) \\ \sin\alpha(b\sin\alpha + \cos\alpha) \\ 0 \end{bmatrix} \tag{3.23}$$

To locate C in the 3D space, one further parameter is needed. Therefore θ is defined as the angle that measures the rotation of the plane π about the direction defined by n_x (Figure 3.5). The rotation matrix Q that aligns η with τ is then defined as:

$$Q = Q(\theta, \alpha) = \begin{bmatrix} -\cos\alpha & -\sin\alpha\cos\theta & -\sin\alpha\sin\theta \\ \sin\alpha & -\cos\alpha\cos\theta & -\cos\alpha\sin\theta \\ 0 & -\sin\theta & \cos\theta \end{bmatrix}. \tag{3.24}$$

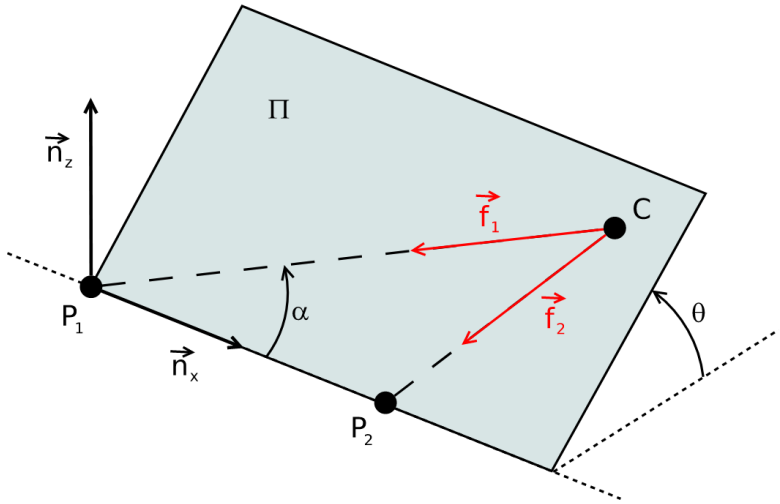

Figure 3.5: Rotation of the plane π of an angle θ about n_x.

In order to find the values for θ and α the following condition is imposed: P_3 and f_3, expressed in τ, must have the same direction. This condition can be stated formally as:

$$^{\tau}P_3 = Q(\theta, \alpha)[^{\eta}P_3 - ^{\eta}C(\alpha, \theta)]. \tag{3.25}$$

Solving for θ and α lead to a fourth degree polynomial that can be solved by means of the Ferrari's closed form solution, leading to four possible real (θ, α)-pairs. Matrices $^{\eta}C$ and Q can then be found through backsubstitution of the pair (θ, α) in the corresponding equations, and eventually the camera center and orientation with

respect to the global reference frame can be determined respectively as:

$$C = P_1 + N^T \, {}^{\eta}C \tag{3.26}$$

$$R = N^T Q^T T \tag{3.27}$$

As previously stated, the choice of the correct solution among the four possible poses requires a fourth point to be employed: further details on this aspect are provided in the next section.

3.5.2 The measurement algorithm

The camera employed is assumed to be optically calibrated. Let T and C be the reference frames fixed to the target satellite and to the camera respectively. The first step of the measurement procedure consists in the detection, in each acquired frame, of the projections ${}^{C}P_i = [{}^{C}x_i, {}^{C}y_i, {}^{C}z_i]^T$ onto the image plane of the points ${}^{T}P_i$ attached to the target. Since both the intrinsic parameters and the distortion coefficient are known, without loss of generality it can be assumed that the points are projected onto an equivalent camera with the same optical center of the real camera and unitary focal length. Then the matching phase takes place and 3D points are univocally associated with their corresponding 2D projections. The algorithm exploits the a priori knowledge of the geometry of the target, i.e. the coordinates of the 3D points with respect to the target fixed frame T are measured.

As discussed in the previous section, the minimum number of features required to determine univocally the relative pose is four. Three points lead to four possible poses while the fourth point ${}^{T}P_4$ is projected onto ${}^{C}\hat{P}_{4,j}$ on the image plane by means of the perspective projection model according to the following equations:

$${}^{C}P_{4,j} = {}^{C}_{T}R_j \, {}^{T}P_4 + {}^{C}t_{T,j} \qquad j = 1 \ldots 4 \tag{3.28}$$

$${}^{C}\hat{P}_{4,j} = \frac{1}{{}^{C}z_{4,j}} \left[{}^{C}x_{4,j}, \, {}^{C}y_{4,j}, \, {}^{C}z_{4,j} \right]^T \qquad j = 1 \ldots 4. \tag{3.29}$$

Only one of the four evaluated projections ${}^{C}\hat{P}_{4,j}$ falls near the measured point ${}^{C}P_{4,j}$ and allows to select the correct rotation matrix ${}^{C}_{T}R$ and translation vector ${}^{C}t_T$.

Both the accuracy and the robustness of the P3P-based algorithm can be improved by exploiting a larger number of features ($n > 4$). The way in which this improvement can be achieved is now presented.

Once the 3D features and their 2D projections are known, the relative pose is determined by means of the Kneip algorithm following the approach discussed in Section 3.5.1. In the case that more that four points are available in the field of view, the solution of the P3P problem can be employed as a first initial step towards the final pose estimation. This is the actual approach of the measurement algorithm.

Two subsequent steps are performed:

1. the P3P solution is embedded in a RANSAC scheme;

2. the outcomes of the RANSAC algorithm are exploited inside a non-linear optimization procedure to refine the estimated pose.

In the RANSAC procedure the P3P problem is solved iteratively by selecting randomly four features in each iteration. These features are used to instantiate a first initial guess for the relative pose which is in turn validated by exploiting the whole available points. This validation step is performed adopting the following procedure: given the relative pose ${}^{C}_{T}T$ of the camera with respect to the target:

a. determine the 2D coordinates of the point ${}^{T}P_i$ by means of the perspective projection model as in eq. 3.28 and 3.29 for all the available points $i = 1 \dots (n-4)$;

b. compute the reprojection error ε_i by comparing the 2D locations of the projected points ${}^{C}\hat{P}_i$ and the measured points ${}^{C}P_i$:

$$\varepsilon_i = ||{}^{C}\hat{P}_i - {}^{C}P_i||_2 \tag{3.30}$$

c. compare the reprojection error ε_i with a user defined threshold l_{th}: if $\varepsilon_i \geq l_{th}$ then the point ${}^{C}P_i$ can be considered as an outlier for the pose used in the current iteration.

The block diagram of the RANSAC routine is shown in Figure 3.6. For each iteration, the number of inliers is accounted for. Therefore the relative pose that is selected as the correct solution is the one that ensure the maximum consensus, i.e. the solution that comprises the maximum number of inliers.

The output of the RANSAC algorithm are two: the selected roto-tanslation ${}^{C}_{T}T$ and the list of the inliers. These outcomes can be therefore employed in a non-linear optimization with the aim of refining the estimated relative pose. The optimized relative

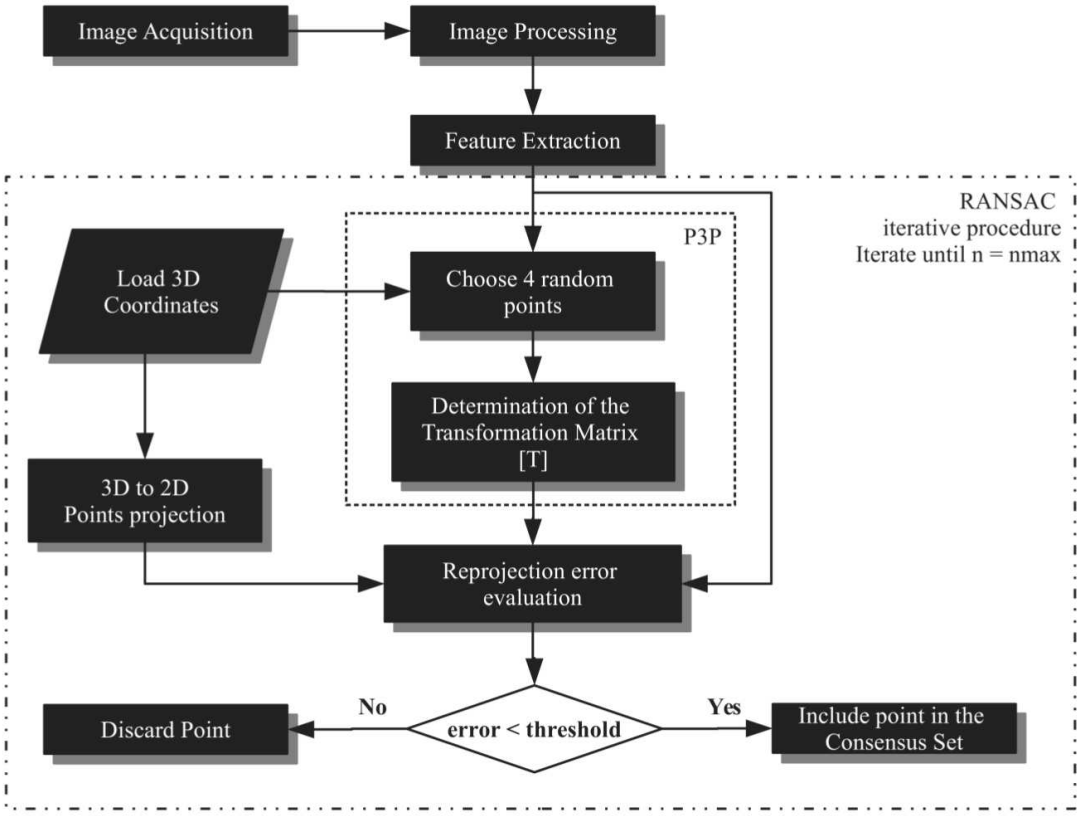

Figure 3.6: Schematic overview of the RANSAC algorithm employed in the relative pose estimation.

orientation, parametrized as a rotation matrix ${}^C_T R$ written in terms of Euler's angles, and the relative position ${}^C t_T$ are evaluated as the arguments that minimize the cost function g of the reprojection errors, considering only the inliers (2D and 3D points) selected by the RANSAC procedure:

$$ {}^C_T T = [\, {}^C_T R, {}^C t_T] = \underset{({}^C_T R, {}^C t_T)}{\arg\min} \sum_{i=1}^{n} ||{}^C \hat{P}_i - {}^C P_i||_2^2. \tag{3.31} $$

The solution of eq. 3.31 is obtained by means of the Levemberg-Marquardt algorithm (see [44]).

3.6 Experimental tests

In the metrological calibration procedure of the visual system as instrument for the satellite position and orientation measurement, a satellite mock-up is mounted both on a high precision motor-driven rotary stage and on a linear slide.

Since the objective of the investigation is to evaluate the performances of the measurement system, the satellite mock-up is kept as simple as possible: two planar surfaces are joined by means of aluminum profile beams to recreate two faces of a nearly cubic spacecraft. On each of the two surfaces four fiducial markers are applied: in particular each marker is placed in the nearby of a corner of the face in which it is positioned. The choice of using four markers per face ensure that up to 40 features can be identified on each face and that the possibility of having degenerate configurations for the P3P solver (i.e. only three aligned features) is avoided. However, if particular lighting conditions occur, the number of identified features may be lower but still sufficient to solve the pose estimation problem.

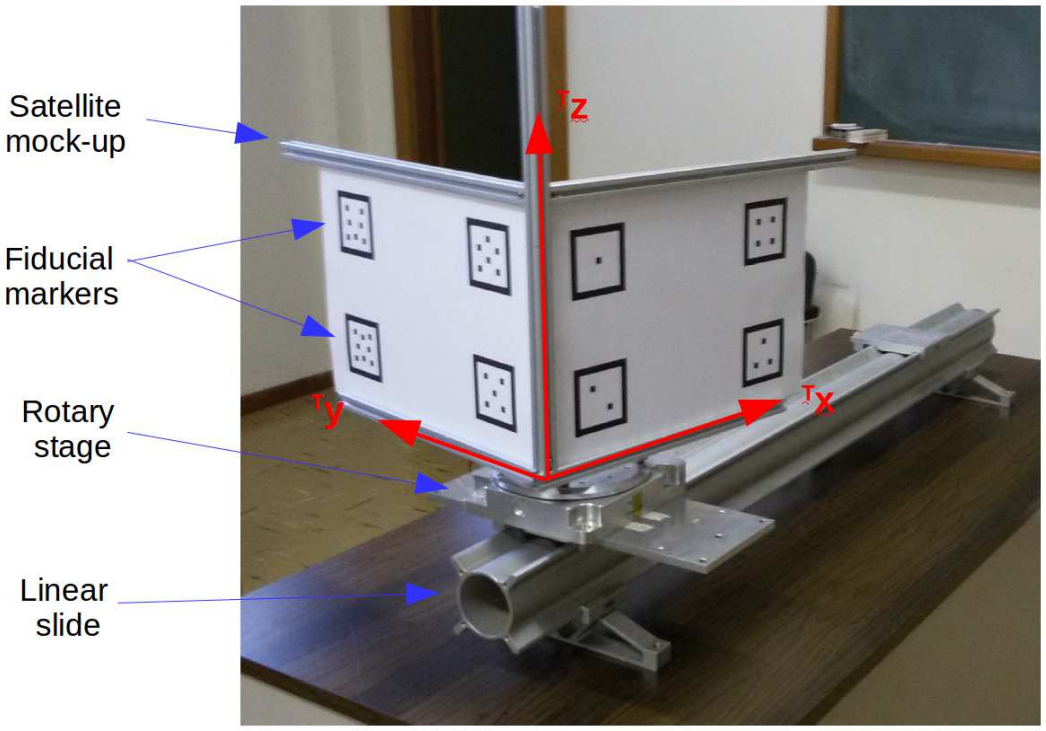

Figure 3.7: Laboratory setup.

The rotary stage is driven by a stepper motor capable of a resolution equal to 1.125 arcseconds, while the linear slide is provided with a graduated scale. Thus, this setup allows to impose linear displacements and/or rotations to the satellite mock-up, and to measure them. In this way the linear displacements and/or rotations measured by the visual system can be compared with known linear displacements and rotation angles. Figure 3.7 depicts the employed setup comprising the satellite mock-up mounted on the rotary stage, which can translate along the linear slide.

The camera used to acquire images, whose characteristics are reported in Table 3.1, is kept fixed at a distance from the satellite mock-up ranging from 1500 mm to 2250 mm approximatively. The optical axis of the camera is substantially kept aligned with the linear slide axis (a relative inclination of 1.3 deg is evaluated).

Table 3.1: Characteristics of the camera employed in the tests.

Camera characteristics	
Resolution	2040 x1086 pixels
Pixel dimensions	5.5 x5.5 μm
Focal length	10.4 mm
Exposure time	300 ms

Calibration coefficients	
f_x	1886.59
f_y	1887.76
c_x	1074.06
c_y	520.55
k_1	-0.09348
k_2	0.13452
k_3	-0.00173
p_1	0.00241
p_2	-0.05872

The two reference frames adopted in the relative pose estimation are: (1) the camera frame C and (2) the target frame T. The unit vectors ${}^{C}x$, ${}^{C}y$, ${}^{C}z$ are oriented according to Figure 3.1: in particular, ${}^{C}x$ lies on the horizontal plane, ${}^{C}y$ points downward and ${}^{C}z$ is directed toward the target. As regard the target fixed reference frame, its origin is located at the bottom corner of the edge created by the junction of the two faces: in particular, ${}^{T}x$ and ${}^{T}y$ follow the lower edge of the faces containing as shown in Fig 3.7 and ${}^{T}z$, pointing upward, completes the frame.

The employed experimental setup allows to impose known displacements to the mock-up along the direction of the linear slide and rotations about the vertical direction. By imposing known displacements to the satellite mock-up, it is possible to evaluate the errors and the uncertainties of the output poses. The two degrees of freedom ensure that different operative conditions are recreated, allowing to perform measurement both in the case in which all the feature points are available and in the case of partial

occlusions.

The image acquisition step is performed by acquiring images of the satellite mock-up placed in 22 different positions along the linear slide, with an axial step of 50 mm. For each linear position, the mock-up attitude is varied of 90 deg in steps of 2 deg: when the attitude angle is 0 or 90 deg the optical axis of the camera is orthogonal to one of the faces and only 4 markers are observed, while in the intermediate angular positions up to 8 markers can be observed.

A total number of $22 \text{ x} 45 = 990$ measurements of position and attitude are acquired using the vision-based algorithm and are then compared to the corresponding imposed values.

Figure 3.8 shows the acquired image, converted to grayscale, of the spacecraft mock-up as it is seen by the monocular system. Figure 3.9 presents the output of the image processing algorithm showing the thresholded image with red circles and crosses showing respectively the location in the image plane of the four corners and the centroids of each fiducial marker.

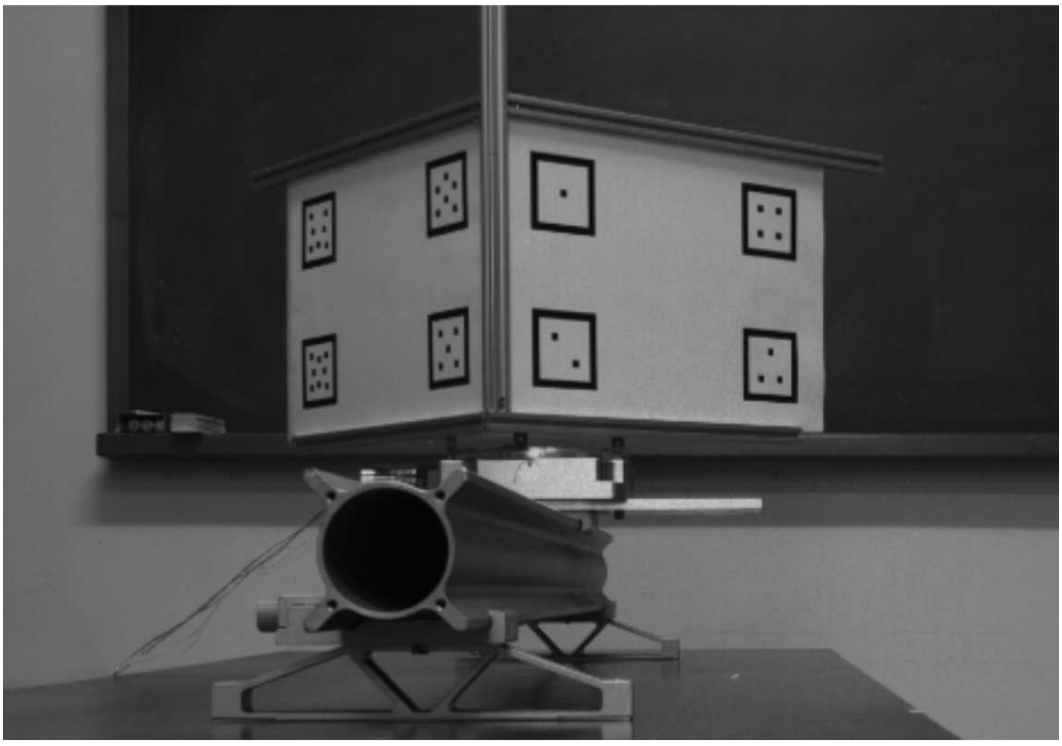

Figure 3.8: Image converted to grayscale showing the spacecraft mock-up as it is seen by the monocular system.

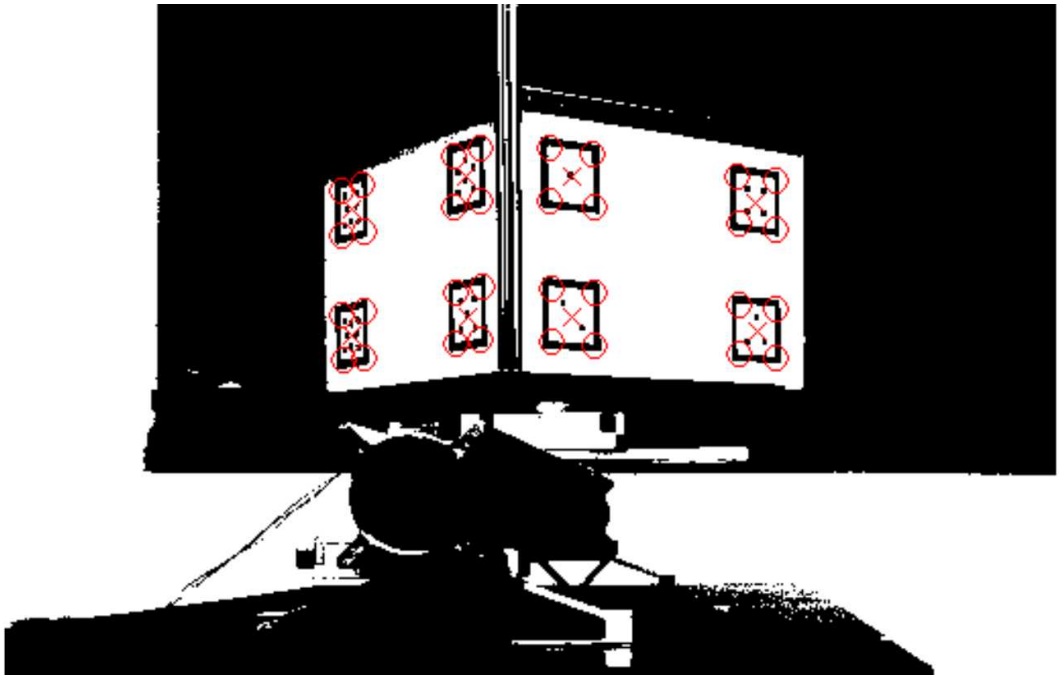

Figure 3.9: Output of the image processing algorithm showing the thresholded image with red circles and crosses showing respectively the location in the image plane of the four corners and the centroids of each fiducial marker.

3.7 Uncertainty analysis

A detailed uncertainty analysis is carried out according to the metrological procedures described in [45] and [46]. The position and orientation uncertainty of the satellite is evaluated as in an indirect measurement by a Monte Carlo propagation approach. The aim of the analysis is to evaluate the uncertainties of the satellite position and attitude as precisely as possible. Thus, since the whole measurement algorithm is highly non-linear, a Monte Carlo simulation is employed instead of the Kline McKlintock propagation formula.

According to [45] and [46], uncertainty sources are expressed by probability density functions (PDFs) and are then propagated to the output pose of the satellite using a Monte Carlo simulation. The experimental set-up, as described in the Section 3.6, can impose to the satellite translations and/or rotations known with an uncertainty at least one order of magnitude better than the estimated values obtained with the vision system. Thus, the compatibility of the experimentally obtained errors (the difference between the values obtained by the vision system and those obtained by the reference instrumentation) with the uncertainties evaluated by the Monte Carlo method can

be checked for all the displacements and rotations imposed to the satellite. Several uncertainty sources are analyzed and evaluated using experimental tests. Particularly, the uncertainty associated with the following quantities are taken into account: the intrinsic parameters of the camera, the positions of the 3D points in the satellite frame, and the positions of the 2D points detected on each image, whose uncertainty is mainly affected by the level of deformation of the markers on the image and by the residual uncorrected optical distortions that the distortion model is not able to remove.

3.8 Results

Considering the estimated angular positions, Fig 3.10 shows the angular error obtained as the difference between the measured attitude angle around the vertical axis and the imposed rotation as a function of both the imposed angle and position, while Figure 3.11 depicts the extended uncertainty affecting the measured angular positions.

Figure 3.12 illustrates the root mean square (RMS) error along with the evaluated uncertainty with a level of confidence of 99.7% and show that observed measurement errors are compatible with the evaluated extended uncertainty.

It can be noticed that, in the attitude angle estimation, both the smallest error and uncertainty are achieved in the middle of the angular range, when the observed markers are not orthogonal to the optical axis and the number of observed feature is high (see Figure 3.18).

Even though the angular positions corresponding to 0 deg and 90 deg are expected to be characterized by similar errors (i.e. the observed face is orthogonal to the optical axis) it can be noticed that differences arise: this is due to the interfering effect of the lighting conditions that limit the number of observed features when the imposed angle is close to 0 deg, as it can be seen in Figure 3.18.

Figure 3.15 shows the position error obtained as the difference between the estimated position and the imposed rotation along the linear slide as a function of both the imposed angle and position. It can be seen from Figure 3.16a that the RMS error is compatible with the evaluated extended uncertainty also in this case. Fig 3.17 show that when the markers are seen in an inclined manner, a lower uncertainty can be observed also for the position measurement, but much more attenuated and less clear.

As it could be expected, the obtained results show that both angle and position

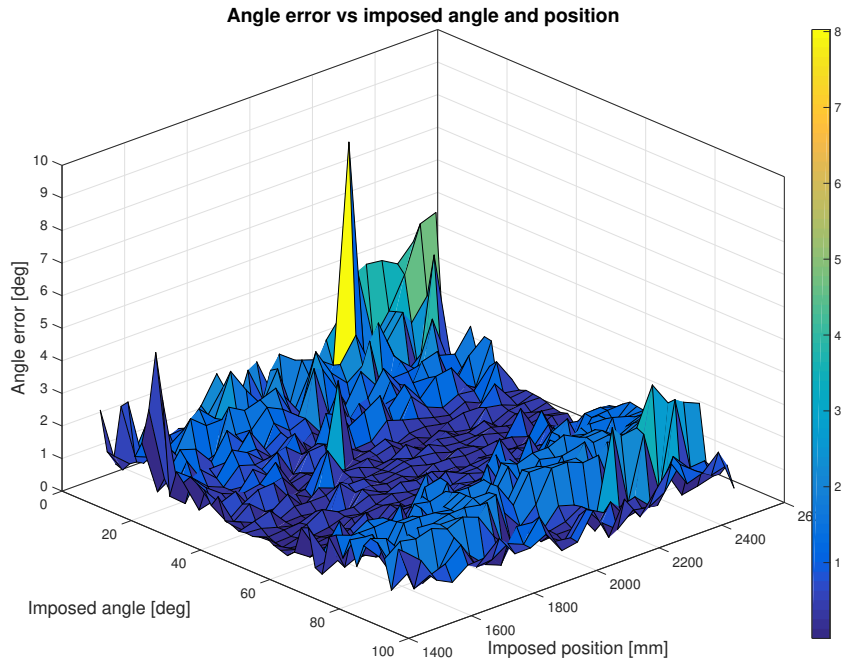

Figure 3.10: Angle error: difference between the estimated attitude angle around the vertical axis and the imposed rotation.

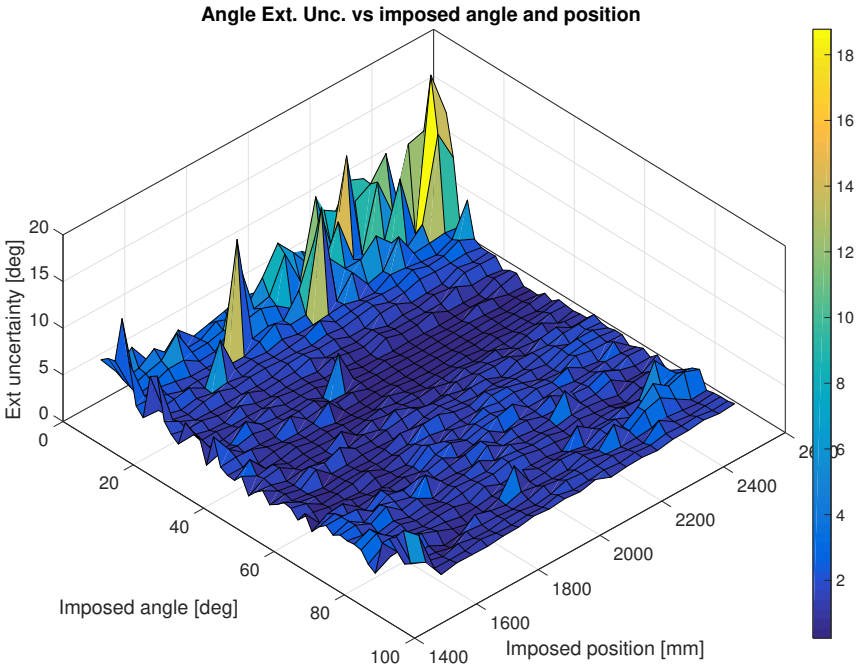

Figure 3.11: Extended uncertainty on the estimated angular position a function of the imposed angles and positions.

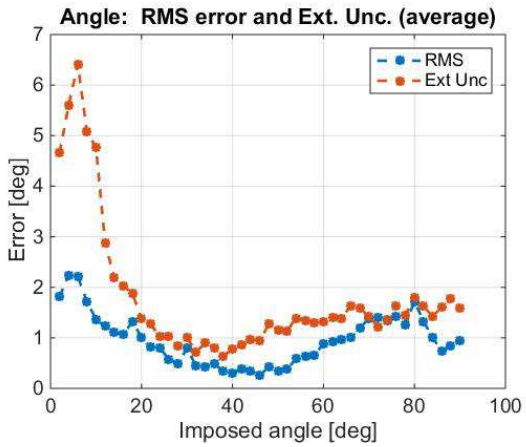

(a) Average angular error as a function of the imposed angle.

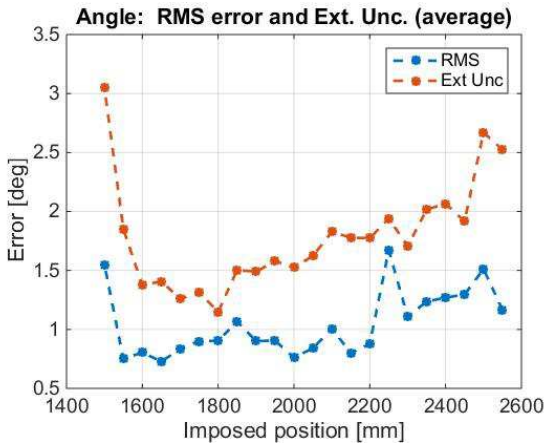

(b) Average angular error as a function of the imposed position.

Figure 3.12: Average angular RMS error and extended uncertainty as a function of the imposed angle (3.12a) and the imposed position (3.12b).

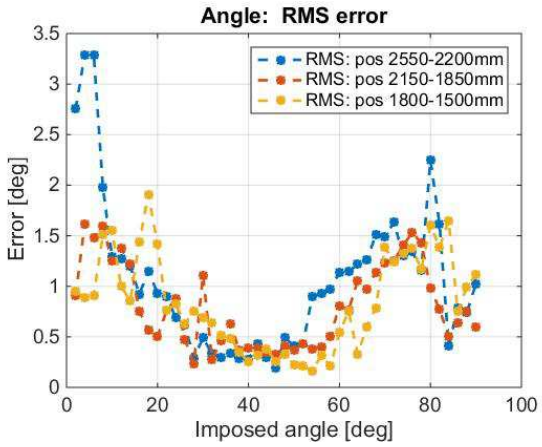

(a) Angular RMS error.

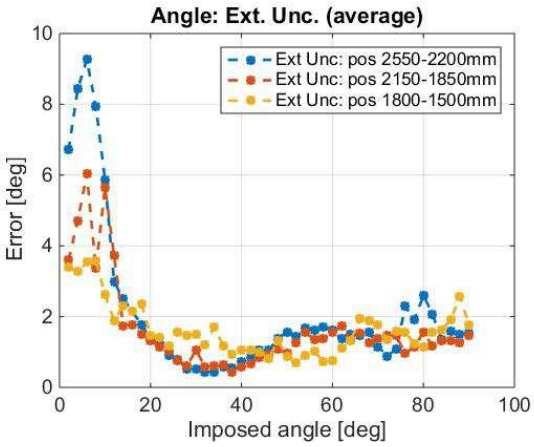

(b) Angular extended uncertainty.

Figure 3.13: Angular RMS error and extended uncertainty as a function of the imposed angle. Blue, red and yellow lines refer to the average values obtained respectively for distances in the range $2550 - 2200$ mm, $2150 - 1850$ mm and $1800 - 1500$ mm.

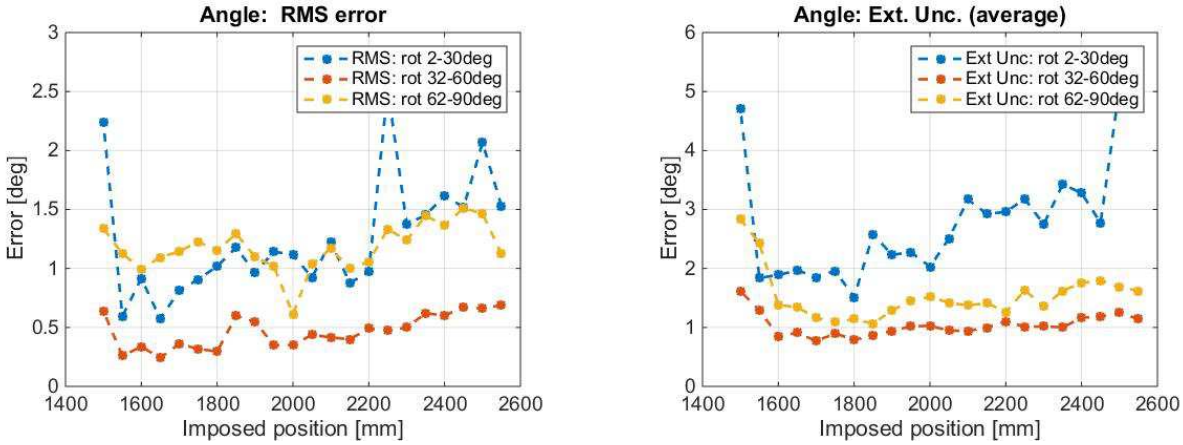

(a) Angular RMS error.

(b) Angular extended uncertainty.

Figure 3.14: Angular RMS error and extended uncertainty as a function of the imposed displacement. Blue, red and yellow lines refer to the average values obtained respectively for imposed angles in the range $(2-30)$ deg, $(32-60)$ deg and $(62-90)$ deg.

errors increase with the distance of the observed object (smaller observed markers yield larger errors).

In general, as regards the measurements about the target position along the axes orthogonal to the displacements direction, the standard uncertainty summarizing the dispersion of the measurements with respect to the mean value is always lower than 2 cm for all the imposed configurations.

The attitude about the horizontal axes described by the roll and the pitch angles, given the employed experimental setup, is constant. In order to assess the performances of the estimation approach in measuring these angles a statistical analysis is performed with the aim of evaluating the dispersion of the measurements about their mean values. Table 3.2 summarizes the obtained results for a finite subset of the imposed configurations: in particular, each row refers to a fixed imposed attitude about the vertical direction and presents the dispersion, in terms of standard deviation σ, for the roll and pitch angles, evaluated on all the imposed positions along the translational direction.

The measured roll and pitch angles show a good stability for all the considered configurations, proving a maximum RMS error with a confidence level of 99.7% lower than 2 deg for all the configurations. It can be observed that the dispersion of the measurements degrades as the imposed angular position approaches the 0 deg and the 90 deg configurations, following the same trend shown by the other kinematic quantities analyzed in this section.

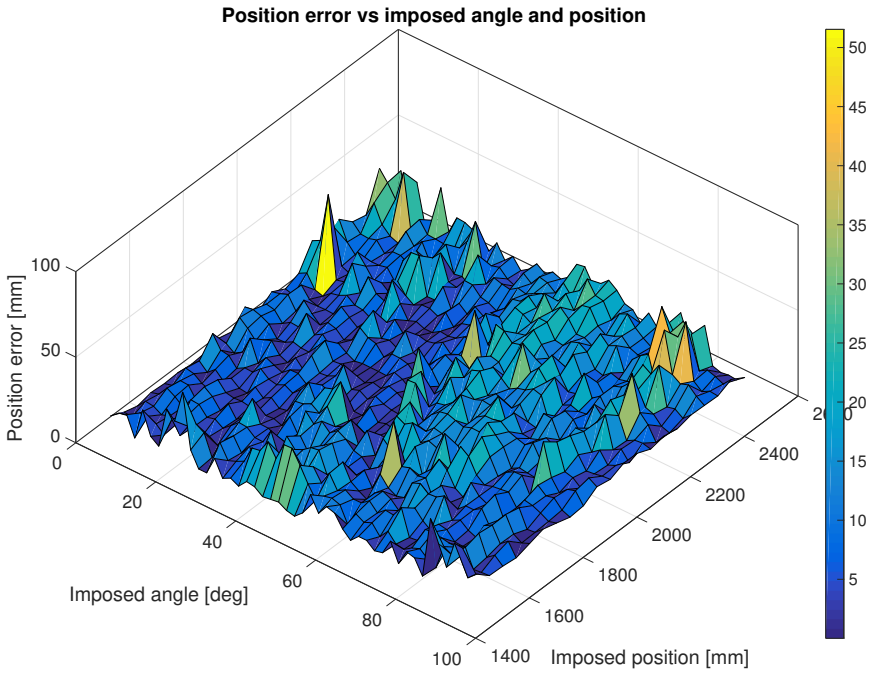

Figure 3.15: Position error: difference between the estimated position along the linear slide axis and the imposed one.

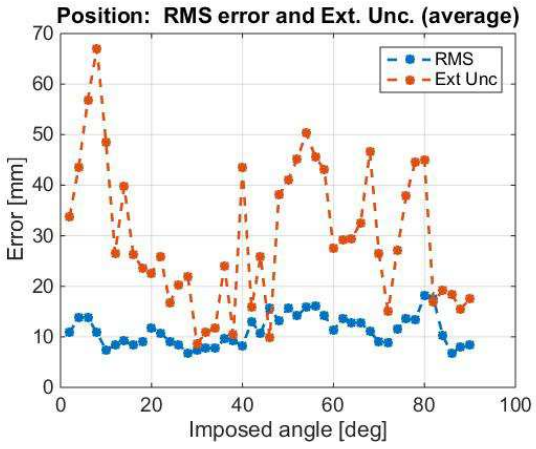

(a) Average position error as a function of the imposed angle.

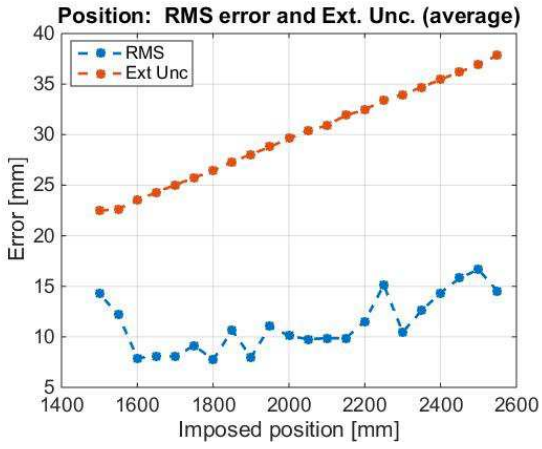

(b) Average position error as a function of the imposed angle.

Figure 3.16: Average position RMS error and extended uncertainty as a function of the imposed angle (3.16a) and of the imposed position (3.16b).

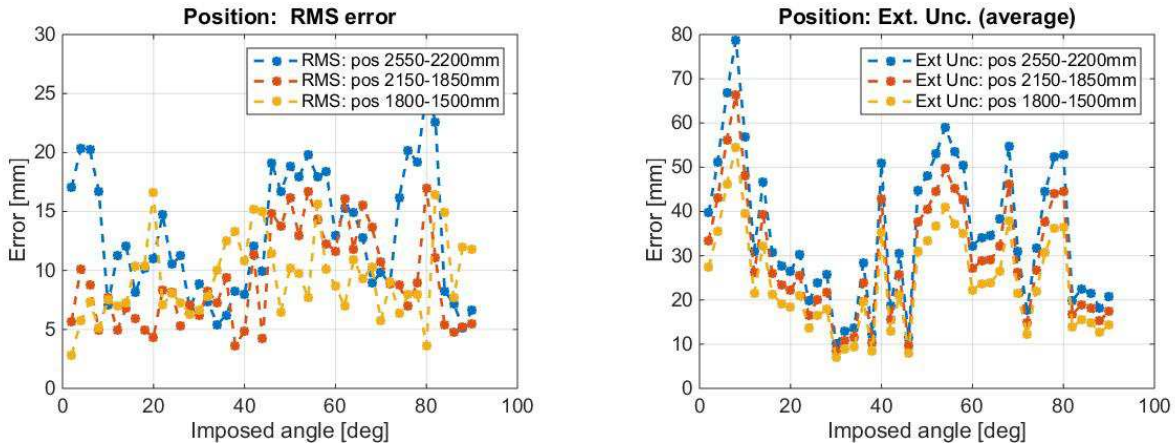

(a) Position RMS error.

(b) Position extended uncertainty.

Figure 3.17: Position RMS error and extended uncertainty as a function of the imposed angle. Blue, red and yellow lines refer to the average values obtained respectively for distances in the range $2550 - 2200$ mm, $2150 - 1850$ mm and $1800 - 1500$ mm.

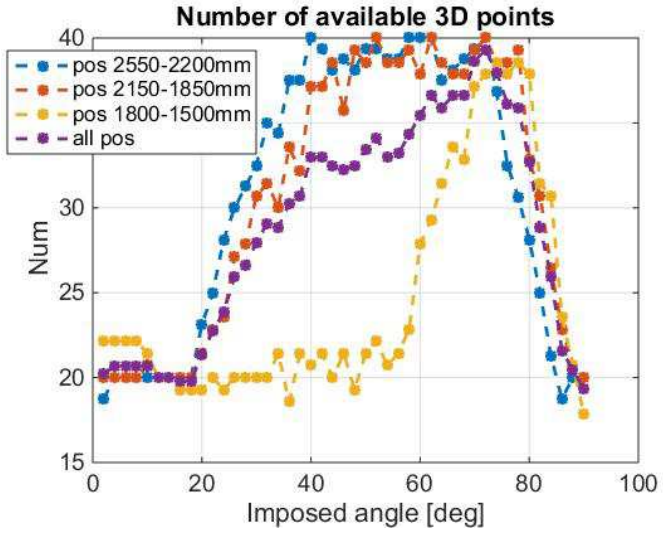

Figure 3.18: Number of feature points correctly identified as a function of the imposed angular position. Blue, red and yellow lines refer to the average values obtained respectively for distances in the range $2550-2200$ mm, $2150-1850$ mm and $1800-1500$ mm. Purple line refer to the value averaged on all positions.

Table 3.2: Standard deviation of the angular measurements about the horizontal axes.

Imposed angle [deg]	σ_{roll} [deg]	σ_{pitch} [deg]
20	0.48	0.10
40	0.23	0.14
50	0.18	0.05
60	0.24	0.24
80	0.18	0.76

3.9 Concluding Remarks

A vision based instrument able to measure the position and orientation of a spacecraft is described and calibrated from a metrological point of view. The instrument comprises a simple camera which observes the external surface of the satellite provided with fiducial markers and a software procedure which employs a closed-form and direct solution of the Perspective from three Points problem, according to the formulation proposed by Kneip et al. The pose estimation procedure is embedded in a RANSAC scheme and refined by means of a non-linear optimization.

Several laboratory tests are performed to evaluate the calibration curves and the output uncertainty of the vision based instrument by imposing known rotational and translational displacements to the satellite mock-up to reproduce different operative conditions. The employed set-up allowed to highlight strengths and weaknesses of the measurement system. In particular, the estimation methodology proves to be efficient and suitable to be employed on a real navigation scenario whenever the optical axis of the camera is sufficiently inclined with respect to the planar faces of the target. On the contrary, the performances of the measurement system degrade as the optical axis is parallel to the unit vectors orthogonal to the target surfaces: in this particular case, one possible recovery action aimed at boosting the metrological performances of the measurement system consists in the modification of the fiducial markers pattern in order to provide the detected landmarks with a three-dimensional distribution also in the case in which a single face of the target spacecraft is observed.

Chapter 4

Development of a contactless localization system for the SPARTANS testbed

4.1 Introduction

The current chapter aims at presenting the development of a localization system for the SPARTANS testbed.

Several approaches are proposed in literature to solve the localization problem within the context of ground-based spacecraft testbeds. In the Synchronized Position Hold Engage and Reorient Experimental Satellite (SPHERES) context, an ultrasound-based measurement system is employed as a means to solve the localization problem [9, 47]. The sequence of operations that allows each satellite to determine its own position in the testing area consists of the following three steps: (1) an infrared pulse is generated by a master micro-satellite to ping the external ultrasound generators, (2) once pinged, the generators produce an ultrasound pulse in a predetermined sequence, (3) by collecting pulses coming form several beacons and evaluating the direction the pulses came from, each micro-satellite can estimate its position. This approach, even if effective, has a downside: the cold gas thrusters that allow the execution of control actions, generate ultrasound pulses which in turn interfere with the measurement step, thus requiring a meticulous planning of the operations time schedule. Therefore the localization step and the actuation of control forces/torques cannot be performed simultaneously.

A different measurement approach is adopted by researchers involved in the de-

velopment of the Autonomous Spacecraft Testing of Robotic Operations in Space (ASTROS) [8] and the Test Environment for Applications of Multiple Spacecraft (TEAMS) [7]. These facilities exploit a Motion Capture system, consisting in a set of infrared cameras, retro-reflective markers and a control station, to track both the attitude and the position of the spacecraft simulators at frequencies up to 250 Hz. The ASTROS testbed, furthermore, takes advantage of a second independent system that exploits a laser to obtain inertial position information of the platforms with sub-millimeter accuracy.

The activities presented within the current chapter focus on two main topics: (1) the development of a high-rate measurement system able to provide information about the planar motion of the micro-satellites on the low-friction table and (2) the development of a global navigation system capable of tracking the motion of each spacecraft module inside its operative volume. In particular, the first part is devoted to the description of an Optical Flow Sensors (OFS) based navigation system employed to track the motion of the Translational Module (TM). The characterization and the calibration procedure of the measurement system are presented. Once the limitations of the OFS system are identified, a first prototype of a global navigation system is proposed: this system relies on a monocular vision system developed to compensate for errors affecting the OFS system. The outcomes of this investigation lead to the second section of the chapter in which the selection, implementation and characterization of an upgraded version of the global navigation system is presented. In particular, the identified measurement apparatus consists of a Motion Capture system which provides global pose estimations at a frequency up to 50 Hz.

4.2 Development of a Optical Flow Sensors based navigation system

The current section describes the development of the OFS based system employed to estimate the planar motion of the TM.

To understand the relevance of this measurement system it is consider the following operative scenario for the SPARTANS testbed, in which the AM performs an attitude maneuver with an arbitrary angular profile. Even if, ideally, the attitude motion is not affected by external disturbances, a certain amount of friction due to the mechanical

joints is present. Even if small, this disturbance couples the azimuthal rotation of the AM to the azimuthal motion of the TM. The quadrature encoders (QE) located at the rotational joint can be employed, given their resolution, ti simulate the acquisition performed using a star tracker, thus allowing to estimate the spacecraft attitude with respect to an inertial reference frame. It is clear that, assuming for simplicity that rotations about the roll and pitch axes are forbidden, if the TM rotates the angular data obtained with the QE refer to the differential rotation that occurs between the AM and the TM, making the purpose of having reference measurements null and void. Let ${}^{G}\Theta_{AM}$, ${}^{T}\Theta_{AM}$, and ${}^{G}\Theta_{TM}$ be respectively the azimuthal position of the AM in the global frame, the azimuthal position of the AM with respect to the TM and of the TM with respect to the global frame. The angular position of the AM in the global frame is obtained simply as ${}^{G}\Theta_{AM} = {}^{T}\Theta_{AM} + {}^{G}\Theta_{TM}$, where Θ_{AM} is the angle measured by the QE. From this simple equation, the need of measuring the angular position of the TM by means of a dedicated measurement system is clear.

In recent years, OFS are employed in numerous applications and in particular for unmanned aerial vehicles and robotic applications [48–50]. The working principle behind the OFS is the same of optical mice used for computers: generally a low resolution imager acquires images of a textured surface and, through a convolution, determines the displacement that occurs between two consecutive frames.

The OFS employed on-board the TM (see Section 2.4.3) are equipped with a lens whose focal length can be adjusted: this feature provides the capability of operating at variable distances from the surface which is imaged. Each OFS, once polled, returns incremental measurements in two dimensions. If two or more sensors are employed togheter it is possible to recover the planar pose (i.e. x, y and the azimuthal position) of the TM. To ensure redundancy of measurements, three OFS are employed for the TM navigation subsystem.

The main reasons that led to the choice of OFS as navigations sensors are the following:

- it is a contactless system that does not interfere with the low-friction motion of the TM;
- its low mass and small dimensions make it a good choice to develop a compact measurement system;

- it is capable of providing high rate measurements (up to more than 6400 Hz);
- it can be easily retrieved on the market, it is cheap and it features a SPI interface making it suitable to be employed along with common off-the-shelf microcontrollers;
- the adjustable focal length makes the measurement system flexible as it can be placed at the most convenient distance from a surface.

The quality of the measurements provided by OFS is dependent on two parameters: the brightness of the acquired surface and the surface quality. In particular the latter is important as it is an indicator of the number of valid features that can be identified onto the image plane and that can be used to measure displacements: an higher quality surface corresponds to more accurate measurements. Both the brightness and the surface quality are returned by the sensors as parameters assessing the quality of the measurements.

To boost the measurment performances of each OFS, the following strategies are adopted.

1. To ensure good lighting conditions, the surface imaged by the each sensor is lighted using a red LED. The choice of the color stems from the highest responsivity (i.e. the electrical output per optical input) of the sensor to wavelengths ranging from approximatively 600 to 700 nm. The schematic mounting layout is shown in Figure 4.1. The inclination of the OFS axis with respect to the LED axis is tuned to avoid that an excessive amount of light is gathered by the sensor, leading to saturation.

2. To increase the surface quality parameter, several patterns are tested. This preliminary evaluation reveals that a chessboard pattern ensures high surface quality levels. Compared to reference values given by the constructor, the relative improvement of the adopted texture is about of 35%.

The outcome of the employed strategies is summarized in Figure 4.2, where the surface quality parameters returned by one of the three OFS is shown: it can be seen that, even if a certain variability is present, the surface quality (SQUAL) value is approximatively equal to the 85% of the maximum allowable value; this result is more than sufficient to keep the number of missed readings low.

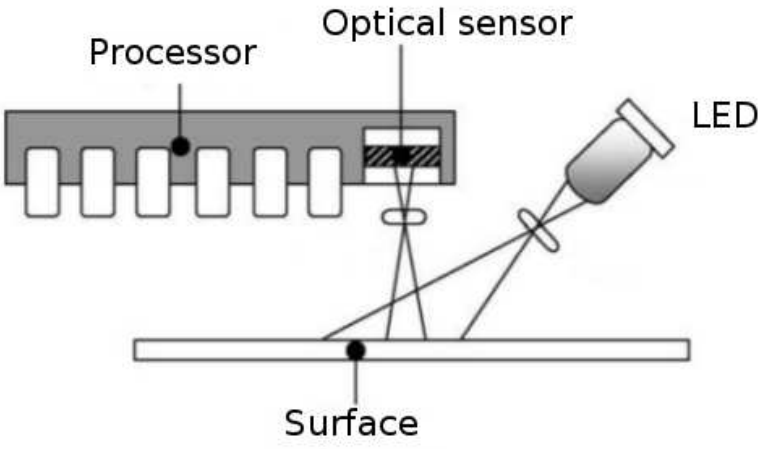

Figure 4.1: Schematic drawing of the OFS mounting with an LED to improve lighting conditions.

4.2.1 The motion tracking problem

The employed measurement strategy aims at solving the following problem: given the 2D raw measurements provided by three OFS mounted aboard the TM, determine the planar motion of the TM with respect to a global reference frame.

The solution of the problem requires the definition of three reference frames: (1) the global reference frame G, (2) the TM fixed reference frame, also dubbed body frame B and (3) OFSs fixed reference frames, whose x_i and y_i axes, with $i = 1,\ 2,\ 3$, are aligned with the i-th OFS measurement axes.

The position and orientation of the i-th OFS with respect to the body frame is described by means of three parameters: r_i and θ_i describe in polar coordinates, the position of the sensor with respect to the body frame, while τ_i define its orientation. Figure 4.3 provides meaningful representation on how the three parameters are defined. In particular τ_i is defined as the angle between axis y_i and the direction orthogonal to r_i, while σ_i, which depends on τ_i and θ_i, is the angle between y_i and ${}^{B}Y$.

Each OFS measures a displacement $[\delta x_i,\ \delta y_i]^T$ occurred during the sampling interval Δt. Let Δz be the incremental measurements vector and ΔS the TM incremental kinematic state vector:

$$\Delta z = [\delta x_1,\ \delta y_1,\ \delta x_2,\ \delta y_2,\ \delta x_3,\ \delta y_3,\ ]^T$$
$$\Delta S = [\Delta X,\ \Delta Y,\ \Delta \Theta]^T$$

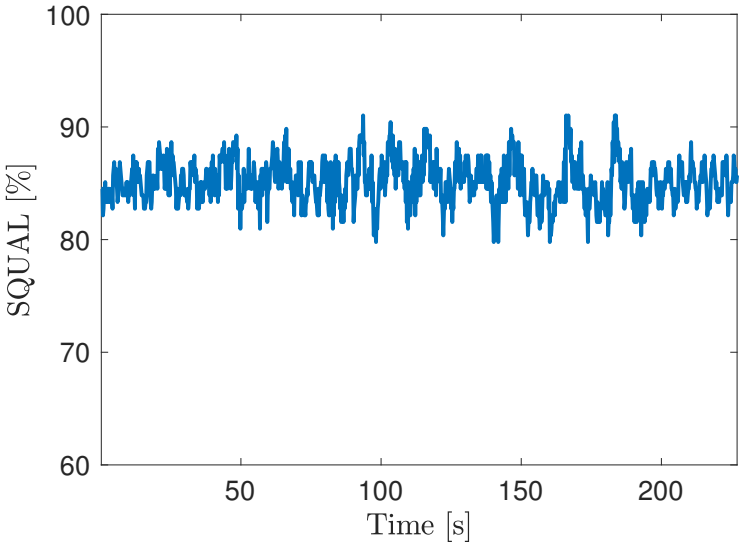

Figure 4.2: Measured surface quality over time in presence of the chessboard pattern and the additional LED.

For each sampling interval, the equation that relates ΔS to Δz can be written as:

$$\Delta z = A \Delta S \tag{4.1}$$

where A is a six-by-three matrix defined as:

$$A = \begin{bmatrix} \cos(\sigma_1) & -\sin(\sigma_1) & -r_1 \sin(\tau_1) \\ \sin(\sigma_1) & -\cos(\sigma_1) & r_1 \cos(\tau_1) \\ \cos(\sigma_2) & -\sin(\sigma_2) & -r_2 \sin(\tau_2) \\ \sin(\sigma_2) & -\cos(\sigma_2) & r_2 \cos(\tau_2) \\ \cos(\sigma_3) & -\sin(\sigma_3) & -r_1 \sin(\tau_3) \\ \sin(\sigma_3) & -\cos(\sigma_3) & r_2 \cos(\tau_3) \end{bmatrix} \tag{4.2}$$

To compute the unknown ΔS, the system can be solved by means of the Moore-Penrose inverse matrix A^+ as:

$$\Delta S = A^+ \Delta z. \tag{4.3}$$

If the pose $[{}^G X,\ {}^G Y,\ {}^G \Theta]$ of the TM is known at the time instant t_{k-1} in the global reference frame, the pose at time t_k can be determined by exploiting the incremental

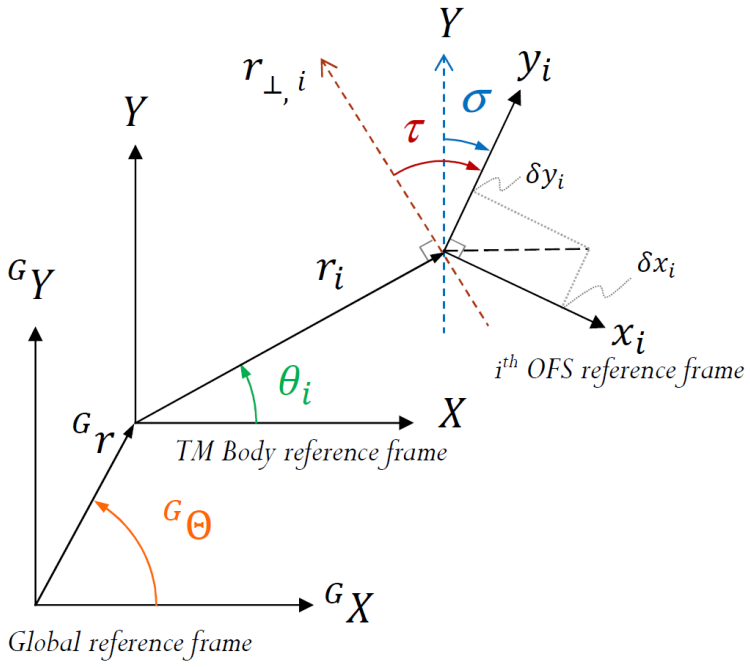

Figure 4.3: Optical Flow Sensors reference frame definition.

kinematic state vector ΔS_k as follows:

$$\begin{bmatrix} {}^GX_k \\ {}^GY_k \\ {}^G\Theta_k \end{bmatrix} = \begin{bmatrix} {}^GX_{k-1} \\ {}^GY_{k-1} \\ {}^G\Theta_{k-1} \end{bmatrix} + \begin{bmatrix} \cos(\Theta_{k-1}) & \sin(\Theta_{k-1}) & 0 \\ \sin(\Theta_{k-1}) & \cos(\Theta_{k-1}) & 0 \\ 0 & 0 & 1 \end{bmatrix} \begin{bmatrix} \Delta X_k \\ \Delta Y_k \\ \Delta\Theta_k \end{bmatrix}. \tag{4.4}$$

Therefore, given an initial estimate of the TM planar position and orientation, the TM pose can be updated at each time step by means of equations 4.3 and 4.4.

4.2.2 Calibration of the OFS based measurement system

Given the kinematic incremental equations 4.3 and 4.4, the tracking of the TM along its planar motion is possible only if the parameters defining the position (r_i, θ_i) and the orientation (τ_i, σ_i) of each OFS with respect to the body frame are known, thus allowing to determine the transformation matrix A. A calibration procedure is therefore needed. The employed calibration procedure consists of two main steps: an initial calibration is performed following the approach proposed in [51] and, subsequently, the calibration parameters are refined by means of an optimization procedure. Before presenting the details of the calibration procedure, the employed experimental setup is briefly described.

Since the development phase of the OFS based measurement system is performed

concurrently to the development of the TM, a preliminary version of the TM is employed. The prototype of the TM reproduces the geometric characteristics of the TM in its final version and allows the housing of the three OFS aboard. In particular, the TM prototype consists of: (1) a central squared aluminum plate; (2) three aluminum profile beams, connected rigidly to the plate, disposed at 120 deg and meeting at the orthocenter of an equilateral triangle; (3) three red LEDs, with a power consumption of 0.4 W each; (4) three OFSs, each housed on a support plate in close proximity of the LEDs; (5) the control electronics (i.e. an Arduino UNO) employed to power the sensors and to acquire and process data by means of the kinematic incremental equations.

The OFSs are placed approximatively at the same distance from the center of the squared plate. The position of the OFS aboard the TM prototype is determined as the result of a tradeoff between two contrasting needs: on one hand, a larger distance has the effect of increasing the sensitivity in measuring rotations (i.e. the larger the distance from the center of rotation, the higher the measured displacement); on the other hand, the distance cannot be increased over a certain limit because of the geometrical constraints given by the TM structure. Thus, the position is determined such that the OFS are placed in the close proximity of the outer edges of the TM.

To calibrate the measurement system, the TM prototype is mounted onto two motorized stages placed one on top of the other. The first stage is capable of providing translational displacements along two orthogonal directions with an accuracy of 0.05 μm, while the second provides rotational displacements with an accuracy of 0.02 deg.

The complete experimental setup employed during the calibration procedure is shown in Figure 4.4.

Raw calibration step

The raw calibration procedure is divided into two main phases: a first translational phase followed by a second rotational phase.

The translational phase is aimed at determining the resolution k_i and the orientation σ_i for each OFS. The estimation of these parameters is performed by imposing several translational displacements to the TM mock-up by means of the linear stages. The known imposed linear motion ($\Delta X,\ \Delta Y$) is then compared to the measurements of the three OFS ($\delta\hat{x}_i,\ \delta\hat{y}_i$), leading to the determination of k_i and σ_i as:

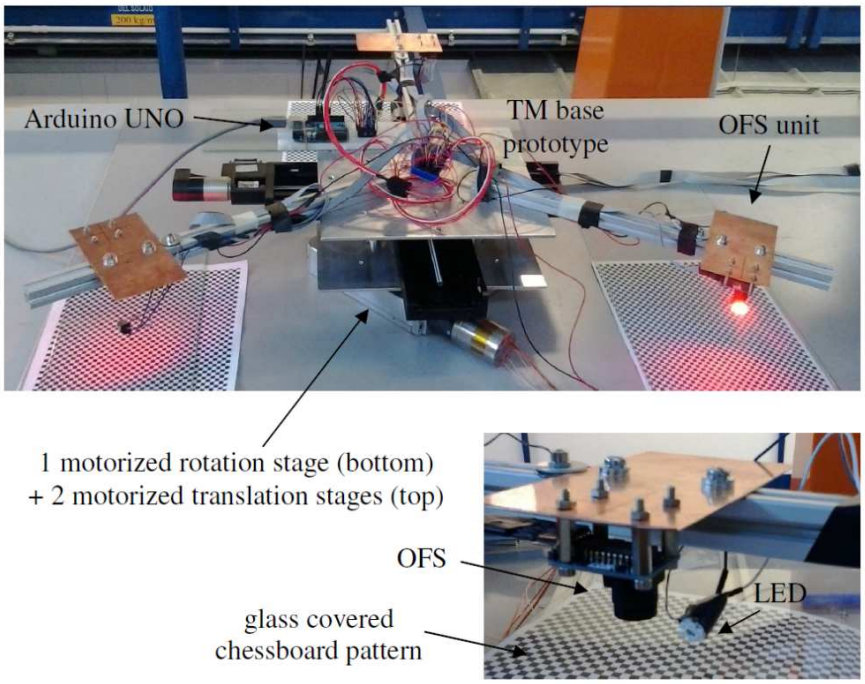

Figure 4.4: Experimental setup used to calibrate the OFS system.

$$k_i = \frac{\sqrt{\Delta X^2 + \Delta Y^2}}{\sqrt{\delta\hat{x}_i^2 + \delta\hat{y}_i^2}} \tag{4.5}$$

$$\sigma_i = \tan^{-1}\left(\frac{\Delta X}{\Delta Y}\right) - \tan^{-1}\left(\frac{\delta\hat{x}_i}{\delta\hat{y}_i}\right) \tag{4.6}$$

where $\delta\hat{x}_i,\ \delta\hat{y}_i$ are the raw measurements provided by the sensors in counts (ct). The mean values $\bar{k}_i$ and $\bar{\sigma}_i$ obtained after the first phase are employed in the following step of the calibration.

The second phase of the raw calibration aims at determining the distance r_i and the orientation τ_i of each OFS with respect to the TM reference frame. A series of known rotational displacements are imposed to the TM mock-up by means of the rotational stage, taking care of aligning the rotation axis of the stage to the origin of the TM frame in order to avoid spurious translational motions. By relating the azimuthal imposed motion $\Delta\Theta$ to the raw measurements $\delta\hat{x}_{i,j},\ \delta\hat{y}_{i,j}$ for each j-th sampling instant, it is possible to retrieve the calibration parameters $r_i,\ \tau_i$ as:

$$r_i = \bar{k_i} \frac{\sum_j \sqrt{\delta\hat{x}_{i,j}^2 \delta\hat{y}_{i,j}^2}}{\Delta\Theta} \tag{4.7}$$

$$\tau_i = \tan^{-1}\left(\frac{\delta\hat{x}_{i,j}}{\delta\hat{y}_{i,j}}\right). \tag{4.8}$$

Once the mean values $\bar{r}_i$ and $\bar{\tau}_i$ are computed, the value of $\bar{\theta}_i$ is computed as follows:

$$\bar{\theta}_i = \bar{\tau}_i - \bar{\sigma}_i. \tag{4.9}$$

Several tests are performed to characterize the calibration parameters. The outcomes of the raw calibration procedure are summarized in Table 4.1, where the mean values and their corresponding RMS error are shown. A detailed description of the maneuvers performed can be found in [52].

Table 4.1: OFS raw calibration procedure results. Uncertainties are computed as RMS values.

i	$\bar{k}_i$ [mm/ct]	$\bar{\sigma}_i$ [deg]	$\bar{r}_i$ [mm]	$\bar{\tau}_i$ [deg]	$\bar{\theta}_i$ [deg]
1	0.60 ± 0.01	298 ± 1	389 ± 6	262.5 ± 0.09	-32.5 ± 1.7
2	0.67 ± 0.02	180 ± 1	392 ± 3	263 ± 1.1	83.1 ± 1.5
3	0.67 ± 0.02	63 ± 2	397 ± 7	264.3 ± 0.5	201.4 ± 2

The results of the raw calibration phase are consistent with the expected values in terms of position and orientation with respect to the TM reference frame.

Refinement calibration phase

The refined calibration phase aims at estimating the optimized calibration parameters that minimize the mean square error between the reference trajectories used in the previous step and the motion reconstructed by means of the OFS.

Let n be the index that identifies the imposed maneuver ΔS_n as the incremental kinematic state vector, $\delta\hat{z}$ the incremental raw measurement vector and $x = [k_1,\ \sigma_1,\ r_1,\ \theta_1,\ k_2,\ \sigma_2,\ r_2,\ \theta_2,\ k_3,\ \sigma_3,\ r_3,\ \theta_3]^T$ the intrinsic parameters vector.

The reconstructed measurement vector $\Delta\Xi_n$ can be retrieved from the imposed motion as:

$$\Delta\Xi_i = \bar{A}(x)\Delta S_n \tag{4.10}$$

where the matrix $\bar{A}$ is defined as:

$$\hat{A} = \begin{bmatrix} c\sigma_1/k_1 & -s\sigma_1/k_1 & r_1 s\tau_1/k_1 \\ s\sigma_1/k_1 & -c\sigma_1/k_1 & r_1 c\tau_1/k_1 \\ c\sigma_2/k_2 & -s\sigma_2/k_1 & r_2 s\tau_2/k_2 \\ s\sigma_2/k_2 & -c\sigma_2/k_2 & r_2 c\tau_2/k_2 \\ c\sigma_3/k_3 & -s\sigma_3/k_3 & r_3 s\tau_3/k_3 \\ s\sigma_3/k_3 & -c\sigma_3/k_3 & r_3 c\tau_3/k_3 \end{bmatrix} \tag{4.11}$$

and c and s stand for sin and cos.

The optimized vector of the intrinsic parameters $\hat{x}$ can be found as the argument that minimizes the sum of the mean square errors:

$$\hat{x} = \arg\min_x \sum_n ||\hat{A}(x)\Delta S_n - \delta\hat{z}_n||_2^2. \tag{4.12}$$

Table 4.2 shows the outcomes of the optimization procedure. It can be noticed that the major modifications to the raw calibration parameters regard mainly r_i and θ_i. As a result of the refinement procedure, the mean square error between reference measurements and reconstructed motions is reduced of 8.6%.

Table 4.2: OFS refinement calibration procedure results.

i	k_i [mm/ct]	σ_i [deg]	r_i [mm]	θ_i [deg]
1	0.599	297.9	383.6	−35.64
2	0.666	179.99	383.1	83.23
3	0.666	62.74	386.5	201.77

4.2.3 Motion reconstruction

To evaluate the accuracy of the OFS based measurement system in estimating the planar pose of the TM, several tests are performed. In particular, combined motions are imposed to the TM by means of the motorized stages (i.e. X, Y and azimuthal displacements). The on-board microcontroller, while the setup moves, performs an on-line estimation of the incremental displacements as described in Section 4.2.1. Finally, in the post-processing phase, the reconstructed motion and the imposed motion are

compared to determine how errors propagates and to identify potential limitations of the measurement approach.

This section presents the results obtained by imposing the following combined maneuver which can be decomposed in four steps: (1) a 50 mm displacement is imposed along the ${}^{G}Y$ direction, (2) the TM rotates about the origin of the global reference frame of an angle of 20 deg, (3) the angular position of the TM is restored to the initial value (i.e. rotation of -20 deg) and finally (4) the TM is brought back to its initial position.

The results of the reconstructed motion are shown in Figure 4.5. In particular Figure 4.5a show the position of the TM in global coordinates and provides a comparison between the imposed and the reconstructed trajectory (respectively red and blue lines). Figure 4.5b depicts the reconstructed azimuthal position as a function of the sampling instant (the count number). The tracking errors are reported on the graphs as the differences between the imposed and measured displacements at the end of each step of the maneuver.

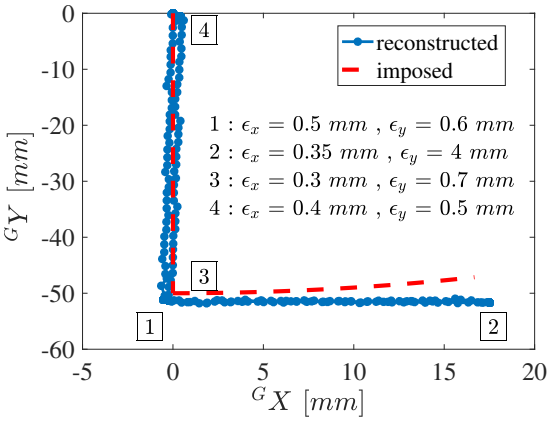

(a) Planar position of the TM with respect to the global frame. The red line and blue line refers respectively to the imposed and the reconstructed displacement.

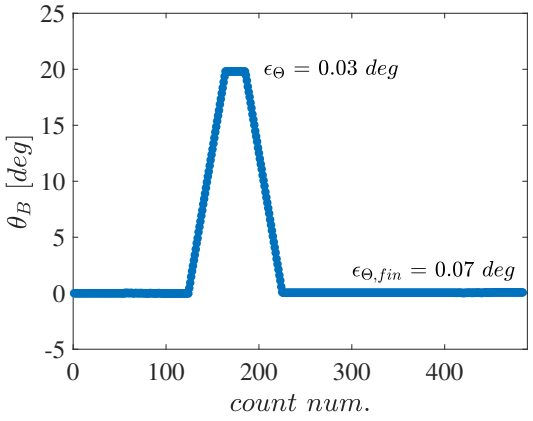

(b) Reconstructed orientation of the TM with respect to the global frame.

Figure 4.5: OFS motion reconstruction results.

The obtained results show that, even if the imposed maneuvers force the TM to follow the same path in opposite directions, the tracking error tend to increase as the displacement increase, resulting, as expected, in an unbounded error accumulation. The most critical aspect is related to the motion reconstruction in presence of azimuthal

displacements: it can be noticed that along the path delimited by the identifiers 1 and 2, the tracking error increases up to a maximum value of $\epsilon_{x,2} = 0.35$ mm and $\epsilon_{y,2} = 4$ mm. Since the motion of the TM is driven by the motion of the motorized stages, the TM follows exactly the same path along the trajectory segments 1-2 and 3-4: it is reasonable to assume that the reduction of error at the end of the maneuver (step 4) is due to a compensation of the error accumulated along the trajectory. More precisely, if one OFS misses some readings along its path from 1 to 2, it will most likely miss the same reading on its way back. In general, the errors do not compensate if the TM follows a generic path.

Given the limited range of displacements allowed by the motorized stages it is not possible extending the investigation to a more general scenario. In the next section this limitation will be overcome.

Two important aspects must be considered: (1) the OFS system is capable of providing high rate measurements with an acceptable uncertainty over the short-term/mid-term period, (2) the measurement system provides incremental measurements and, to retrieve the pose of the TM with respect to the global reference frame, the initial position is required as an a priori information. The next section tackles these problems and propose a first solution to solve them.

4.3 Development of the camera-aided optical flow sensor based navigation system

The current section presents the first effort aimed at improving the performances of the TM navigation system.

As stated in the previous section the OFS based navigation system, even if it proved to be capable of tracking the motion of the TM with good short-term accuracy, has two main downsides: it provides only incremental measurements (i.e. it requires the knowledge of the initial pose with respect to the global reference frame to propagate the measurements) and it is affected by unbounded errors.

In order to boost the performances of the measurement system and to improve its reliability in providing planar pose estimations, an additional measurement system is added to the measurement chain. The main idea is to implement a second system with two main functional requirements:

- the system must provide an estimation of the TM pose with respect to the global reference frame;
- the system must be employed to update the measurements of the OFS system with the aim of keeping the estimation error bounded;
- the measurement system must not interfere with the motion of the TM.

To satisfy these requirements, a monocular vision system is employed. The idea is to develop a first prototype of the global localization system, operating at a lower rate with respect to the OFS system, that allows a cost-effective validation of the whole measurement approach. Since the operative scenario in which the SPARTANS modules operates is known and structured, it is reasonable to design the measurement system within a cooperating scenario: this implies the assumption of operating with an a priori knowledge of the geometry of the scene. Therefore, a set of fiducial markers to be placed on-board the TM is designed and employed.

After presenting the employed experimental setup, the measurement approach is described and pose estimation results are provided.

4.3.1 Experimental setup

The upgraded OFS based localization system is developed at a more advanced development stage of the TM: even if the shape of the TM is evolved towards its final configuration, the OFS assembly is not modified from a geometrical point of view with respect to the one described in Section 4.2.2. However, new features are implemented in the setup: (1) the TM is almost completed and close to its final configuration as it features the pneumatic subsystem employed to feed the air skids; furthermore all the support plates are mounted.

In this configuration the TM is employed into two different modes: (1) the TM is mounted on top of the two motorized stages (see Section 4.2.2) so that known displacements can be imposed; (2) the TM can undergo an arbitrary planar low-friction motion without any constraint given by the motorized stages thanks to the air cushion generated by the pressurized airflow.

On top of the TM, and more precisely in the close proximity of the OFS, three fiducial markers are placed. Given the low number of markers to be recognized, it is reasonable to adopt a simple design that ensure the recognition of each marker and

that provides a sufficient number of relevant features to be processed and employed in the pose estimation phase. The adopted markers are similar to the ones presented in Section 3.3 but characterized by slightly reduced dimensions: according to the maximum surface available on-board the TM, the square-shaped markers have a side of 5 cm.

A low cost camera (Odroid USB camera) is employed with the aim of acquiring at a given frequency the motion of the TM. To this purpose, the camera is placed above the operative area in which the TM can translate and rotate, with its optical axis directed towards the vertical descending direction. The main problem related to this configuration is that, by tracking the markers aboard the TM, the camera can only estimate the motion of the TM in its own reference frame. To express the position of the TM with respect to the global frame, also the pose of the camera with respect to the global frame is required. Therefore, four additional markers are placed on the surface on which the TM operates. These markers are thought to be processed in the pre-operational phase such that the pose of the camera can be determined in the global frame before the actual acquisition begins.

The planar surface allowing the low-friction displacements is a reduced scale prototype of the test table described in Section 2.5 consisting of a marble table with dimensions of 1200 x800 mm, a chessboard pattern printed on a paper sheet covered by a 1 cm thick glass sheet. The setup is completed by the electronics aboard the TM which are required for the OFS data acquisition and processing.

Figure 4.6 shows the schematic layout of the experimental equipment employed during the testing phase.

4.3.2 Measurement approach

This section presents how the pose of the TM is estimated by means of the OFS system and the external camera.

Four main reference frames are defined: (1) the External Global reference frame G, (2) the Camera fixed reference frame C, (3) the TM Body reference frame B and (4) the i-th OFS fixed reference frame i.

The first step to solve the localization problem consists in the reconstruction of translational and rotational displacements by means of the incremental measurements provided by the OFS. The mathematical approach employed for the observation model

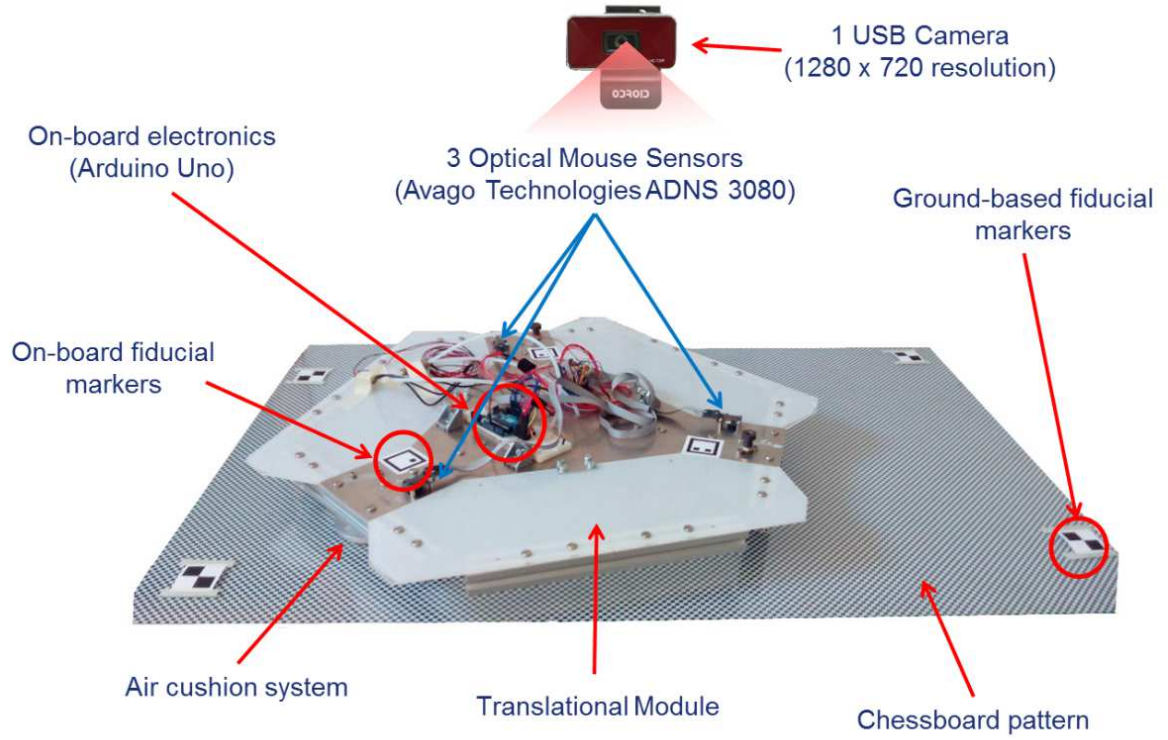

Figure 4.6: Experimental setup used in the development of the camera-aided OFS based localization system.

is presented in Section 4.2.1.

The second step consists in the determination of the TM pose with respect to the global frame by means of the monocular vision system.

After the acquisition, each frame is processed to identify all the fiducial markers placed within the field of view. Since the location of both the ground based markers and the camera is fixed in the global reference frame and relative displacements between this components are not allowed, the identification of the ground-based markers is performed during the pre-processing phase immediately before the TM maneuver starts. For the estimation of the TM motion, the image processing pipeline follows a similar approach to the one described in Section 3.4. To summarize, each frame is first converted into a binary image by means of a thresholding operation and residual speckles are filtered out by means of morphologic operations; all the connected areas in the image are then processed and labeled to identify the parent-child relationship between black and white areas within the image. The Douglas-Peucker algorithm is employed to simplify the borders of the connected regions within the image and, if a

region is characterized by four vertices, it is labeled as a candidate to be recognized as a valid marker. After checking the number of holes (i.e. black dots contained within the marker frame), the region is either recognized as a valid marker or rejected.

The geometry of the TM is known, as well as the 3D coordinates of the fiducial markers with respect to the Body fixed frame. When the TM resides in the field of view of the camera, the 3D known points can be associated to their 2D projections on the image plane. Given these quantities, estimating the pose of the TM is equivalent to solve the Perspective from n Points (PnP) problem. The solution to the problem is obtained by exploiting three points within the solution approach proposed by [43] and using a fourth point to solve the ambiguity among the four possible solutions.

The number of features extracted by each marker is equal to five, thus leading to a number of 15 available features per image. Given the overabundant number of data available, the P3P solution is embedded in a RANSAC scheme to reject outliers and to select the pose that includes the maximum number of features in the consensus set [17].

The outcomes of the two measurement steps can be summarized as follows:

- the OFS system provides incremental estimations of the planar displacements of the TM;

- the monocular vision system provides two kind of measurements:

  (1) through the processing of the ground based markers, the position and orientation of the camera frame with respect to the global reference frame is determined as the four-by-four transformation matrix ${}^{C}_{G}T$;

  (2) the processing of the features extracted from the markers aboard the TM leads to the determination of the pose of the camera frame with respect to the TM body frame, i.e. ${}^{C}_{B}T$.

Therefore, the pose of the TM in the global frame can be determined by means of the vision system with the following equation:

$$ {}^{B}_{G}T \quad = \quad {}^{B}_{C}T \cdot {}^{B}_{C}T = \begin{bmatrix} {}^{C}_{B}R^{-1} & -{}^{C}_{B}R^{-1} \cdot {}^{C}t_{B} \\ 0_{1\,\mathrm{x}3} & 1 \end{bmatrix} \begin{bmatrix} {}^{C}_{G}R & {}^{C}t_{G} \\ 0_{1\,\mathrm{x}3} & 1 \end{bmatrix}. \tag{4.13} $$

To merge the measurements coming from the two acquisition system a data fusion is performed.

4.3.3 Data filtering

An estimation of the TM linear position and azimuth is provided by both the OFS system at high-frequency and the external vision-based system at a lower frequency. To fuse the data coming from the two systems an Extended formulation of the Kalman filter (EKF) is employed [53].

Let $X_k = [x_k,\ y_k,\ \theta_k]^T$ be the TM state vector. If linear and azimuthal incremental displacements estimated using the three OFS are treated as input vector $u_k = \Delta S_k = [\Delta X_k,\ \Delta Y_k,\ \Delta\theta_k]^T$ with a corresponding error $w_k = [w_{x,k},\ w_{y,k},\ w_{\theta,k}]$, the state equation of the EKF can be written as:

$$X_{k+1} = f(X_k, u_k, w_k) \tag{4.14}$$

or, in an extended form, as:

$$\begin{aligned} x_{k+1} &= x_k + (\Delta X_k + w_{x,k})\cos\theta_k - (\Delta Y_k + w_{y,k})\sin\theta_k \\ y_{k+1} &= y_k + (\Delta X_k + w_{x,k})\sin\theta_k + (\Delta Y_k + w_{y,k})\cos\theta_k \\ \theta_{k+1} &= \theta_k + \Delta\theta_k + w_{\theta,k} \end{aligned} \tag{4.15}$$

where w_k is modeled as a zero-mean gaussian noise with convariance matrix Q_k, i.e $Q_k \sim \mathcal{N}(0, Q_k)$, with:

$$Q_k = \mathrm{diag}[\sigma^2_{w_x,k},\ \sigma^2_{w_y,k},\ \sigma^2_{w_\theta,k}]. \tag{4.16}$$

The observation model is devoted to updating the state by integrating the contribution given by the external camera. Let $z_k = [x_{c,k}, y_{c,k}, \theta_{c,k}]^T$ be the TM planar pose estimated through the vision system as shown in equation 4.13 (i.e. the planar position and orientation of the TM in global frame are extracted from the transformation matrix ${}^B_G T$). The observation model can be implemented as:

$$z_k = HX_k + v_k \tag{4.17}$$

or, in extended form, as:

$$\begin{bmatrix} x_{c,k} \\ y_{c,k} \\ \theta_{c,k} \end{bmatrix} = \begin{bmatrix} 1 & 0 & 0 \\ 0 & 1 & 0 \\ 0 & 0 & 1 \end{bmatrix} \begin{bmatrix} x_k \\ y_k \\ \theta_k \end{bmatrix} + \begin{bmatrix} v_{x,k} \\ v_{y,k} \\ v_{\theta,k} \end{bmatrix} \tag{4.18}$$

where v_k is the measurement noise vector modeled as a zero-mean gaussian noise with covariance matrix R_k, i.e. $v_k \sim \mathcal{N}(0, R_k)$:

$$R_k = diag[\sigma^2_{v_x,k},\ \sigma^2_{v_y,k},\ \sigma^2_{v_\theta,k}] \tag{4.19}$$

Given the non linearity of the state equation, a linear Kalman filter cannot be employed and therefore its extended formulation is adopted. The Time Update and the Measurement Update steps are implemented as follows:

- Time Update Phase:

$$X_{k+1|k} = f(X_{k|k}, u_k, 0) \tag{4.20}$$

$$P_{k+1|k} = F_k\, P_{k|k}\, F_k^T + G_k\, Q_k\, G_k^T \tag{4.21}$$

- Measurement Update Phase:

$$K_k = P_{k|k-1} H^T [\, H\, P_{k|k-1} H^T + R_k\,]^{-1} \tag{4.22}$$

$$\widehat{X}_{k|k} = \widehat{X}_{k|k-1} + K_k[\, z_k - H\, \widehat{x}_{k|k-1}\,] \tag{4.23}$$

$$P_{k|k} = P_{k|k-1} - K_k\, H\, P_{k|k-1} \tag{4.24}$$

where P is the state covariance matrix, K the Kalman gain and F, G are the jacobians of the state equation computed respectively with respect to the state vector and the external input (in this case the OFS measurements):

$$F_k = \left.\frac{\partial f}{\partial X}\right|_{X_k,u_k,0} = \begin{bmatrix} 1 & 0 & -\Delta X_k \sin\theta_k - \Delta Y_k \cos\theta_k \\ 0 & 1 & \Delta X_k \cos\theta_k - \Delta Y_k \sin\theta_k \\ 0 & 0 & 1 \end{bmatrix} \tag{4.25}$$

$$G_k = \left.\frac{\partial f}{\partial u}\right|_{x_k,u_k,0} = \begin{bmatrix} \cos\theta_k & -\sin\theta_k & 0 \\ \sin\theta_k & \cos\theta_k & 0 \\ 0 & 0 & 1 \end{bmatrix} \tag{4.26}$$

At the beginning of the pose estimation procedure, the TM pose in the global frame is initialized by means of the measurement of the camera. For each sampling interval, the incremental measurements of the OFS are parsed in the Time Update step to propagate the motion relying only on the OFS data. When the camera performs a new measurement, the provided pose information is processed in the Measurement Update step so that the state vector resulting from the time update can be corrected as shown in equation 4.23.

4.3.4 Test and results

To evaluate the performances of the measurement approach based on the two separated acquisition systems, several tests are performed using the two different experimental setup configurations as described in Section 4.3.1. The test campaign is subdivided into two parts.

First test phase

In the first phase of the test campaign, the TM motion is imposed using the motorized stages with the aim of determining, given the imposed displacement, the error associated to the measurements of the OFS and of the camera.

Each test in this phase is structured as follows:

- the TM is provided with a known planar displacement by means of the motorized stages. The overall imposed maneuver is subdivided into intermediate steps consisting either in pure translational or rotational displacements in the global reference frame;
- the planar motion is estimated by means of the OFS system for the whole duration of the maneuvers;
- the external camera performs an image acquisition each time a single intermediate step of the maneuver is terminated.

Figure 4.7 shows the angular profile obtained from the execution of a simple test maneuver: in this specific case, an azimuthal displacement of 4 deg is imposed to the TM, followed by a rotation of -4 deg. The reference trajectory is shown by the red dashed line within the graph. As the black dashed line shows, the OFS system measures a rotation slightly lower than the imposed one. The blue circles indicate the measurements performed by means of the vision system at the end of each step of maneuver. It can be seen that the camera provides better performances in tracking the angular motion of the TM as the tracking error is lower if compared to the estimations of the OFS system.

Different operative conditions are reproduced by means of the motorized stages and several tests are performed to determine the error affecting the planar pose estimation provided by the two measurement systems. To this extent, Figure 4.8 presents the

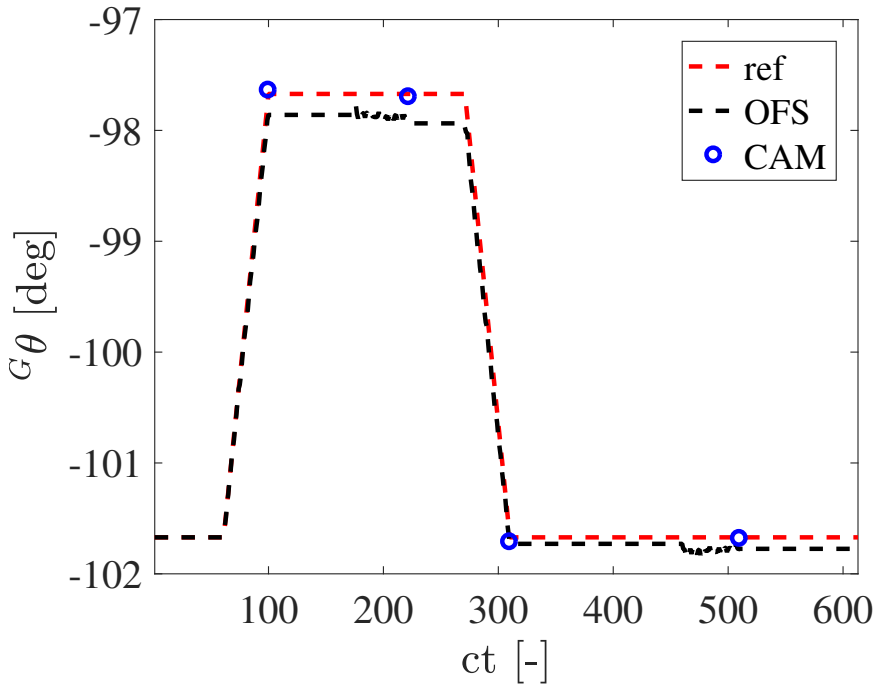

Figure 4.7: Angular profile imposed to the TM during a test maneuver. The red dashed line shows the reference trajectory imposed by means of the motorized rotational stage, the black dashed line refers to the OFS measurements while blue circles show the camera measurements.

sequence of errors obtained at the end of each step of the performed maneuvers. The obtained results shows a slightly drifting behavior of the error associated to the OFS system, in particular along the x direction. It must be considered that, as already discussed in the previous sections, the limited range of displacement allowed by the motorized stages and the execution of simple maneuvers keep the errors of the OFS system limited. This limitation in the investigation is overcome in the second phase of test.

The measurement errors obtained in this phase of test are employed to characterize the RMS error associated to the camera measurements over more than 90 maneuver steps as summarized in Table 4.3. The RMS error is treated as an input for the measurement procedure as it is implemented in the second test phase.

Second test phase

The motorized stages provide a valuable mean to impose known displacements to the TM and to determine the measurement errors. However, the limited range of al-

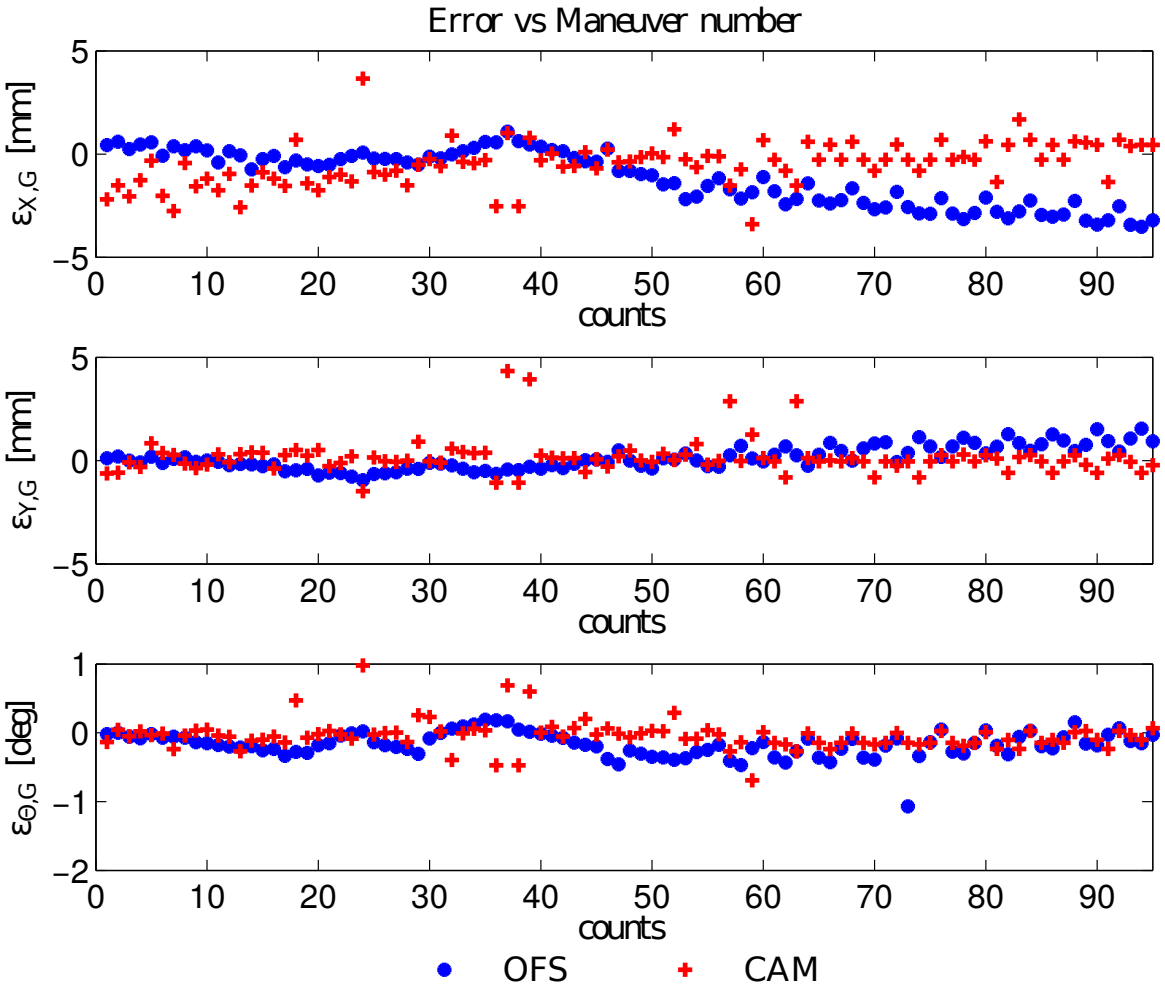

Figure 4.8: Translational Module pose estimation errors in global frame G. Blue lines refer to OFS measurements, red lines to camera measurements. Errors are computed using as a reference the known displacements imposed by means of the motorized stages.

lowed displacements provides a limitation in the measurement system characterization. Therefore, the localization system is tested in a different operative scenario. In this test phase the main differences with respect to the previous phase are two: (1) the TM is free to move on the flat table on the thin air layer generated by the air skids so that the motion is no more constrained to the motorized stages; (2) the measurements provided by the two acquisition systems are now merged by means of the EKF as presented in 4.3.3. Since the principal objective of the tests is the characterization of the measurement system and to understand its main limitations, the real time processing of the data is not required: thus, data are processed with an offline procedure.

Several tests are performed by imposing displacements to the TM by hand. This

Table 4.3: Root Mean Square Error affecting the vision based pose estimation process computed after the first testing phase.

Variable	**RMS Error**
x_c	0.39 mm
y_c	0.42 mm
θ_c	0.1 deg

operation is needed since, at the moment of the writing of this thesis, the actuation of translational control actions is still being developed and tested and therefore cannot be employed in the setup.

In this phase the vision system and the OFS system acquire data periodically with a sampling frequency of 0.2 Hz and 20 Hz respectively.

The process noise employed within the EKF is determined starting from considerations on the intrinsic parameters of the three OFS: in particular the covariance matrix is initialized as:

$$Q = \text{diag}([5 \cdot 10^{-4}\ \text{mm}^2,\ 5 \cdot 10^{-4}\ \text{mm}^2,\ 7 \cdot 10^{-6}\ \text{rad}^2]). \tag{4.27}$$

As regard the measurement noise associated to the data assimilation step of the filter (i.e. measurement update) some preliminary considerations must be done. First of all, the localization of the TM in the global frame is made possible by the combination of two measured poses that describe the position and orientation of the camera respectively in the global and in the TM body frames (see eq. 4.13). The overall uncertainty on the TM pose is therefore the result of the uncertainty affecting both ${}^C_G T$ and ${}^C_B T$.

Let $\xi_1 = [\phi_1,\ \theta_1,\ \psi_1,\ t_{x1},\ t_{y1},\ t_{z1}]$ be the vector containing the three Euler angles and the three components of the translation vector that describe the pose of the camera in global frame. Analogously $\xi_2 = [\phi_2,\ \theta_2,\ \psi_2,\ t_{x2},\ t_{y2},\ t_{z2}]$ describe the pose of the camera in TM frame. The transformation matrices can therefore be written as:

$${}^C_G T = {}^C_G T(\phi_1,\ \theta_1,\ \psi_1,\ t_{x1},\ t_{y1},\ t_{z1}) \tag{4.28}$$

$${}^C_B T = {}^C_B T(\phi_2,\ \theta_2,\ \psi_2,\ t_{x2},\ t_{y2},\ t_{z2}) \tag{4.29}$$

Since ${}^B_G T = {}^B_C T \cdot {}^C_G T$, the vector $\xi' = [\xi_1,\ \xi_2]$ can be defined so that ${}^B_G T = {}^B_G T(\xi')$.

The six parameters defining the pose of the body in global frame, namely $\xi =$

$[\phi,\ \theta,\ \psi,\ t_x,\ t_y,\ t_z]$ are determined from the components of the ${}^{B}_{G}T$ matrix as follow:

$$\phi = g_1(\xi') = \tan^{-1}\left(\frac{{}^{B}_{G}T_{2,3}}{{}^{B}_{G}T_{3,3}}\right) \tag{4.30}$$

$$\theta = g_2(\xi') = \sin^{-1}({}^{B}_{G}T_{1,3}) \tag{4.31}$$

$$\psi = g_3(\xi') = \tan^{-1}\left(\frac{{}^{B}_{G}T_{1,2}}{{}^{B}_{G}T_{1,1}}\right) \tag{4.32}$$

$$t_x = g_4(\xi') = {}^{B}_{G}T_{1,4} \tag{4.33}$$

$$t_y = g_5(\xi') = {}^{B}_{G}T_{2,4} \tag{4.34}$$

$$t_z = g_6(\xi') = {}^{B}_{G}T_{3,4} \tag{4.35}$$

where the subscripts i, j in $T_{i,j}$ indicate the (i, j)-th element of the matrix.

To the purpose of the localization of the TM, only $\psi,\ t_x,\ t_y$ are of our interest. However they have are in general dependent on all the parameters contained in the vector ξ'.

The uncertainty on the parameters in ξ' is estimated as the RMS error measured during all the maneuvers performed during the first test phase: let the error on these parameters be identified by the vector $u_{\xi'} \in \mathbb{R}^{12}$.

The uncertainty on $\psi,\ t_x,\ t_y$ therefore can be determined by means of the Kline-McClintock propagation formula as:

$$u_{\xi,i} = \sqrt{\sum_j \left(\frac{\partial g_i}{\partial \xi'_j}\right)^2 u^2_{\xi'_j}} \qquad i = 3, 4, 5; \quad j = 1 \ldots 12. \tag{4.36}$$

Equation 4.36 is employed for each step of the data assimilation to update the uncertainty affecting the camera measurements so that the measurement covariance matrix can be evaluated as $R = \mathrm{diag}([u^2_{t_x}\ u^2_{t_y}\ u^2_{\psi}])$.

Figure 4.9 shows the output of the measured planar pose with respect to the global reference frame when both the camera and the OFS measurements are employed. The measurements provided by the OFS (continuous blue line) show a drifting behavior with respect to the estimations provided by the camera (red dots) that act like a

reference used to reset the uncertainty on the pose estimation under a certain level (black dashed line).

By parsing the state covariance matrix associated to all the measured poses along the trajectory of the TM, the maximum level of uncertainty on the measured pose, which occurs immediately before the measurement update step, shows a value of $\sigma_{max} = [7.38\,\text{mm},\ 7.38\,\text{mm},\ 1.76\,\text{deg}]$.

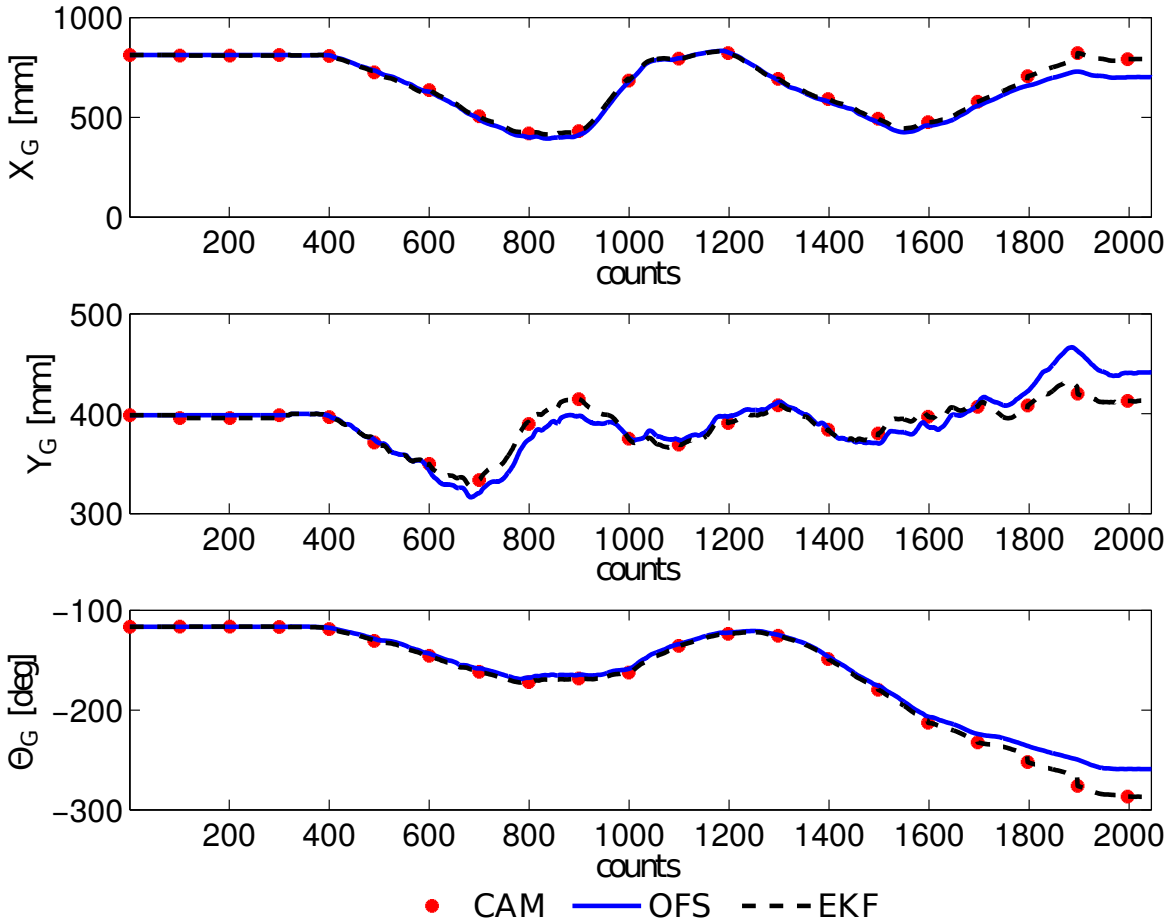

Figure 4.9: Measured pose in terms of planar position and azimuth with respect to the global reference frame. The continuous blue line, red dots and dashed black line refer to the measurements provided by the OFS, the camera and the EKF respectively.

The adopted filtering techniques proves to be effective in keeping the uncertainties on the pose estimation bounded. Moreover, by employing a higher acquisition rate for the camera the uncertainty can be further kept at a lower level.

The developed measurement approach however shows some limitations: (1) the first prototype of the localization system employs a low budget camera that is not taylored for high rate acquisitions, (2) the employed image processing step must be optimized

to enable the real-time capabilities of the measurement system. Given these reasons, the localization prototype is used as a starting point to identify the final configuration of the SPARTANS global navigation system, as presented in the next section.

4.4 Development of the global navigation system

The current section is aimed at presenting the final version of the global navigation system as it is implemented in the SPARTANS facility.

The development of the first prototype of the localization system demonstrated the feasibility of the measurement approach for the localization problem based on the OFS system combined to a monocular vision system.

As the development of the SPARTANS testbed proceeds towards its final configuration, new challenges arise: the global navigation system therefore must be updated in order to be capable of tracking the motion of one or more spacecraft modules operating on the test table.

Some important aspects must be considered in the design and the selection of the technology for the global navigation system: in fact if a single camera is used (1) the displacements of the micro-satellites aboard the test table can lead to occlusions, (2) the dimensions of the test table lead to a decrease in the spatial resolution if a spacecraft module is too far apart from the camera.

The selection of a Motion Capture system is therefore performed as this measurement system ensures the fundamental requirement of non interfering with the motion of the micro-satellites and of providing global coverage over the whole test table area. Furthermore, it overcomes the limitations of all the incremental measurement systems aboard the SPARTANS modules (OFS, QE) providing a shared common global reference frame.

As briefly described in Section 2.6, the global navigation system consists of a set of 6 infrared digital cameras, some passive retro-reflective markers and an external control station devoted to gathering and processing the information made available by the cameras. The employed Motion Capture is a commercial system, developed by BTS Engineering, featuring 6 Sony XC-75 infrared cameras with a resolution of 768(H)x494(V) pixel. The lens mount allow to adjust the depth of field so that the performances of the system can be adjusted accordingly.

4.4.1 Global navigation system setup

The integration of the Motion Capture within the SPARTANS facility requires to find a tradeoff between the spatial constraints given by the laboratory and the need of providing a global coverage of the test table.

To understand the parameters that drive the definition of the global navigation setup, the functioning principles of the measurement system must be clear. After a proper calibration procedure, each retroreflective marker in the field of view of at least two cameras can be tracked and its position in the 3D space can be determined by means of triangulation. If more than two cameras recognize the same marker, redundant measurements are provided resulting in an increased accuracy. Therefore, the placement of the cameras within the laboratory is crucial to ensure that the cameras field of views overlap over the largest possible operative volume.

The laboratory provides an operative surface of approximatively 6x5 m with the ceiling at a height of 3 m. The test table, placed in the central portion of the laboratory, has a surface of 2x3 m and its upper surface is placed at 0.9 m above the floor. Considering that the height of each spacecraft simulator is of about 0.85 m, the operational volume which is required to be covered by the Motion Capture is determined.

To identify the most convenient placement of the cameras, some numerical simulations are performed with the aim of determining the maximum operative volume covered by the six cameras taking into account all the spatial constraints. The outcomes of the analysis showed that a good configuration consists in the placement of the cameras on a circumference with a radius of approximatively 2.5 m around the test table. Each camera is oriented such that its optical axis points downwards with an inclination of about 25 deg, and its projection passes through the center of the test table. Numerical simulations shows that the 62% of the operative volume is covered by six cameras, while the remaining part is in sight of at least two cameras. Figure 4.10 shows the 3D model of the operative test volume with the six camera field of views depicted as blue pyramids and the volume covered by all the cameras shown as a red polyhedron.

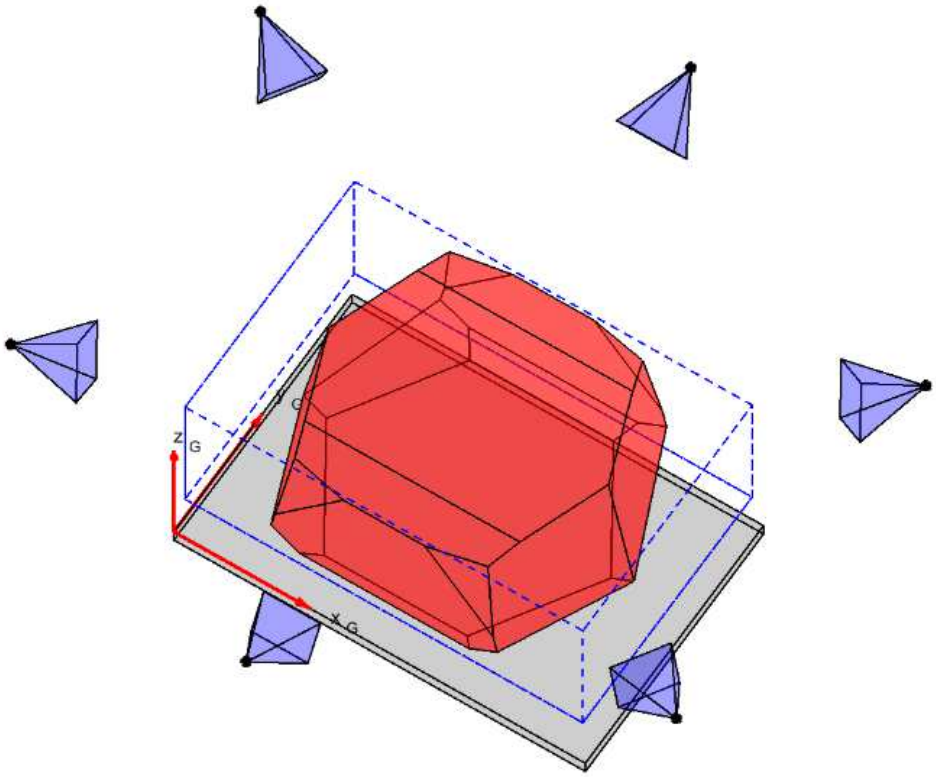

Figure 4.10: 3D model of the test table with the associated operative volume. The six camera placement is shown by the blue pyramids while the operative volume in sight of the six cameras is depicted as a red polyhedron.

4.4.2 Motion tracking

The output of the Motion Capture system consists in the 3D location of the retroreflective markers in the operative volume. However, the global navigation system is aimed at providing pose estimations of the spacecraft modules in the global reference frame. This objective is achieved by placing a predefined number of markers aboard the AM in order to define relevant features in a known position to be tracked. In particular, three markers labeled as M_0, M_1, M_2 are placed on the three top corners of the AM framework by means of custom made plastic supports. The location of the markers is defined for two main reasons: (1) given that each AM can rotate with roll and pitch angles in the range $[-40, +40]$ degrees, the markers in each of these positions have a low probability of not being visible from at least two IR cameras and (2) the baseline between two markers is maximized, so that the uncertainty on the direction defined by a pair of markers is reduced.

The following reference frames are defined:

- The external global frame G, depicted in green in Figure 4.11, which is a Local Vertical - Local Horizontal (LVLH) frame defined during the initialization procedure of the Motion Capture System using a set of three perpendicular sticks equipped with retroreflective markers;
- the frame B, shown in blue in Figure 4.11, fixed to the AM with its origin ${}^{B}O$ coincident with the center of rotation of the mechanical joints system;
- the motion capture MC frame, shown in red in Figure 4.11, defined by means of the three markers aboard the AM.

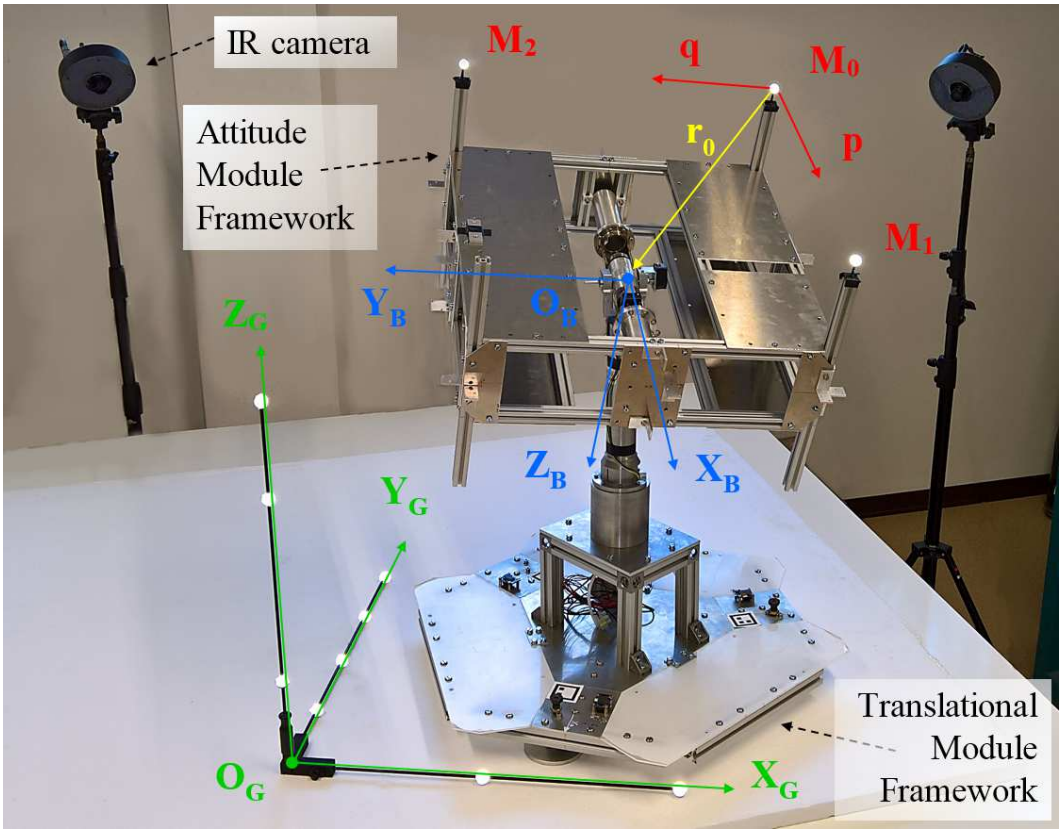

Figure 4.11: Experimental setup with the AM framework placed on the TM framework and two of the six IR cameras. The retro reflecting markers are the bright circles. The Global Reference Frame (RF) is depicted in green, the Body RF is depicted in blue and the three retro reflecting markers M_0 , M_1 and M_2 on board the AM are labeled in red.

In order to define the body frame by means of the Motion Capture system, the three markers on-board the AM are employed to define the MC frame: in particular

the markers define the unit vectors used to identify the directions of the ${}^{MC}x$ and ${}^{MC}y$ axes. Let the vectors p and q be defined as $p = \overrightarrow{M_0M_1}$ and $q = \overrightarrow{M_0M_2}$. Thus the MC axes can be defined as:

$$\begin{aligned} {}^{MC}x &= p \\ {}^{MC}y &= q \\ {}^{MC}z &= \frac{p \times q}{||p \times q||} \end{aligned} \tag{4.37}$$

Nominally the position of the three markers is known in the AM frame and the directions they define are aligned to the ${}^{B}x$ and ${}^{B}y$ axes. Thus, the location of the origin of the body frame ${}^{B}O$ is determined by applying a translation $r_0 = [260, 260, 230]$ mm to the marker M_0.

Once the reference frames are defined, the attitude of the AM in G can be estimated by simply computing the rotation matrix ${}^{G}_{MC}R$ from the MC to the global reference frame as the rotation matrix containing as columns the unit vectors ${}^{MC}x$, ${}^{MC}y$, ${}^{MC}z$. The roll ϕ, pitch ϑ and yaw ψ angles are then computed as:

$$\phi = \tan^{-1}({}^{G}_{MC}r_{3,2}/{}^{G}_{MC}r_{3,3}) \tag{4.38}$$

$$\vartheta = \sin^{-1}(-{}^{G}_{MC}r_{3,1}) \tag{4.39}$$

$$\psi = \tan^{-1}({}^{G}_{MC}r_{2,1}/{}^{G}_{MC}r_{1,1}). \tag{4.40}$$

4.4.3 Calibration of the global navigation system

In nominal conditions, the MC reference frame perfectly matches the body frame. However, this matching condition between the two frames of reference is not valid since imprecisions on positioning the markers on board the AM framework are present and the uncertainty on the markers positions estimated by the Motion Capture system cannot be avoided.

A refinement calibration procedure is therefore required with the aim of: (1) making ${}^{B}O$ as close as possible to the center of rotation of the mechanical joints and (2) making the axes of the Motion Capture RF aligned with the ones of the body reference frame. The importance of having these two frames of reference aligned is due to the fact that, in future developments, the Motion Capture measurements and the QE measurements will be fused together through Kalman filtering.

Calibration Procedure for the Origin Position

The calibration procedure for the origin of the body reference frame exploits a simple but effective idea: during any motion of pure attitude, the center of each spherical marker on board the AM is allowed to move on the surface of a sphere with radius r and whose center coincides with the center of rotation of the joints.

Given this assumption, an attitude motion is imposed by hand to the AM and, by means of the Motion Capture system, the 3D coordinates of the three markers are measured at 50 Hz, i.e. $M_{i,k} = [x_{i,k}, y_{i,k}, z_{i,k}]^T$ where $i = 0, 1, 2$ and $k = 1 \dots m$ refers to the acquisition step. The acquired data are employed to compute the coordinates of the of the origin ${}^B\widehat{O} = [{}^B\widehat{x},\ {}^B\widehat{y},\ {}^B\widehat{z}]$ and the three radii r_0, r_1 and r_2 that minimize the following sum of squared residuals:

$$f = \sum_{k=1}^{m} \sum_{i=0}^{2} \epsilon_{i,k}^2 \tag{4.41}$$

where $\epsilon_{i,k}$ is the residual defined as:

$$\epsilon_{i,k} = \sqrt{(x_{i,k} - x_B)^2 + (y_{i,k} - y_B)^2 + (z_{i,k} - z_B)^2} - r_i \tag{4.42}$$

The attitude motion imposed by hand to the AM in terms of roll, pitch and yaw angles is shown in Figure 4.12 where the angular profiles refer to the attitude of the MC reference frame with respect to the global reference frame.

Figure 4.13 shows the results of the least square analysis performed on a set of data acquired for approximatively 50 s (about 2500 acquisition steps). The time profile of the three coordinates of the nominal origin ${}^BO$ are shown in solid red line. It can be noticed that an offset between the nominal center of rotation and the actual one is present: this statement is supported by the fact that the coordinates of ${}^BO$ show a visible oscillation during the imposed attitude motion. The coordinates of the calibrated origin ${}^B\widehat{O}$ are marked in solid blue line and their mean values are shown in dotted black line. It can be observed that the calibrated coordinates does not show any evident dependency on the imposed attitude motion and they present only a random oscillation around their mean values due to the measurement noise of the Motion Capture System.

Calibration Procedure for the Axes Alignment

To ensure that the axes of the MC reference frame are aligned to the ones of the body frame, in addition to the measurements of the Motion Capture an auxiliary

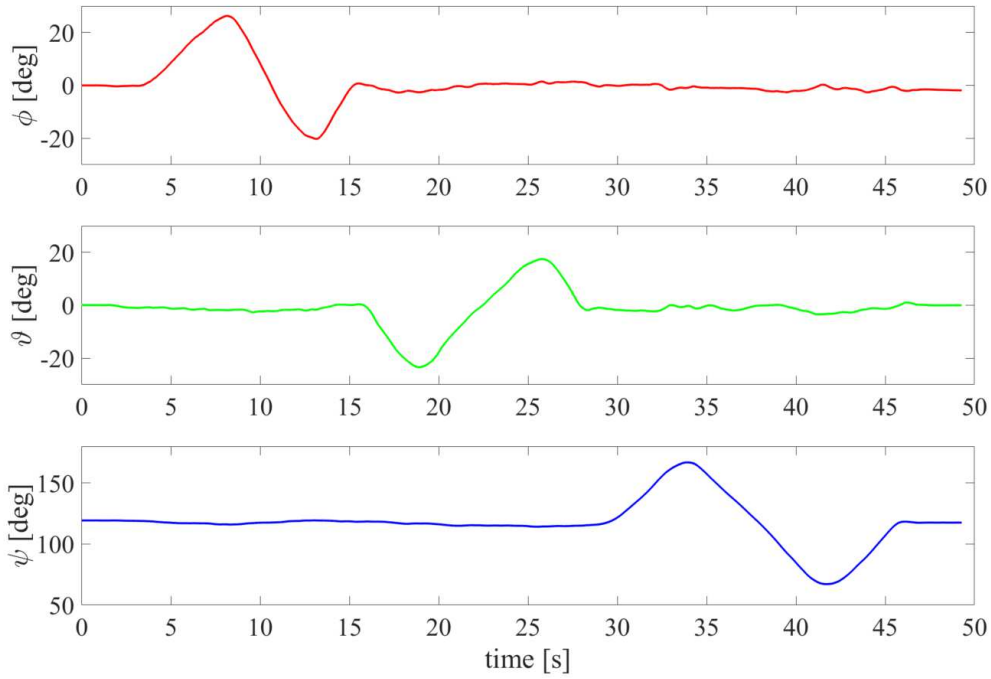

Figure 4.12: Attitude motion in terms of roll, pitch and yaw angles imposed during the calibration procedure to determine the AM center of rotation.

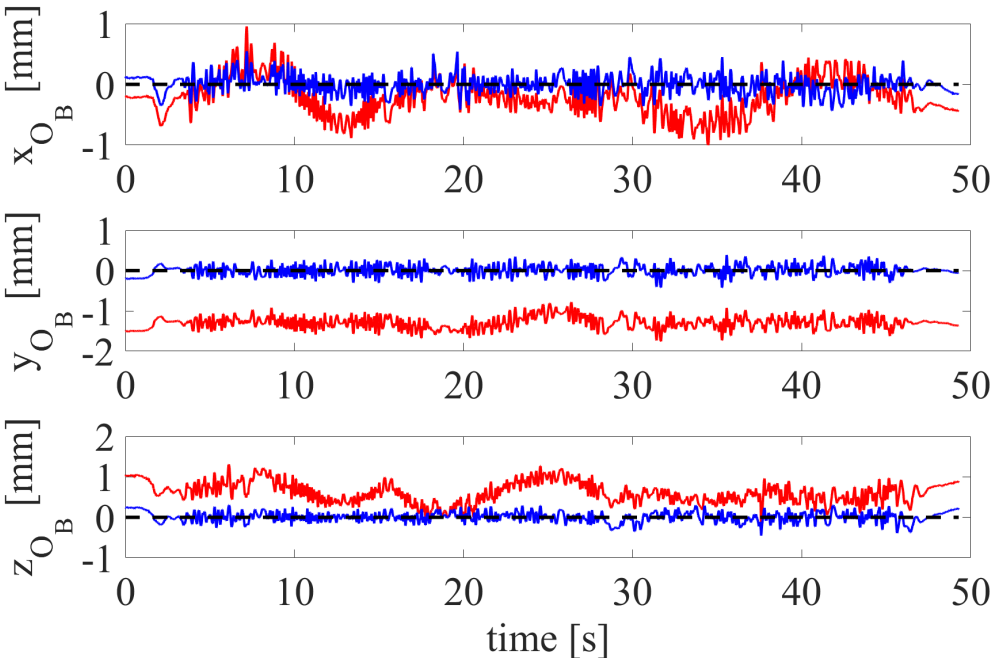

Figure 4.13: Coordinates of the center of rotation ${}^{B}O$ in the Global Reference Frame. The nominal coordinates are marked in solid red line and the calibrated coordinates are marked in solid blue line with the corresponding mean values marked in dotted black line. The calibrated mean values are taken as reference (zero values in the plots).

measurement system is required. Since the QEs at the mechanical joints provide a direct estimation of the attitude of the AM with a resolution of 0.09 deg, the QEs are employed.

The measurements of the markers positions provided by the Motion Capture system are first used to compute the rotation matrix from the Motion Capture RF to the Global RF ${}^{G}_{MC}R(M_0, M_1, M_2)$, as described in Section 4.4.2. The encoder measurements ϕ_{QE}, ϑ_{QE} and ψ_{QE} are then used to compute the rotation matrix from the body frame to the global reference frame ${}^{G}_{B}R(\phi_{QE}, \vartheta_{QE}, \psi_{QE})$.

The three Euler angles ϕ_{mis}, ϑ_{mis} and ψ_{mis} representing the misalignment between the two frames of reference are evaluated from the rotation matrix

$$ {}^{B}_{MC}R = {}^{G}_{B}R^{T} \cdot {}^{G}_{MC}R \tag{4.43} $$

as:

$$ \begin{aligned} \phi_{mis} &= atan({}^{B}_{MC}r_{3,2}/{}^{B}_{MC}r_{3,3}) \\ \vartheta_{mis} &= asin(-{}^{B}_{MC}r_{3,1}) \\ \psi_{mis} &= atan({}^{B}_{MC}r_{2,1}/{}^{B}_{MC}r_{1,1}) \end{aligned} \tag{4.44} $$

To ensure a reliable estimation of the misalignment angles, the measurements provided by the two acquisition system must be synchronous in order to ensure that the data provided refer to the same sampling interval.

At the moment of writing this thesis, the synchronization of these two measurement systems is not implemented yet. To overcome this limitation, the calibration procedure is performed in static conditions, i.e. the acquisition is performed for a sequence of imposed static attitude positions of the AM in order to measure $(\phi_{QE,i},\ \vartheta_{QE,i},\ \psi_{QE,i})$ and $(M_{0,i},\ M_{1,i},\ M_{2,i})$ referring to the same AM orientation.

The two sets of measurements related to the same attitude sequence are then combined as in equation 4.43 to obtain a corresponding sequence of misalignment angles $(\phi_{mis,i}, \vartheta_{mis,i}, \psi_{mis,i})$.

Figure 4.14 shows the sequence of the 19 static attitude steps in terms of Euler angles acquired with the Motion Capture system that are used to evaluate the misalignment roll, pitch and yaw angles. The resulting sequence of misalignment angles ϕ_{mis}, ϑ_{mis} and ψ_{mis} is reported in Fig. 4.16 along with the associated uncertainty. The final misalignment angles are determined as the mean values of the corresponding

sequences, resulting in:

$$\begin{aligned} \overline{\phi}_{mis} &= 0.49 \text{ deg} \\ \overline{\theta}_{mis} &= 0.16 \text{ deg} \\ \overline{\psi}_{mis} &= 0.06 \text{ deg}\,. \end{aligned} \tag{4.45}$$

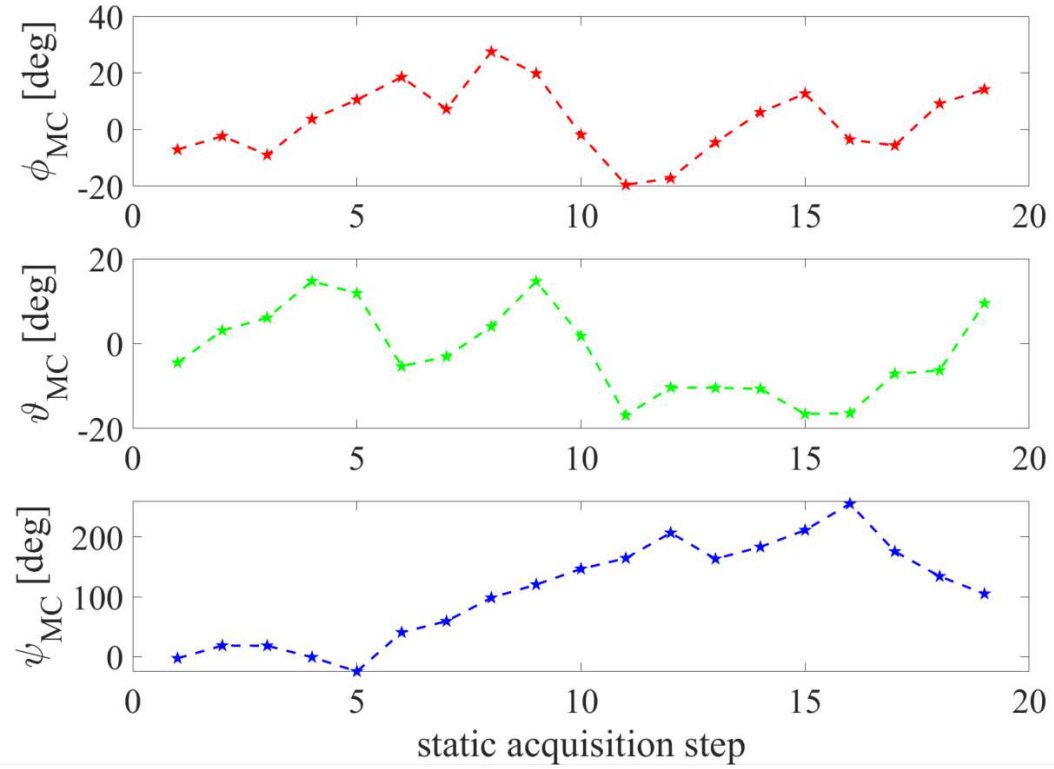

Figure 4.14: Sequence of static roll ϕ, pitch ϑ and yaw ψ angles acquired with the Motion Capture System and used in the calibration procedure for the axes alignment.

4.4.4 Uncertainty analysis

To assess the quality of the pose measurements, an uncertainty analysis is performed. The uncertainty is evaluated for the following three quantities: (1) the three Euler angles ϕ, ϑ and ψ evaluated using the Motion Capture system, (2) the origin ${}^{B}\widehat{O}$, and (3) the three Euler angles that correct the misalignment between the attitude measurements performed by the Motion Capture system and the QEs. In all these three cases, the output quantities are evaluated as indirect measurements (i.e., calculated variables), whose input quantities are the 3D positions of the markers detected by the Motion Capture system and the angular direct measurements obtained by means of the optical encoders.

The uncertainty evaluation in these indirect measurements is performed by the Kline McClintock propagation formula [45]:

$$u_y = \sqrt{\sum_{i=1}^{n} \left(\frac{\partial y}{\partial x_i}\right)^2 u_{x_i}^2} \tag{4.46}$$

where y is the indirect measurement and x_i are the input quantities.

The following uncertainty sources are considered in the uncertainty analysis: (1) the uncertainty due to the resolution of the quadrature encoders used to measure the motion of the mechanical joints system and (2) the uncertainty on the markers positions measured by the Motion Capture System. In particular, after the initialization procedure of the Motion Capture, the uncertainty on the 3D position of the markers is returned as a type A standard uncertainty. In the operative conditions in which the tests are performed, an uncertainty of $u_x = 0.4$ mm is determined and it is assumed equal for each coordinate and for each of the three markers.

Uncertainty of the Euler Angles

The uncertainty of the three Euler angles is evaluated assuming the coordinates of the three markers x_i, with $i = 1 \dots 9$, as independent variables and with uncertainty $u_{x_i} = u_x$, for each i.

The computation of the partial derivatives of the Euler angles with respect to the markers coordinates is performed by means of the Matlab Symbolic Toolbox. It can be demonstrated that the following expressions hold:

$$u_\vartheta = \frac{\sqrt{2}}{b} u_x \tag{4.47}$$

$$u_\psi = \frac{\sqrt{2}}{b_{xy}}\, u_x = \frac{\sqrt{2}}{b\, cos\vartheta}\, u_x \tag{4.48}$$

where b is the mean distance between the markers M_0 and M_1, equal to 520.0 mm, and b_{xy} is the projection of b on the global x-y plane.

Equation 4.47 show that the uncertainty on the pitch angle ϑ is constant with a value of 0.06 deg. The uncertainty on the yaw angle ψ, as shown in equation 4.48, is dependent on the length of the projection of the vector joining two markers onto the global horizontal plane. An upper and lower bound to the value of u_ψ can be found if the actual configuration of the AM is taken into account: in fact, due to the mechanical

constraints of the rotational joints system, the pitch angle ranges from -40 to 40 deg. Therefore the uncertainty u_ψ is limited within the range between 0.06 and 0.08 deg.

As regards the uncertainty on the roll angle u_ϕ, a simple equation to characterize the upper and lower bound of the uncertainty cannot be found. To characterize this parameter within the operative rotational conditions of the AM a numerical analysis is performed: the attitude of the AM is varied in a range of $[-40, +40]$ deg for the roll and pitch angles and in a range of $[0, 360]$ deg for the yaw angle. For each of the sampled simulated attitudes, the uncertainty $u_\phi = u_\phi(\phi,\ \vartheta,\ \psi,\ u_{x_i})$ is evaluated and, at the end of the procedure, the maximum and minimum values of u_ϕ are recorded, resulting respectively in a value of 0.06 deg and 0.09 deg.

Figure 4.15 shows in red the standard uncertainty profiles of the Euler angles for the attitude maneuver used in the origin calibration procedure as shown in Fig. 4.12, with the computed maximum and minimum values of the uncertainties marked with blue dashed lines. For the pitch angle, the experimental data and the theoretical one are superimposed. For the roll and yaw angles, the experimental data (red) show to be in accordance with the maximum and minimum theoretical uncertainty levels.

Uncertainty of the Origin Position

The position of the origin O_B in the Global RF is computed as:

$$^G\widehat{O}_B = {}^GM_0 + {}^G\widehat{r}_0 = {}^GM_0 + {}^G_{MC}R(M_0, M_1, M_2)\,{}^B\widehat{r}_0 \tag{4.49}$$

where ${}^B\widehat{r}_0 = [259.3, 260.1, 228.7]$ mm is the output of the calibration procedure described in Section 4.4.3.

Considering equation 4.49, three sources of uncertainty can be identified: (1) the uncertainty on the ${}^GM_0$ position $u_{G_{M_0}} = [0.4, 0.4, 0.4]^T$ mm, (2) the uncertainty on the rotation matrix ${}^G_{MC}R$, which is in turn due to the uncertainty on the markers positions and (3) the uncertainty on ${}^B\widehat{r}_0$, which is computed from the results of the least square analysis of equation 4.41 as $u_{B_{r_0}} = [0.2, 0.2, 0.1]$ mm.

The first step of the analysis consists in the identification, by means of a numerical analysis, of the maximum value of uncertainty associated with ${}^G\widehat{r}_0$: to this purpose, the Kline McClintock propagation formula is employed assuming the Euler angles as independent variables. The values of the uncertainties on ϕ, ϑ and ψ are evaluated as described in the previous subsection. Given the following parametrization of the rotation matrix ${}^G_{MC}R$ as a function of the roll ϕ, pitch ϑ and yaw ψ angles

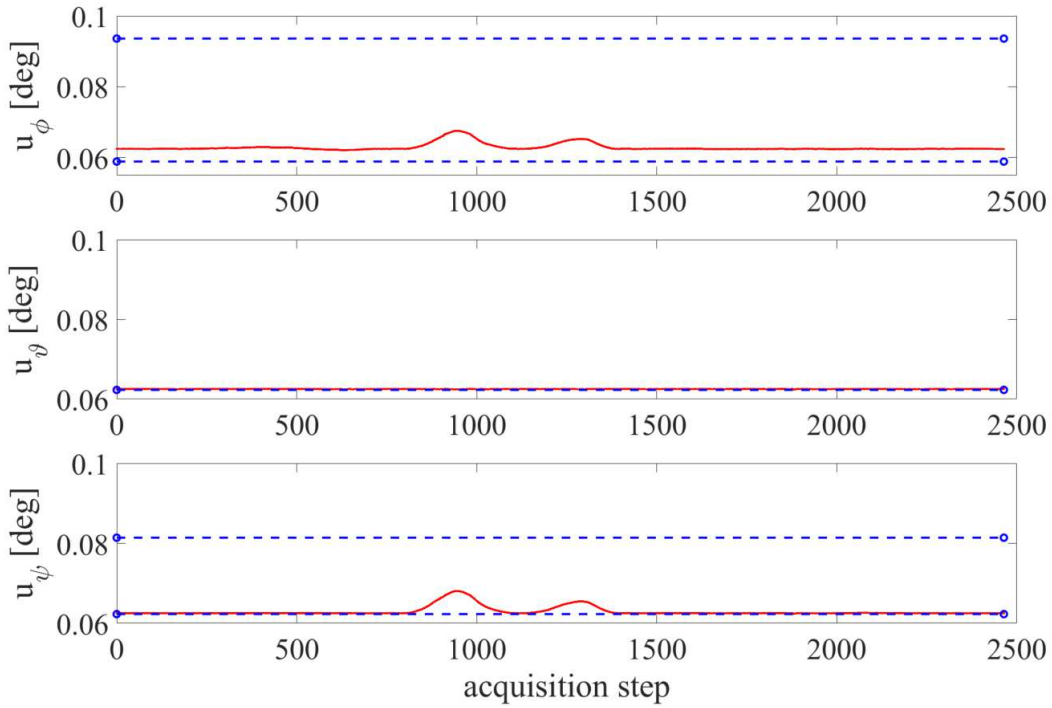

Figure 4.15: Uncertainty profiles of the Euler angles for the attitude maneuver used in the origin calibration procedure, marked with a solid red line. The theoretical maximum and minimum values of the uncertainties are marked with a dashed blue line.

$$
{}^{G}_{MC}\mathbf{R} = \begin{bmatrix} \cos\psi\,\cos\vartheta & \cos\psi\,\sin\phi\,\sin\vartheta - \cos\phi\,\sin\psi & \sin\phi\,\sin\psi + \cos\phi\,\cos\psi\,\sin\vartheta \\ \sin\psi\,\cos\vartheta & \sin\phi\,\sin\psi\,\sin\vartheta + \cos\phi\,\cos\psi & \cos\phi\,\sin\psi\,\sin\vartheta - \cos\psi\,\sin\phi \\ -\sin\vartheta & \cos\vartheta\,\sin\phi & \cos\vartheta\,\cos\phi \end{bmatrix} \tag{4.50}
$$

the uncertainty level on ${}^{G}\widehat{r}_0$ results to be equal to $u_{G_{r_0}} = [0.6, 0.6, 0.5]$ mm.

The uncertainty on the origin position can therefore be evaluated from the combination of $u_{G_{M_0}}$ with $u_{G_{\widehat{r}_0}}$ leading to:

$$u_{G\widehat{O}_B} = [0.7, 0.7, 0.7] \text{ mm}.$$

Uncertainty of the Misalignment Euler Angles

To estimate the uncertainty associated to the misalignment angles in each static acquisition step, the Kline McClintock propagation formula is applied to Equations 4.44: the independent variables in this analysis are the Euler angles provided by the Motion Capture System whose uncertainty maximum values are evaluated at a previous

step of the analysis, and the Euler angles measured by the encoders, whose standard uncertainties $u_{QE} = 0.09$ deg are calculated considering the encoder resolution.

Figure 4.16 shows the mean values of the misalignment angles for each static acquisition step and the associated extended uncertainty band.

After parsing the whole set of measurements, the resulting extended uncertainty of the misalignment angles are:

$$u_{\overline{\phi}_{mis}} = 0.09 \text{ deg}$$
$$u_{\overline{\vartheta}_{mis}} = 0.08 \text{ deg}$$
$$u_{\overline{\psi}_{mis}} = 0.08 \text{ deg}$$

with a confidence level of 99%.

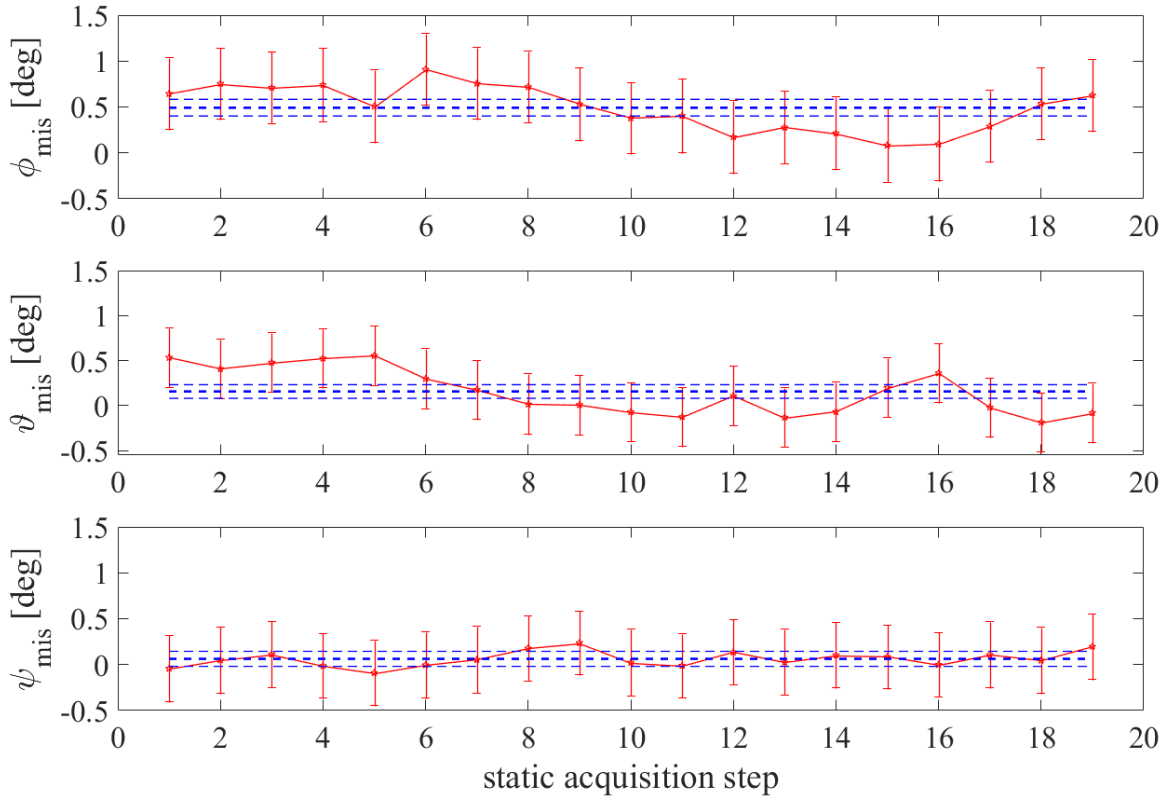

Figure 4.16: Misalignment angles ϕ_{mis} ϑ_{mis} and ψ_{mis} for each static acquisition step, marked with red stars, and the associated extended uncertainty band. The mean values of the misalignment angles and the corresponding extended uncertainty bands are marked with dotted blue lines.

The proposed calibration procedure allows to characterize the Motion Capture system from a metrological point of view. In particular it allows to compensate for sys-

tematic errors affecting the pose estimation of the AM.

The performed analysis shows that, by tracking the three retroreflective markers aboard the AM, the Motion Capture system is able to provide the following estimations:

- the AM pose is determined with a standard uncertainty lower than 0.1 deg;
- the localization of the origin of the AM body frame in global coordinates ${}^{G}\widehat{O}$ is performed with a standard uncertainty of 0.7 mm for each of the 3D coordinates;
- the misalignment angles between the MC reference frame and the body frame are estimated with a maximum extended uncertainty of 0.09 deg for each angle.

4.5 Concluding Remarks

In the present chapter the development of a localization system for the SPARTANS testbed is presented in three main steps, following the development stages of the SPARTANS facility. The incremental OFS-based measurement system is presented and the calibration procedure employed is shown. The performances of the incremental measurement system are assessed and the identification of its main limitations led to the implementation of an external monocular vision system to be employed in a Kalman filter scheme for data filtering. The investigation proved the feasibility of employing the OFS system for obtaining high rate planar pose measurements and the vision system for providing periodic measurement updates at a lower rate.

Finally the Motion Capture system is presented. The system provides the capability of estimating the pose of the micro-satellites operating on the test table ensuring global coverage. A calibration procedure is presented along with the assessment of uncertainty affecting the provided pose estimations.

In the sight of future developments, the Motion Capture enables two important features: (1) given the sub-millimeter accuracy provided in range measurements, it can be used to provide reference pose estimations to be used to assess the micro-satellites GN&C strategies and (2) the measurements provided can be used to reset navigation errors for the on-board instrumentation acting as a GPS-like system within the laboratory.

Chapter 5

Stereoscopic vision-based navigation

5.1 Introduction

The current chapter is aimed at presenting a relative state estimation strategy based on an Extended Kalman Filter that employs only the measurements provided by a stereoscopic vision system. The developed estimation approach is valid under the assumption that the geometry of the target spacecraft is known along with its inertial characteristics. However, its formulation is kept general so that, in a future development phase, it can be extended in order to deal with uncooperative targets.

In the last decades the development of reliable techniques for performing autonomous proximity operations is of great interest in the space community. One of the core components that enable the achievement of this objective is the capability of an active orbiting spacecraft of determining its dynamic state with respect to a target object which may be either artificial or natural, cooperative or not cooperative. This key technology is crucial in the field of spacecraft formation flight, on-orbit servicing, debris removal and space exploration, just to name a few. The need of autonomy is dictated by the fact that, in many practical scenarios, the idea of controlling spaceborne operation from the ground is not feasible due to possible lacks of coverage or delays in the communications.

The selection of both the specific navigation algorithms and the on-board sensors is highly dependent on the considered mission profile. As briefly discussed in Chapter 3, Light Detection and Ranging (LIDAR) systems, which fall within the category of active sensors, in general ensure large operational ranges with constant accuracy level. 3D positions and intensity data can be provided but at the cost of generating large

amount of data. LIDARs can be effectively embedded in relative navigation tasks in poor visibility conditions but their employment as primary navigation sensors is highly dependent on the on board available resources: this makes the applicability of these systems not feasible for satellites with low mass, volume and power budgets.

An efficient alternative to LIDARS is represented by opto-electronic (OE) systems as their range of applicability is much wider since they can be used in applications with power and mass limitations (i.e. small and micro satellites). The measurements provided by these sensors can be processed to perform complete pose estimations: of course, the capability of estimating the relative state is dependent on the distances between the chaser satellite and the target and the dimensions of the target itself.

Both cooperative and uncooperative visual navigation approaches are of high interest to the space community. Even if cooperative pose determination was successfully demonstrated on orbit [54, 55], there is the interest of companies and space agencies to launch and operate satellite formations or, given the economical benefits of on-orbit servicing operations [56], to inspect, maintain and repair already orbiting spacecraft. Usually, monocular techniques are sufficient to operate relative navigation tasks between passively cooperative targets. Many solutions were proposed to this purpose: Orbital Express performed relative navigation tasks at ranges up to 150 m by employing corner cube reflectors enlightened by means of dedicated LEDs [57], the PRISMA mission employed instead LEDs mounted on the target surface obtaining brighter returns on the image plane with respect to any other object in the scene determining the relative pose by solving the P4P problem. As regards the possibility of using stereo techniques, a feasibility study performed by means of numerical simulations is presented in [58].

The need of developing reliable navigation strategies to cope with uncooperative targets is dictated mainly by the fact that the space debris population is steeply increasing, and consequently the collision risk for objects in space. This fact pushes researchers and institutions to develop robust solutions to face this issue in order to prevent the possibility, in the future, that spaceborne operations may be compromised by the occurrence of catastrophic impacts. In general, the relative navigation problem when dealing with uncooperative targets (i.e. space debris, asteroids) can be tackled in two ways: one basic solution consists in the generation of the 3D model of the observed object using the measurements provided by the vision system during an initial

monitoring stage and, subsequently, using those information to perform approaching maneuvers exploiting model-based techniques. Another solution adopts the concept of Simultaneous Localization and Mapping (SLAM) in which the active spacecraft determine its trajectory with respect to the target object while building the 3D map of the observed object. In addition, when dealing with non-cooperative objects, the inertial characteristics of the target are unknowns of the estimation problem.

The work presented in [59] present a solution to solve the SLAM problem for an unknown space target spinning around one of its principal axis of inertia exploiting a smoothing approach. This strategy, if compared to a standard filtering technique, shows better convergence capabilities even if characterized by a heavier computational cost. The algorithm proved to be capable of estimating the complete relative state of the target along with its center of mass and the ratios of the principal components of the inertia matrix.

In [60], the relative state estimation problem is tackled by means of an Iterated Extended Kalman Filter (IEKF) based SLAM approach, exploiting the sole data provided by a stereoscopic vision system. The inertial characteristics of the observed target are identified by means of a Maximum a Posteriori approach that relies on the execution of a user-defined number of IEKFs in parallel, each considering a tentative value for the inertial parameters. In this context, the recent work presented in [61] presents a customized IEKF method for measuring the relative motion parameter along with the inertial characteristics of the target. The estimation architecture of the relative state is similar to [59], but less burdensome thanks to the employment of the IEKF. Also in this case, the rotational dynamical model does not consider external torques applied to the target so that only the inertia ratios are estimated.

A broad and comprehensive overview on cooperative and uncooperative spacecraft pose determination techniques for close-proximity operations is provided in [62].

The chapter is structured as follows: the first part introduces the orbital software simulator that is employed to simulate numerically the behavior of the target and the chaser spacecraft along their orbits. Once the conceptual architecture of the software simulator is outlined, the navigation module, responsible for the implementation of the relative state estimation algorithm, is presented. The performances of the navigation filter are therefore assessed by means of numerical simulations in two different scenarios. First, the estimation capabilities of the navigation system are evaluated for an orbital

scenario. Then, to the purpose of validating the proposed navigation strategy within the SPARTANS ground-based testbed context, a numerical simulation is performed by reproducing in a 3D simulated environment the characteristics of a spacecraft module of the testbed. In particular, the micro-satellite is equipped with custom-made circular markers that allow an easy extraction of relevant features from the acquired images. An image processing procedure is presented to collect measurements by means of the vision system and the performances of the filter are assessed within the simulated laboratory environment. Finally, experimental tests are performed in laboratory to prove the effectiveness of the navigation strategy and to assess its performances.

5.2 The orbital dynamic software simulator

This section presents in more detail the orbital dynamic propagator, written in C/C++, which is employed in the execution of numerical simulations involving one or more spacecraft. In particular it is employed for validating the relative navigation strategy as described in the next sections. This overview is aimed at clarifying the strategy and the methodological approach used in tackling the estimation problem.

The software simulator consists of seven main modules or macro-functionalities:

- the *Attitude and Position Dynamic Propagator* module, which is responsible for propagating the dynamic state of a resident space object through the integration of the dynamics equations;
- the *Sensors* module, which is responsible for the modeling the behavior of the sensors system: in particular, it provides a set of measurements according to the dynamic state of the satellites;
- the *Navigation* module, which provides an estimation of the current dynamic state of the system considering its dynamic behavior and the measurements provided by the *Sensors* module;
- the *Guidance* module, which is responsible for determining the reference trajectory to be followed given the current time instant and dynamic state;
- the *Control* module, which implements the control logic which is required to reach the desired dynamic state given the current state of the system;

- the *Actuators* module, that models the behavior of the actuators system while performing the control actions computed by the *Control* module;
- the *Environment* module, that computes the perturbative forces and torques on the system dynamics deriving from the interaction of the spacecraft with the environment (e.g. aerodynamic drag, radiation pressure, accelerations due to higher harmonics of the gravitational field of the central body).

Since the software simulator is implemented following an object oriented approach, each spacecraft can be completely defined at software level by means of these seven modules. Figure 5.1 shows the top level architecture and the simplified data flow of the simulator. The modules are grouped into two main sections: the PLANT, which represents the real world, and the GN&C system, that represents the decisional core of the spacecraft and that interacts with the real world by means of the sensors and the actuators. According to the notation employed, X refers to the satellite dynamic state obtained by the dynamic propagator, Z is the vector of the measurements, $\hat{X}$ is the output of the navigation module and represents the estimated dynamic state, X_{ref} is the reference state and u_{dist}, u_{calc} and u_{comm} are respectively the disturbances, the computed and the commanded control actions.

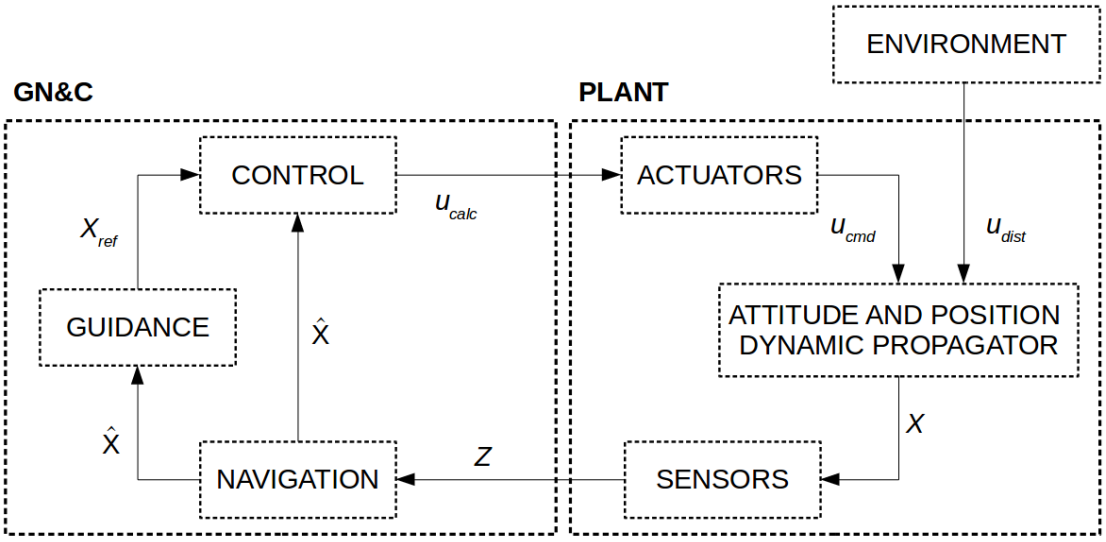

Figure 5.1: Software simulator top level architecture and data flow.

As previously stated, the objective of the current investigation is the estimation of the relative dynamic state of a target spacecraft only using visual data provided

by the stereoscopic system aboard the chaser satellite. The target satellite is modeled as a system whose dynamic is freely evolving along its orbit. On the contrary, the chaser satellite is modeled as an active spacecraft capable of gathering measurements, performing GN&C tasks and commanding control actions. However, since the definition of the control strategies required to perform autonomous maneuvers is beyond the objectives of this work, the main software modules that are exploited in modeling the chaser are the *Dynamic Propagator*, the *Sensors* and the *Navigation* modules.

The translational dynamics of each spacecraft is propagated employing the equation of motion of the Keplerian two body problem:

$$\ddot{r} = -\mu \frac{r}{||r||^3} + u_c + u_d \tag{5.1}$$

where $r = [x,\ y,\ z]^T$ is the position vector in Earth centered inertial frame, μ is the Earth gravitational constant and $u_c,\ u_d$ are respectively the accelerations due to control actions and to disturbances (i.e. orbital perturbations).

The attitude dynamics is propagated by means of the Euler equations:

$$I\dot{\omega} + \omega \times I\omega = \tau_c + \tau_d \tag{5.2}$$

where I is the inertia matrix of the spacecraft, ω the absolute angular velocity and $\tau_c,\ \tau_d$ the resultant of the control torques and disturbance torques respectively.

The attitude of each spacecraft is described using unit quaternions following the vector-scalar notation such that the scalar part is the last component of the vector $q = [q_1, q_2, q_3, q_4]^T$. The attitude kinematics is therefore described by:

$$\dot{q} = \frac{1}{2} Q\omega \tag{5.3}$$

where

$$Q = \begin{bmatrix} q_2 & -q_3 & q_4 \\ -q_1 & q_3 & q_4 \\ q_1 & -q_2 & q_4 \\ -q_1 & -q_2 & -q_3 \end{bmatrix}. \tag{5.4}$$

The task of generating stereo measurements by means of the *Sensors* module requires the knowledge of the true state of the target with respect to the chaser. A dedicated software method is developed to this purpose: in particular, starting from

the dynamic state of the two satellites, it computes the relative state vector in chaser reference frame. This quantity is then provided to the *Sensors* module that, through the perspective projection model, simulates the measurement generated by a stereo camera system. The top level schematic diagram summarizing the process is shown in Figure 5.2.

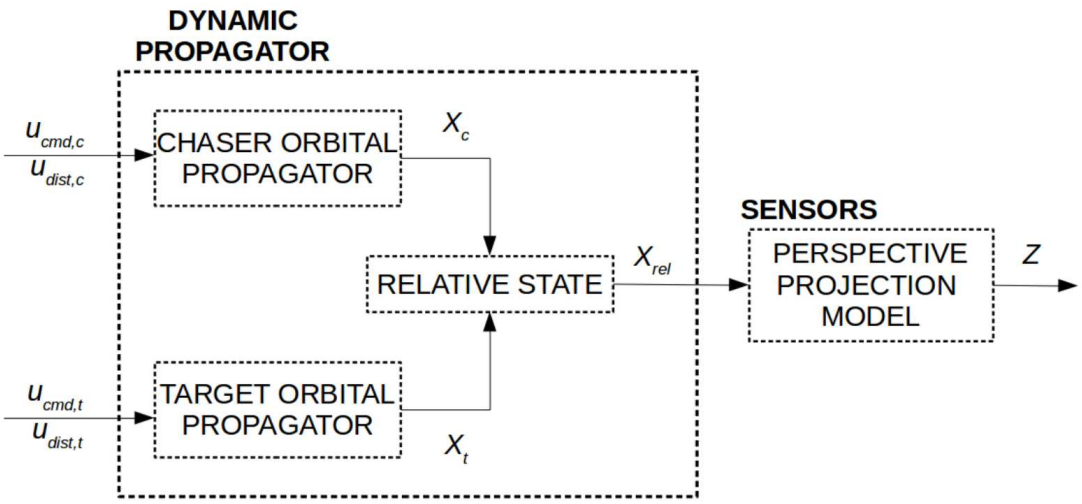

Figure 5.2: Top level schematics and data flow for the generation of simulated stereo measurements.

5.3 Stereoscopic vision-based navigation

This section is aimed at presenting the development of the stereoscopic vision-based relative navigation system. The proposed estimation approach relies on an Extended Kalman Filter (EKF) under the assumption that the geometry of the target and its inertial characteristics are known. Even if these assumptions limit the applicability of the estimation approach to partially known spacecraft, it is reasonable to assume that prior information of the target in many real cases is available at the moment of performing relative GN&C tasks.

A simplified geometry of the target is assumed in order to validate the navigation filter. The target is modeled as a cube-shaped satellite with a side of 2 m. It is provided with a uniform distribution of landmarks and, in particular, 9 feature points are located on each face. Once a feature point resides in the field of view of the stereoscopic system, that point is immediately recognized and associated to the 3D model of the

target spacecraft. As regards the simulated orbital environment, the techniques to be employed in order to recognize and track the feature points are not discussed as their implementation is beyond the scope of this work. However, Section 5.5 introduces the proposed methodology to validate the navigation filter within the SPARTANS context and presents a simple image processing algorithm to extract relevant features from custom-made circular fiducial markers.

5.3.1 Reference frames and adopted notation

In the current scenario two objects are considered: the chaser and the target spacecraft. The standard right-hand Earth centered inertial (ECI) frame I is used: it is defined by the center of the Earth, its X axis points in the vernal equinox direction and the Z axis towards the celestial north pole. C and T are respectively the right-hand chaser fixed reference frame, centered at the chaser center of mass, and the right-hand target fixed frame, centered at the target center of mass. In particular, C is defined such that, when the chaser satellite is three-axis stabilized about its Local Vertical-Local Horizontal (LVLH) frame, the x_C direction is identified by the unit vector directed from the spacecraft radially outward, z_C is normal to the orbital plane, positive in the direction of the instantaneous orbital angular momentum, and y_C that completes the dextral triad.

In the next sections the following notation is used: ρ, $\dot{\rho}$ and $\ddot{\rho}$ are the three-by-one vectors describing respectively the position, the velocity and the acceleration of the target center of mass in chaser frame. Analogously, considering a feature point P_i located onto the target surface, its location with respect to the chaser frame is denoted by ρ_i. The relative angular velocity of the target is denoted by ω, while the attitude of T with respect to C is described by the unit quaternion q. Therefore, the relative state is completely described by means of the state vector X:

$$X = [\rho^T, \dot{\rho}^T, q^T, \omega^T]^T, \qquad X \in \mathbb{R}^{13}. \tag{5.5}$$

5.3.2 Process model

Modeling the relative translational and rotational dynamics is crucial to design a reliable autonomous navigation strategy. Several models are proposed in literature to describe relative orbital translational motions. The most famous is the one proposed

by Clohessy and Wiltshire [1] in which an approximated linear model is proposed under the hypotesis that the distance between two spacecraft is small with respect to their distance from the Earth's center and under the assumption that the target spacecraft is moving on a circular orbit. In order to overcome the limitations introduced by the linearization, a non-linearized model is employed.

Relative translational dynamics

Equation 5.1 is the second order differential equation that governs the motion of a body orbiting around the Earth. The equation can be written for the chaser and the target, in inertial frame I, by replacing the variable r respectively with r_C and r_T:

$$ {}^{I}\ddot{r}_C = -\mu \frac{{}^{I}r_C}{||r_C||^3} + {}^{I}u_C \tag{5.6} $$

$$ {}^{I}\ddot{r}_T = -\mu \frac{{}^{I}r_T}{||r_T||^3} \tag{5.7} $$

where ${}^{I}u_C$ is the vector of the control accelerations acting on the chaser satellite. Since the motion of the target is assumed to evolve freely or, from a more general perspective, the control actions actuated by the target are unknown, the control acceleration term is neglected in equation 5.7.

The position and the acceleration of the target with respect to the inertial frame can also be written as a function of r_C and ρ:

$$ {}^{I}r_T = {}^{I}r_C + {}^{I}\rho \tag{5.8} $$

$$ {}^{I}\ddot{r}_T = -\mu \frac{{}^{I}r_C + {}^{I}\rho}{||{}^{I}r_C + {}^{I}\rho||^3}. \tag{5.9} $$

Equations 5.6 and 5.9 provide the absolute acceleration of the chaser and the target satellite in inertial frame. However, the purpose of the dynamical model is to obtain the relative acceleration in chaser reference frame. Since C is not inertial, apparent accelerations must be considered. Thus, the absolute acceleration of the target in chaser frame can be written as:

$$ {}^{C}\ddot{r}_T = {}^{C}\ddot{r}_C + {}^{C}\ddot{\rho} + {}^{C}\omega_C \times ({}^{C}\omega_C \times {}^{C}\rho) + {}^{C}\dot{\omega}_C \times {}^{C}\rho + 2\,{}^{C}\omega_C \times {}^{C}\dot{\rho} \tag{5.10} $$

where ω_C is the angular velocity of the chaser.

Solving 5.10 for ${}^{C}\ddot{\rho}$ leads to:

$$\begin{aligned} {}^{C}\ddot{\rho} = &- \mu \ {}^{C}_{I}R \left(\frac{{}^{I}r_C + {}^{I}\rho}{||{}^{I}r_C + {}^{I}\rho||^3} - \frac{{}^{I}r_C}{||r_C||^3} + \ {}^{I}u_C \right) - {}^{C}\omega_C \times ({}^{C}\omega_C \times {}^{C}\rho) + \\ &- {}^{C}\dot{\omega}_C \times {}^{C}\rho - 2 \, {}^{C}\omega_C \times {}^{C}\dot{\rho} \end{aligned} \tag{5.11}$$

where ${}^{C}_{I}R$ is the rotation matrix from the inertial to the chaser frame. Equation 5.11 is the second order differential equation that describes the translational orbital dynamics between the two orbiting objects under the Newton's second law assumption.

Relative rotational dynamics

The Euler's equation allows to describe the rotational dynamics of a rigid body. Equation 5.2 can be written for the chaser and the target respectively as:

$$I_C \, {}^{C}\dot{\omega}_C + \ {}^{C}\omega_C \times (I_C \ {}^{C}\omega_C) = \ {}^{C}\tau \tag{5.12}$$

$$I_T \, {}^{T}\dot{\omega}_T + \ {}^{T}\omega_T \times (I_T \ {}^{T}\omega_T) = 0 \tag{5.13}$$

where ${}^{C}\tau$ is the resultant of the external torques acting on the chaser, I_C and I_T are respectively the inertia matrices of the chaser and the target. As for the relative translational dynamics, the torques applied to the target are unknown and therefore the right-hand side of equation 5.13 is assumed to be zero.

The relative angular velocity in chaser reference frame is defined as:

$$\begin{aligned} {}^{C}\omega = \ & {}^{C}\omega_T - {}^{C}\omega_C \\ = \ & {}^{C}_{T}R \, {}^{T}\omega_T - {}^{C}\omega_C \end{aligned} \tag{5.14}$$

where ${}^{C}_{T}R$ is the rotation matrix from the target to the chaser frame.

Combining equations 5.12, 5.13 and 5.14, the relative rotational dynamics can be expressed as:

$${}^{C}\dot{\omega} = - \, {}^{C}_{T}R \, I_T^{-1} \left[{}^{T}\omega_T \times (I_T \, {}^{T}\omega_T) \right] + I_C^{-1} \left[- {}^{C}\tau + {}^{C}\omega_C \times (I_C \, {}^{C}\omega_C) \right]. \tag{5.15}$$

The rotation matrix ${}^{C}_{T}R$ is obtained from the quaternion q describing the orientation of the target with respect to the chaser frame:

$${}^{C}_{T}R = \begin{bmatrix} q_1^2 - q_2^2 - q_3^2 + q_4^2 & 2(q_1q_2 + q_3q_4) & 2(q_1q_3 - q_2q_4) \\ 2(q_1q_2 - q_3q_4) & -q_1^2 + q_2^2 - q_3^2 + q_4^2 & 2(q_2q_3 + q_1q_4) \\ 2(q_1q_3 + q_2q_4) & 2(q_2q_3 - q_1q_4) & -q_1^2 - q_2^2 + q_3^2 + q_4^2 \end{bmatrix}^T \tag{5.16}$$

and the relative attitude kinematics is described by:

$$\dot{q} = \frac{1}{2} Q \omega \tag{5.17}$$

where

$$Q = \begin{bmatrix} q_2 & -q_3 & q_4 \\ -q_1 & q_3 & q_4 \\ q_1 & -q_2 & q_4 \\ -q_1 & -q_2 & -q_3 \end{bmatrix}. \tag{5.18}$$

5.3.3 Observation model

The current section introduces the observation model which is required to extract informations from the acquired stereo images.

The chaser satellite is provided with two cameras in a stereoscopic configuration. The stereo rig consists of two parallel cameras with focal length f, separated by a baseline b. The right camera frame R and the left camera frame L are respectively centered at the optical center of their corresponding device. For each camera frame, the x direction is defined by the unit vector that joins L to the R origin, the z direction is aligned with the camera optical axis and points towards the image plane, while the y direction completes the dextral reference frame.

Often, to simplify the estimation process, one of the two camera frames is assumed to be coincident with the chaser reference frame. In order to keep the employed formulation as general as possible, the current work considers the position and the orientation of both cameras distinct from C. In particular the right camera R is placed along the y_C axis at a distance of 1 m from the chaser center of mass, while the left camera is is located at a distance of 1 m along y_C and of b along z_C. Moreover, L and R are rotated such that their optical axes are aligned with the y_C direction which is, in case of a three-axis stabilized chaser, the direction identified by the spacecraft velocity.

In this context, the rotation matrix that transforms coordinates from the chaser to the left/right reference frame is:

$${}^{L}_{C}R = {}^{R}_{C}R = \begin{bmatrix} 0 & 0 & -1 \\ -1 & 0 & 0 \\ 0 & 1 & 0 \end{bmatrix}. \tag{5.19}$$

Moreover, the position of R and L in chaser frame are respectively defined by ${}^{C}t_R = [0\ 1\ 0]^T$ and ${}^{C}t_L = [0\ 1\ b]^T$.

The schematic layout showing the adopted stereo configuration is shown in Figure 5.3.

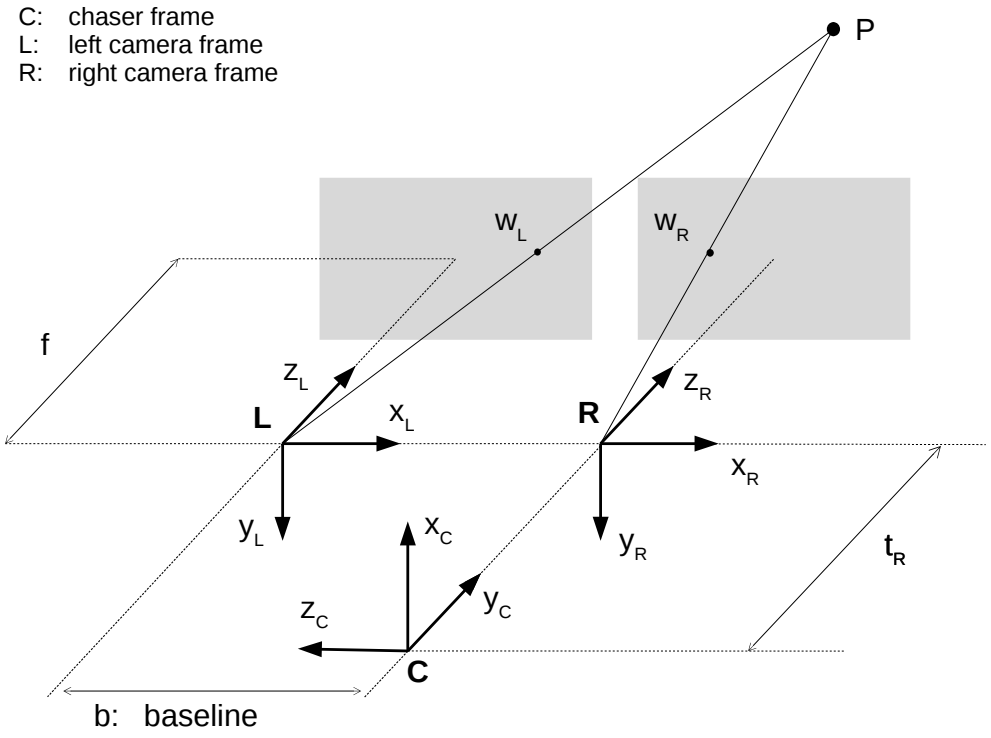

Figure 5.3: Stereo rig model employed in the numerical simulations.

Considering the pinhole camera model and the and exploiting the perspective projection model, a 3D feature point can be projected onto the image plane. By following this approach, each landmark on the target surface can be tracked and expressed in the 2D image planes.

Let P_i be a landmark being tracked by the vision system. Its coordinates with respect to the target reference frame are known as soon as the point is univocally recognized. To exploit the perspective projection model, the coordinates of P_i must be transformed to right camera coordinates to determine ${}^{R}\rho_i = [x_i,\ y_i,\ z_i]^T$:

$$ {}^{R}\rho_i = {}^{R}_{C}R\left({}^{C}\rho + {}^{C}_{T}R\ P_i - {}^{C}\ t_R\right) \tag{5.20} $$

Therefore, the projection of P_i onto the right camera are determined as:

$$\begin{aligned} u_{R,i} &= f\frac{x_i}{z_i} \\ v_{R,i} &= f\frac{y_i}{z_i} \end{aligned} \tag{5.21}$$

and for the left camera:

$$\begin{aligned} u_{L,i} &= f\frac{x_i + b}{z_i} \\ v_{L,i} &= f\frac{y_i}{z_i} \end{aligned} \tag{5.22}$$

Further information can be obtained by considering the optical flow. A formulation that relates the 3D motion to the optical flow is derived in [63]. In particular, the formulation exploits the fact that every point of a rigid body share the six motion parameters relative to a viewer-centered reference frame. This relationship can be written by means of the following equations:

$$\begin{bmatrix} \dot{u}_{R,i} \\ \dot{v}_{R,i} \end{bmatrix} = \begin{bmatrix} \frac{1}{z_i}A(u_{R,i}, v_{R,i}) & B(u_{R,i}, v_{R,i}) \end{bmatrix} \begin{bmatrix} {}^R\dot{\rho} \\ {}^R\omega \end{bmatrix} \tag{5.23}$$

and

$$\begin{bmatrix} \dot{u}_{L,i} \\ \dot{v}_{L,i} \end{bmatrix} = \begin{bmatrix} \frac{1}{z_i}A(u_{L,i}, v_{L,i}) & B(u_{L,i}, v_{L,i}) \end{bmatrix} \begin{bmatrix} {}^L\dot{\rho} \\ {}^L\omega \end{bmatrix} \tag{5.24}$$

where $[{}^R\dot{\rho},\ {}^R\omega]$ and $[{}^L\dot{\rho},\ {}^L\omega]$ are the relative translational and angular velocity of the target with respect to the right and left camera frames respectively. It must be noticed that the relative velocities that appear in equation 5.23 and 5.24 are dependent on the the velocity components of the relative state vector, i.e. ${}^C\rho$ and ${}^C\omega$. The matrices A and B are dependent on the 2D positions of the feature points and on the focal length. They are defined as:

$$A(u, v) = \begin{bmatrix} -f & 0 & u \\ 0 & -f & v \end{bmatrix} \tag{5.25}$$

$$B(u, v) = \begin{bmatrix} \frac{uv}{f} & -f - \frac{u^2}{f} & v \\ f + \frac{v^2}{f} & -\frac{uv}{f} & -u \end{bmatrix}. \tag{5.26}$$

From a practical point of view, the optical flow is determined by considering the instantaneous location of a feature point in two consecutive images. Thus, considering the cameras frame rate, the image velocity can be computed.

The last information that is exploited in the observation model is the disparity as it allows, through triangulation, to obtain information about the depth at which a feature point is located with respect to the camera frames. In particular, it is simply computed as the difference between the u-coordinate of a feature point in left and right camera frames:

$$d_i = u_{L,i} - u_{R,i}. \tag{5.27}$$

The developed observation model allows to relate, for each time instant and for each tracked feature point, the vector of the measurements $\hat{z}_i$ to the relative state vector X:

$$\hat{z}_i = h(X) = [u_{R,i}\ v_{R,i}\ u_{L,i}\ v_{L,i}\ \dot{u}_{R,i}\ \dot{v}_{R,i}\ \dot{u}_{L,i}\ \dot{v}_{L,i}\ d_i]^T. \tag{5.28}$$

5.3.4 Filtering procedure

The process and the observation models derived in the previous sections show that the relative state estimation problem is strictly non-linear. In this case, the employment of an optimal estimator is not feasible from a computational point of view, leading to the necessity of adopting an approximated estimation scheme.

The Kalman Filter (KF), introduced in the 1950s by Rudolph E. Kalman, is a technique for filtering and prediction in linear systems that allows to obtain the state estimate that minimizes the mean square error [64]. The KF, however, is not suitable to be employed with non-linear dynamic and/or observation equations. The Extended Kalman Filter (EKF) provides a solution that allows to overcome this linearity assumption: the non-linear equations are linearized by means of a first-order Taylor expansion making the KF structures available to be employed with the non-linear dynamical system.

The navigation filter's goal is to obtain an estimate of the system state X based on the measurement vector $\hat{z}$. The non-linear dynamics of the filter is described by the process and the observation model respectively as:

$$\dot{X} = f(X) + w \tag{5.29}$$

$$\hat{z} = h(X) + v \tag{5.30}$$

where the vectors w and v are respectively the process and the measurement noise modeled as white, gaussian, independent random processes with zero mean. Their

covariance matrices are defined as follows:

$$Q = E[ww^T] \tag{5.31}$$

$$R = E[vv^T]. \tag{5.32}$$

The following notation is here adopted: X_k^- is the a priori state estimate at step k obtained from the estimation process at the previous time instant, X_k^+ is the a posteriori state estimate at step k given the measurement z_k, and P_k^-, P_k^+ are their corresponding error covariance matrices.

The first operation to be performed to instantiate the filtering algorithm is the definition of the initial state X_0 and its corresponding covariance matrix P_0. These quantities are employed to initialize the a priori state X_k^+ and its corresponding error covariance matrix P_k^+.

Once the filter is initialized, the filtering strategy can be iterated for any time instant k. Two subsequent steps are executed: (1) the Time Update step and (2) the Measurement Update step.

Time Update step

In the time update step the process model is exploited to obtain a forecast of the expected state at the next time instant. In particular the expected state vector is computed using the discrete time version of equation 5.29:

$$X_{k+1}^- = f(X_k^+). \tag{5.33}$$

The evaluation of the Jacobian of the process equation f with respect to the state vector X is needed to propagate the error covariance matrix:

$$F_k = \left.\frac{\partial f}{\partial X}\right|_{X=X_{k+1}^-}. \tag{5.34}$$

From a practical point of view, in this work the Jacobians are computed numerically using the software tool described in [65]. The forecast error covariance matrix is therefore computed as:

$$P_{k+1}^- = F_k P_k^+ F_k^T + Q. \tag{5.35}$$

Measurement Update step

The measurement update step is also called data assimilation step. For each time instant k, the current step exploits two information: the forecast state vector X_{k+1}^- along with its error covariance matrix P_{k+1}^-, and the vector of the measurements $\hat{z}$ with covariance R. The correction to the estimated state is performed as follows:

$$X_{k+1}^+ = X_k^- + K\left(\hat{z} - h(X)|_{X=X_k^-}\right) \tag{5.36}$$

where K is the Kalman gain matrix:

$$K = P_{k+1}^- H^T \left(HP_{k+1}^- H^T + R\right)^{-1} \tag{5.37}$$

and H is the Jacobian matrix of the measurement equations:

$$H = \left.\frac{\partial h}{\partial X}\right|_{X=\hat{X}}. \tag{5.38}$$

Finally, the error covariance matrix is updated:

$$P_{k+1}^+ = (I - KH)P_{k+1}^-. \tag{5.39}$$

The outputs of the measurement step are X_{k+1}^+ and P_{k+1}^+ and they constitutes the inputs for the time update step at the subsequent time instant.

5.4 Numerical simulations: orbital scenario

In this section the assessment of both the convergence and the robustness of the navigation filter through numerical simulations is presented.

The chaser and the target spacecraft are considered to be orbiting around the Earth on a circular equatorial Low Earth Orbit (LEO) at an altitude of 500 km (Figure 5.4).

The cameras mounted aboard the chaser have a focal length of 8.1 cm and a resolution of 2048 x2048 pixels. The two cameras are separated by a baseline of 1 m. The choice of the camera characteristics is performed by taking into account sensors available on the market at a reasonable cost. The minimum range at which a feature object can be seen from both the cameras of the stereo rig is of about 5 m. This value can be considered acceptable in the scenario under investigation: in fact, while performing an inspection maneuver, estimating the motion parameters of the target does not require

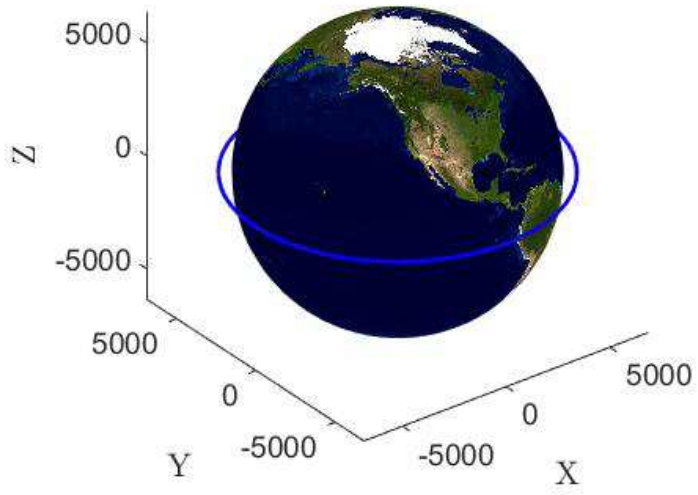

Figure 5.4: Equatorial orbital trajectory of the chaser and the target spacecraft defined for the numerical simulations.

to perform any close proximity operations (e.g. docking). If the objective is to perform a complete docking maneuver, either the design of the stereoscopic system may be modified to fulfill the mission requirements or the final phases of the approaching maneuver may be handled by means of an alternative navigation approach (e.g. by means of monocular techniques).

To initialize the filter, the covariance matrices Q, R and P have to be defined. As regards the measurement covariance matrix, the noise introduced by the optical sensors can be quantified in 1 pixel [66]. Considering that the vision system is assumed to acquire data at a frame rate of 10 fps, the matrix R is initialized as:

$$R = \text{diag}\left([1,\ 1,\ 1,\ 1,\ 200,\ 200,\ 200,\ 200,\ 2]\right) \text{pixel}^2.$$

The process covariance matrix Q has to be selected to ensure the convergence of the filter and, in particular, it is defined as a diagonal matrix composed by:

$$\begin{aligned}
\sigma_\rho^2 &= 10^{-2} \cdot [1,\ 1,\ 1]\ \text{m}^2 \\
\sigma_{\dot{\rho}}^2 &= 10^{-4} \cdot [1,\ 1,\ 1]\ \text{m}^2/\text{s}^2 \\
\sigma_q^2 &= 10^{-2} \cdot [1,\ 1,\ 1,\ 1] \\
\sigma_\omega^2 &= 0.25 \cdot [1,\ 1,\ 1]\ \text{deg}^2/\text{s}^2.
\end{aligned}$$

The state covariance matrix is initialized such that it is equal to the process covariance matrix: $P = Q$.

In the performed simulations, the chaser is assumed to be three-axis stabilized about the Euler-Hill reference frame (LVLH frame). Moreover, the state of the chaser is assumed to be known thanks to the information provided by the on board position and attitude determination subsystem.

The initial relative state X is defined by:

$$\begin{aligned} \rho &= [0,\ 40,\ 0]\ \text{m} \\ \dot{\rho} &= [0,\ 0,\ 0]\ \text{m/s} \\ q &= [0,\ 0,\ 0,\ 1] \\ \omega &= [0.1,\ 0,\ 0.1]\ \text{deg/s} \end{aligned}$$

while the initial guess provided to the EKF is:

$$\begin{aligned} \rho_0 &= [0.4,\ 42,\ 0.2]\ \text{m} \\ \dot{\rho}_0 &= [0,\ 0,\ 0]\ \text{m/s} \\ q_0 &= [0,\ 0,\ 0,\ 1] \\ \omega_0 &= [0,\ 0,\ 0]\ \text{deg/s}. \end{aligned}$$

The performance of the filter are assessed by evaluating the tracking error for an acquisition period of 100 s. In particular, the errors on the position, the translational velocity and the angular velocity are computed as the difference between the estimated quantities and their reference values, while the attitude tracking error is converted from quaternions to the Euler angles representation in order to improve the readability of the results.

Figures 5.5, 5.6, 5.7 and 5.8 show respectively the tracking error on the estimated position, translational velocity, attitude and angular velocity. The obtained results show the convergence of the filter: in particular, the tracking error on both the position and the attitude quickly converge to zero. The tracking error on the velocities show a slower convergence, probably due to a poor coupling of the measurement equations with the rotational and translational velocity.

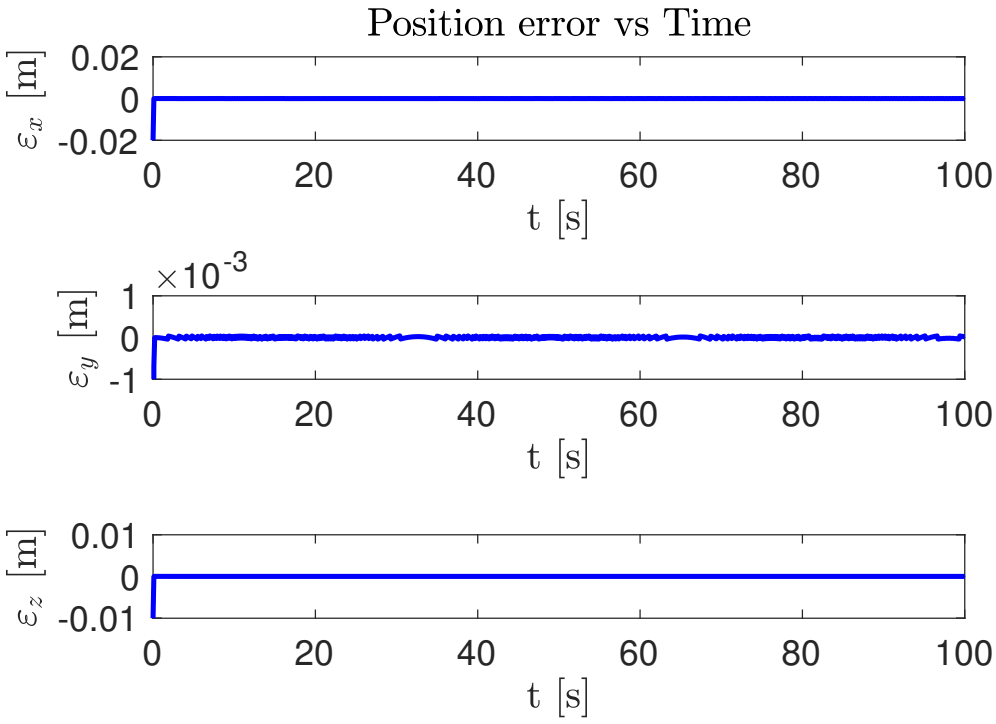

Figure 5.5: Relative position error.

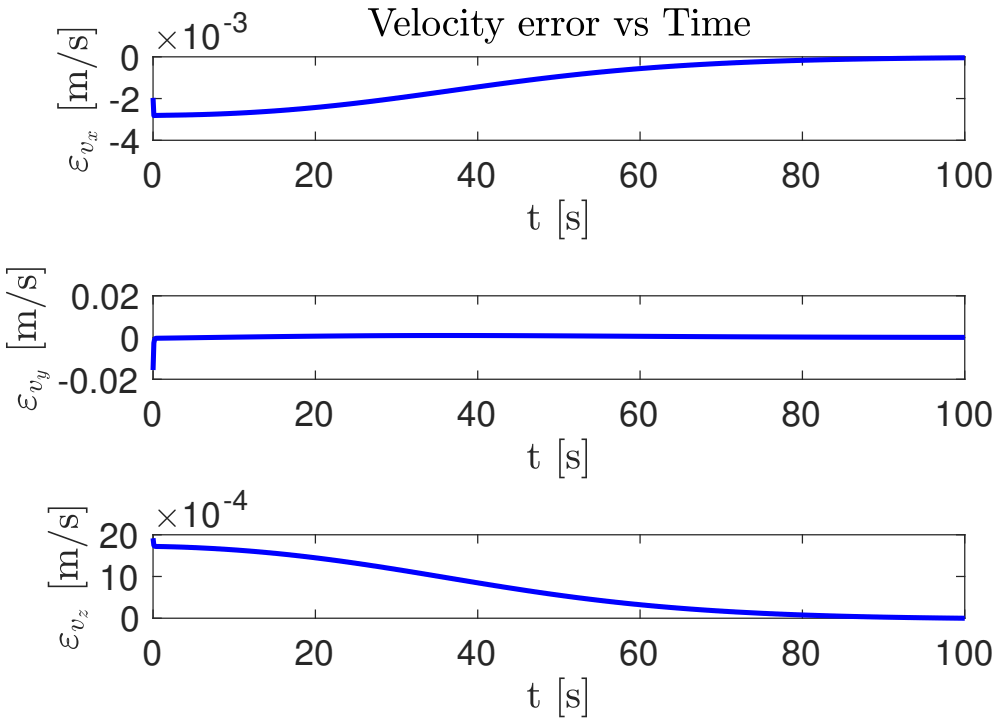

Figure 5.6: Relative velocity error.

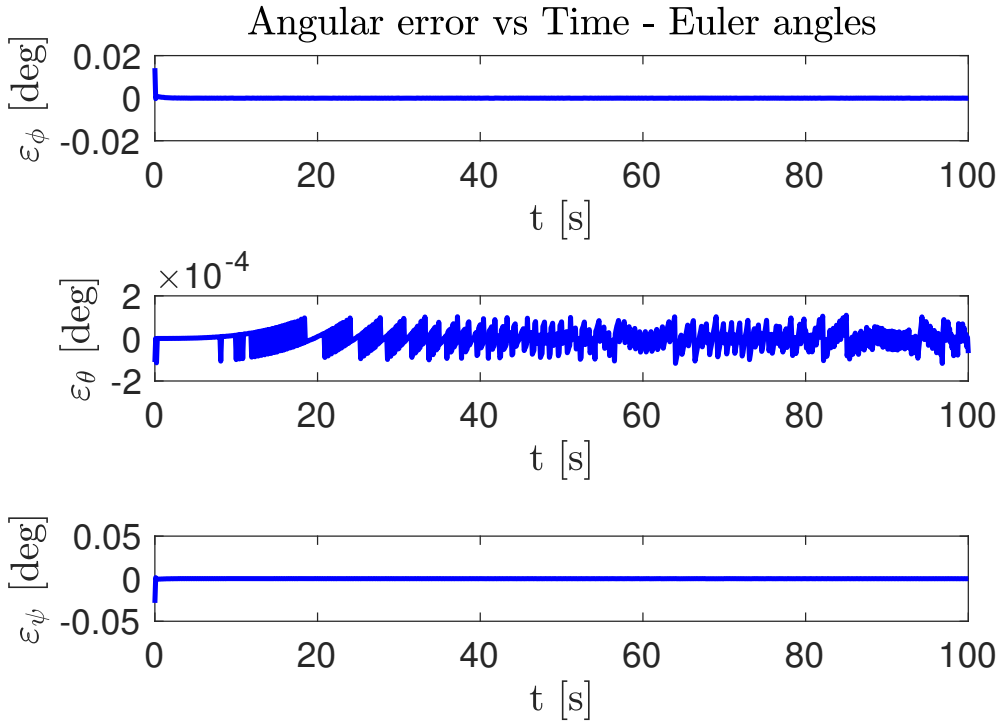

Figure 5.7: Relative attitude error.

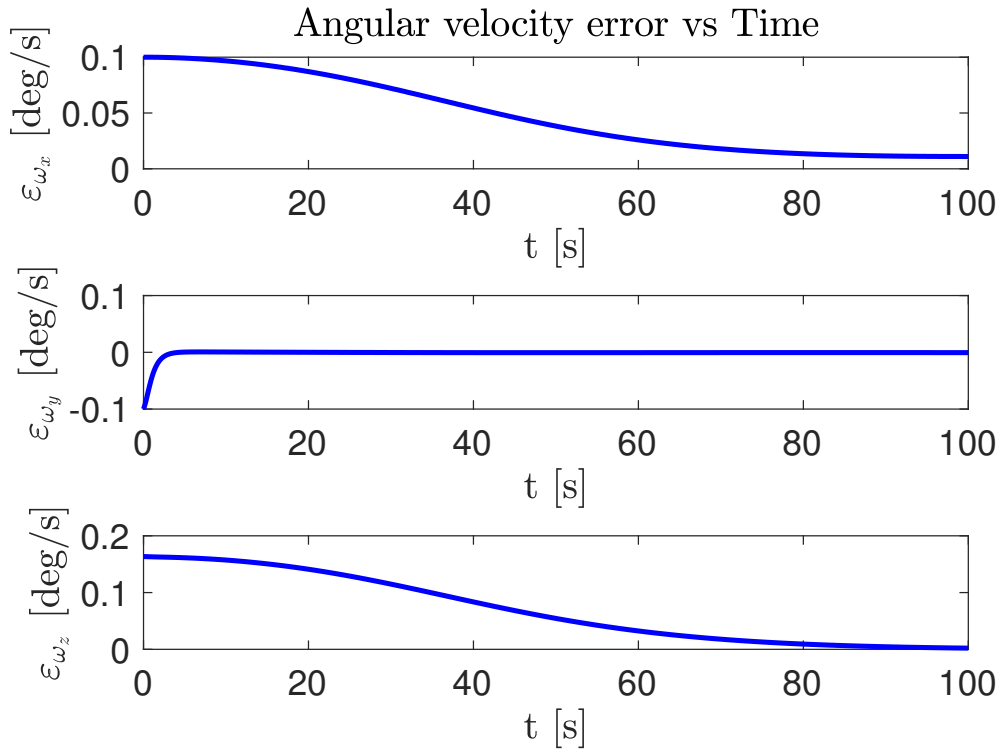

Figure 5.8: Relative angular velocity error.

In order to test the robustness of the navigation filter, several simulations are per-

formed with an increasing imposed measurement noise. Figures 5.9, 5.10, 5.11 and 5.12 show the tracking errors when the measured projections of the 3D landmarks onto the image planes are affected by a zero-mean, white, gaussian random noise with a standard deviation of 1 pixel. Also in this case, the convergence of the filter is guaranteed and, as expected, the error starts assuming a more oscillating behavior. In general, this effect is more evident as the imposed measurement noise increases and it can be partially limited by properly tuning the process covariance matrix.

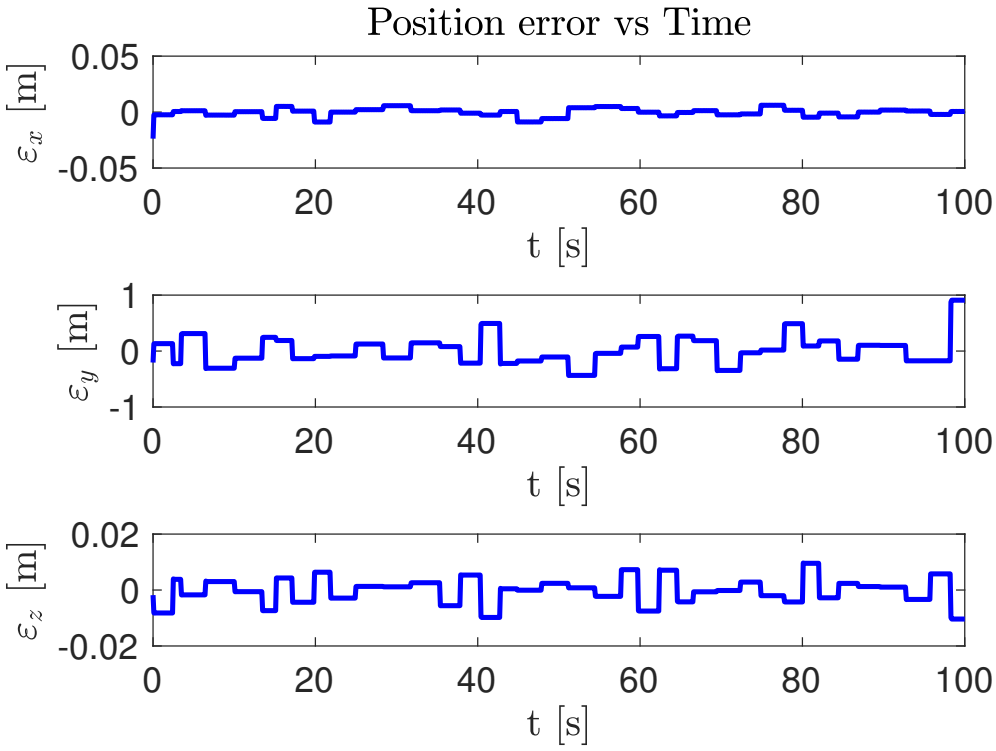

Figure 5.9: Relative position error. A random gaussian noise with a standard deviation of 1 pixel is imposed to the measured landmarks 2D positions.

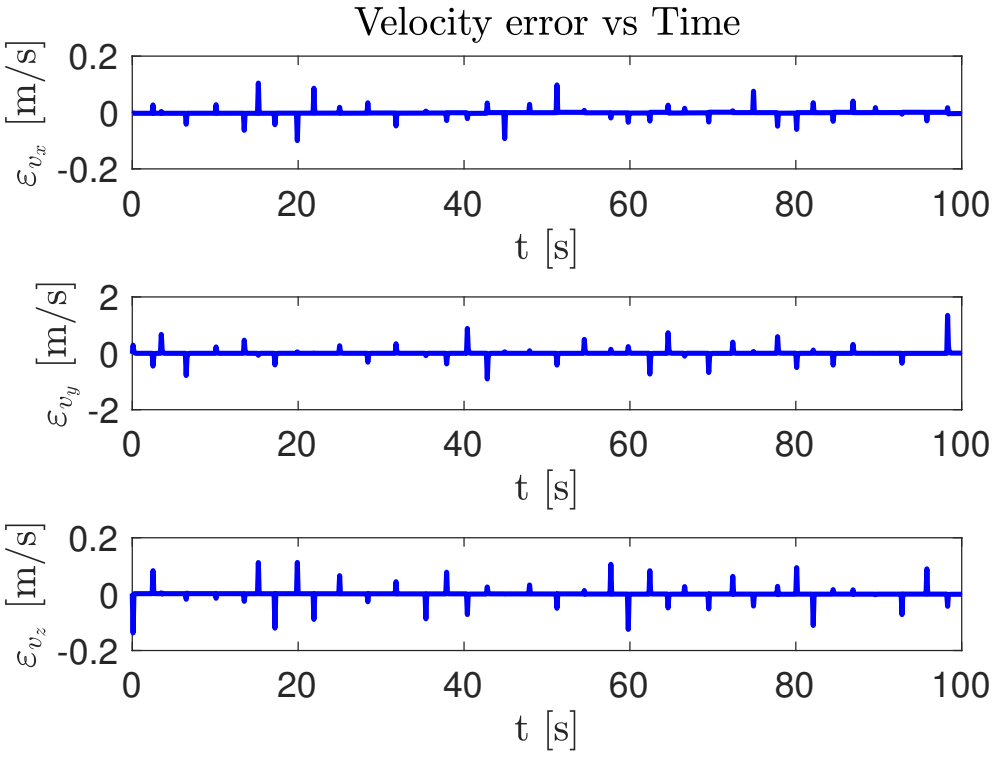

Figure 5.10: Relative velocity error. A random gaussian noise with a standard deviation of 1 pixel is imposed to the measured landmarks 2D positions.

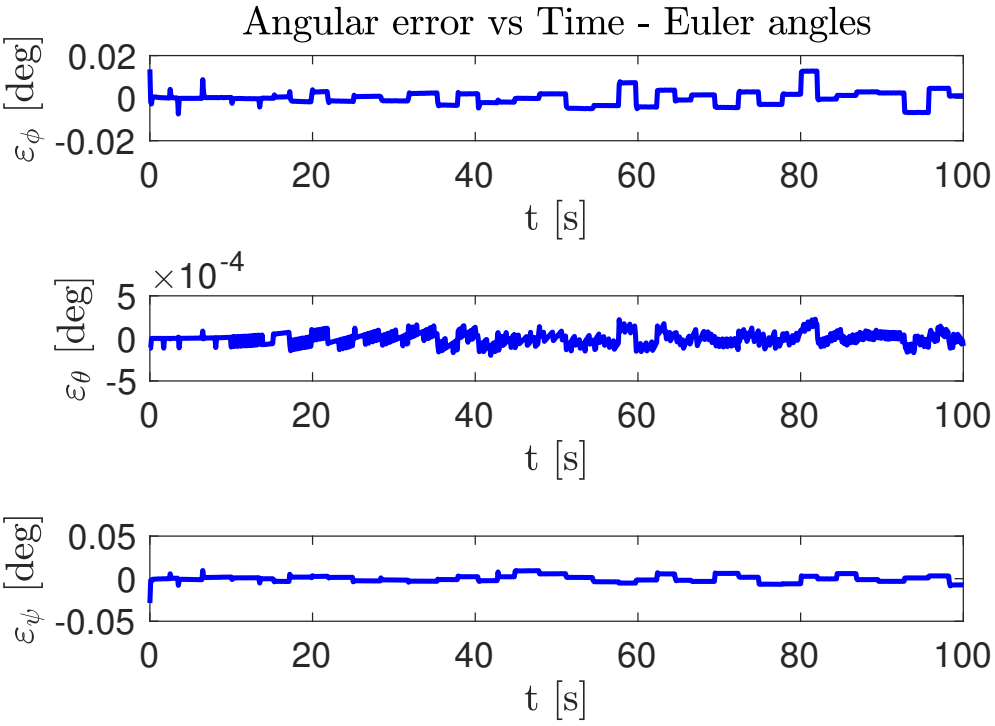

Figure 5.11: Relative attitude error. A random gaussian noise with a standard deviation of 1 pixel is imposed to the measured landmarks 2D positions.

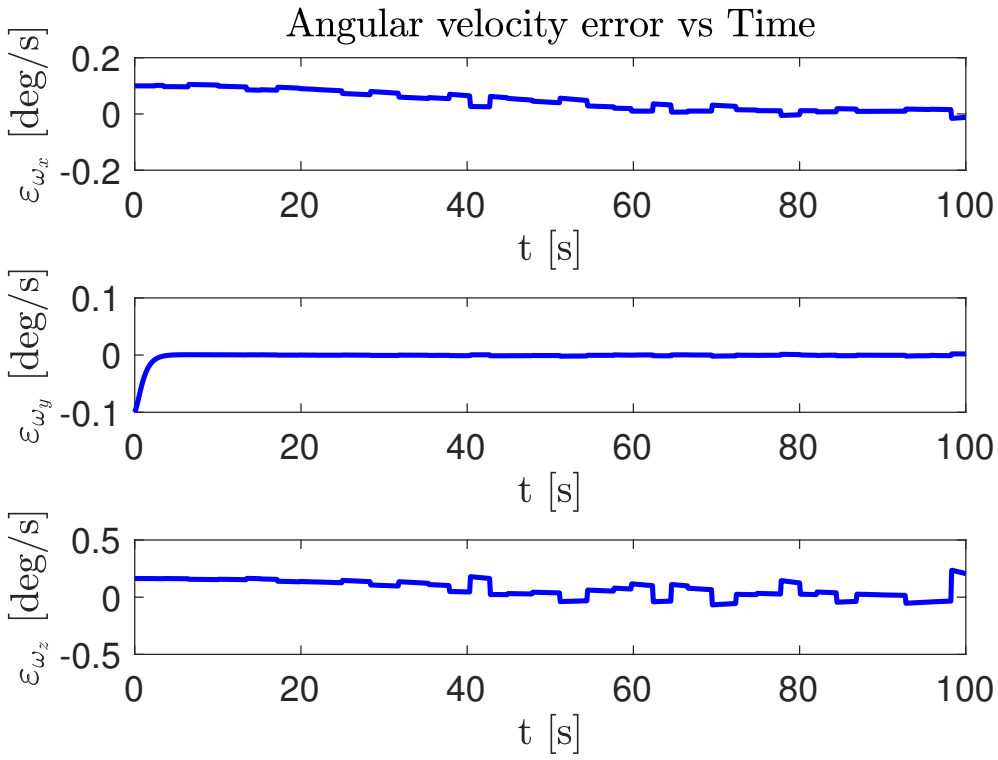

Figure 5.12: Relative angular velocity error. A random gaussian noise with a standard deviation of 1 pixel is imposed to the measured landmarks 2D positions.

5.5 Numerical simulations: towards laboratory testing

Once the navigation filter is validated in a simulated orbital scenario, the development pipeline requires the experimental validation of the filter using the SPARTANS spacecraft simulator. This section presents the steps performed to reach this objective and, in particular, investigates the performances of the navigation filter in a 3D simulated environment which is representative of the laboratory testing conditions. It must be said that, at its current development stage, the SPARTANS testbed features one complete spacecraft module, while the second is being built. Therefore, the execution of coordinated maneuvers is not possible at the moment.

5.5.1 Definition of the testing scenario

The navigation filter, as previously discussed, requires the knowledge of the geometry of the observed target. The simplest way to accomplish this objective is by

providing the target with a known pattern that can be univocally recognized by the vision system.

The square-shaped markers described in Chapter 3, even if effective, are not taylored to be employed in an on-line estimation scheme since the required image processing for the recognition phase is quite demanding from a computational point of view. Moreover, each marker provides an excessively high number of landmarks that, within the filtering scheme, can lead to large observation matrices with a consequent increase in the time required to perform the measurement update phase. A solution that overcomes these downsides consists in the employment of circular fiducial markers [29,67]. Circular markers are passive and their geometric properties ensure that the locations of their centroids are invariant to three rotational and one rotational degrees of freedom, and almost invariant with respect to the remaining two degrees of freedom. Also in this case, the dimensions of the markers have to be selected in order to maximize the visibility of the circles while considering the size of the available area on the spacecraft surfaces. According to the SPARTANS micro-satellites dimensions, three circular markers are placed on each lateral face of the AM. These three types are all different and, in particular, they can be distinguished according to their type:

Type A marker: it consists of two concentric contrasting circles with a radial ratio of 5:3. The outer and the inner circles are respectively withe and black;

Type B marker: it consists of a black circle placed within a white square that provides the contrast necessary to identify correctly the circle on a dark background;

Type C marker: it consists of a white circle.

Each face of the spacecraft is therefore univocally identified by defining a structure, called pattern, that considers the mutual locations of the three markers. Since the SPARTANS micro-satellites have a limited allowed angular range in terms of roll and pitch, the developed patterns can be identified with no ambiguity. Moreover, the number of markers on each face is kept low in order to ensure a low dimension of the matrices involved in the data assimilation of the filter while providing enough information to estimate the relative dynamic state.

The circle recognition phase is fundamental within the filtering scheme and, in sight of a real-time implementation of the filter, the recognition must be fast and reliable.

The ellipse detector presented in [68] is therefore employed as it proves to be faster with respect to common state-of-the-art algorithms and to work also in case of partial occlusions.

The image processing algorithm employed to extract relevant landmarks from the acquired images of the micro-satellite can be subdivided into the following steps:

1. Image acquisition and rectification.

2. Circle detection: for each image all the circular shapes are searched exploiting the ellipse detector described in [68].

3. Markers recognition: each detected circle is processed with the aim of avoiding false matchings between 2D and 3D coordinates. This operation exploits the a priori knowledge on the characteristics of the markers: markers A are recognized if two circles in the image plane are concentric and the ration between their area is comprised within a given range, while the recognition of markers B and C involves the evaluation of the mean intensity of the pixels contained within the detected circles. False detections are filtered out thanks to a robust hypothesis-verification testing approach.

4. Pattern recognition: when three markers placed on the same face are correctly recognized, the pattern can be initialized. This leads to the identification of the face on which the markers are placed and, consequently, the correct association of the 2D centroids to their 3D coordinates expressed in the target reference frame. This operation is required only when a new face of the target appears. Once a pattern is already initialized, instead, it is tracked along its trajectory allowing also to extract information about the image velocities.

5. All the measurements gathered are passed to the navigation filter for the relative state estimation.

Figure 5.13a shows the AM 3D model, modeled as a black box and equipped with the circular markers, as it is implemented in the simulated laboratory environment. All the geometric characteristics of the 3D model are representative of the real module. Figure 5.13b show an intermediate step in the identification of the circular markers: the green circles show the candidate circles which possibly describe a marker and, in

particular, it can be seen that false detections occur. The subsequent image processing steps are devoted to filtering out false detections.

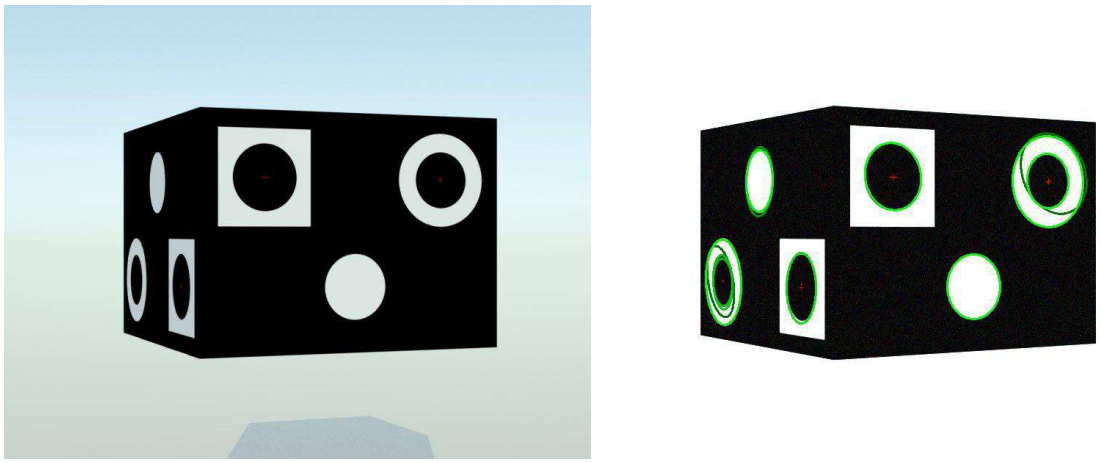

(a) Synthetic image of the AM.

(b) Intermediate image processing output. The green circles show possible candidates to be recognized as markers.

Figure 5.13: 3D model of the Attitude Module, equipped with contrasting circular markers, employed for visual relative navigation.

5.5.2 Numerical simulations: laboratory scenario

For the reasons discussed at the beginning of Section 5.5, the validation of the navigation filter is performed considering a simulated 3D environment, as representative as possible of the actual laboratory configuration. In contrast to the orbital simulations, the system dynamics is simulated in a 3D virtual environment. The chaser satellite is assumed to be static and observing the target satellite which is in turn spinning about the local vertical. Since in this case the filter is applied to a ground scenario, the process model of the filter is modified accordingly in order to neglect all the orbitals terms appearing in equations 5.11 and 5.15. The observation model is instead unaffected by the modified operative scenario.

The stereo rig employed to acquire stereo images consists of two identical parallel cameras with a resolution of 800 x618 pixels, separated by a baseline of 20 cm and with a frame-rate of 48 fps.

For the simulations presented in this section, the relative state of the target is expressed in the right camera frame as it is defined in Figure 5.3.

Two different types of simulations are performed: (1) in the first simulations the

filter is provided with an initial guess on the relative state which is affected by a gross error in the knowledge of the orientation and the angular velocity in order to assess the convergence of the filter dynamics, while (2) in the second part of the simulations the initial guess provided to the filter is close to the actual relative state in order to assess the effects of the measurement noise on the filter dynamics.

First simulated scenario: large initial error

In the first scenario the filter is required to handle a gross error as regards the initial guess on the relative state. The measurement covariance matrix R is initialized as:

$$R = \text{diag}\left([1,\ 1,\ 1,\ 1,\ 4608,\ 4608,\ 4608,\ 4608,\ 2]\right) \text{pixel}^2.$$

while the process covariance matrix Q, selected to ensure the convergence of the filter, is defined as a diagonal matrix composed by:

$$\begin{aligned}
\sigma_\rho^2 &= 10^{-2} \cdot [1,\ 1,\ 1]\ \text{m}^2 \\
\sigma_{\dot\rho}^2 &= 10^{-2} \cdot [1,\ 1,\ 1]\ \text{m}^2/\text{s}^2 \\
\sigma_q^2 &= 2.5 \cdot 10^{-3} \cdot [1,\ 1,\ 1,\ 1] \\
\sigma_\omega^2 &= 10^{-2} \cdot [1,\ 1,\ 1]\ \text{deg}^2/\text{s}^2.
\end{aligned}$$

The state covariance matrix, also in this case, is initialized such that it is equal to the process covariance matrix: $P = Q$.

The initial relative state X is defined by:

$$\begin{aligned}
\rho &= [-0.2,\ 0,\ 2.7]\ \text{m} \\
\dot\rho &= [0,\ 0,\ 0]\ \text{m/s} \\
q &= [0,\ 1,\ 0,\ 0] \\
\omega &= [0,\ -72,\ 0]\ \text{deg/s}
\end{aligned}$$

while the initial guess provided to the EKF is:

$$\begin{aligned}
\rho_0 &= [0.1,\ 0.2,\ 3]\ \text{m} \\
\dot\rho_0 &= [0.2,\ 0,\ 0.3]\ \text{m/s} \\
q_0 &= [0,\ 0,\ 0,\ 1] \\
\omega_0 &= [0,\ 0,\ 0]\ \text{deg/s}.
\end{aligned}$$

Figures 5.14, 5.15, 5.16 and 5.17 show respectively the tracking error on the estimated position, translational velocity, attitude and angular velocity. The obtained results show the fast convergence of the filter for the estimated position. As in the orbital case, the tracking error on the translational and rotational velocities converges slowly to zero. Even if the filter is initialized with a large error on both the angular velocity and the attitude, it proves to be efficient in converging around the actual relative state. However, some fluctuations in the error time profiles are still visible. The requirement of ensuring the convergence of the filter leads to give a major weight to the measurements that, as shown by the oscillating behavior of the error, introduce a large uncertainty on the estimated relative state. Table 5.1 summarizes the performances of the filter in the considered scenario by showing the mean value, the standard deviation and the maximum value of the tracking error on the 12 motion parameters in the last 3 s of the simulation.

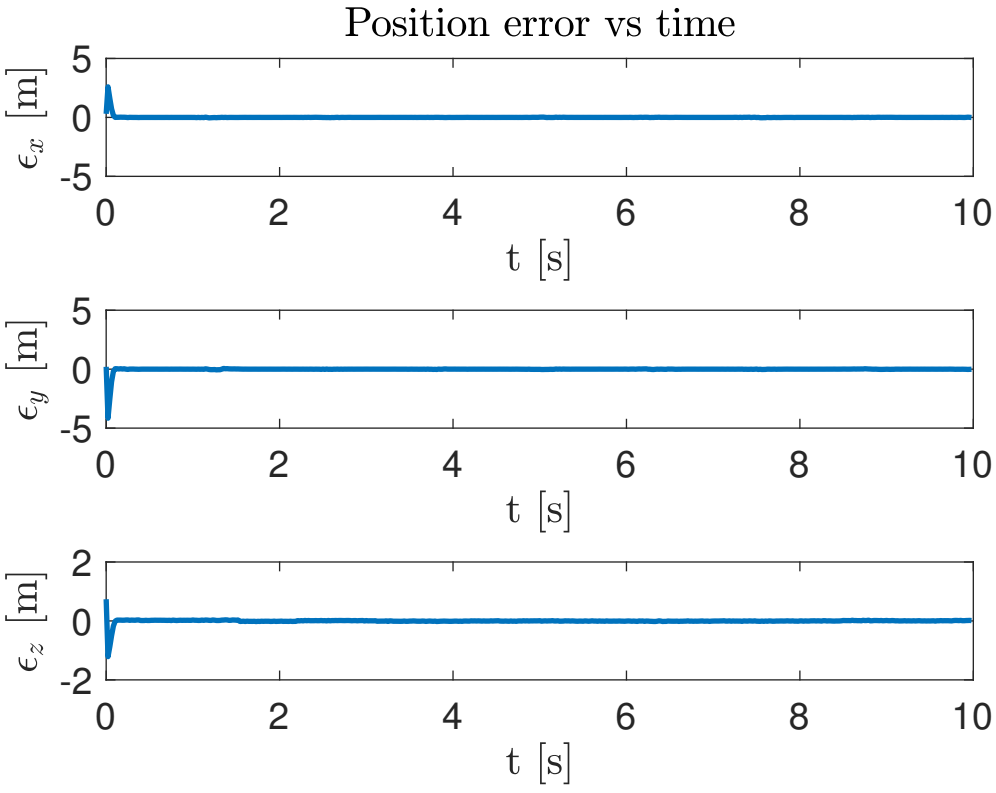

Figure 5.14: Relative position error obtained from the first simulated scenario.

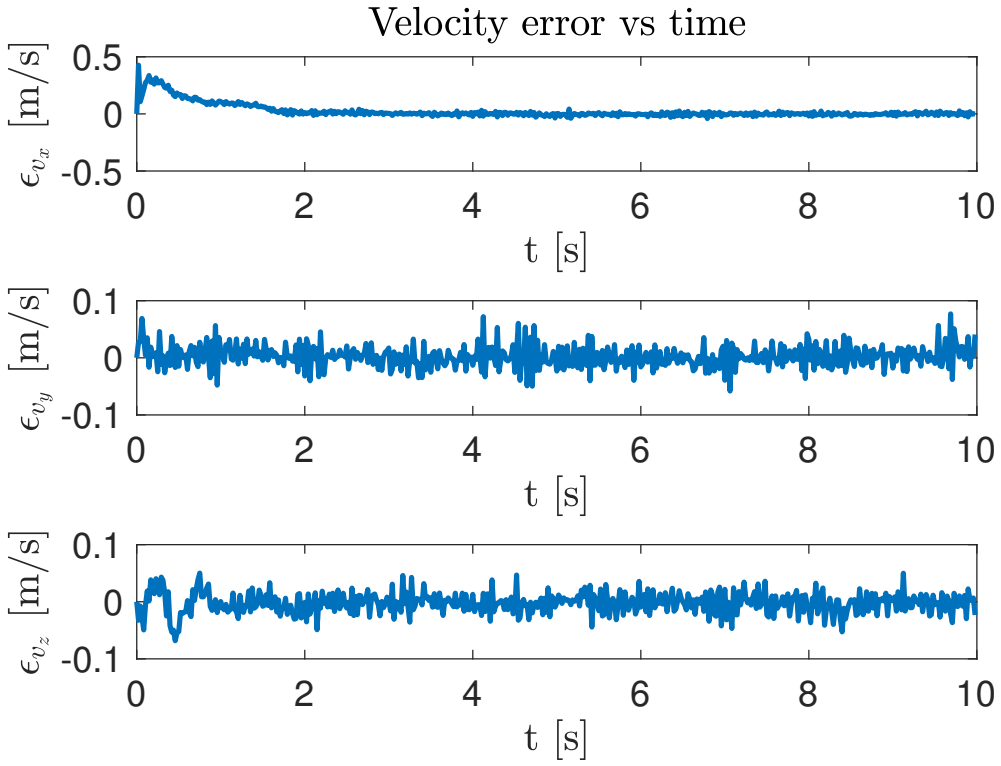

Figure 5.15: Relative velocity error obtained from the first simulated scenario.

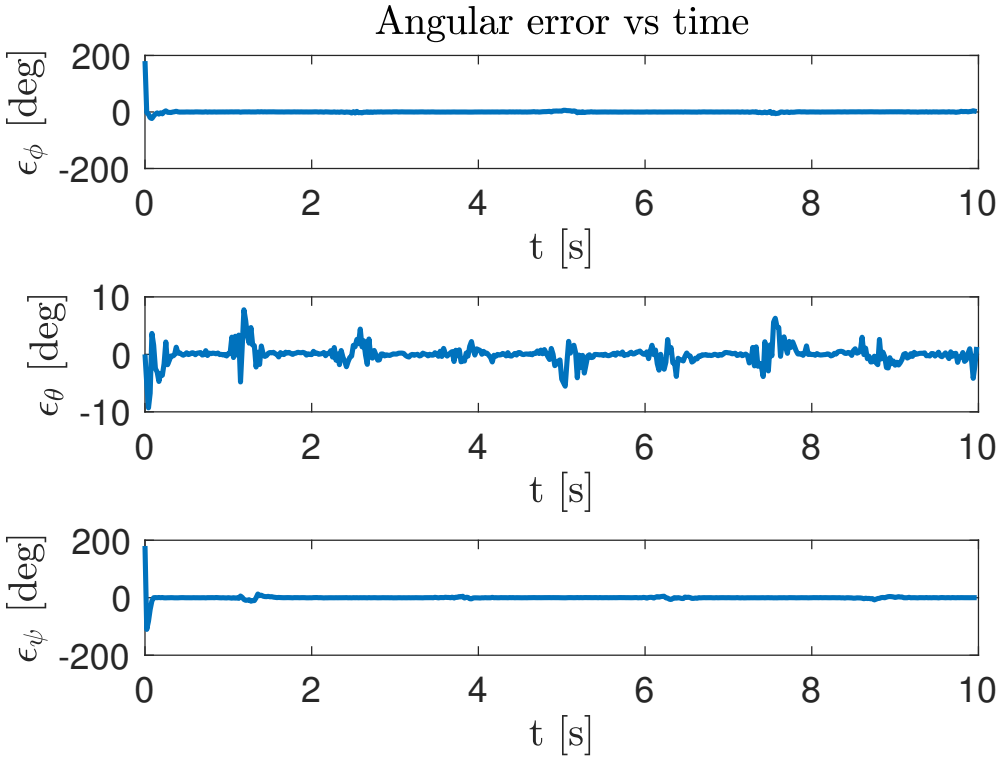

Figure 5.16: Relative attitude error obtained from the first simulated scenario.

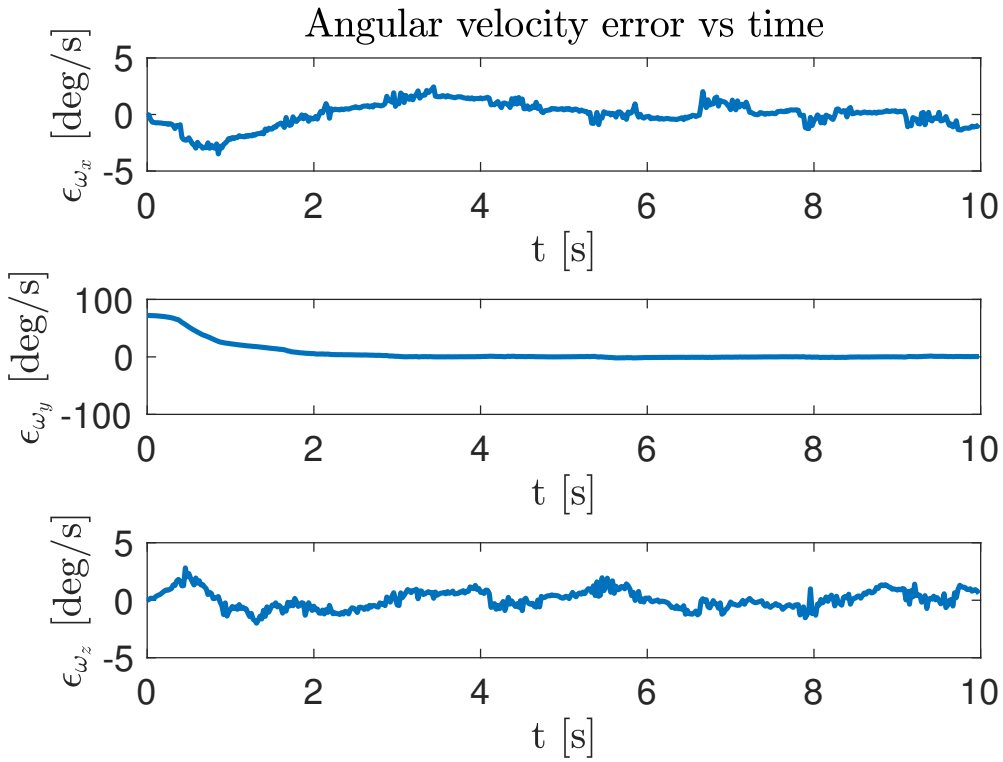

Figure 5.17: Relative angular velocity error obtained from the first simulated scenario.

Table 5.1: Tracking error performances of the navigation filter in the first simulated scenario.

First simulated scenario			
Parameter	Tracking error		
	mean	std dev.	max
ρ_x [m]	$2 \cdot 10^{-4}$	$6.3 \cdot 10^{-3}$	$1.7 \cdot 10^{-2}$
ρ_y [m]	$1 \cdot 10^{-3}$	$8.5 \cdot 10^{-3}$	$3.5 \cdot 10^{-2}$
ρ_z [m]	$4 \cdot 10^{-4}$	$8.6 \cdot 10^{-3}$	$1.9 \cdot 10^{-2}$
$\dot{\rho}_x$ [m/s]	$1.4 \cdot 10^{-3}$	$1.2 \cdot 10^{-2}$	$2.6 \cdot 10^{-2}$
$\dot{\rho}_y$ [m/s]	$2.1 \cdot 10^{-3}$	$1.8 \cdot 10^{-2}$	$7.6 \cdot 10^{-2}$
$\dot{\rho}_z$ [m/s]	$2.5 \cdot 10^{-3}$	$1.7 \cdot 10^{-2}$	$5.2 \cdot 10^{-2}$
ϕ [deg]	$4.3 \cdot 10^{-2}$	1.0	5.7
θ [deg]	$8.8 \cdot 10^{-2}$	1.3	6.2
ψ [deg]	$1.01 \cdot 10^{-1}$	1.5	4.1
ω_x [deg/s]	$3.1 \cdot 10^{-2}$	0.63	2.1
ω_y [deg/s]	$1.5 \cdot 10^{-1}$	0.58	1.4
ω_z [deg/s]	$2.2 \cdot 10^{-1}$	0.66	1.5

Second simulated scenario: small initial error

The second simulation scenario aims to assess the accuracy of the filter in tracking the relative state of the target. To this purpose, the fileter is initialized by setting the initial guess very close to the actual relative state vector. To limit the effects of the measurement noise a major weight is given to the state covariance matrix, which is defined by:

$$\begin{aligned}
\sigma_{\rho}^2 &= 10^{-2} \cdot [1,\ 1,\ 1]\ \mathrm{m}^2 \\
\sigma_{\dot{\rho}}^2 &= 10^{-4} \cdot [1,\ 1,\ 1]\ \mathrm{m}^2/\mathrm{s}^2 \\
\sigma_{q}^2 &= \cdot 10^{-6} \cdot [1,\ 1,\ 1,\ 1] \\
\sigma_{\omega}^2 &= 10^{-4} \cdot [1,\ 1,\ 1]\ \mathrm{deg}^2/\mathrm{s}^2.
\end{aligned}$$

The matrix P and Q, as well as the target dynamical state are the same as the first considered scenario.

Figures 5.18, 5.19, 5.20 and 5.21 shows the tracking error obtained when the dynamical model is trusted more with respect to the first scenario. The obtained results show that the filter dynamics show a better behavior compared to the previous case. However, oscillations in the error profiles are still visible, in particular as regards the estimated orientation and angular velocity.

Even if the filter is expected to eliminate the error oscillations, the results show that the measurement obtained by the image processing procedure introduce a non-negligible disturbance to the filter dynamics. In particular, the fluctuations of the error occurs whenever one of the target faces is seen with an high inclination angle. It is reasonable to assume that the ellipse detector, in that situation, is not able to determine the circle centroids with sufficient accuracy, introducing de facto a measurement error that periodically alters the estimated state.

Table 5.2 summarizes the performances of the filter in the second scenario showing the mean value, the standard deviation and the maximum value of the tracking error on the 12 motion parameters in the last 3 s of the simulation. In particular, if compared to Table 5.1, the relative state estimation in this second scenario is more accurate.

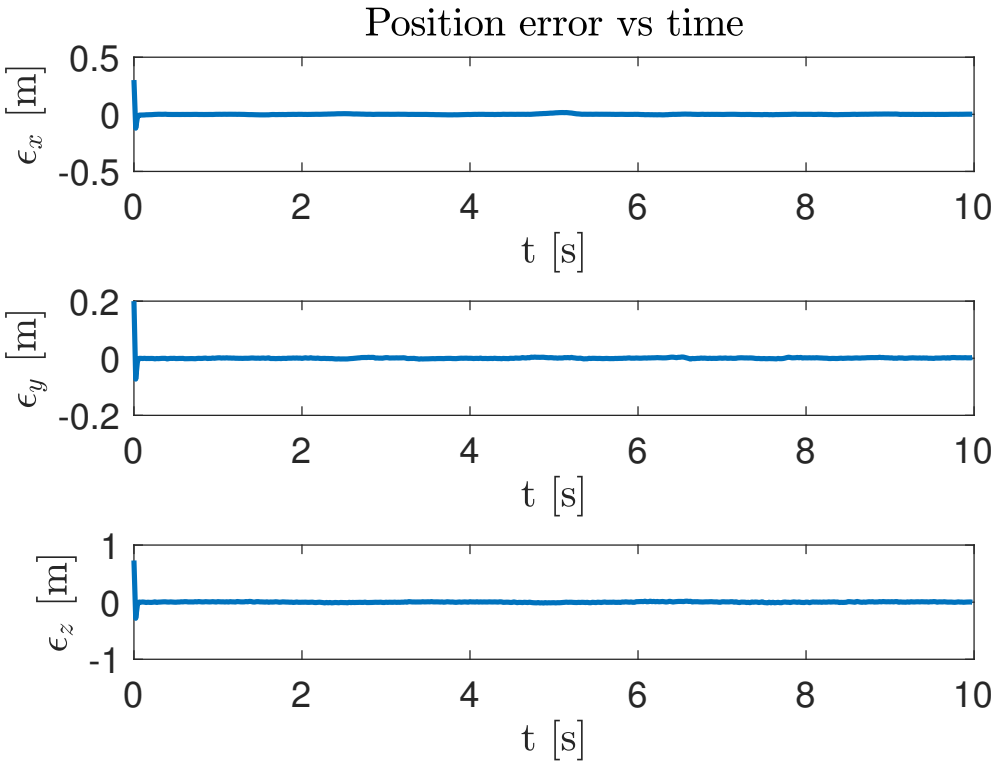

Figure 5.18: Relative position error obtained from the second simulated scenario.

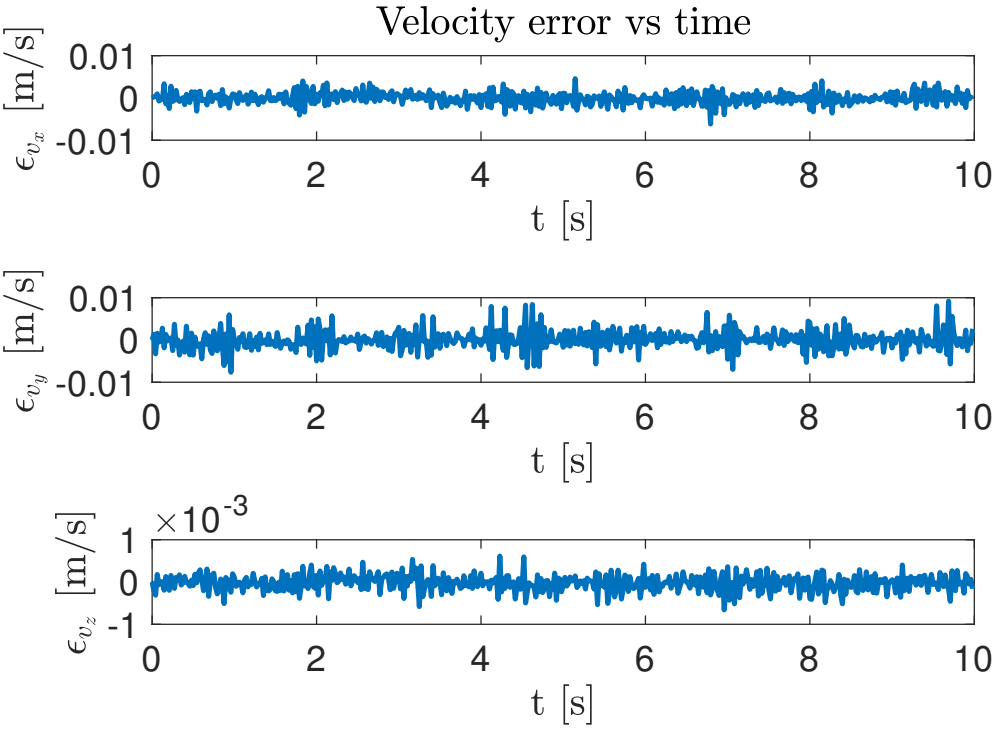

Figure 5.19: Relative velocity error obtained from the second simulated scenario.

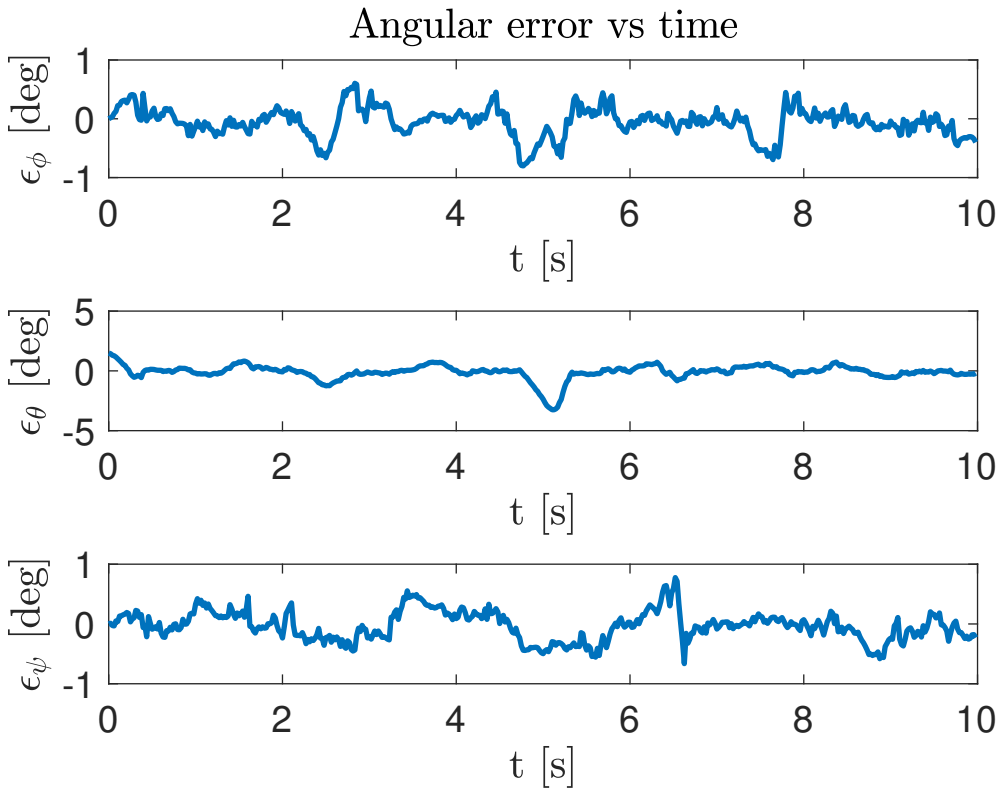

Figure 5.20: Relative attitude error obtained from the second simulated scenario.

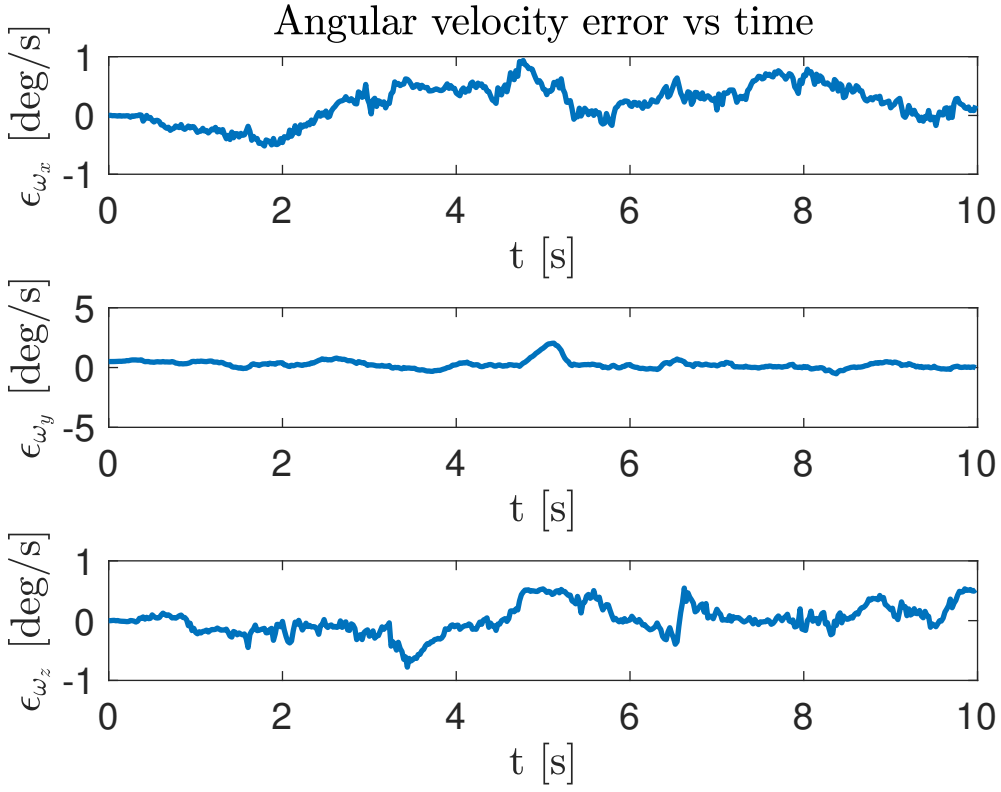

Figure 5.21: Relative angular velocity error obtained from the second simulated scenario.

Table 5.2: Tracking error performances of the navigation filter in the second simulated scenario.

Second simulated scenario			
Parameter	Tracking error		
	mean	std dev.	max
ρ_x [m]	$4 \cdot 10^{-4}$	$1.3 \cdot 10^{-3}$	$2.5 \cdot 10^{-2}$
ρ_y [m]	$7 \cdot 10^{-4}$	$1.1 \cdot 10^{-3}$	$3.3 \cdot 10^{-2}$
ρ_z [m]	$1.6 \cdot 10^{-3}$	$5.0 \cdot 10^{-3}$	$1.2 \cdot 10^{-2}$
$\dot{\rho}_x$ [m/s]	$< 1 \cdot 10^{-4}$	$1.3 \cdot 10^{-3}$	$3.5 \cdot 10^{-3}$
$\dot{\rho}_y$ [m/s]	$< 1 \cdot 10^{-4}$	$2.4 \cdot 10^{-3}$	$8.1 \cdot 10^{-3}$
$\dot{\rho}_z$ [m/s]	$< 1 \cdot 10^{-4}$	$2 \cdot 10^{-4}$	$< 1 \cdot 10^{-4}$
ϕ [deg]	$9.1 \cdot 10^{-2}$	$2.0 \cdot 10^{-1}$	$4.4 \cdot 10^{-1}$
θ [deg]	$1.3 \cdot 10^{-2}$	$3.0 \cdot 10^{-1}$	$7.3 \cdot 10^{-1}$
ψ [deg]	$8.5 \cdot 10^{-2}$	$1.7 \cdot 10^{-1}$	$5.2 \cdot 10^{-1}$
ω_x [deg/s]	$3.4 \cdot 10^{-1}$	$2.2 \cdot 10^{-1}$	$7.8 \cdot 10^{-1}$
ω_y [deg/s]	$7.4 \cdot 10^{-2}$	$1.9 \cdot 10^{-1}$	$4.8 \cdot 10^{-1}$
ω_z [deg/s]	$1.1 \cdot 10^{-1}$	$1.7 \cdot 10^{-1}$	$5.3 \cdot 10^{-1}$

5.6 Experimental tests

The current section presents the experimental activity performed in order to validate the numerical procedures described in the previous section by means of the SPARTANS facility.

The experimental setup consists of the following main components:

- Spacecraft simulator. A single spacecraft simulator is employed to reproduce the dynamic behavior of the target spacecraft: the spacecraft module is operational in its 3 degrees of freedom configuration such that only rotational displacements are allowed (i.e. the TM is replaced by an aluminum plate supporting the mechanical joints and the AM structure). The AM is equipped with five black plastic sheets forming an outer shell that allows the housing of (1) the circular fiducial markers employed for the visual navigation tasks and (2) the retro-reflective markers recognized by the Motion Capture system;

- DUO stereo camera. The stereo camera is responsible for feeding the navigation filter with visual measurements of the observed target at 10 Hz. The measure-

ment system is placed on top of the laboratory test table such that the target spacecraft is always inside the cameras field of view and it is kept fixed in space thanks to a custom-made aluminum support structure;

- Motion Capture system. The Motion Capture system is responsible for measuring the pose of the target spacecraft at 50 Hz, providing a reference trajectory which is used to assess the performances of the navigation filter.

Figure 5.22 presents the setup employed during the laboratory testing phase highlighting, in particular, the placement of both the spacecraft module and the stereo camera on the test table. Figure 5.23 shows three subsequent steps of the image processing procedure for one channel of the stereo rig: in particular, Figure 5.23a shows the acquired raw image, Figure 5.23b highlights all the candidate ellipses retrieved by means of the ellipse detector and Figure 5.23c illustrates the final result, in particular it shows the ellipses that describe the detected markers after the hypothesis-verification routine that filters out false detections.

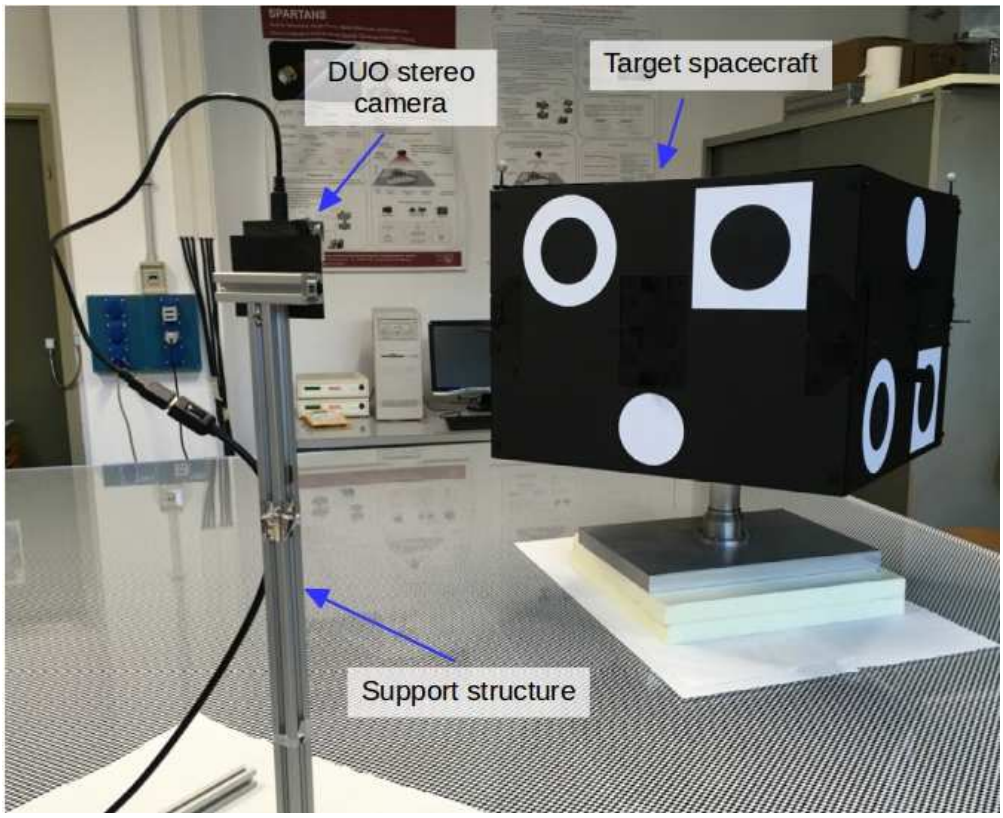

Figure 5.22: Laboratory setup employed during the experimental validation of the navigation filter.

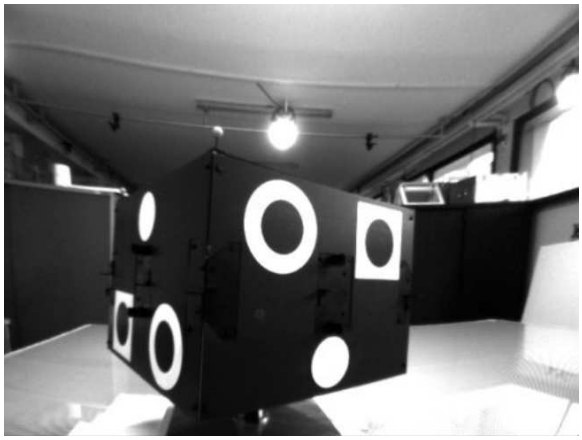

(a) Raw image acquired by one channel of the stereo camera.

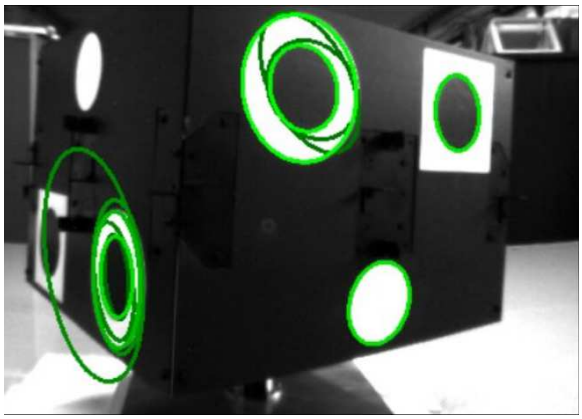

(b) Intermediate image processing output: the green circles show possible candidates to be recognized as markers.

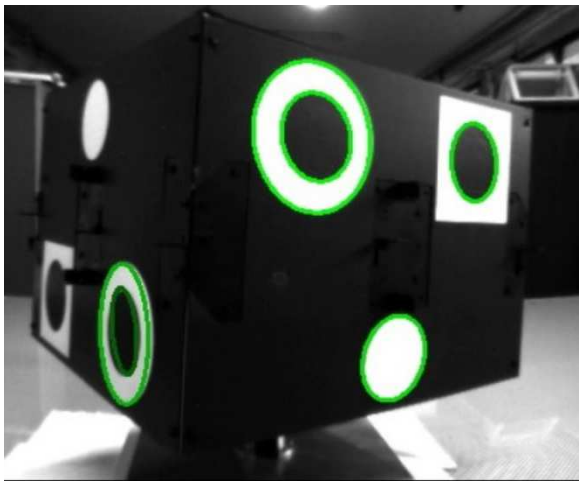

(c) Final image processing output: the green circles show the markers recognized after the hypothesis-verification procedure to exclude false detections.

Figure 5.23: Images acquired by one channel of the stereo camera during the image processing routine.

At the moment of performing the tests, the AM is still under development and therefore the rotational motion during the testing phase is imposed by applying an initial angular momentum by hand.

The EKF is initialized as follows:

- the measurement covariance matrix R is:

$$R = \text{diag}\left([1,\ 1,\ 1,\ 1,\ 200,\ 200,\ 200,\ 200,\ 2]\right) \text{ pixel}^2;$$

- the process covariance matrix Q is selected in order to ensure the convergence of the filter and it is defined as a diagonal matrix composed by:

$$\begin{aligned}
\sigma_\rho^2 &= 10^{-6} \cdot [1,\ 1,\ 1]\ \text{m}^2 \\
\sigma_{\dot\rho}^2 &= 10^{-6} \cdot [1,\ 1,\ 1]\ \text{m}^2/\text{s}^2 \\
\sigma_q^2 &= 10^{-4} \cdot [1,\ 1,\ 1,\ 1] \\
\sigma_\omega^2 &= 64 \cdot [1,\ 1,\ 1]\ \text{deg}^2/\text{s}^2;
\end{aligned}$$

- the initial guess provided to the EKF is:

$$\begin{aligned}
\rho_0 &= [0,\ 0,\ 0.82]\ \text{m} \\
\dot\rho_0 &= [0,\ 0,\ 0]\ \text{m/s} \\
q_0 &= [0,\ 1,\ 0,\ 0] \\
\omega_0 &= [0,\ 0,\ 0]\ \text{deg/s}.
\end{aligned}$$

The a priori knowledge of the AM motion allows to select the proper process covariance matrix Q: in particular it must be noticed that the value of σ_ω^2 is much higher that the one employed in the previous sections. This is due to the fact that, in the laboratory scenario, the AM is subjected to an impulsive angular acceleration which is the result of an external torque. However, the navigation filter is designed to deal with resident space objects whose dynamics is freely evolving. Therefore, in order to cope with the applied external torque, the observation model have to be trusted more.

In order to assess the performances of the EKF, the MC data are processed and compared to the ones provided by the navigation filter. Two main issues arise in reaching this objective: (1) the MC system and the EKF provide measurements of the target dynamic state respectively in global and in chaser reference frames and (2) since the two acquisition systems are not synchronized, the time delay between the two measurement segments must be estimated. The first problem is solved by estimating, through the solution of a minimization problem, the rigid transformation that aligns the

chaser reference frame with the global frame. Once all the measurements are referred to a common frame (i.e. the target frame T), the synchronization is performed by exploiting the cross-correlation between two signals coming from the two acquisition systems. In particular, the estimated time delay is equal to $\delta t = 0.8\,\mathrm{s}$.

Figure 5.24, 5.25, 5.26 and 5.27 show respectively the relative position, velocity, attitude and angular velocity: in particular, the red continuous lines refer to the EKF estimations while the blue dashed lines refer to the reference relative dynamic state estimated by the MC system.

It can be noticed that the dynamics of the EKF always converges to the reference trajectory. Two main phases can be identified in the performed maneuver: (1) a first phase ranging from 0 s to about 5 s in which the target is not moving and in which the EKF converges to the reference trajectory and (2) a phase ranging from 5 s to about 22 s in which the target is spinning about its z-axis with a slow decrease of the rotational velocity due to the friction characterizing the mechanical joints. Even if the angular acceleration is not negligible in the transition from the first to the second phase (the mean angular acceleration is of about 35 $\mathrm{deg}\,/\,\mathrm{s}^2$), the EKF proves to converge efficiently to the reference trajectory.

Figure 5.28, 5.29, 5.30 and 5.31 show respectively the tracking error on the relative position, velocity, attitude and angular velocity. By analyzing the error profiles it can be noticed that during the first phase of the acquisition, the tracking error converges to zero. When the external torque is applied to the target, as expected, the error level increases: this is evident in particular if the position and attitude errors are considered.

The estimated angular velocity and its corresponding error show a noisy profile: this is due to the high covariance associated to this vector within the navigation filter. Given the highly non-linear formulation of the filter, the oscillations of the angular velocity error profile have the effect of affecting all the estimated dynamic parameters: in particular, this effect is evident if Figure 5.28 and 5.30 are considered.

The estimated relative velocity, in contrast to the other dynamic quantities, shows the lower variation due to the measurement noise: this behavior is, as expected, due to the a priori knowledge of the motion imposed to the target.

Table 5.3 summarizes the tracking error performances of the navigation filter in the performed experimental test.

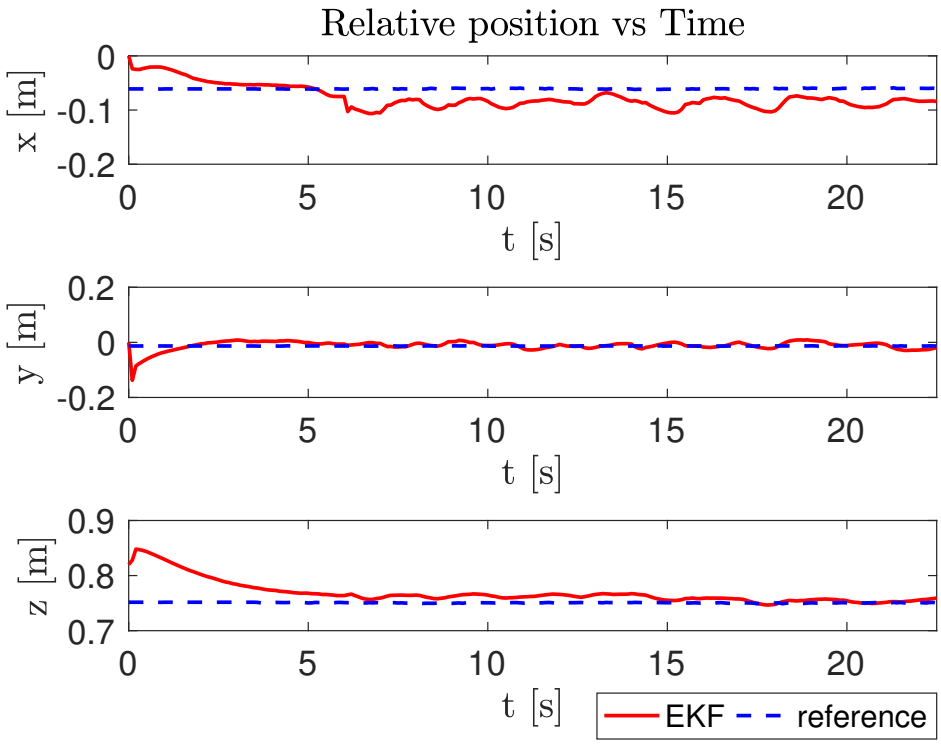

Figure 5.24: Relative position obtained during the experimental test. The red continuous line and the blue dashed lines refer respectively to EKF and MC data.

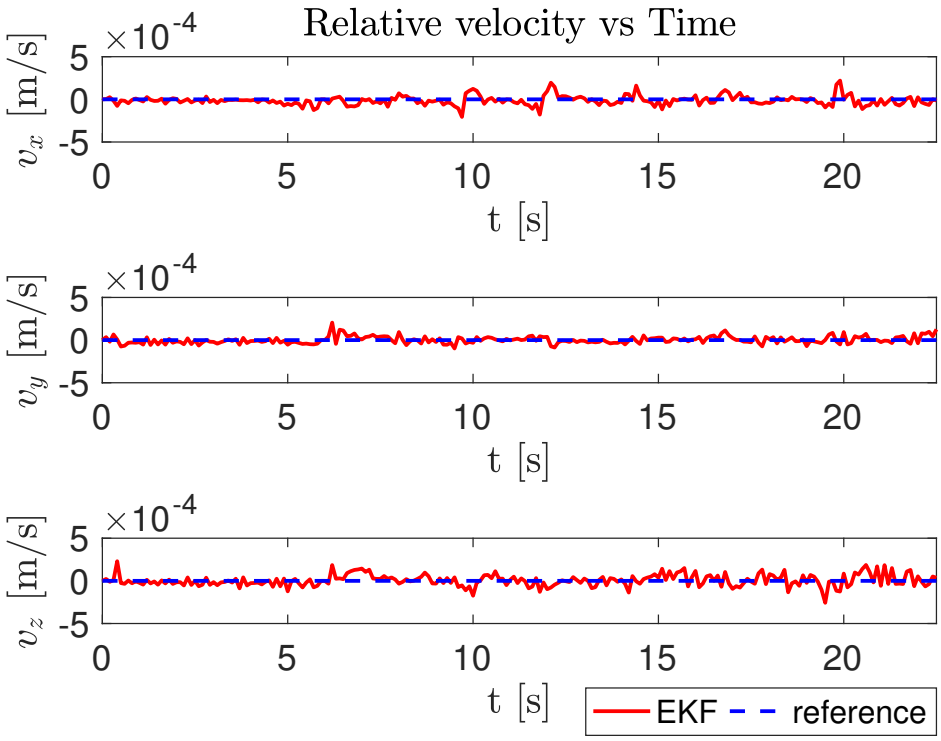

Figure 5.25: Relative velocity obtained during the experimental test. The red continuous line and the blue dashed lines refer respectively to EKF and MC data.

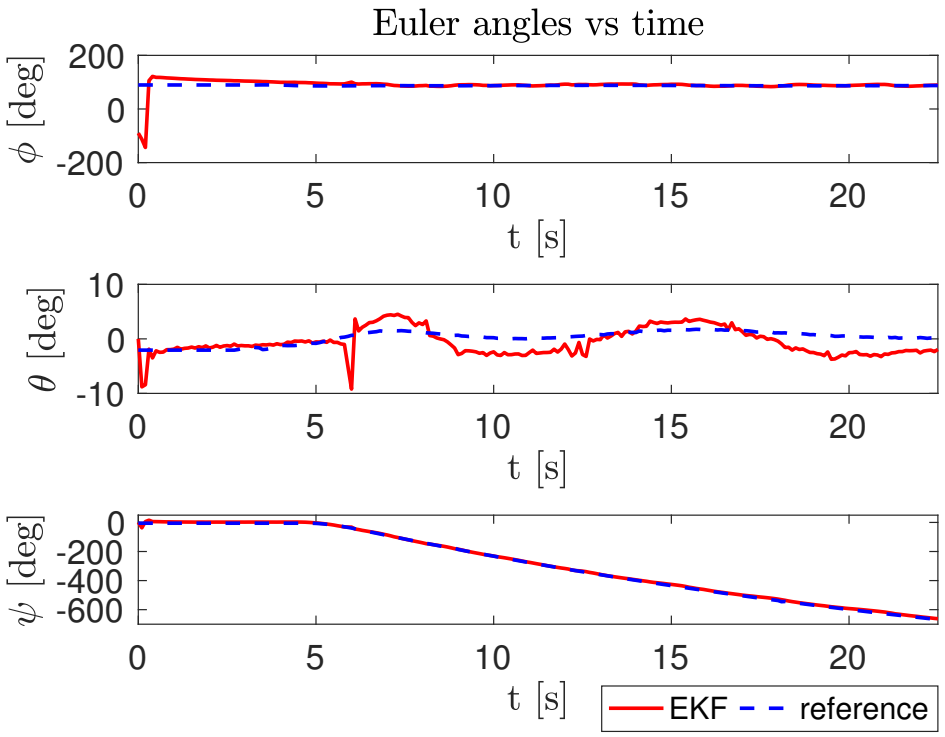

Figure 5.26: Relative attitude obtained during the experimental test. The red continuous line and the blue dashed lines refer respectively to EKF and MC data.

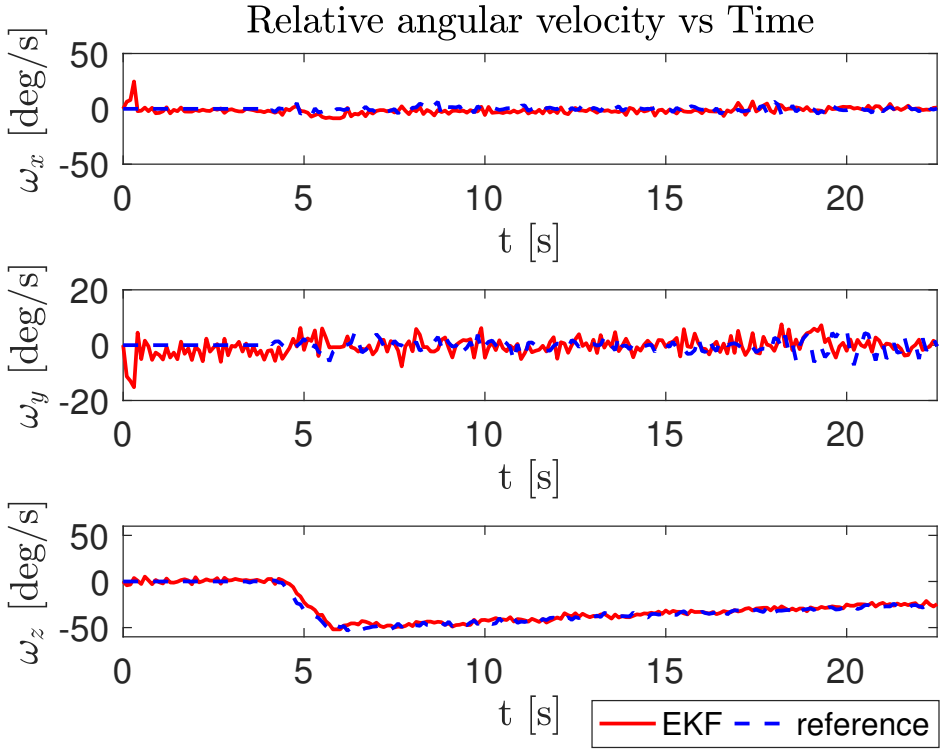

Figure 5.27: Relative angular velocity obtained during the experimental test. The red continuous line and the blue dashed lines refer respectively to EKF and MC data.

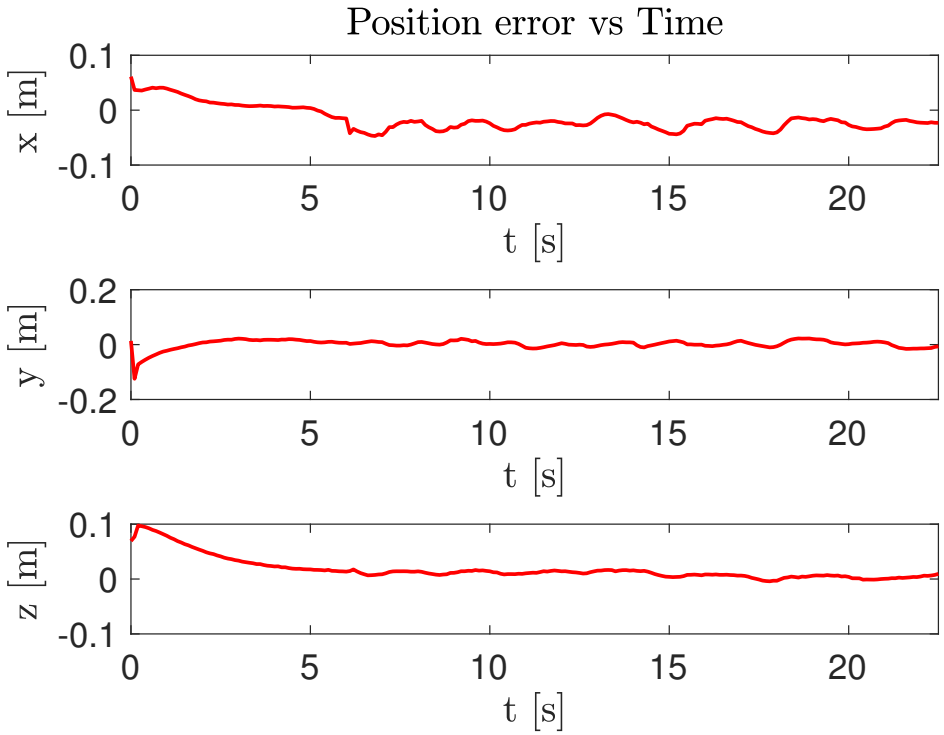

Figure 5.28: Relative position error obtained during the experimental test.

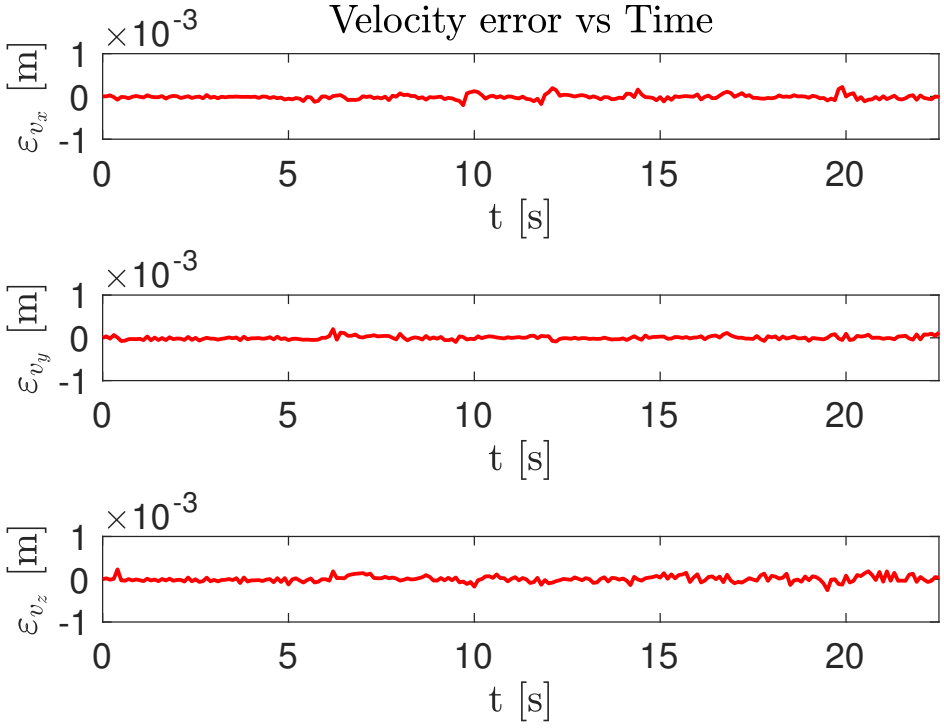

Figure 5.29: Relative velocity error obtained during the experimental test.

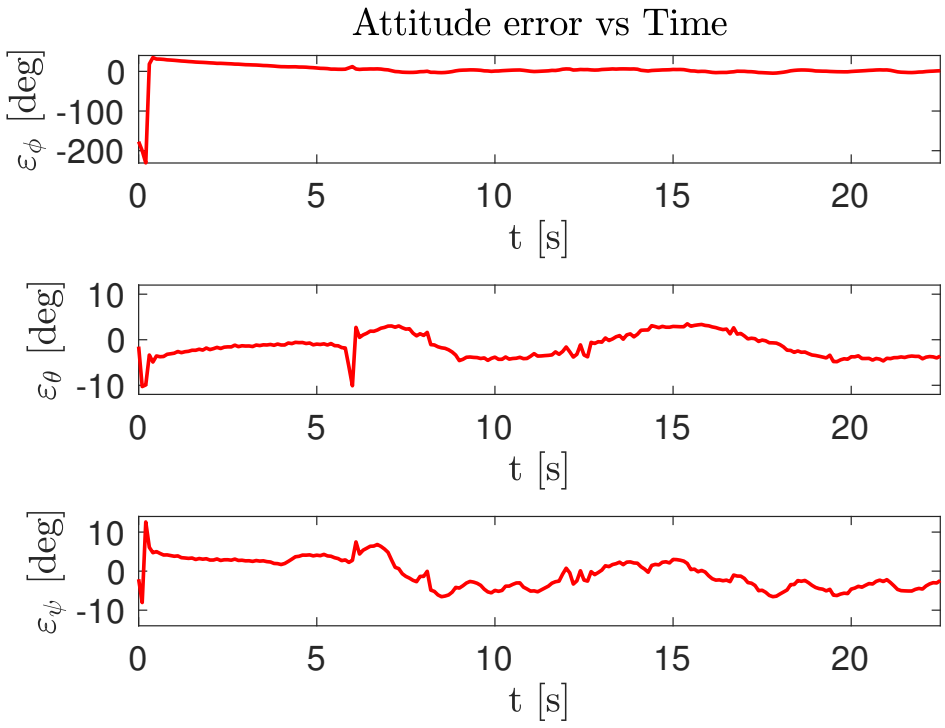

Figure 5.30: Relative attitude error obtained during the experimental test.

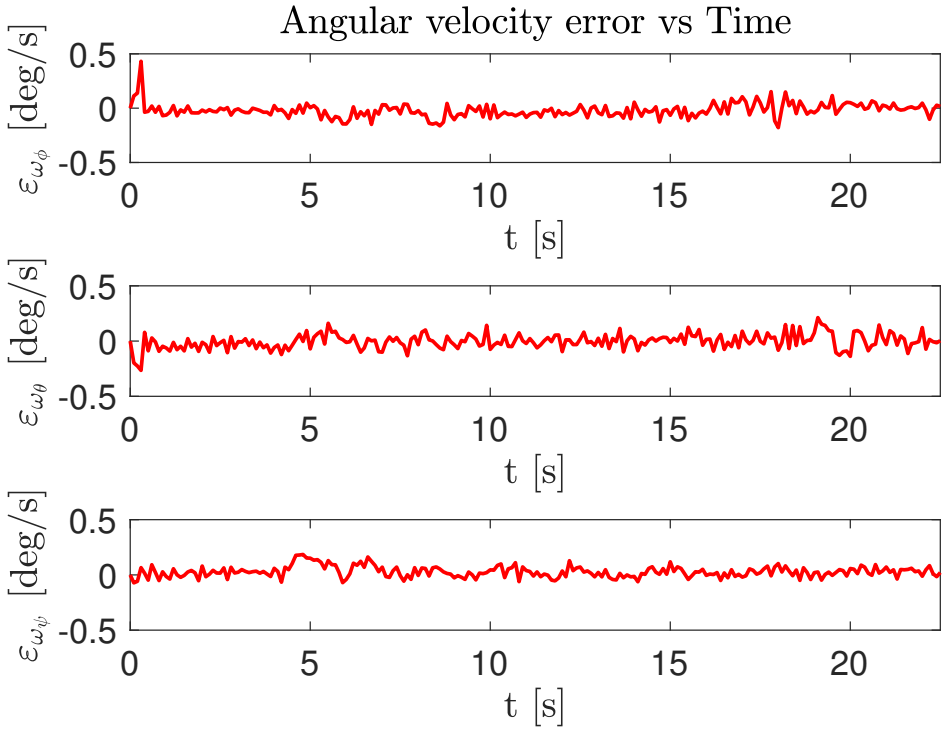

Figure 5.31: Relative angular velocity error obtained during the experimental test.

Table 5.3: Tracking error performances of the navigation filter for the experimental test.

Experimental test			
Parameter	Tracking error		
	mean	std dev.	max
ρ_x [m]	-0.0253	0.008	0.0421
ρ_y [m]	0.0032	0.0118	0.0224
ρ_z [m]	0.0028	0.0032	0.0094
$\dot{\rho}_x$ [m/s]	$< 1 \cdot 10^{-4}$	$1 \cdot 10^{-4}$	$2 \cdot 10^{-4}$
$\dot{\rho}_y$ [m/s]	$< 1 \cdot 10^{-4}$	$< 1 \cdot 10^{-4}$	$1 \cdot 10^{-4}$
$\dot{\rho}_z$ [m/s]	$< 1 \cdot 10^{-4}$	$1 \cdot 10^{-4}$	$1 \cdot 10^{-4}$
ϕ [deg]	-0.22	2.53	5.98
θ [deg]	-3.65	1.67	5.39
ψ [deg]	-4.50	1.23	7.48
ω_x [deg/s]	1.76	3.37	9.54
ω_y [deg/s]	1.98	3.86	9.41
ω_z [deg/s]	-0.70	1.95	4.70

The obtained experimental results show the effectiveness of the navigation filter also in the laboratory scenario. The tracking performances, however, are limited by the current state of development of the second AM: in particular, as soon as the construction of the AM will be completed, it will be possible controlling the attitude of the spacecraft module in order to compensate for friction, resulting in a torque free motion that will allow a finer tuning of the navigation filter and therefore leading to improved tracking performances.

5.7 Concluding Remarks

In the current chapter, the development of the stereoscopic vision-based navigation filter is presented. The navigation strategy relies on an Extended Kalman Filter that exploits only stereoscopic visual data to estimate the relative state of a target object with respect to a chaser satellite under the assumption that the geometry of the observed object is known.

The navigation filter is tested into two different scenarios. In the first scenario, the orbital dynamics of two spacecraft is reproduced by means of numerical simulations and

the filter performances are assessed showing the convergence of the proposed estimation approach with sub-centimeter and sub-degree accuracy. In case of measurement noise the filter still converges but it shows a less stable behavior that have to be corrected by a proper tuning of the process covariance matrix. The second scenario, instead, considers the environmental conditions that characterize the SPARTANS testbed with the aim of proposing a strategy to validate the navigation filter by performing experimental tests on the ground with two spacecraft modules of the SPARTANS facility. The proposed methodology relies on the development of a known pattern consisting of custom made circular contrasting markers and a corresponding image processing procedure to extract relevant data from the acquired images. The filter is therefore tested in this context showing the applicability of the estimation scheme also within the laboratory context on the ground. However, due to the measurement noise introduced by the image processing procedure, the filter requires to be provided with a reliable first tentative state at the moment of the initialization: if this condition is fulfilled, the relative dynamic state is estimated with centimeter and degree accuracy.

Chapter 6

Conclusions

The aim of my Ph.D. activities has been focused on the development and testing of vision based estimation strategies for relative navigation tasks in the context of Spacecraft Formation Flight and proximity operations. This objective was achieved by means of both numerical simulations and experimental tests.

During my doctoral activities, a set of software tools has been developed to simulate the behavior of spacecraft operating on orbit, allowing to validate numerically vision based navigation strategies. The experimental validation in a relevant and representative environment of the proposed strategies was possible thanks to the employment of the SPARTANS ground-based testbed, under development at the Center of Studies and Activities for Space (CISAS) "G. Colombo" of the University of Padova. This facility consists of robotic units that allow the reproduction, in a controlled environment, of the relative position and attitude motions of satellites operating in formation or in close proximity, allowing therefore to extensively study GN&C strategies in a controllable and easily accessible environment. Each unit of the simulator is characterized by 5 degrees of freedom, 3 rotational and 2 translational, and features 5 main subsystems that allow the autonomous execution of attitude and position maneuvers.

The first activity of my Ph.D. concerned the characterization of a monocular vision system for relative pose determination of a cooperative spacecraft. An original custom-made set of fiducial markers was proposed along with the required image analysis procedure to extract relevant points from the acquired images. The estimation of the relative pose is obtained by solving the perspective-from-three points problem followed by a subsequent pose refinement procedure that exploits first an iterative RANSAC scheme for eliminating false or inaccurate matchings and subsequently a non-linear

optimization to further refine the pose. The metrological performances of the proposed approach were assessed following an experimental approach: known displacements were imposed to the satellite mock-up and, by comparing the estimated poses with the imposed ones, the measurement error was characterized. The average accuracy was around 1 cm and 1 deg on the relative position and attitude respectively, and in particular, the approach showed to work better when the camera optical axis was inclined of at least 20 deg with respect to the normal direction of the target surface.

This activity was followed by the development of the global navigation system for the SPARTANS testbed. In particular, the estimation approach followed subsequent development phases, implementing in a first phase a measurement system based on the joint employment of a monocular vision system and a set of three Optical Flow Sensors and, in a second phase, the employment of a Motion capture system in substitution of the monocular system. This activity enabled the possibility of gathering reference measurement to be employed as groundtruth to assess the performances of the relative navigation strategies and, in general, of the adopted GN&C approaches. Moreover, the global navigation system allowed to update, with sub-millimeter and sub-degree accuracy, the absolute state of the spacecraft units in a GPS-like manner.

The last activity of my Ph.D. regarded the development of a navigation strategy, based on an Extended Kalman filter, aimed at estimating the relative state of a target spacecraft by employing the sole measurements provided by a stereoscopic vision system, under the assumption that the geometry and the inertial properties of the target are known. The filter was designed in order to be capable of overcoming the typical linearization assumptions proper of the linearized relative translational model proposed by Clohessy and Wiltshire. The effectiveness of the proposed strategy was validated at first by means of numerical simulations in two different scenarios. In the first case, an orbital scenario was considered and in particular the dynamics of two satellites flying in a leader-follower formation is simulated. In the second case, the operative conditions of the SPARTANS laboratory were reproduced by means of a 3D simulated environment in sight of the experimental validation of the navigation filter by means of the spacecraft units. A simple pattern based on contrasting circular markers was employed to generate a set of known landmarks on the surface of the target satellite and relative image processing procedure was presented. Finally, the estimation approach was validated by means of laboratpry testing. Even if further investigation about the effects

of the measurement noise on the filter are required, the proposed navigation algorithm proved to be capable of estimating the relative dynamic state of an observed target with centimeter-level and degree-level accuracy.

As regards the future activities, the SPARTANS team is working with the aim of performing proximity coordinated maneuvers between two units of the spacecraft simulator. To reach this objective, it is mandatory (1) to complete the construction of the second spacecraft simulator and (2) to optimize the software procedures in order to ensure the execution of the GN&C algorithms in real-time. The final objective is to perform coordinated maneuvers exploiting visual data provided by a stereo camera and processed by means of the navigation filter as presented in the current work, and commanding control actions computed by means of either PID or MPC controllers, as discussed in [11].

Bibliography

[1] W Clohessy and R Wiltshire. Terminal guidance system for satellite rendezvous. *SYSTEM*, 4(1), 1960.

[2] Elaine M Hinman and David M Bushman. Soviet automated rendezvous and docking system overview. 1991.

[3] Simone D'Amico, Jean-Sebastien Ardaens, and Sergio De Florio. Autonomous formation flying based on gps—prisma flight results. *Acta Astronautica*, 82(1):69–79, 2013.

[4] Jana L. Schwartz, Mason A. Peck, and Christopher D. Hall. Historical review of air-bearing spacecraft simulators. *Journal of Guidance, Control and Dynamics*, 2003.

[5] M. Sabatini, G. B. Palmerini, and P. Gasbarri. A testbed for visual based navigation and control during space rendezvous operations. *Acta Astronautica*, 117:184–196, dec 2015.

[6] M. W. Regehr, A. B. Acikmese, A. Ahmed, M. Aung, K. C. Clark, P. MacNeal, J. Shields, G. Singh, R. Bailey, C. Bushnell, A. Hicke, B. Lytle, and R. E. Rasmussen. The formation control testbed. In *2004 IEEE Aerospace Conference Proceedings (IEEE Cat. No.04TH8720)*, volume 1, page 564 Vol.1, March 2004.

[7] Markus Schlotterer and Stephan Theil. Testbed for on-orbit servicing and formation flying dynamics emulation. In *AIAA Guidance, Navigation, and Control Conference*, pages 2–5, 2010.

[8] Panagiotis Tsiotras. Astros: A 5dof experimental platform for research in spacecraft proximity operations. Georgia Institute of Technology, 2014.

[9] Simon Nolet. The spheres navigation system: from early development to on-orbit testing. In *In AIAA Guidance, Navigation and Control Conference and Exhibit. AIAA*, 2007.

[10] Sergio Tronco. *Development and testing of hardware simulator for satellite proximity maneuvers and formation flying.* PhD thesis, January 2016.

[11] Andrea Valmorbida. *Development and testing of model predictive control strategies for spacecraft formation flying.* PhD thesis, January 2014.

[12] Mark O Hilstad, John P Enright, Arthur G Richards, and Swati Mohan. The spheres guest scientist program. *Space Systems Laboratory, Massachusetts Institute of Technology*, 2003.

[13] Carsten Schedlinski and Michael Link. A survey of current inertia parameter identification methods. *Mechanical systems and signal processing*, 15(1):189–211, 2001.

[14] Richard T Howard, Andrew F Heaton, Robin M Pinson, and Connie K Carrington. Orbital express advanced video guidance sensor. In *Aerospace Conference, 2008 IEEE*, pages 1–10. IEEE, 2008.

[15] John A Christian, Shane B Robinson, Christopher N D'Souza, and Jose P Ruiz. Cooperative relative navigation of spacecraft using flash light detection and ranging sensors. *Journal of Guidance, Control, and Dynamics*, 2014.

[16] John A Christian and Scott Cryan. A survey of lidar technology and its use in spacecraft relative navigation. In *Proceedings of the AIAA Guidance, Navigation, and Control Conference, Boston, MA, USA*, pages 19–22, 2013.

[17] Martin A Fischler and Robert C Bolles. Random sample consensus: a paradigm for model fitting with applications to image analysis and automated cartography. *Communications of the ACM*, 24(6):381–395, 1981.

[18] Yalin Xiong and K. Turkowski. Creating image-based vr using a self-calibrating fisheye lens. In *Proceedings of IEEE Computer Society Conference on Computer Vision and Pattern Recognition*, pages 237–243, Jun 1997.

[19] D. C. Brown. Decentering Distortion of Lenses. *Photometric Engineering*, 32(3):444–462, 1966.

[20] CC Slama, C Theurer, and SW Henriksen. Manual of photogrammetry (no. ed. 4) american society of photogrammetry. 1980.

[21] R. Tsai. A versatile camera calibration technique for high-accuracy 3d machine vision metrology using off-the-shelf tv cameras and lenses. *IEEE Journal on Robotics and Automation*, 3(4):323–344, August 1987.

[22] Zhengyou Zhang. A flexible new technique for camera calibration. *IEEE Trans. Pattern Anal. Mach. Intell.*, 22(11):1330–1334, November 2000.

[23] C Brown Duane. Close-range camera calibration. *Photogramm. Eng*, 37(8):855–866, 1971.

[24] Bruno Caprile and Vincent Torre. Using vanishing points for camera calibration. *International journal of computer vision*, 4(2):127–139, 1990.

[25] Richard Szeliski. *Computer Vision: Algorithms and Applications*. Texts in Computer Science. Springer, 2011.

[26] Sergio Garrido-Jurado, Rafael Muñoz-Salinas, Francisco José Madrid-Cuevas, and Manuel Jesús Marín-Jiménez. Automatic generation and detection of highly reliable fiducial markers under occlusion. *Pattern Recognition*, 47(6):2280–2292, 2014.

[27] Hirokazu Kato and Mark Billinghurst. Marker tracking and hmd calibration for a video-based augmented reality conferencing system. In *Augmented Reality, 1999.(IWAR'99) Proceedings. 2nd IEEE and ACM International Workshop on*, pages 85–94. IEEE, 1999.

[28] M. Fiala. Designing highly reliable fiducial markers. *IEEE Transactions on Pattern Analysis and Machine Intelligence*, 32(7):1317–1324, July 2010.

[29] Brent E Tweddle and Alvar Saenz-Otero. Relative computer vision-based navigation for small inspection spacecraft. *Journal of Guidance, Control, and Dynamics*, 2014.

[30] Nobuyuki Otsu. A threshold selection method from gray-level histograms. *IEEE transactions on systems, man, and cybernetics*, 9(1):62–66, 1979.

[31] David H Douglas and Thomas K Peucker. Algorithms for the reduction of the number of points required to represent a digitized line or its caricature. *Cartographica: The International Journal for Geographic Information and Geovisualization*, 10(2):112–122, 1973.

[32] Francesc Moreno-Noguer, Vincent Lepetit, and Pascal Fua. Accurate non-iterative o (n) solution to the pnp problem. In *Computer vision, 2007. ICCV 2007. IEEE 11th international conference on*, pages 1–8. IEEE, 2007.

[33] Dawei Leng and W. Sun. Finding all the solutions of pnp problem. In *2009 IEEE International Workshop on Imaging Systems and Techniques*, pages 348–352, May 2009.

[34] Daniel F. Dementhon and Larry S. Davis. Model-based object pose in 25 lines of code. *International Journal of Computer Vision*, 15(1):123–141, Jun 1995.

[35] Richard Hartley and Andrew Zisserman. *Multiple view geometry in computer vision*. Cambridge university press, 2003.

[36] Yi Ma, Stefano Soatto, Jana Kosecka, and S Shankar Sastry. *An invitation to 3-d vision: from images to geometric models*, volume 26. Springer Science & Business Media, 2012.

[37] Bert M Haralick, Chung-Nan Lee, Karsten Ottenberg, and Michael Nölle. Review and analysis of solutions of the three point perspective pose estimation problem. *International journal of computer vision*, 13(3):331–356, 1994.

[38] Long Quan and Zhongdan Lan. Linear n-point camera pose determination. *IEEE Transactions on pattern analysis and machine intelligence*, 21(8):774–780, 1999.

[39] Xiao-Shan Gao, Xiao-Rong Hou, Jianliang Tang, and Hang-Fei Cheng. Complete solution classification for the perspective-three-point problem. *IEEE transactions on pattern analysis and machine intelligence*, 25(8):930–943, 2003.

[40] K Somani Arun, Thomas S Huang, and Steven D Blostein. Least-squares fitting of two 3-d point sets. *IEEE Transactions on pattern analysis and machine intelligence*, (5):698–700, 1987.

[41] Berthold KP Horn, Hugh M Hilden, and Shahriar Negahdaripour. Closed-form solution of absolute orientation using orthonormal matrices. *JOSA A*, 5(7):1127–1135, 1988.

[42] Berthold KP Horn. Closed-form solution of absolute orientation using unit quaternions. *JOSA A*, 4(4):629–642, 1987.

[43] Laurent Kneip, Davide Scaramuzza, and Roland Siegwart. A novel parametrization of the perspective-three-point problem for a direct computation of absolute camera position and orientation. In *Computer Vision and Pattern Recognition (CVPR), 2011 IEEE Conference on*, pages 2969–2976. IEEE, 2011.

[44] Adriaan Van den Bos. *Parameter estimation for scientists and engineers*. John Wiley & Sons, 2007.

[45] JCGM/WG 1 2008 Working Group et al. Evaluation of measurement data–guide to the expression of uncertainty in measurement. Technical report, Tech. Rep. JCGM 100, 2008.

[46] Metrology JCfGi. Evaluation of measurement data—supplement 1 to the guide to expression of uncertainty in measurement; propagation of distributions using a monte carlo method. *Bureau International des Poids et Mesures*, 2008.

[47] Simon Nolet, Alvar Saenz-Otero, David W Miller, and Amer Fejzic. Spheres operations aboard the iss: Maturation of gn&c algorithms in microgravity. In *30th Annual AAS Guidance and Control Conference*, pages 07–042, 2007.

[48] H. Lim, H. Lee, and H. J. Kim. Onboard flight control of a micro quadrotor using single strapdown optical flow sensor. In *2012 IEEE/RSJ International Conference on Intelligent Robots and Systems*, pages 495–500, Oct 2012.

[49] Sungbok Kim and Sanghyup Lee. Robust velocity estimation of an omnidirectional mobile robot using a polygonal array of optical mice. *International Journal of Control, Automation, and Systems*, 6(5):713–721, 2008.

[50] Andrés F Rodrıguez, Evan Andersen, Justin M Bradley, and Clark N Taylor. Wind estimation using an optical flow sensor on a miniature air vehicle. In *AIAA Guidance, Navigation and Control Conference and Exhibit*, 2007.

[51] Andrea Bonarini, Matteo Matteucci, and Marcello Restelli. A kinematic-independent dead-reckoning sensor for indoor mobile robotics. In *Intelligent Robots and Systems, 2004.(IROS 2004). Proceedings. 2004 IEEE/RSJ International Conference on*, volume 4, pages 3750–3755. IEEE, 2004.

[52] Andrea Valmorbida, Sergio Tronco, Mattia Mazzucato, Stefano Debei, and Enrico C Lorenzini. Optical flow sensor based localization system for a cooperating spacecraft testbed. In *Metrology for Aerospace (MetroAeroSpace), 2015 IEEE*, pages 568–573. IEEE, 2015.

[53] M. Mazzucato, A. Valmorbida, S. Tronco, M. Costantini, S. Debei, and E. Lorenzini. Development of a camera-aided optical mouse sensors based localization system for a free floating planar robot. In *2016 IEEE Metrology for Aerospace (MetroAeroSpace)*, pages 388–392, June 2016.

[54] T Weismuller and M Leinz. Gn&c technology demonstrated by the orbital express autonomous rendezvous and capture sensor system. In *29th annual AAS guidance and control conference*, pages 4–8. AAS Breckenridge, 2006.

[55] Per Bodin, Ron Noteborn, Robin Larsson, Thomas Karlsson, Simone D'Amico, Jean Sebastien Ardaens, Michel Delpech, and Jean-Claude Berges. The prisma formation flying demonstrator: Overview and conclusions from the nominal mission. *Advances in the Astronautical Sciences*, 144(2012):441–460, 2012.

[56] Bryan L Benedict. Investing in satellite life extension–fleet planning options for spacecraft owner/operators. In *AIAA SPACE 2014 Conference and Exposition*, page 4445, 2014.

[57] Jerry E LeCroy, Dean S Hallmark, and Richard T Howard. Effects of optical artifacts in a laser-based spacecraft navigation sensor. In *SPIE Conference Proceedings*, volume 6555, pages 1–11, 2007.

[58] Giancarmine Fasano, Michele Grassi, and Domenico Accardo. A stereo-vision based system for autonomous navigation of an in-orbit servicing platform. *AIAA Infotech@ Aerospace*, 2009.

[59] Brent Edward Tweddle. *Computer vision-based localization and mapping of an unknown, uncooperative and spinning target for spacecraft proximity operations.* PhD thesis, Massachusetts Institute of Technology, Department of Aeronautics and Astronautics, 2013.

[60] Shai Segal, Avishy Carmi, and Pini Gurfil. Stereovision-based estimation of relative dynamics between noncooperative satellites: Theory and experiments. *IEEE Transactions on Control Systems Technology*, 22(2):568–584, 2014.

[61] Vincenzo Pesce, Michèle Lavagna, and Riccardo Bevilacqua. Stereovision-based pose and inertia estimation of unknown and uncooperative space objects. *Advances in Space Research*, 59(1):236–251, 2017.

[62] Roberto Opromolla, Giancarmine Fasano, Giancarlo Rufino, and Michele Grassi. A review of cooperative and uncooperative spacecraft pose determination techniques for close-proximity operations. *Progress in Aerospace Sciences*, 93:53–72, 2017.

[63] David J. Heeger and Allan D. Jepson. Subspace methods for recovering rigid motion i: Algorithm and implementation. *International Journal of Computer Vision*, 7(2):95–117, 1 1992.

[64] Rudolph Emil Kalman et al. A new approach to linear filtering and prediction problems. *Journal of basic Engineering*, 82(1):35–45, 1960.

[65] Claus Bendtsen and Ole Stauning. Fadbad, a flexible c++ package for automatic differentiation. Technical report, Technical Report IMM–REP–1996–17, Department of Mathematical Modelling, Technical University of Denmark, Lyngby, Denmark, 1996.

[66] John L Barron, David J Fleet, and Steven S Beauchemin. Performance of optical flow techniques. *International journal of computer vision*, 12(1):43–77, 1994.

[67] L Gatrell, WILLIAM Hoff, and Cheryl Sklair. Robust image features: Concentric contrasting circles and their image extraction. *Proc. of Cooperative Intelligent Robotics in Space, Washington, USA*, 1991.

[68] Michele Fornaciari and Andrea Prati. Very fast ellipse detection for embedded vision applications. In *Distributed Smart Cameras (ICDSC), 2012 Sixth International Conference on*, pages 1–6. IEEE, 2012.